SILESIAN UNIVERSITY OF TECHNOLOGY

FACULTY OF CHEMISTRY

Electrochemical and spectroelectrochemical studies of electronic interactions in donor-acceptor-donor (DAD) and donor-acceptor (DA) systems

Doctoral Thesis

by

Marharyta Vasylieva

Supervisor: Dr hab. inż. Przemysław Data, prof. PŚ.

Co-supervisor: Dr inż. Małgorzata Czichy

Gliwice 2021

Acknowledgments

I am grateful to my supervisor Prof. Przemyslaw Data for introducing me to the issues of conductive polymers, indicating research topics and scientific supervision.

I would like to thank the co-supervisor dr. Malgorzata Czichy for her time, fruitful discussions, and valuable advice.

The work was funded as part of the Marie Skłodowska-Curie Actions of the European Union's Horizon 2020 Research and Innovation Programme. EXCILIGHT (Donor-Acceptor light-emitting exciplexes as materials for easily to tailor ultra-efficient OLED lighting) H2020-MSCA-ITN-2015/6744990.

Donor-Acceptor Light Emitting EXCIplexes as Materials for Easy-to-Tailor Ultra-efficient OLED LIGHTing
H2020-MSCA-ITN-2015/ 674990

Table of Contents

Glossary 5

1 Introduction 7

2 Aim and scope of work 9

3 Literature review 10

3.1 Molecular theory 10

3.2 Fundamental electronic parameters 14

3.3 Fundamentals of electrochemistry 18

3.4 Charge carriers 23

3.5 Conjugated compounds and polymers 28

3.6 OLED design 31

3.7 Principles of thermally activated delayed fluorescent molecule design 34

3.8 Acceptor units 37

3.8.1 1,8-Naphtalimide 37

3.8.2 Tetrazine 38

3.9 Donor units 41

3.9.1 Carbazole 41

3.9.2 Phenoxazine 44

3.9.3 Phenothiazine 46

3.9.4 Dimethyl-acridine (DMAC) 49

4 Experimental part 51

4.1 Materials and techniques 51

4.2 List of compounds 58

5 Results and discussion 61

5.1 Analysis of compounds based on the NPTI acceptor unit 61

5.2 Analysis of compounds based on the DA acceptor unit. 81

5.3 Analysis of compounds based on the TA acceptor unit. 96

5.4 Polymerization 107

6 Conclusions 120

7 Bibliography 123

8 Supplements 129

8.1 Supplement 1 129

8.2 Supplement 2 136

8.3 Supplement 3 142

8.4 Supplement 4 151

8.5 Supplement 5 158

Glossary

ΔEst	The singlet-triplet energy gap
a.u.	Arbitrary units
AE	Auxiliary electrode
BODIPY	4,4-difluoro-4-bora-3a,4a-diaza-s-indacene
CBZ	Carbazole substituent or donor group
CV	Cyclic Voltammetry
DA	[*d*]pyridazine acceptor group
DCM	Dichloromethane
DD	diradical dication
DFT	Density Functional Theory
DMAC	Dimethylacridine substituent or donor group
DPV	Differential Pulse V
EA	Electron affinity
E_g	Energy gap
EML	Emission layer
EQE	External quantum efficiency of the device
ESR	Electron Spin Resonance
ETL	Electron transporting layer
Fc/Fc^+	Ferrocene/ferrocenium redox couple
HF	The Hartree-Fock method
HIL	Hole injection layer
HOMO	Highest occupied molecular orbital
HTL	Hole transporting layer
IP	Ionization potential
IPES	Inverse Photoemission Spectroscopy
ITO	Indium tin oxide
LSDA	Local Spin Density Approximation
LUMO	Lowest unoccupied molecular orbital
MO	Molecular orbital
NMR	Nuclear Magnetic Resonance
NPTI	1,8-naphthalimide

OLED	Organic Light-Emitting Diode
PHOLED	Phosphorescence Organic Light-Emitting Diodes
PLED	Polymer OLED
PLQY	Photoluminescence quantum yield
PTZ	Phenothiazine substituent
PXZ	Phenoxazine substituent
RC	Radical cation
RE	Reference electrode
RHE	Reversible hydrogen electrode
TA	1,2,4,5 – tetrazine group
TADF	Thermally activated delayed fluorescent
TPA	Triphenyl amine
TD DFT	Time-Dependent Density Functional Theory
UPS	Ultraviolet Photoelectron Spectroscopy
WE	Working electrode

1 Introduction

The course on using renewable energy sources and reducing existing energy costs is a major factor in the creation of new devices. Equally important is the reduction of production costs through the introduction of new technologies. In the age of modern, rapidly developing electronics, new materials such as conjugated compounds, possessing photo- and electroluminescent properties, attract interest as materials for molecular optoelectronics and in particular as potential elements of electroluminescent diodes, displays, and photovoltaic cells. The main advantage of organic compounds is the ability to customize their properties, including the color of the emitted light by modifying their molecular structure.

The conjugated organic molecules can be simultaneously tested for use as active substances in solar cells and OLED matrices. The first generations of conjugated compounds used in organic electronics had photovoltaic properties and also worked in OLED. The rapid development of molecular electronics reduces the production costs of optoelectronic systems such as OLED matrices. In addition to production costs, two other important parameters affect the price of OLED matrices. Over the last 30 years (since the creation of the first diode), a tremendous amount of work has been done to formulate the basic principles for selecting materials and production methods.

The first of these parameters is the cost of the OLED system, which is proportional to the energy needed to display the image and process efficiency. The second important parameter is the practical working time (operation) of the OLED matrix defined as the time of trouble-free operation. It is assumed that the pixels should work without burnout for more than 2 years (i.e. longer than the standard warranty period). One way to improve the efficiency of the lighting process is to use the phosphorescence process and produce PHOLEDs (Phosphorescence Organic Light-Emitting Diodes) systems.

The use of organic molecules in electronics is a fairly large niche, due to the ability to vary properties by introducing new groups. Also, an important aspect of using organic molecules is the relatively low cost of production on an industrial scale, compared to inorganic analogs. In addition to important characteristics such as efficiency and lifetime, it is also crucial to understand the behavior and metamorphoses of the materials used under the influence of the electric field and light. The solution to the above-mentioned problems would lead to the understanding of organic electroluminescence phenomena and outline a strategy for the successful fabrication of new devices.

Investigation of the kinetics and mechanism of electrochemical processes involving organic compounds is important for the designing of new emitters and OLED devices. The use of various methods of analysis allows us to understand the behavior of the molecules in the electric field.

2 Aim and scope of work

The doctoral thesis encompasses the fundamental result of the research aimed at determining the effects of different donor and acceptor groups on compound physical-chemical properties. The selection of test compounds was dictated by the electrochemical studies of D–A or D–A–D and the lack of available experimental data in the literature on the electropolymerization process of carbazole derivatives.

The object of the study was differently substituted 1-8 naphtalimide (NPTI), pyridazine (DA), and tetrazine (TA) acceptor cores with the varieties of donor groups like carbazole (CBZ), phenoxazine (PXZ), a phenothiazine (PTZ) and dimethylacridine (DMAC). A comparison of the properties of a series of compounds differing in the number of electroactive substituents will allow assessing their impact on the electropolymerization process and electrochemical stability. The electrochemical studies would allow us to optimize the polymerization process and to determine the basic properties of both the initial monomer and the resulting oligomer product. Moreover, the electrochemical techniques would be used for indirect estimation of the energy values of HOMO and LUMO levels and the energy gap value of the compound (E_g), whose knowledge is necessary at the stage creating optoelectronic devices. Modification of the chemical structure of a compound can lead to significant changes in its properties, hence it is important to trace the relationship between the chemical structure of monomers and their properties and to determine the relationship between the properties of the monomer and electrochemically synthesized conductive oligomer. Determining this type of relationship is the basis for designing the chemical structures of monomers that will lead to obtaining materials with the desired properties. The broad electrochemical, spectroscopic, and spectroelectrochemical studies will allow us to understand the mechanisms of physical processes that occur in materials under the influence of applied voltage which is particularly important in terms of their subsequent use in optoelectronic devices.

3 Literature review

3.1 Molecular theory

Every time, in the beginning, there is an idea, an idea which further is applied. In the case of organic compounds, the molecules are firstly designed to theoretical contain particular properties. Moreover, the synthesis of every compound takes time and, to lower the cost and screen the compounds, the theoretical approach is considered. As a common practice, the group of different molecular structures will be investigated by the theoretical method, and after will choose the best one for synthesis.

Every change in molecule structure on an electronic level affects their properties and behavior. The organic molecule at a ground state receives or loses an electron from an excited state through electron layer reconfiguration. Using molecular orbital theory, a single covalent bond can be expressed as a linear combination of two electronic wave functions. For example, for a molecule with a single bond, were observed a bonding σ orbital with lower energy and an antibonding σ^* orbital with higher energy. [1]

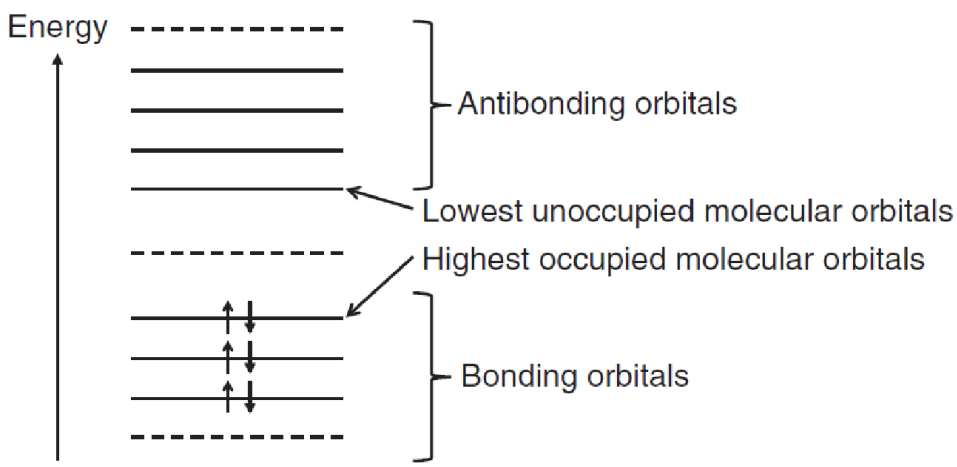

Figure 1. The schematic electron configuration of a molecule.[1]

The orbital, which has the maximum energy is called the *highest occupied molecular orbital* (HOMO). It is the electron filled orbitals comparing with others. The absolute value of HOMO usually correlates with ionization potential (IP), which means minimal energy, which needs to extract one electron from the HOMO. Conversely, the unfilled electron orbitals are

called the *lowest unoccupied molecular orbital* (LUMO) (**Figure 1**). This orbital has the lowest electron energy. The absolute values of LUMO energy are correlated to an electron affinity (EA) of the molecule. Electron affinity is the energy released when one electron is added to the LUMO. [1]

Explaining energy levels, assume a molecule in ground state S_0, which has 2 electrons on HOMO (**Figure 2**). In the S_0 state, electrons occupy orbitals from the lowest to higher energy. When a molecule absorbs energy, an electron makes the transfer from a bonding orbital to an antibonding orbital. This state is called S_1 or the first excited state. It is important to remember that a change in energy level occures without pin changes. According to the same principle, the other states are called S_2, S_3, etc. (**Figure 2**).

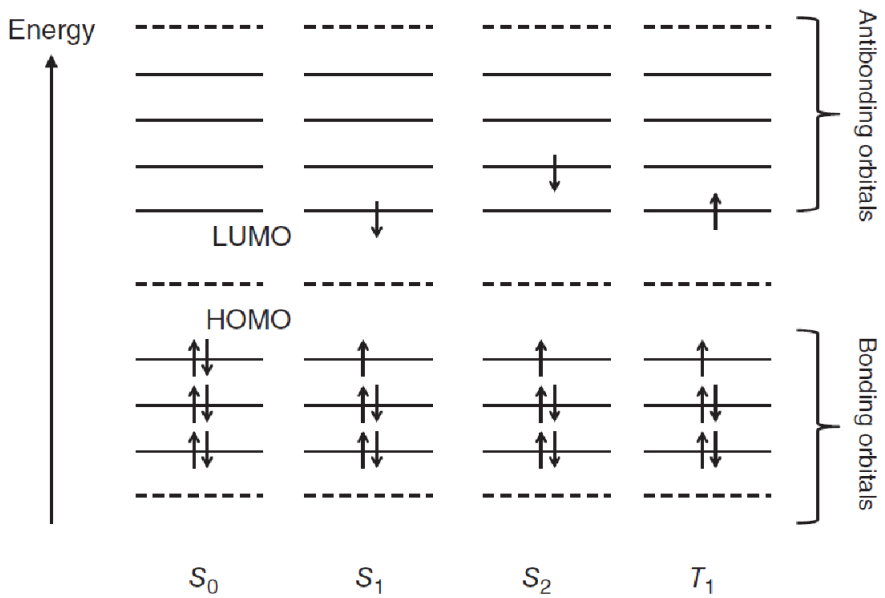

Figure 2. Electron configuration in the ground state and excited states.[1]

When the electron changes spin to the opposite it means that formed a new triplet state. The formation of a triplet state is required to absorption photon energy. As a result of this transfer was observed changes in molecular configuration, for example, transfer to more stable in terms of energy, which entails changes in energy levels of orbitals. [1]

There are several methods of predicting molecular levels of energy:

The Hartree-Fock method (HF) is the basis for energy and wavefunction calculations on the ground-state molecules. The HF method for excited states has been refined in various

approximations and basis functions. The latter development of methods (investigation) shown the excited state wavefunctions without referring to the ground state. [2]

The HF equations can derive from a variational principle, that E is minimal.

$$E = \langle \phi | H | \phi \rangle \tag{1}$$

Here H is the total Hamiltonian of the system of A particles, and ϕ is a single Slater determinant. In nuclear physics one often uses a restricted HF principle of which we now describe a few cases.[3]

The molecular orbitals (MO's) of excited states are usually non-orthogonal (except by symmetry) to the MO's of the ground state and the same in case the total wavefunction of these states. This fact causes difficulties in determining the values of operators between two states as well as in the calculation of energy and estimation values of excited states.[2]

Using HF calculation is a popular method for calculation, but in HF calculations should have the following properties:

- The calculation should be simple, only a few parameters could be used.
- There are two extremes: nuclear matter and ^{4}He.

Parameters should be fitted to reproduce the energy and density of two nuclear matter is an extrapolation to very heavy nuclei, here the volume effect will be connected with binding. Another one is the smallest 4-n nucleus, which has a binding energy per particle of 7 MeV per particle. These objects could be determined as a surface. [3]

Density functional theory (DFT) based on Hohenberg-Kohn theorems, is imperative for modern quantum-chemical calculation of materials and molecules. At its theoretical core show that all ground-state properties of a many-electron system are uniquely determined by that system's electron density distribution function over space. This theory assumed that an exact function that yields the exact energy of a system from its exact density. Using a minimal number of functions (minimization of function) as a fixed electron number gives us the exact electron density and energy. [4]

On the one hand, the Hamiltonian operator completely characterizes all states of the system, the excited states as well as the ground state are determined by the ground-state density. On the other hand, this operator is responsible for the function, which is determined in addition to its electron number also its external potential, in other words, the ground-state density. Though, the attitude of considering DFT as a ground-state theory has been justified because, so far, there exists no formalism, like the Kohn- Sham formalism for ground states, that exploits the formal dependence of excited states on the ground-state density and leads to a feasible procedure to treat excited states within DFT. [5]

The time-dependent density functional theory (TDDFT) is known as an onerous formalism for the treatment of excitation energies using the DFT framework. It has been applied for the calculation of excitation energies of simple molecules and large systems. However, in cases where the ground-state description begins to break down, as is the case for dissociating molecules, care has to be taken with practical TDDFT with approximate functionals. It has been noticed that excitations involving large changes in the charge density tend to be underestimated by TDDFT because present-day exchange-correlation functionals are in some sense too local.[6] TDDFT methods are computationally more expensive than semi-empirical methods but allow easy studies of dye molecules of medium size. Full TDDFT calculations become more time-consuming with dyes of more than 100 atoms of second-row elements. The approximate TDDFT method, however, also allows the calculation of large chromophores. TDDFT studies are not restricted to dyes in their singlet excited states. Moreover, this method allows one to study more complex photophysical processes following spectral excitation, such as deactivation processes. [7]

To properly and fastly calculate the theoretical values, we need to employ certain approximations:

- LSDA (local spin density approximation). This uses the standard local exchange functional and the local correlation functional of Vosko, Wilk, and Nusair (VWN)
- BLYP. This combines the standard local exchange functional with the gradient correction of Becke and uses the Lee-Yang-Parr correlation functional (which also includes density gradient terms).
- Becke3LYP (B3LYP). This function is a hybrid of exact (Hartree—Fock) exchange with local and gradient-corrected exchange and correlation terms, as first suggested by Becke. [8]

Calculation based on optimization geometry as a minimum of the potential energy, determining excited states using hybrid B3LYP, BLYP, LDA methods, and 6-31G*, cc-pVDZ basis sets. For geometry optimization for the organic molecules method, B3LYP showed smaller errors.[9,10]

3.2 Fundamental electronic parameters

In the organic materials, there are several fundamental parameters important for applications in organic electronics but the most one are IP – ionization potential, EA – electron affinity, which corresponds to HOMO, LUMO energies of an organic molecule, and a bandgap (energy gap) which is the energy between the highest occupied and lowest unoccupied molecular orbitals.

There are several methods for determining the energy gap (the difference between levels of energy) The fundamental energy gap is determined as the difference between the ionization potential and electron affinity:

$$E_{fund} = IP - EA \tag{2}$$

This energy gap (2) can be determined via a combination of gas-phase ultraviolet photoelectron spectroscopy and electron attachment spectroscopy. [11]

The main parameters responsible for the appearance of photoemission peaks are the electronic polarization, the intra, and intermolecular vibrations, the intermolecular electronic transfer, the structural disorders, and the bandwidth. The electronic polarization is the electronic cloud of the molecular unit A can deform to take into account the arisen positive charge. For example, it was calculated the orbital levels of the species A and A^+, the intraatomic and intramolecular relaxations and the intramolecular polarization could be estimated too. [12]

Let's explain it in reaction:

$$A \rightarrow A^+ + e^- \tag{3}$$

This reaction is described by Nernst's law

$$\mu = E_f = E_0^{ox} + \frac{RT}{nF} \ln \frac{[A^+]}{[A]} \tag{4}$$

where μ is the chemical potential, E_f – is Fermi level.

During the UPS experiment was determined E_0^{0x} and later was calculated IP. For reduction E_0^{red}, which is correlated with EA. The doping effect is a limitation of UPS (especially of determination value between energy levels) due to shifting Fermi level from the middle. It does not mean, that using UPS is possible to measure the bandgap of undoped materials. Dopped materials are critical to determining the first unoccupied electronic states. A whole picture of the localization of the occupied and unoccupied electronic states could be obtained by linking the direct photoemission spectra and inverse photoemission (IPES) results. [12] Experimentally via a combination of UPS and IPES, the difference is equal to the

level of the material, or the molecular fundamental gap. For π-conjugated organic material energy of photonic absorption can be defined by optical methods. It is caused to the formation of a bound electron-hole pair, in other words, the formation of excitons, which is the same in the case of condensed-matter physics. [11]

The calculated energy gap the difference between the calculated HOMO and LUMO energy levels only provides a similarity to the fundamental gap.

$$E_g = HOMO - LUMO \tag{5}$$

The correlation of that approximation and real results depends on the specifications of the computational methodology (for DFT, the high dependence between the nature of the exchange-correlation functional and the amount of Hartree–Fock exchange). [11]

The bandgap (optical gap) of a molecule is the energy between the lowest electronic transition accessible and the absorption of a single photon. Generally, the optical gap E_{opt} is heavily lower than the gap determining by another method. that can be caused by the fact, that the electron and hole remain electrostatically converge to one another in the excited state. [11]

The optical band gap was calculated from the onset wavelength of absorption by

$$E_g^{opt} = \frac{1240}{\lambda_{onset}} \tag{6}$$

where E_g^{opt} is the optical bandgap and λ_{onset} is the onset wavelength of absorption. This wavelength is corresponding to the π-π* transition. [13]

One of the most popular methods for approximation values of ionization potential and electron affinity is cyclic voltammetry measurements. For calculation, IP and EA are used the oxidation and reduction potentials carried out in solution. [11] According to Hartree–Fock calculations and following Koopmans' theorem, the energy of the HOMO level can be considered as (minus) the vertical ionization potential (IP) while the LUMO energy represents (minus) the vertical electron affinity (EA, where we adopt the IUPAC definition, i.e., the electron affinity is the negative of the energy change when adding an electron to the neutral species; within this definition, most π-conjugated systems have positive EA values since the extra electron is bound). [11]

Electron affinity and ionization potential for materials for organic electronics applications are usually determined by the following electrochemical methods: cyclic voltammetry (CV) and differential pulse voltammetry (DPV). Generally, the CV technique involves the application of forward and reverse linear potential scans to a working electrode immersed in a solution containing electrochemically active compounds (compounds, which make redox forms) and supporting electrolyte. The oxidation and reduction potentials are

estimated by the onset potential, defined as the potential at which the initial injection of electrons from the HOMO or to the LUMO becomes evident by an increase of anodic or cathodic current. [14]

The reduction is a process, which usually starts by adding one electron on the LUMO of aromatic hydrocarbon R (**Figure 3**).[15]

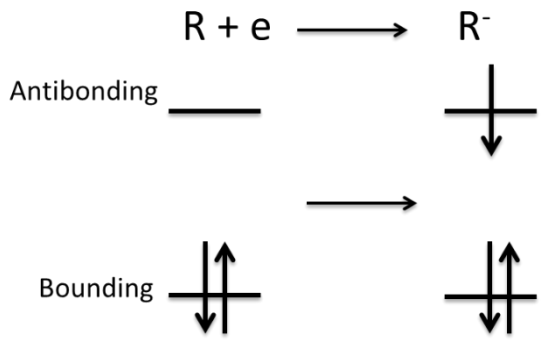

Figure 3. Scheme of the reduction process

This step is usually fast and reversible: the potential, at which the reduction starts correlates with molecular orbital calculations of the energy of the LUMO. A similar situation is oxidation reactions but in this case, one electron was removed from the highest occupied molecular orbital (HOMO). The formation of the cation radical was shown in **Figure 4.** [15]

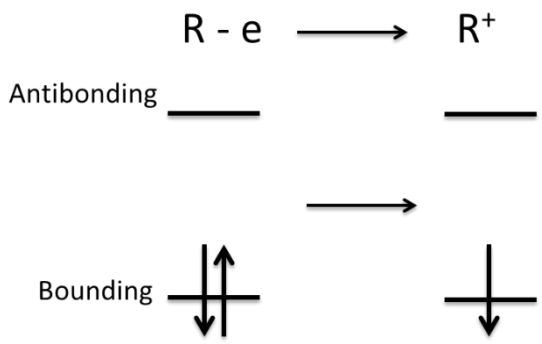

Figure 4. Scheme of the oxidation process

Oxidation is fast as a reduction process, and oxidation potential values correlate to HOMO. Although the potentials measured by CV are often bothered in this case by the fast

following reaction of the radical cation. That's why for calculation energies were used *onsets* potentials of process. [15]

Using the fact, that the first electron transfer step correlated with the position of the LUMO or the HOMO, structural changes can affect the energies of the molecular orbitals and the reduction and oxidation potentials. Increased conjugation in an aromatic hydrocarbon makes lowers the LUMO and higher the HOMO so that both oxidation and reduction of a highly conjugated system occurs more easily. [15]

3.3 Fundamentals of electrochemistry

The electrochemical analysis is an important skill to teach in chemistry curricula because it is a critical tool in current high-impact chemical research. Electrochemistry enables researchers to analyze a variety of systems extending from molecules to materials that encompass research themes ranging from clean energy to substrate activation in biological systems. [16] Nowadays, electrochemistry represents an important piece of chemistry and many technological advances come from the combination of different materials in electrochemical cells. [17]

Electroanalysis technics can be divided into two groups: electrodics and ionics. The greater part of this type of analysis belongs to the field of electrodics. [18] All electrochemical technics can be devived into two groups: static and dynamic. In the static technique, the current is not passed through the analyte's solution. Potentiometry, in which we measure the potential of an electrochemical cell under static condition, is of the most important quantitive electrochemical methods. Dynamic techniques in which we allow current to flow through the analyte's solution comprises the largest group of interfacial electrochemical techniques, such as coulometry (in which we measure current as a function of time), amperometry, and voltammetry (in which we measure current as a function of a fixed or variable potential (**Figure 5**).

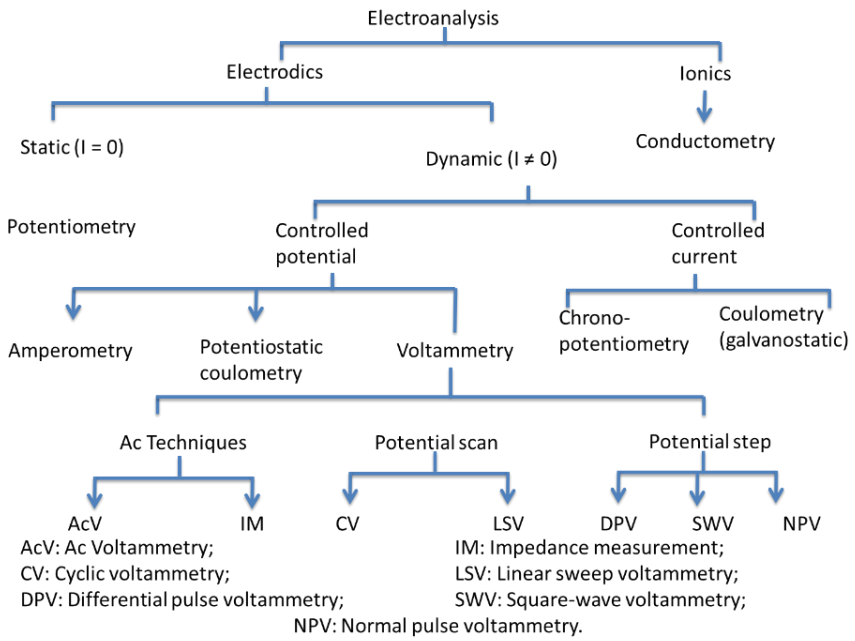

Figure 5. Different technics, which are used in electroanalysis. [18]

Cyclic voltammetry (CV) and differential pulse voltammetry are two techniques to measure redox potentials. CV is a linear potential sweep method that varies an applied potential in an electrochemical cell while recording the resulting current.

A theoretical expression for the peak current for a reversible cyclic voltammogram was derived as a function of the scan rate to give the Randles – Sevcik expression.

$$i_p = 0.446nFA[A]\sqrt{\frac{nFvD}{RT}} \tag{7}$$

Where is i_p – current maximum, *n*- number of electrons transferred in the process,
A - electrode area, *F*- Faraday constant, *[A]* – concentration of the sample, *v*- scan rate,
D –diffusion coefficient, *R* – gas constant, *T* – temperature.
And for 298 K this equation is

$$i_p = 29 \cdot 10^5 A[A]\sqrt{n^3 vD} \tag{8}$$

According to this equation, the dependence of the peak current, i_p, on scan rate, *v*, follows a characteristic square-root law, which provides a tell-tale sign of the presence of a diffusion-controlled process. [19]

The redox potential, $E_{1/2}$, is determined using two peaks that arise as the applied potential in cycle to as witching potential and then back to the starting potential. E_{pc} and E_{pa} are the peaks observed on the cathodic and anodic scans, respectively. For a perfectly reversible system, the voltage difference between the two peaks in a CV scan should be close to

$$\left|E_{PC} - E_{pa}\right| = \frac{2.3RT}{nF} \tag{9}$$

where R is the gas constant, F is Faraday's constant, n is the number of electrons involved in the electrochemical event, and T is the temperature (K). At 298 K, $\frac{2.3RT}{nF} = 0.059\ V$ for a one-electron process. [16]

Further

$$\frac{i_{pc}}{i_{pa}} = -1 \tag{10}$$

where i_{pc} and i_{pa} are the cathodic and anodic peaks, respectively. The ratio of the peak currents should be a negative one because the absolute value of the heights should be the same on the forward and reverse scans, and one current is positive while the other is negative. Taken together, the ratio of peak currents and the difference between the peak potentials

reveal the reversibility of the reaction; the closer the peak current ratio is a too negative one and the closer the peak potential difference is to $\frac{2.3RT}{nF}$, the more fully thermodynamically reversible, or Nernstian, the reaction is. [16]

Two qualities, parameterized by the standard electron rate constant k_0 and the mass transport to or from the working electrode mass transport, determine the CV. The electron transfer rate constant for a reduction and oxidation process is a function of the applied potential and can be described as

$$k_{red} = k_0 exp\{-anF(E - E^0)/(RT)\} \tag{11}$$

and

$$k_{ox} = k_0 exp\{-(1 - a)nF(E - E^0)/(RT)\} \tag{12}$$

where k_0 is the standard electron-transfer rate constant in cm/s at the standard potential E^0, a is the so-called transfer coefficient (a measure of the symmetry of the activation energy barrier for the oxidation and reduction processes), n is the number of the transferred electrons, F is the Faraday constant, E the applied potential, R the ideal gas constant, and T the absolute temperature. The exponential dependence of k on the potential E results in a steep rise in the current. This leads to a depletion of the concentration of the corresponding species at the electrode. Now, diffusion is the only process in an unstirred solution by which the reactant can move to the electrode surface. As diffusion is slow, the current does not increase exponentially with E as (3) and (4) indicate but decreases after the species reacted on the electrode surface and so a depletion layer results. The mass transport is given by Eq.(5) [20]:

$$m_{trans} = (\pi nFDv/(RT))^{1/2} \tag{13}$$

In each case the slowest process determines the electrochemical behavior:

- If $k_0 >> m_{trans}$ Diffusion is controlled and the electrode process is reversible.
- $k_0 \approx m_{trans}$. Quasi-reversible (or intermediate) case, diffusion, and electron transfer are in the same order
- $k_0 << m_{trans}$ The process is irreversible. The mass transport is faster than the electron transfer and the electron transfer. [20]

One should note here that electrochemical and chemical reversibility are different things: chemical irreversibility means that one of the redox partners is removed from the

electrode by chemical reaction, electrochemical irreversibility means that the electron transfer is hindered. [20]

There are several processes during the oxidation and reduction process, not only formation cation, anion radical (**Figure 6**).

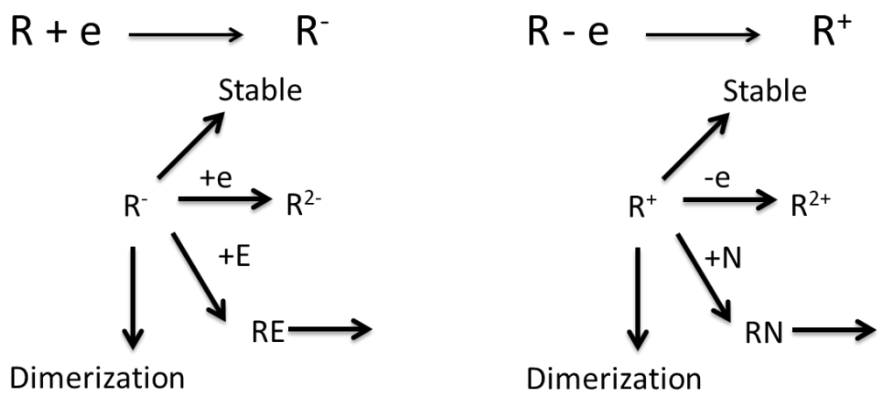

Figure 6. Scheme od possible processes during reduction reaction (left) and oxidation reaction (right). [15]

The main goal of oxidation and reduction processes is the formation of charged particles (polarons). When these processes are non-reversible, it means that during the Red-Ox process was formed stable (or not stable product) on the surface of the electrode or in solution. Another process is the transition from the first to the second step of the reaction. In these cases, bipolarons were formed (R^{2-} and R^{2+}). Also in this step were formed dimers. In this scheme, E is an electrophilic species (**Figure 6**) (in case of reduction reaction), such as H^+ or CO2, which can attack the anion radical and produce a species that is frequently easier to reduce than the parent R. For oxidation reaction radicals could be attacked by nucleophilic agents, such as pyridine, hydroxyl ion. cyanide ion. [15]

Taking into account that the conduction processes, as well as the generation of electrons, depending on several parameters (temperature, the concentration of the investigated compound, diffusion coefficient, electrolyte conductivity) potential of oxidation/reduction can be different in different systems. That is why for non-aqueous solutions it is recommended to use standards, for example, ferrocene/ ferrocenium (Fc/Fc^+) redox couple standard. [21]

Voltammetry methods are based on applies a constant and/or varying potential at an electrode's surface and measure the resulting current with a three-electrode system. For electrochemical measurements, one uses 2-, 3-electrode, and electrochemical cells. (**Figure 7**).

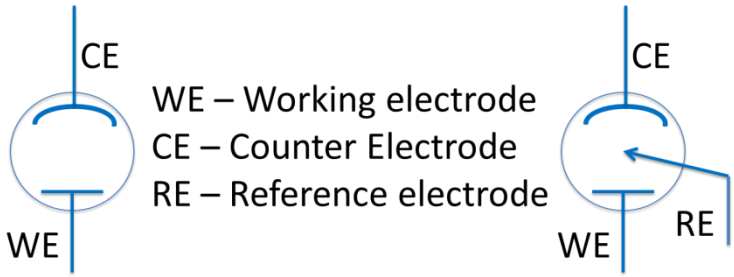

Figure 7. Scheme of 2 and 3 electrode electrochemical cell.

Two-electrode experiments measure the whole cell, that is, the complete voltage dropped by the current across the whole electrochemical cell is measured: working electrode, electrolyte, and a counter electrode. In this case, the reference electrode is connected with the counter (auxiliary) electrode. The 2-electrode electrochemical cell is used when the voltage of the cell is significant. It is applicable for batteries, supercapacitors.

For 3-electrode mode, an additional reference electrode is used. This type of cell has several advantages: changes in the working electrode potential are separated from the changing potential of the counter electrode. That is why this cell is more useful for laboratory experiments and tests. In this case, voltage is measured between the working and reference electrode.

3.4 Charge carriers

Behaviour of charge carriers are quite important for understanding electrochemical properties. For example, semiconductors, which may be easily reduced and electrons are introduced into the unoccupied orbitals are referred to as *n*-type semiconductors. In contrary, materials which may be easily oxidized, removing electrons from occupied orbitals, and generating holes are referred to as *p*-type semiconductors. Two kinds of mobile electronic charge carriers can be distinguished, electrons in the conduction band and holes in the valence band, the latter behaving like positively charged particles of about electron mass. [22] The charge carrier mobility depends strongly on temperature and electric field. [23]

Doping with acceptor or donor molecules causes partial oxidation (*p*-doping) or reduction (*n*-doping) of the polymer molecule, respectively. As a result positively or negatively charged quasi-particles are created presumably polarons in the first step of doping. When doping proceeds, the reaction among polarons takes place, leading to energetically more favorable quasi-particles, i.e, a pair of charged solitons (bipolarons) in materials with a degenerate ground state. [24]

Dopants may be classified as:

- Neutral dopants: I_2, Br_2, AsF_2, Na, K, $FeCl_3$ etc.
- Ionic dopants: $LiClO_4$, CF_3SO_3Na, BuNClO etc.
- Organic dopants: CF_3COOH, CF_3SO_3Na, p-$CH_3C_6H_4SO_3H$
- Polymeric dopants: polyvinylsilane (PVS), polyphenylene sulfide (PPS), etc. [24]

A polaron is a quasiparticle that interacts with the polarization oscillations of a crystal lattice especially ionic crystals such that an autolocalized state of the current carriers. An autolocalized state is a particular case of a localized state and is qualitatively different from the free state of a particle. Autolocalization occurs in a homogeneous medium due to the internal properties of the medium. The phenomenon is different from localization in an external potential. [25]

Figure 8 shows the process of polarons formation during *p*-doping of polypyrrole. [24] The positive polaron forms a localized single occupied level (binding orbital) together with an unoccupied level (non-binding orbital), which are separated from the valence and conduction bands by charge transfer from or to these orbitals by *p*-doping

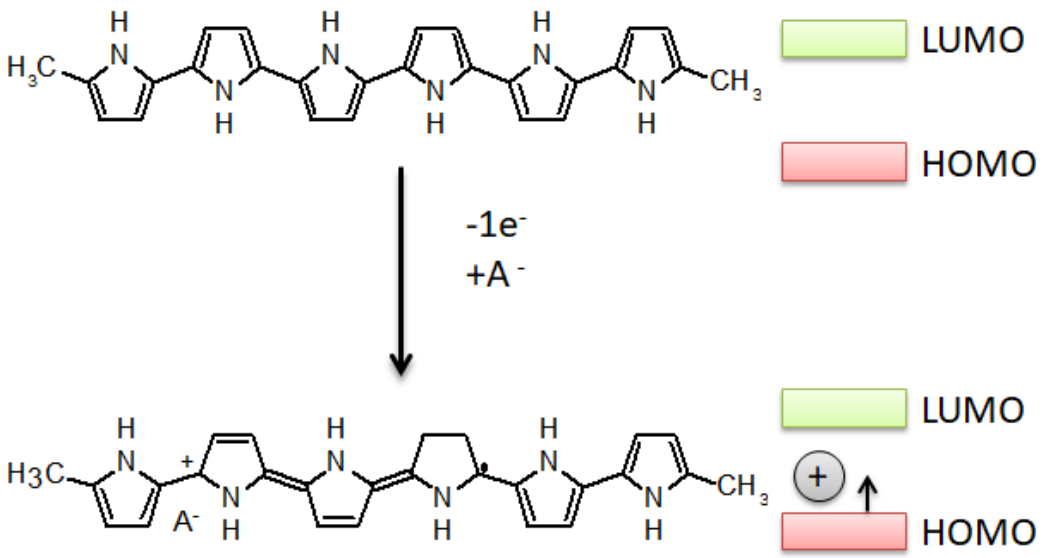

Figure 8. Formation of polaron in a polypyrrole chain. [24,26]

The positive polaron forms a localized on binding orbital (single occupied level) together with a non-binding orbital (an unoccupied level), which are separated from the valence and conduction bands by charge transfer from or to these orbitals by doping

A similar situation takes place for the negative polaron - the binding orbital is fully occupied, and the non-binding orbital is occupied by one electron. [27]

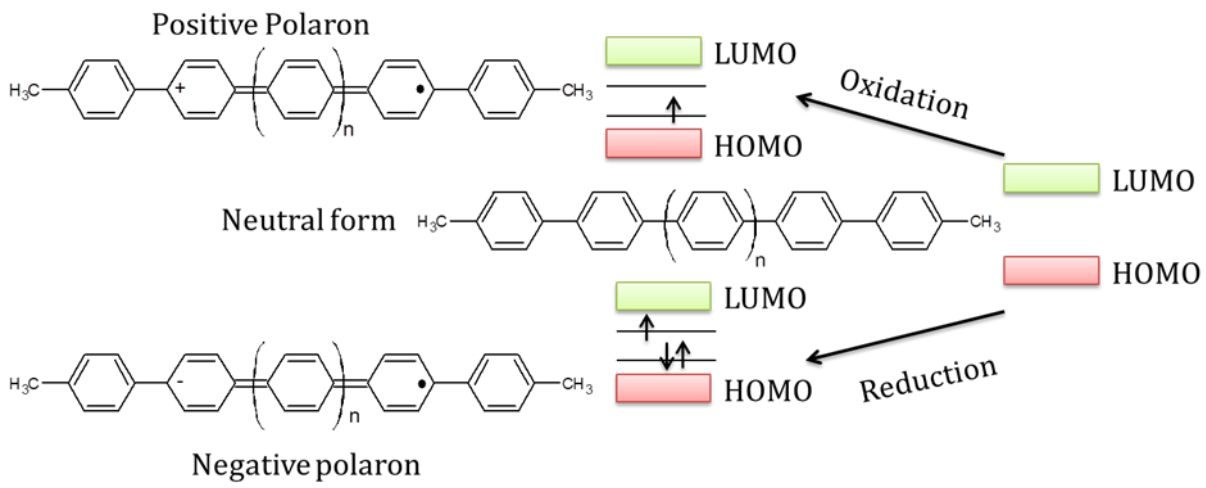

Figure 9. Electronic and structural changes of polyphenylene during oxidation (*p*-doping) and reduction (*n*-doping). [28]

The electronic transitions for these materials are in the visible and ultraviolet range, which means that the appearance of bands corresponding to the oxidized forms can be

observed in the electron spectra. [29] The presence of unpaired electrons also leads to the appearance of paramagnetic properties and the possibility of detection by electron paramagnetic resonance spectroscopy

Polarons (positive and negative) resulted in the creation of bipolarons (positive and negative.) Two identical charged particles can be localized in one polarization potential well, forming a bipolaron. A bipolaron is also a well-known phenomenon and is thought to be a carrier of a superconducting current in many materials. The polarization potential well for a bipolaron in the simple model is deep enough for only one localized level, in contrast to more accurate theories in which several levels can exist. [25]

The formation of bipolaron is possible for the scheme. **(Figure 10)**

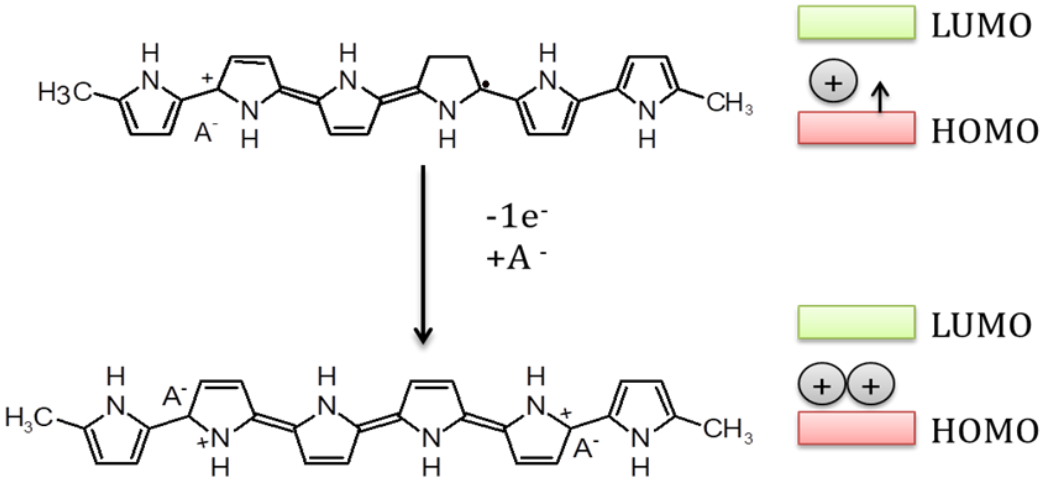

Figure 10. Formation of bipolaron in a polypyrrole chain. [24,26]

This process could be explained as transformation cation to dication due to electrochemical oxidation. Positive bipolarone in the energy diagram can be represented as two localized unoccupied states: the bonding and non-bonding orbital, which are separated from the valence band~~.~~ and conductivity due to charge transfer from or to orbitals due to doping.

However, it is also possible to form bipolarons from two polarons located on adjacent chains - such systems are called π-dimers (**Figure 11**). [30]

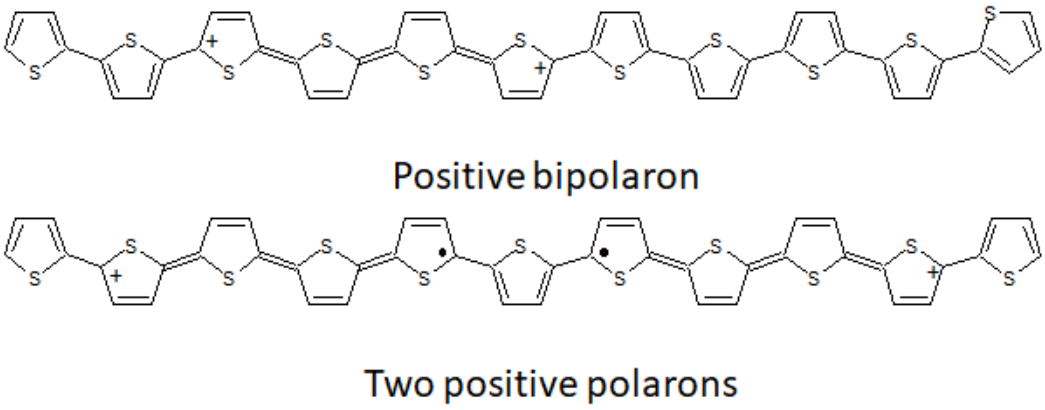

Figure 11. Schematic structures of a positive bipolaron and two positive polarons in polythiophene. [30]

The system establishes an equilibrium between both types of charge carriers, and its position is influenced by the doping degree, relaxation of the polymer chain, and interactions with the doping counterion.[30]

The scheme of the formation of positive and negative bipolarons is shown in **Figure 13**.

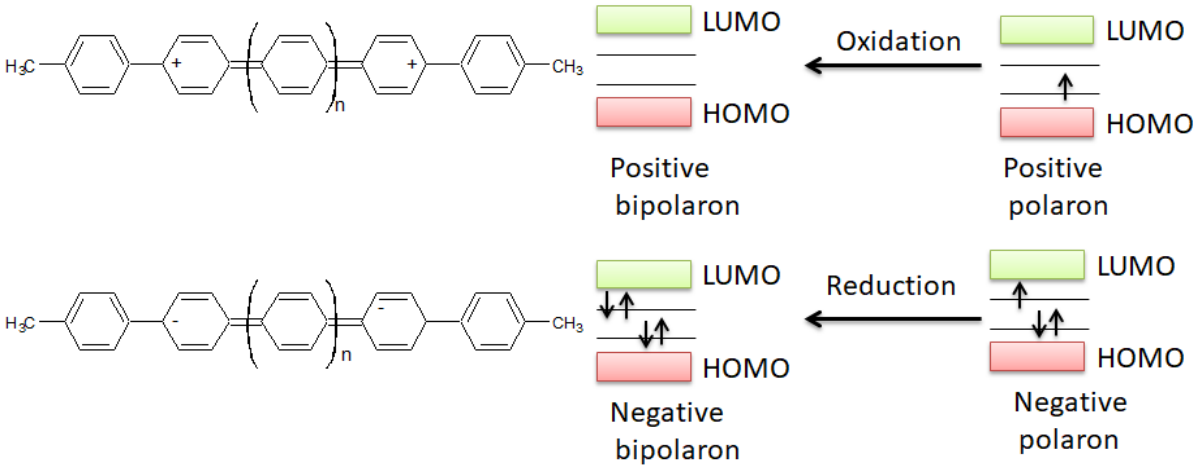

Figure 12. Electronic and structural changes of polyphenylene during oxidation (*p*-doping) and reduction (*n*-doping).[28]

Voltammetric techniques used in electroanalysis monitor the flow of current as a function of potential, time, and mass transport. Additional data are often required and are accessible, in particular, via in situ spectroelectrochemical techniques. Connecting a spectroscopic technique such as UV/Vis/NIR spectroscopy to an electrochemical experiment, a wealth of complementary information as a function of the potential, time, and mass transport are available. This type of technique gives us information about short-lived unstable

intermediates and spectroscopic information disentangling the composition of complex mixtures of reactants can be obtained Using electrochemical approaches it is possible to generate a well-defined amount of intermediates controlled by the charge forced through the working electrode. In this way, interesting intermediates (e.g. radicals or radical ions) can be generated electrochemically in a much more controlled and localized manner compared to, for example, conventional photochemical methodology. [19]

Spectroelectrochemistry as a method of analysis includes a large group of coupling methods such as:

- In Situ UV/VIS/NIR Optical Spectroelectrochemistry (The light absorption of reaction intermediates generated at the electrode surface.)
- In Situ Electron Spin Resonance (Molecules with unpaired electrons may be detected by a magnetic field)
- In Situ Raman And Resonance Raman Spectroscopy or Microscopy (detection of strength vibration bands and other changed during the electrochemical process)
- In Situ Luminescence Spectroscopy (Changes in chemiluminescence processes)
- In Situ Nuclear Magnetic Resonance. (NMR detecting changes in compounds, which occur during the electrochemical process. [19]

Using these technics allows to investigation nor the only presence of charge carries, but also estimates changes in structure during doping. For example, using UV/VIS/NIR spectroelectrochemistry could be distinguished polaronic and bipolaronic bands, which appearing during the doping process. The ESR spectroelectrochemistry dives also information about the spin density of polarons, but not of bipolaron due to diamagnetic nature, which cannot be detected by ESR (**Figure 12**).

3.5 Conjugated compounds and polymers

Conjugation is the overlap of one p-orbital with another across an intervening sigma bond. Conjugation is formed by means of alternating single and double bonds (**Figure 13**).

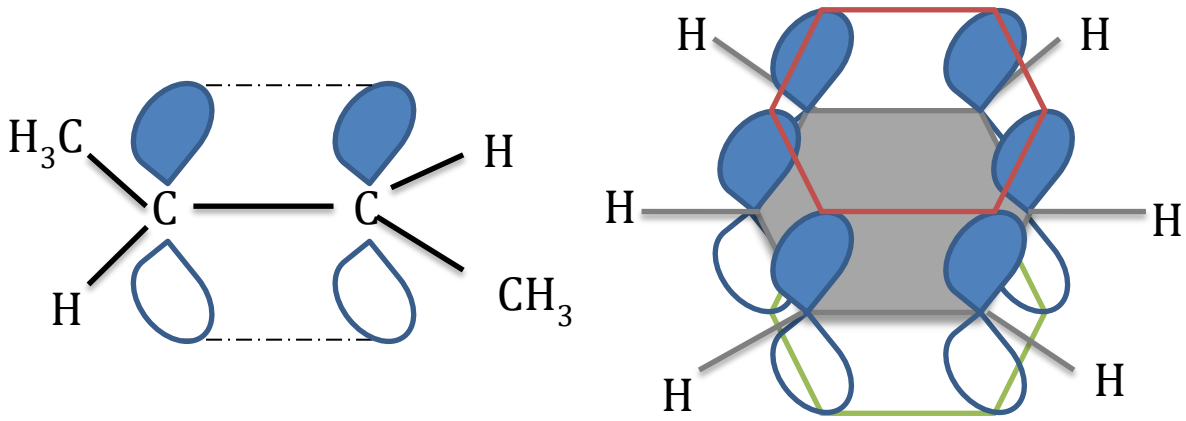

Figure 13. P orbital conjugation on 2-butane and benzene.

Compounds which include benzene rings, carbonyl group C=O, imine group C=N, vinyl group C=C have conjugation too. Also, homo-conjugation is obtained in case compounds that include the diene group. These compounds can be linear (butadiene, 2-butane as an isolated conjugation), cyclic (benzene, furan, pyridine), or combined (Cinnamalgehyde) (**Figure 14**).

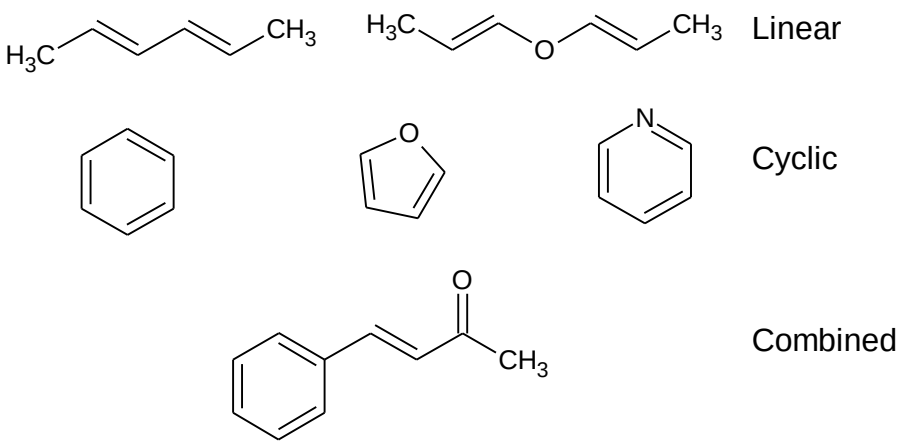

Figure 14. Different compounds with conjugation.

The presence of conjugation has an effect on the properties of compounds. For example, π-conjugation is anticipated to lead to an even lower LUMO level. For solid-state conjugation would enhance the intermolecular packing π-π staking. [31]

Absorbance properties have been studied on an exemplary group of 2,7-*di*-conjugated 9,9-*di*-alkylfluorenes derivatives. In this investigation was mentioned, that compounds with smaller conjugation lengths have absorbance maxima below than compounds with long conjugation lengths. Also, fluorescence maxima are blue-shifted due to conjugation length. [32] It means that conjugation decreases E_g comparison to not conjugated compounds.

For organic electronic devices are common to use not only conjugated compounds but also conjugated polymers (**Figure 15**). The Nobel Prize in Chemistry 2000 was awarded jointly to Alan J. Heeger, Alan G. MacDiarmid, and Hideki Shirakawa "for the discovery and development of conductive polymers."

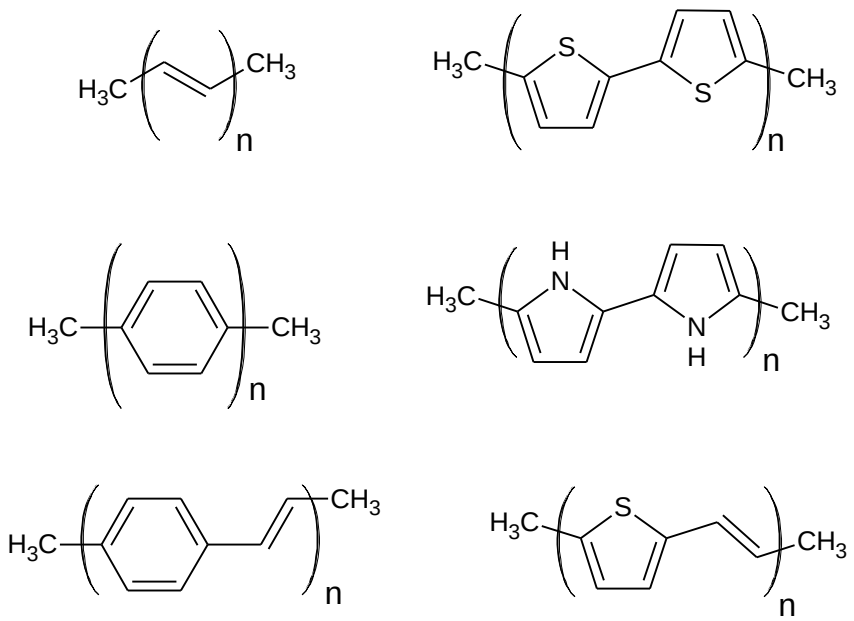

Figure 15. Structures of conjugated polymers, which are used at organic electronic devices: trans-polyacetylene; polythiophene; poly(p-phenylene); polypyrrole; poly(p-phenylenevinylene); poly(2,5-thienylenevinylene). [30]

Conducting polymers are considered as an alternative against conjugated compounds (monomers) for the following reasons: semiconducting properties, as evidenced in a number of reports on solid-state devices, such as Schottky barrier devices, electroluminescent displays, and field-effect transistors; formation of the oxidized polymer upon irradiation, due to electron injection into solution; easy production in the form of thin films with variable thickness; good environmental stability and high hole mobility. [17]

Conducting polymers are frequently called “synthetic metals” because they present electric, electronic, magnetic, and optical properties inherent to metals or semiconductors

while retaining the mechanical properties of conventional polymers. These properties are intrinsic to the doped material, being completely different from those originated from a physical mixture of a non-conductive polymer with a conducting material, such as metal or carbon powder. In intrinsic conducting polymers the conductivity is assigned to the delocalization of p-bonded electrons over the polymeric backbone, exhibiting unusual electronic properties, such as low energy optical transitions, low ionization potentials, and high electron affinities. [17,33]

The polymeric analog of OLED is PLED, which is generally fabricated by deposition from solution. Due to the ease and low cost of device fabrication via solution processing, the PLED displays attract much attention. In addition, the solution process is typically carried out at room temperature, which allows a device to be made onto a flexible organic substrate. These patterning methods of PLED are more promising for large-size, high-resolution displays than the shadow mask technique, which is the patterning method for small-molecule OLEDs.[34]

Conjugated oligomers, extrapolating the linear curve of the HOMO-LUMO gap against the reciprocal of the number of monomer units (1/n) affords a prediction of the bandgap for the corresponding polymer. [35]

The delocalized electronic structure of polymers (polymers based on polyacetylene, polyaniline, polyphenylene, polypyrrole, polyphenylenevinylene, polythiophene, polyfluorene, etc.) is partly responsible for the good stability and mobility of the charge carriers created upon doping (i.e., partial oxidation or reduction), electrical conductivities in the range of 1±100 S/cm being reached in most cases. This conjugated structure is also responsible for a strong absorption (and often emission) in the UV-VIS range. [36]

The spectroelectrochemical behavior of polymers was similar to monomers, differences were only in shifting of polymer and polaron band. The electrochromic properties are usually described by the behavior of those bands. [37]

Concerning the architecture of the π-conjugated bond network, systems may be classified as either linear or star-shaped, spreading spatially across two or more discrete directions. Fundamentally, the structure of the latter comprises a central “core” and no less than three “arms,” protruding from it. Accordingly, linear structures may be considered “two-armed systems,” in which the core and arms may be pronounced (copolymers) or uniform (homopolymers). [38]

3.6 OLED design

The electroluminescence phenomenon in semiconductors was first observed by Round at the beginning of the 20th century. Light-emitting diodes, commonly named LED, are the reverse of photovoltaic cells. While in this last the light is used to produce an electrical voltage, in a LED a voltage is applied to produce light. [17]

The chronological sequence of development reflects the emergence of OLED technologies, including the following:

- Small-molecule OLED (SMOLED);
- Polymer OLED (PLED);
- Passive-matrix OLED (PMOLED);
- Active-matrix OLED (AMOLED) displays. [1]

In experiments using tetracene-doped anthracene crystals and materials [39], OLED emission had been observed before the so-called first OLED paper in 1987 [40,41]. OLED device consists of a glass substrate, two electrodes (anode and cathode), and the active layer between electrodes (**Figure 17**). Unfortunately, the operating voltage and efficiency levels were insufficient for the actual application. The later Tang and Vanslyke paper outlined the main principles for the fabrication of efficient OLED that remain valid until today [41]:

1. Significant enhancement of the recombination efficiency by using a layered structure using multiple different materials (heterostructure).
2. Fabrication of low-voltage, high-quality devices through evaporation.
3. Appropriate choice of electron and hole injection materials and work functions for cathode/anode electrodes.
4. High electric field obtained by ultrathin-film formation.

OLED devices could emit very dim light before these developments, but the high-luminance operation was achieved only after the first OLED paper. [1]

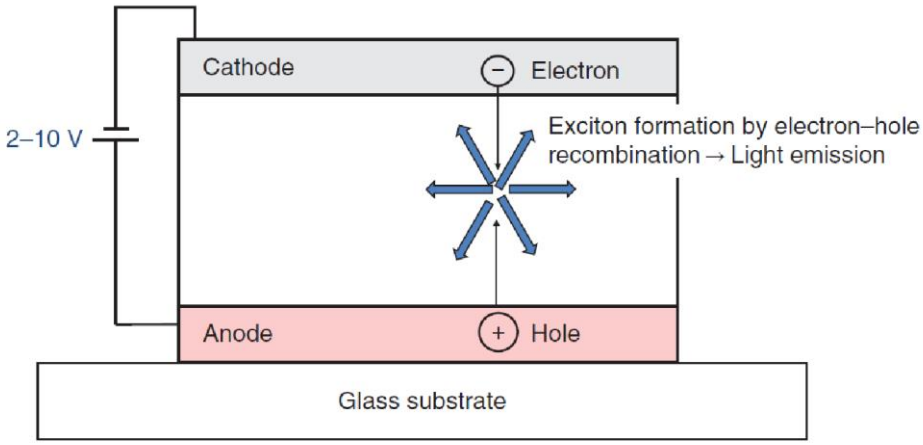

Figure 17 Diagram of the OLED emission mechanism. [1]

Figure 17 shows the simplest scheme, which was proposed in 1987. Later it was proposed to divide the active layer into electron transport and emission layers. After, this scheme was modified, and later the gar was subdivided into types: electron transporting layer, emission, hole transporting, and hole injection layers (**Figure 18**). Charge carriers are electrons and holes that move towards each other. The number of charge carriers strongly affects the efficiency of the device. one of the advantages of this method of construction of devices is a wide range of molecules in the emission layer. [1]

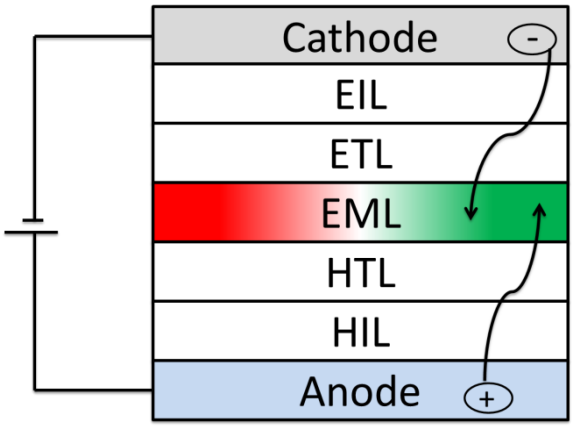

Figure 18. Scheme of OLED device using sharing by multiple layers.

The abbreviations in **Figure 18** are as follows:

- Electron injection layer (EIL) – provides electron;
- Electron transport layer (ETL) −serves for electron injection from the cathode and transport of electrons;

- Emission layer (EML) − electron/hole transport and their recombination;
- Hole transport layer (HTL) − for hole transport from HIL to EML layer;
- Hole injection layer (HIL) − for hole injection from the anode. [1]

Optimal HIL materials used in OLEDs have the following common properties: the highest occupied molecular orbital (HOMO) level should be located between the HOMO levels of the ITO and HTL materials; absorption of red, blue, and green (RGB) emission from the EML should be minimized; the glass transition temperatures should be high. [42] One of the most popular hole injection materials is PEDOT: PSS ((poly(3,4-ethylenedioxythiophene):poly(styrene sulfonate)), but now using small molecules based on benzo-dipyrroles (BDPs) and phenothiazine/phenoxazine derivatives become more popular. [42,43] The molecular design imparts the hole transport materials with the following features: high thermal stabilities with relatively high glass transition temperatures, easy solution-processability; high hole mobility, efficient hole injection, and electron-blocking ability.[44] One of the most popular materials to be used as HTL is *N,N′*-Di(1-naphthyl)-*N,N′*-diphenyl-(1,1′-biphenyl)-4,4′-diamine (NPB), triphenylamine (TPA) and its derivatives more known as TDATA, TCTA, etc.[44–47] Compounds for ETL usually have high electron-injection rate, high electron mobility, hole-blocking ability, and wide singlet-triplet energy gap to block exciton diffusion. Usually compounds based on silole, triazole, phenanthroline, dipyrenylpyridine derivatives are used for ETL. [46,48,49] These layers are important to increase the efficiency of the device, especially to enable effective recombination in EML.

3.7 Principles of thermally activated delayed fluorescent molecule design

The rapid development of the device is due to its widespread use. Especially the creation of a device based on flexible surfaces (films) allowed to further increase the production of organic-based displays, compared to liquid crystal displays, [50] although this type of screen has also disadvantages, such as short lifetime. The main problem of the dispatchers was the stability of the emission layer. This problem has been solved by the expensive iridium-containing complexes (PHOLED), but the manufacture of such devices is quite expensive and tedious. The use of organic substances makes it possible to make displays of different colors, which decreases the costs of manufacturing but has a fairly low time of life. [50] To understand the processes taking place in the device and to create displays with a long lifespan, it is necessary to understand the basic processes that take place in it. The thermally activated delayed fluorescent (TADF) requires a transition between electronic levels, and for this transition to be as effective as possible, the HOMO and LUMO levels must be separated. Therefore, donor-acceptor systems are often used for OLED products. Such systems have advantages, such as the possibility of controlling the luminescent properties by adjusting donor or acceptor group in π-conjugated systems, and relatively high mobility of the charge carriers. [51]

There are several other important parameters for TADF compounds such as ΔE_{ST} and Photoluminescence Quantum Yield (PLQY). PLQY could be determined by the next equation:

$$\phi = \frac{\#photons\ emitted}{\#photons\ absorbed} \tag{14}$$

ΔE_{ST} is associated with the conversion of a triplet exciton into a singlet exciton, while PLQY is associated with the probability of a radiation transition. The most important physical parameter of the TADF emitters is the ΔE_{ST}, which is related to the reverse intersystem crossing rate (k_{RISC}) by the following equation.

$$k_{RISC} \infty\ exp(-\frac{\Delta E_{ST}}{k_b T}) \tag{15}$$

The ΔE_{ST} value can also be defined as the difference between the energies of the singlet (E_s) and the triplet state (E_T).

These energies can be defined by the following equation:

$$E_s = E + K + J; \tag{16}$$

$$E_T = E + K - J, \tag{17}$$

where E is the orbital energy and K is the electron repulsion energy. In one molecule, the electronic arrangement of the singlet and triplet states is the same, and the values of E and K are also the same in singlet and triplet states.

It should also be born in mind that there must be some stabilization of the singlet and triplet states. The triplet state is stabilized by the presence of unpaired electrons in different orbitals, while the singlet state is destabilized by the presence of paired electrons in one orbital. The degree of stabilization is expressed by the J factor. The values of the degree of stabilization can be calculated using the overlap integers (HOMO) and (LUMO). That is, where the small values of J, there must be a small value of the overlap integral. In other words, these orbitals are supposed to be split apart. Despite the facts mentioned above, it is fashionable to take donor-acceptor systems for such purposes. [50]

Such groups as carbazole, phenoxazine, phenothiazine, amine, diamine, acridine demonstrate efficient donor properties. Among the acceptor groups, the most popular of them are diphenyl sulfone, phenylbutazone, aromatic calcium, aromatic triazole, oxadiazole, thiadiazole, benzothiazole, benzoxazole, quinoxaline, anthraquinone, and heptazine. Based on the values of HOMO and LUMO, it is fashionable to estimate the strength of the acceptor and the donor (**Figure 19**).

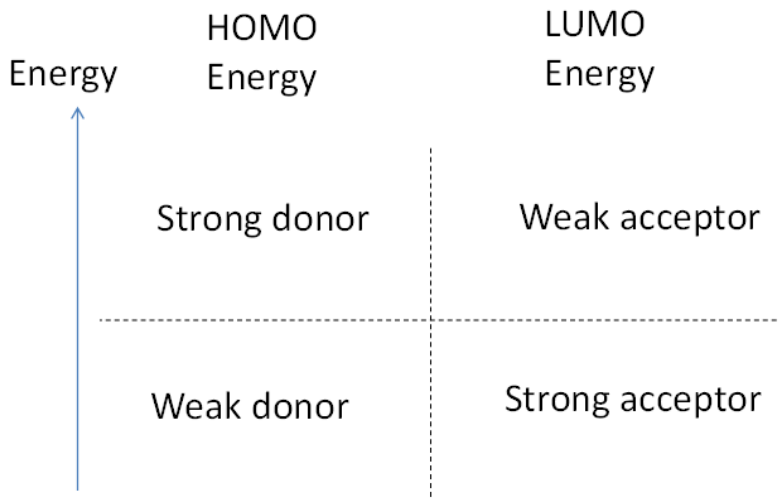

Figure 19. Dependence of donor/acceptor strength on the energy level.

The figure shows that low HOMO values are typical of weak donors, and low LUMO values are typical of strong acceptors. Conversely, high HOMO values are characteristic of strong donors and high LUMO values are for weak acceptors. The simplest way to estimate the value of energy (HOMO) and (LUMO) is to do a mathematical simulation for a molecule.

Usually, the basic set B3LYP 6-31G, which is built into Gaussian 09 and Schrödinger software, is used. Based on the simulations, phenoxazine, phenothiazine is regarded as strong donors, carbonitrile derived moieties can be used as strong acceptors [50] in addition to strong electron-withdrawing moieties including nitro (NO_2) and cyano (CN) functionalities. [52]

For increasing the efficiency of the device (EQE), not only small ΔE_{st} and high PLQY are important.

$$EQE = \frac{Photon\ s|s\ ec}{electron\ s|s\ ec} = \frac{(total\ power\ of\ photons)/(enegrgy\ of\ one\ photon)}{(Current)/(Cherge\ of\ one\ elctrone)} \quad (18)$$

There is a strong dependence between the External Quantum Efficiency of the device and PLQY.

$$EQE = \eta_{out} \cdot \eta_{fl} \cdot \gamma \cdot \eta_{fr} \quad (19)$$

Where η_{out} is the outcoupling (usually it's 20-30% maximum outcoupling efficiency); η_{fl} is the PLQY; $\gamma = 1,$ the charge balance factor; $\eta_{fr} = 0.25$ (for fluorescence emitter only 25% singlet excitons are formed directly from charge recombination. [1]

For this reason in design different π-linkers were used (**Figure 20**). Thus, various π-conjugated bridges, including triple or double bonds in aromatic, heteroaromatic, and mixed combinations, have been utilized as suitable-linkers. [52–55].

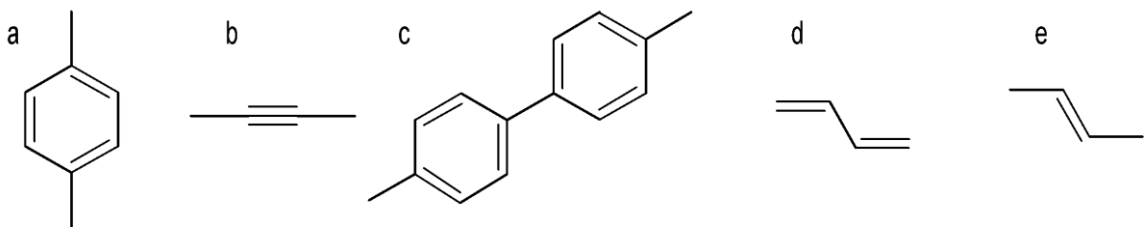

Figure 20. Popular linkers, which are used in D-A and D-A-D systems: a)Phenyl; b) acetyl; c) biphenyl; d) 1,3-butadiene; e) ethylene.

Phenyl linker was often used for high PLQY, etc. Generally, a phenyl linker is demanded to increase the D–A separation distance and relieve the twisted angle between D and A.[56] However, not in all cases, the linker was useful. Compounds, which include 4-dimethylaniline (DMA) donor group and $C(CN)_2$ acceptor group were synthesized with linker (CN) and without. Regarding CV results it is worth mentioning, that compounds without linkers undergo a reversible one-electron oxidation process. Compounds, which include CN-group, participate in a single, irreversible two-electron process. [54] It means that more efficient electron interaction is at the more planar structure.

3.8 Acceptor units

3.8.1 1,8-Naphtalimide

1,8-Naphthalimide derivatives can be used as biological markers, antitumor agents, fluorescent switches and sensors, and in liquid crystal displays. One of the advantages of 1,8-naphthalimide is the flat structure of the acceptor itself, and such a derivative is relatively easy to be modified by donor groups (**Figure 21**). [57] Among different types of EL materials 1,8-naphthalimide derivatives attracted attention due to the high quantum photoluminescence yields and good optical, thermal, and chemical stability. [58] Theoretical calculations show that such compounds have good properties for the transport of charge, and also have a large gap between HOMO and LUMO. [59] Usually, N-alkyl substituents were used for increasing the solubility of compounds. For non-alkyl substituents was determined LUMO level from CV of -3.19 eV, from DTF calculation from –3.16 eV to -2.94 eV for substituents, which consists of the pyrrole group. For thiophene substituents LUMO levels are from -3.36 eV to -3.10 eV and from -3.07 eV to -2.62 eV using CV and DFT calculation, respectively. [60] Investigation of properties depending on the length of substituents shown that E_{red} was in the range from 1.21 V (all potentials were mentioned vs Fc/Fc^{+}, in case other electrode or standard it was mentioned below potential) to -1.07 V (LUMO levels were in the range -3.25 eV to 3.11 eV) and the energy gap, which were calculated from the absorbance spectrum, were in the range 3.39–3.40 eV. [61] Comparing DTF calculation of N-pentyl-1,8-naphthalimide with different donor groups, it was mentioned that the LUMO level of energy is within the range from -2.68 eV to -2.59 eV, and from CV this range is from -3.5 eV to -3.29 eV. [62] A charge is localized on the naphthalene ring.

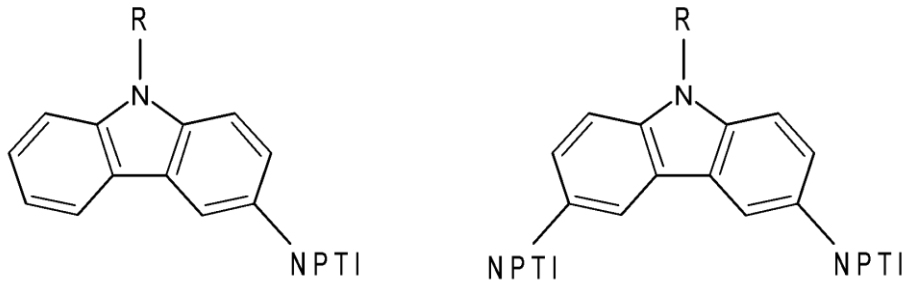

Figure 21. 3-substituted carbazole and 3,6-disubstituted carbazole. R- alkyl substituent. [57]

Absorbance spectra of mono- and disubstituted carbazole by NPTI showed an absorbance band at 344 nm and 398 nm, which is typical of naphthalimide based donor-acceptor systems. The absorption band at 344 nm can be attributed to the naphthalimide moiety, while the lowest energy absorption band can be attributed to the extended π-conjugated state involving the electron-donor carbazole and the electron-acceptor naphthalimide moieties. [57]

Among the various types of EL materials, 1,8-naphthalimide derivatives attracted attention due to the high quantum photoluminescence yields and high optical, thermal, and chemical stability. [58]

Spectroelectrochemical data (during the reduction process) was mentioned decreasing absorbance in the range 340–380 nm and increasing absorbance in the range 480-760 nm. [63] increasing absorbance can correspond to the formation of the anionic form of 1,8-naphthalimide.

There are quite rich hyperfine structures during the reduction process. Registered ESR spectra of the anion radicals generated through the reduction of each monomer have revealed an extremely rich hyperfine structure. This structure arises as a result of the interaction of the radical with both naphthalic hydrogens and imide nitrogen. ESR signals appeared at the potential, corresponding to the onset of the monomer reduction process, indicating the proceeding generation of anion radicals. The radical anions of derivatives of naphthalimide are fairly stable. [60] For diimide-based compounds, EPR measurements show that for all obtained radical anions spin-density is distributed over the diimide core. It was concluded based on simulation of EPR spectra which assumed isotropic hyperfine interaction of an unpaired electron with two nitrogen and four hydrogens atoms for PI-1 and with two nitrogen and eight hydrogen atoms. [63]

3.8.2 Tetrazine

Tetrazine has three isomers, one of them 1,2,4,5-tetrazine a common known as s-tetrazine. Comparing with a benzene ring, tetrazine has 4 more electronegative substituents, which means that tetrazine has a high electron affinity (**Figure 22**).

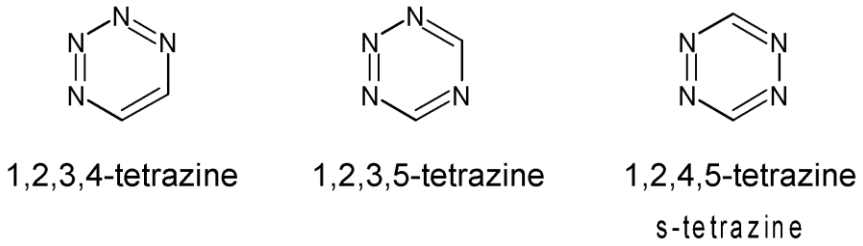

Figure 22. Isomers of tetrazines.

Nowadays, *s*-tetrazine is used as an acceptor unit for design molecules for sensors, photovoltaic cells, electrochromic devices.[64,65]. There are a lot of works devoted to the investigation of s-tetrazine based compounds with substitutions. DFT calculation showed that the LUMO orbital is generally a π*-MO localized over the tetrazine ring, on which its aromatic substituents have a limited influence. For 3,6-diphenyl - tetrazine, DFT calculation showed that this structure is quite flat, and this fact can be useful for the further design of donor-acceptor complexes (**Figure 23**). [66]

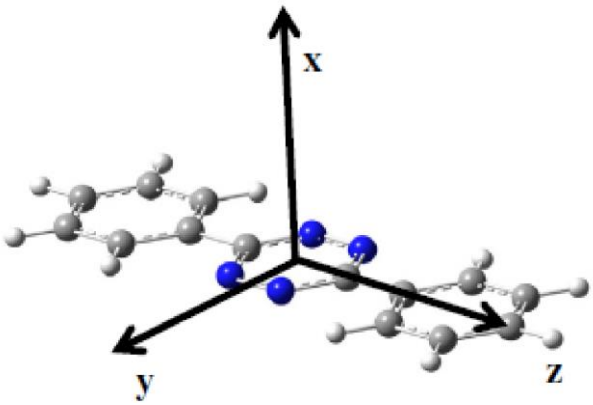

Figure 23. Rod-sphere model of a space structure of 3,6-*di*phenyl-*s*-tetrazine. [66]

In this case, the LUMO level is localized only on the tetrazine ring, but LUMO+1 is localized on the whole molecule. The LUMO level for monomers is around -2.8 eV. HOMO level for this unit is lower than -6.3 eV. for polymers based on diphenyl-*s*-tetrazine is -3.322 ± 0.032 eV for n→∞, where n – number of the diphenyl-*s*-tetrazine units. [66] Tetrazine derivatives have a reversible reduction process with reduction potential from -1.12 V to -0.77 V. [22] Reduction potential of tetrazine depends on the atom directly linked to tetrazine.

A chlorine atom on the tetrazine moiety for all the synthesized derivatives stabilizes the anion radical better than the oxygen link, so the reduction of the chlorine-substituted tetrazine core is easier. [67] The position of π–π** transition strongly depends on the substituent nature, it correlates linearly with their electron-donating or withdrawing character. The π–π* transition for tetrazine derivatives is around 520 nm, and there is a high absorption coefficient at 530 nm around 75000 $L \cdot mol^{-1} \cdot cm^{-1}$. [68]

Spectroelectrochemical investigation of *s*-tetrazine-triphenylamine for the reduction part shown small decreasing absorbance at 300 nm and a slight band grew at 470 nm. EPR investigations of the formation of radical anion of *s*-tetrazine-triphenylamine shown that anion was formed by splitting signals from 4 atoms of *N* (with high resolution) with hyperfine constant 0.53 mT. [69]

3.9 Donor units

3.9.1 Carbazole

Carbazole (CBZ) as an *N*-containing heterocycle is a promising donor group for Organic materials with thermally activated delayed fluorescence and organic light-emitting diode (OLED), because of the small singlet−triplet energy splitting, which allows effective reverse intersystem crossing (RISC). [70]

Optimization geometry DFT calculation showed, that both CBZ and NPTI are planar, and the rotation angle is 60.3°. In the case of CBZ based compounds electron density is mainly localized on the CBZ unit revealing small interaction with the NPTI unit (**Figure 24**). [57]

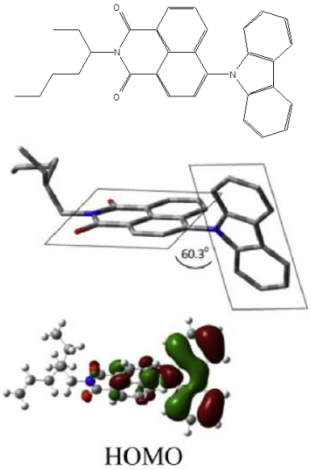

Figure 24. Geometry optimization of monosubstituted CBZ and graphic model of HOMO wavefunction. [57]

For other combinations of compounds based on CBZ and NPTI it was shown that as the angle between the planes decreases, the electron density on the NPTI unit becomes closer. [57] In the case of one acceptor group and two donors, e.g. diphenyl sulfone derivatives, the angle between donor and acceptor group is about 52°, but DFT calculation showed spatial separation of HOMO and LUMO. In this case, HOMO was determined as -5.60 eV. [71]

For example, CBZ with pyridine derivatives has calculated HOMO levels in the range of -5.34 eV to -5.31 eV. [72] Compounds containing CBZ and BODIPY have HOMO levels from -5.13 eV to -5.00 eV. [73] CBZ with triazine derivatives has a little bit higher levels of ionization potential from -5.06 eV to -5.21 eV.[74]

Cyclic voltammetry showed that the oxidation process has a non-reversible character. The first oxidation peak is located between 0.4 V and 0.59 V. The low oxidation potential is caused by the large number of CBZ groups, which can be explained by a small inductive effect. [73]

CBZ derivatives, which has activate 6 positions, are quite sensitive to the oxidation process, and it can undergo a dimerization process with lower oxidation potential (above 0.1 – 0.2 V lower than the oxidation potential of monomer) therefore the products are characterized by lower electrochemical stability. [57] Carbazole-triazine derivatives showed an oxidation signal at 0.81 V. [75]

Compounds based on *N*-(4-methyl-phenyl)-carbazole derivatives during the oxidation process showed an increasing band at 417 nm which corresponds to radical cation and band 917 nm corresponds to a mixture of radical cation and dication. [76] During the spectroelectrochemical investigation of PTZ compound substituted with CBZ, the increasing absorbance bands at 442 nm and 1097 nm referred to radical cation and the increasing band at 688 nm referred to dication oxidation form. [77]

In the case of electrochemical oxidation of carbazole-triazine derivatives the following changes were mentioned: the disappearance of the band at 360 nm (associated with absorption of the carbazole); formation of the single band at 500 nm (corresponds to the formation of polymer); increasing band in the range 850 – 1450 nm which is characteristic for radical cation. The absorbance band at 710 nm corresponds to dication formation caused by applying higher potentials. The isosbestic point is located at 500 nm. [78]

ESR spectrum of *N*-(4-methyl-phenyl)-carbazole derivatives has a hyperfine structure, which is easy to be simulated with a high correlation constant of 99.8%. Five types of different groups with different constant were mentioned: 8.77 G (2N), 3.06 G (2H), 2.90 G (2H), 0.95 G (4H), and 0.90 G (6H). This simulation showed that all nitrogen and hydrogen atoms affected the hyperfine structure. Remarkably, both nitrogen atoms have the same hyperfine coupling constant, which indicates spin delocalization over the two redox centers. [76]

Radical cation of compound PTZ-CBZ was localized at the PTZ moiety. ESR spectrum was simulated using hyperfine constant 7.49 G for 1N and 3.84 G for 2H. A radical cation is delocalized over the π-conjugated backbone, but the nitrogen and sulfur atoms also contribute to the structure. [77]

During several scans, the CBZ unit can form an electroactive polymer film on the surface of the electrode. Poly-CBZ derivatives have Ox/Red couples from 0.73 V to 1.16 V

and from 0.81 V to 1.36 V respectively. The CV was mentioned that during several scans maxima of anodic current decreased. It means that polymer deposition onto the electrode surface caused a loss of electrode active surface. Polymers based on the CBZ unit were characterized by absorbance at 300 nm, which is stable during the spectroelectrochemical experiment. During this investigation decreasing of absorbance at 480 nm and 580 nm was observed. [79] For polymers based on PXZ substituted by carbazole, oxidation potential was less by about 0.2-0.3 V compared with the monomer unit. [77]

Polymers based on 3,6-carbazole derivatives have oxidation potential from 0.59 V to 0.71 V. Shape of CV curve – the potential shift between the monomer peak and peak of the electrodeposited layer suggests that the layer is formed by species that are more conjugated than monomer. Using absorbance spectra π–π* transition was determined at 404 nm. During the oxidation process increasing of absorbance bands at 672 nm and 960 nm and isosbestic point at 430 nm was observed, which suggests the presence of polarons and bipolarons in the conducting layer. But some polymers didn't have any significant changes. [75]

Polymers based on triarylbenzene-carbazole have two oxidation states. The first oxidation (0.82 V) corresponds to the formation of carbazole radical cation which oxidates to carbazole dication at 1.28 V. The formation of carbazole dication is a result of coupling between the carbazole radical cations and the deposited polymeric carbazole on the working electrode. With the increasing number of scans, the peak current increases, indicating the successive deposition of dimeric or oligomeric carbazole units on the working electrode. These polymeric films have high absorbance below 300 nm and lower about 350 nm. [80]

Polymer-based on carbazole-triazine derivative during oxidation showed increasing absorbance bands at 455 nm, 1000 nm, and 1480 nm which is characteristic of radical cation, after conversion into dication with the absorption band at 540 nm and 700 nm. [78] Polymers based on CBZ –TPA (Triphenylamine group) showed two groups of π-π* transition: band at 296 nm corresponds to CBZ moiety and bands at 307 nm, 327 nm correspond to TPA moiety. During the oxidation process, the formation of polarons (with theoretical bandgap 2.87 eV, a wavelength at 432 nm) was observed. During this process bands at 294 nm and 324 nm decreased and bands at 300 nm and 420 nm in the UV-VIS region and 1038 nm in the NIR region increased. [81] The recorded signals of these types of polymers have a *g*-factor value of 2.0027, which is close to that of the nitrogen atom (2.003). For the simulation of these signal Lorentz distribution model (suggests the existence of many paramagnetic centers of various origins or various neighborhood well distributed in the polymer) was used, combined by the sum of two Lorentz distribution functions with constants 3.0 G and 4.5 G. [81]

For polymers based on PTZ substituted by carbazole during the oxidation process was mentioned decreasing absorbance band at 310 nm (and 326 nm for polymer-based on PXZ instead PTZ), which is correspond to neutral particle, increasing polaronic band at 427 nm for poly-PTZ-CBZ and 413 nm for poly-PXZ-CBZ, and bipolaronic band at 729 nm for poly-PTZ-CBZ and 688 nm for poly-PXZ-CBZ. [77] For polymers based on PTZ substituted by carbazole during the oxidation process decreasing of absorbance band at 310 nm was observed, which corresponds to neutral particle, increasing polaronic band at 427 nm for poly-PTZ-CBZ and 413 nm for poly-PXZ-CBZ, and bipolaronic band at 729 nm for poly-PTZ-CBZ and 688 nm for poly-PXZ-CBZ. [77]

3.9.2 Phenoxazine

PXZ is well known as an electron-donating (including electron-rich nitrogen and oxygen) non-planar group. This compound is interesting due to avoiding aggregation and the formation of different intermolecular excimers.

DFT calculation shows that in the case of thiatriazole-phenyl-phenoxazine almost perpendicular twist between the phenoxazine and the thiatriazole-phenyl moieties takes place. It means a complete spatial separation of the HOMO and LUMO, which suggests the charge transfer effect with HOMO equal to -5.35 eV (**Figure 25**).[82]

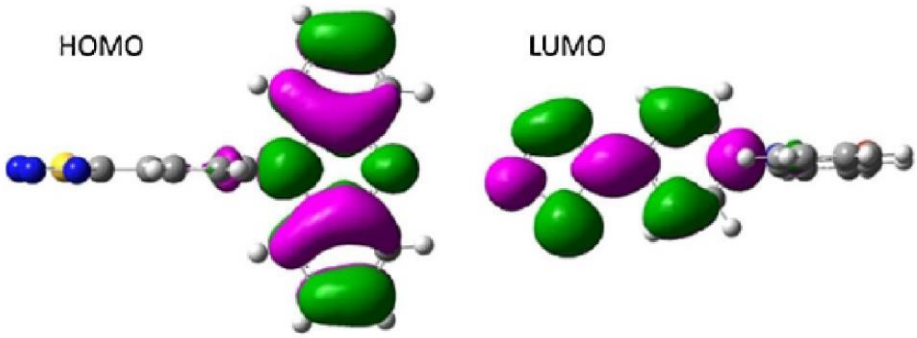

Figure 25. Calculated distribution HOMO (left) and LUMO (right) of Phenoxazine-thiatriazole-phenyl. [82]

For other functionalized PXZ, DFT calculations shown that HOMO localized at electron-donating phenoxazine, with a HOMO level around -4.91 eV.[83] In the case of two

donor groups with diphenyl sulfone acceptor unit, calculated angles between donors and acceptor group are 88°,89° and the HOMO level is -4.88 eV. [71]

PXZ-quinoxaline derivatives demonstrate a weak dependence on the number of donor groups. DFT calculation showed that for a compound with 1 donor group HOMO level is -5.17 eV and for 3 donor groups a little higher -5.14 eV. The wavelengths of π–π* transition were 594 nm and 618 nm respectively. The angle between the PXZ group and the quinoxaline group is 84°, and in the case of 3 donors, these angles are 75°-83°. [84]

Phenoxazine isoquinoline derivatives with steric stroke have much higher calculated HOMO levels of energy -4.57 eV and -4.61 eV. [85] Compound based on Phenoxazine coumarin has a non-reversible oxidation peak at 0.90V (which is equal to HOMO levels -5.70 eV). The wavelength of π–π* transition was determined as 420 nm. [83] *10H*-phenoxazine isoquinoline derivatives have oxidation potential from 0.30 V to 0.32 V and wavelength of π–π* transition at 420 nm, which is equal to the bandgap of 2.9 eV. [85] Dipiridino-di-benzophenazyn-*10H*-phenoxazine derivatives have a highly twisted structure with dihedral angles of 85° disabling electronic interactions between the D and the A components, HOMO levels for these compounds are -5.39 V. In the case of two donor groups with diphenyl sulfone acceptor unit oxidation potential is 0.35 V and HOMO levels were calculated at -5.09 eV. [71]

N-Trifluoromethyl phenoxazines group has a maximum of absorbance at 322 nm. In case the presence of substituents in position 3,7 was observed a redshift absorbance peak closer to the visible region. (359 nm in case of phenyl substituent, 386 nm in case of *tri*-fluoromethyl-phenyl substituent, and 356 nm in case of 1-phenylethan-1 one substituent). [86] *10H*-phenoxazine propanoic acid during oxidation showed a decreasing absorbance peak at 230 nm and 320 nm and increasing at 410 nm and 530 nm. [87] Oligomers based on phenoxazine with a polydispersity index of 1.35 during oxidation have a decreasing absorbance band at 442 nm wavelength, which is characteristic of a neutral particle. Increasing at 605 nm is characterized by radical cation (polaron) and increasing at 1016 nm is characterized by dication (bipolaron). The isosbestic point was observed at 496 nm. [88]

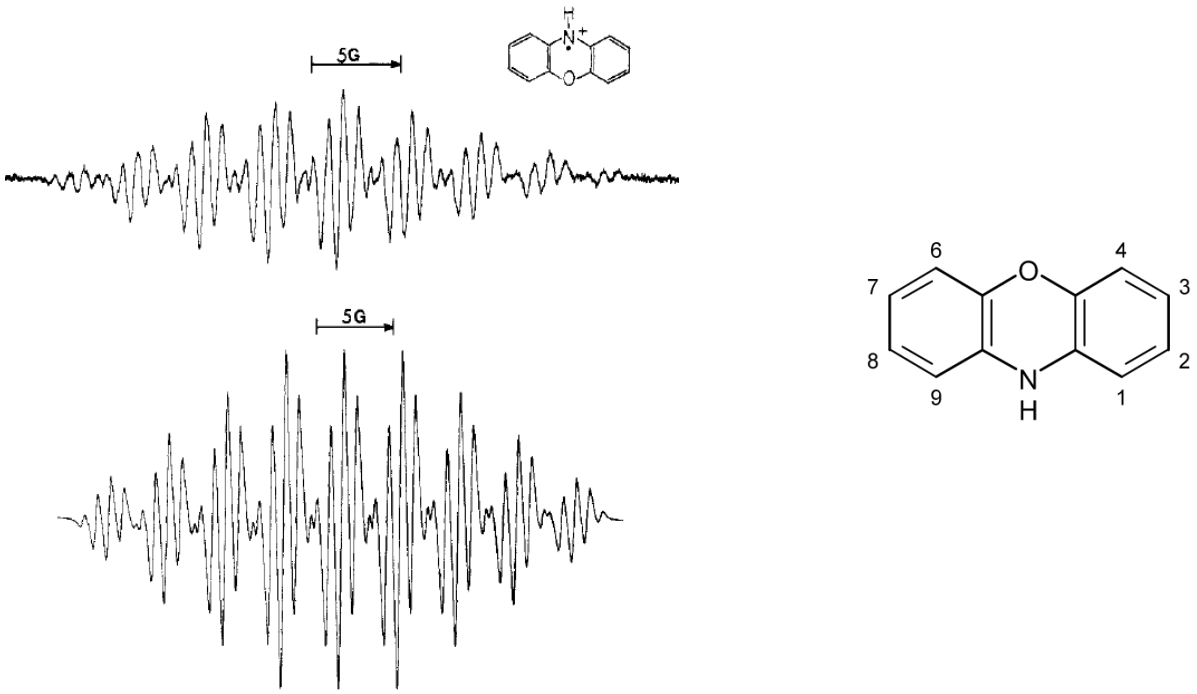

Figure 26. Simulated (up) and experimental (bottom) spectra of photolyzed phenoxazine in the presence of air. [89]

ESR-spectra of photolyzed phenoxazine in the presence of air has well defined hyperfine structure, and simulation of this structure *N* 7.80 G, *NH* 7.80 G, *3H,7H* 3.90 G, *1H,9H* 0.87 G *4H,6H* 0.86 G (**Figure 26**). [89]

Generally, PXZ-based compounds give ESR-spectrum with a well-defined hyperfine structure. For example, in monosubstituted *Ni*-porphyrin the EPR signal showed that the first electron was removed from the nitrogen atom of the aromatic PXZ donor. Simulation of the spectrum yielded coupling constants with one *N* atom equal to 8.3 G and with one set of two hydrogen atoms equal to 2.9 G. However for di-substituted *Ni*-porphyrin spectrum consists of a quintet with a line intensity ratio of 1:2:3:2:1 corresponds to two equivalent nitrogen atoms with a hyperfine coupling constant of 4 G. This value is attributed to the biradical with a strong spin-spin exchange coupling.[90] In case oligomers with PXZ, dication is non-paramagnetic, and wasn't possible to measure proper EPR spectra.[88]

3.9.3 Phenothiazine

Phenothiazine, as an analog of the PXZ unit, is a rich electron-donating group. For phenothiazine-coumarin derivatives. DFT calculations have shown that HOMO localized at electron-donating phenothiazine, with a HOMO level of around -5.456 eV with π–π*

transition at 416 nm [83] In the case of two donor groups with a diphenyl sulfone acceptor unit, the angle between donors and acceptor group is 81°,82°, and the HOMO level was calculated –5.21 eV. [71]

Phenothiazine functionalized BODIPYs have π–π* transitions in the range 450-580 nm. Compounds with one acceptor group have higher (-5.43 eV and -5.48 eV) calculated HOMO level of energy than compounds with two acceptor groups (-5.76 eV and -5.80 eV). The calculated dihedral angle values between PTZ and BODIPY are 51.8° (for compound A-D) and 53.1° (for compound A-D-A), it means that these compounds have twisted structure. For compounds with linker (acetylene linker), the calculated dihedral angles between donor and acceptor parts are 1.1° (for compound D-π-A) and 3° (for compound A-π-D-π-A), which exhibit nearly planar geometry. [91]

For phenothiazine-triphenyltriazine derivatives for two conformers (axial and equatorial) using DFT calculations was mentioned that both conformers relax to the same configuration in the first excited state (S1) (θa = 90°, θb = 180°) (**Figure 27**). [92]

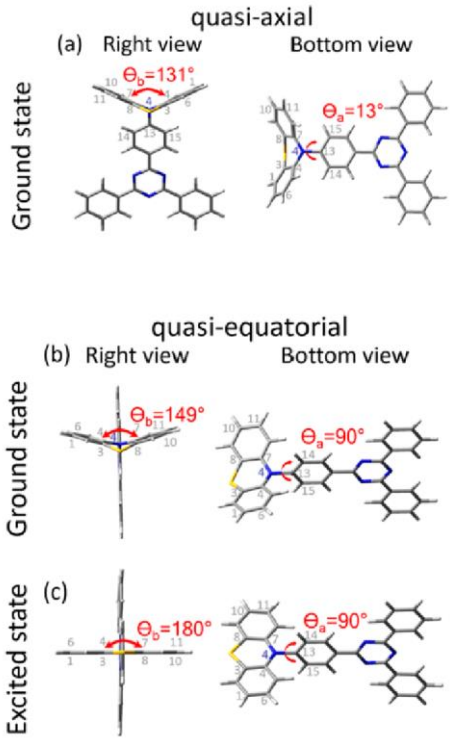

Figure 27 DFT calculation of phenothiazine-triphenyltriazine derivatives. [92]

Compound based on phenoxazine coumarin has a non-reversible oxidation peak at 1.05 V (which is equal to HOMO levels -5.85 eV). Wavelengths of π–π* transition were determined as 504 nm. [83] In this case, two donor groups with diphenyl sulfone acceptor unit

oxidation potential are 0.54 V and HOMO levels were calculated -5.35 eV. [71] The signal from the oligomer of PTZ *N*-nonydiphenyl units obtained on the CV is a combination of low and high conjugated oligomeric parts. These peaks appear at -0.08 V and 0.15 V. [88]

Phenothiazines functionalized BODIPYs have oxidation potential at 0.85 V (A-D) and 0.95 V (A-D-A) and phenothiazines functionalized BODIPYs with acetylene linker have much higher potentials of 0.87 V (A-π-D) and 0.9 V (A-π-D-π-A). compounds with two acceptor groups have higher oxidation potentials than compounds with one group, this fact indicates that the incorporation of two acceptors BODIPY units decrease the electron density on phenothiazine and the result is the higher oxidation potential. [91]

Dyads based on PTZ-anthraquinone derivatives have oxidation potential in the range of 0.10 – 0.23 V and DFT calculation showed that the HOMO level is located at PTZ moiety. [93]

Compounds based on phenothiazine-triphenylamine have oxidation potential from 0.41 to 0.63 V vs NHE, and the wavelength of π–π* transition was determined as 305 nm, which means an energy gap of 4.07 eV. [94]

Oligomers based on phenoxazine with polydispersity index 1.771 during oxidation have a decreasing absorbance band at 422 nm, this wavelength is characterized by a neutral particle. Increasing at 617 nm is characterized by radical cation (polaron) and increasing at 1007 nm is characterized by dication (bipolaron). The isosbestic point was observed at 480 nm. [88]

In the case phenothiazine-triazine derivative, during oxidation was mentioned two broad absorption bands 550−700 nm and 750−1100 nm, Which bands correspond to the formation cation radical. oxidation to higher potential suggests to formation dication with characteristic visible bands at 1050 nm and the bands at 450–550 nm. [78]

The ESR spectrum of helicenes derivatives based on PTZ unit, PTZ-PTZ showed a five-line splitting, which is mainly attributed to the hyperfine coupling interactions from two equivalent *N* nuclei (splitting constant 0.58 mT) This result indicates that the generated radical spin is equally delocalized over the two phenothiazine moieties. [95]

Electron paramagnetic resonance is useful to confirm stable cation radicals. For triethoxysilylated phenothiazines, the ESR spectrum reveals a g-value of 2.005 typical for phenoxazine radical cation. The high symmetry of the signal corresponds to the isotropic environment. [96]

For $(PTZ)_n$-anthraquinone dyads ESR signals consist of three signals split by about 0.34 mT. For dyad, which consists of 1 PTZ group *g*-factor value g = 2.0055 and splitting

constants 1N = 0.66 mT, 1H = 0.24 mT, 2H = 0.11 mT. For dyad with 3 PTZ group signal consists of two lines (*g*-factor 2.0041) splitting with constants 1N = 0.665 mT and 2H = 0.110 mT. [93]

3.9.4 Dimethyl-acridine (DMAC)

In the case two donor groups, with a diphenyl sulfone acceptor unit, the angle between donors and acceptor group are 90°,91°, and HOMO level were calculated –5.09 eV. [71]

For DMAC-pyrimidine derivatives, the angle between HOMO and LUMO orbitals was determined from 88.91° to 90.38°. The π–π* transition was calculated as 350–400 nm. The electron density distribution HOMO was localized on the planar DMAC unit. From XRD investigation it was mentioned that the angle between DMAC group and linker (phenyl linker) is 85.49°–88.78° and the angle between linker and acceptor group (pyrimidine) is 15.28°–17.87°. For DMAC-pyrimidine derivatives, the HOMO level was determined as -5.34 eV. [97]

DMAC-imidazole derivatives have a good reversible oxidation process and the HOMO level was determined -5.3 eV -5.32 eV. It is so close to the results from the DFT calculation. The theoretical HOMO level was localized on electron-rich DMAC with a value of -4.86 eV -4.97 eV. The dihedral angle between the donor group and linker (phenyl linker) is in range 35.4°–42.1°, and the angle between linker and acceptor group is 27.1°–32.4°. The wavelength of π–π* transition, in this case, was determined by 311 nm 367 nm. [98]

DMAC-quinoxaline derivatives have a small difference depending on the number of donor groups. DFT calculation showed that for a compound with 1 donor group HOMO level is -5.26 eV and for 3 donor groups a little bit higher -5.17 eV. The HOMO level rises accordingly with the enhancement of electron-donating ability. The wavelengths of π-π* transition were 541 nm and 551 nm respectively. The angle between the DMAC group and the quinoxaline group is 87°, and in the case of 3 donors, these angles are 87°–88°.[84]

For acridine derivatives, especially 9-phenyl acridine was mentioned, that during photoirradiation increasing absorbance band 400-450 nm corresponds to the formation of the radical cation. [99]

For 9-Hydroxy-10-methyl-9-phenyl-9,10-dihydropyridine during the oxidation process (0.56 V) was mentioned increasing the absorbance band at 425 nm which corresponds to radical cation. [100]

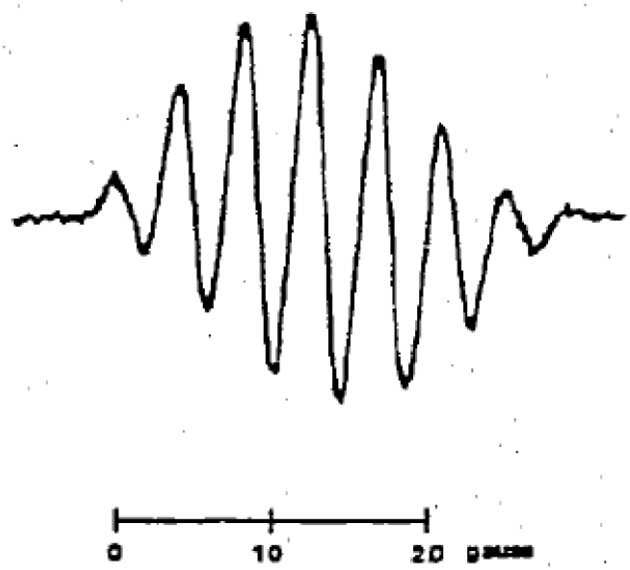

Figure 28. ESR spectrum of acridine. [101]

ESR spectrum of acridine showed a split structure in ratio 1:4:7:8:7:4:1 (**Figure 18**). [101] This spectrum is characterized as a metastable triplet state with a splitting constant of 4.4 G. It is interesting, that changing protons to deuterium involved a split structure with a ratio of 1:1:1, and the splitting constant, in this case, is 10.1 G.[101]

4 Experimental part

4.1 Materials and techniques

Cyclic voltammetry

The electrochemical cell comprised of the platinum 1 mm diameter working electrode, an $Ag|Ag^+$ electrode as a pseudoreference electrode, and a platinum coil as an auxiliary electrode (**Figure 29**). Cyclic voltammetry measurements were conducted at room temperature at a potential scan rate of 50 mV/s and were calibrated versus ferrocene/ferrocenium redox couple. The investigation was carried out using CH Instruments 660 potentiostat.

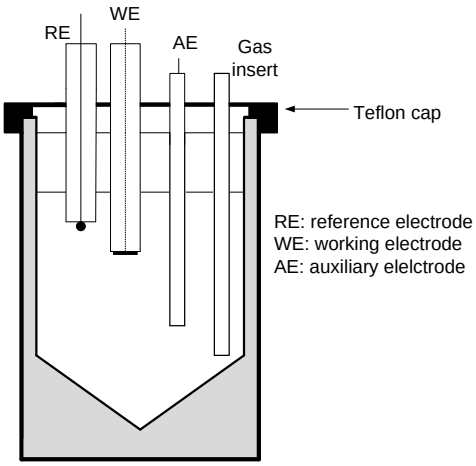

Figure 29. Cell for cyclic voltammetry.

Cyclic voltammetry measurements were conducted using 1.0 mM concentrations of all compounds. The studied compounds were dissolved in 0.1 M solutions of Bu_4NBF_4 (99% purity, Sigma Aldrich, used as an electrolyte) in dichloromethane (DCM) CHROMASOLV (99.9% purity, Sigma Aldrich).

All values of potentials in the thesis are shown vs Fc/Fc^+ couple. From the potentials of the onset of redox peaks of samples, it is possible to estimate the ionization potential (IP) and the electron affinity (EA) provided that these potentials are expressed on the absolute potential scale i.e. concerning the vacuum level. The absolute potential of Fc/Fc^+ in non-aqueous electrolytes is 5.1 V. [102] The equations (1) and (2) are given above.

The HOMO-LUMO levels were determined electrochemically, using cyclic voltammetry (CV) analysis through the estimation of the electron affinity and the ionization potentials which are similar to the HOMO and LUMO energies.

Usually, redox potentials are measured in solution, but levels of energy are scaled in a vacuum. It was assumed that the formal potential Fc/Fc^+ in the Fermi scale versus saturated calomel electrode (SCE) in acetonitrile is 5.1 eV. It follows that (in the physical potential scale): [14]

$$E_{HOMO} = -(E_{[onset,ox\ vs.\ Fc/Fc^+]} + 5.1) \quad (20)$$

$$E_{LUMO} = -(E_{[onset,red\ vs.\ Fc/Fc^+]} + 5.1) \quad (21)$$

The calculation of the energy gap (E_g^{opt}) between levels was performed from the absorbance spectrum. For calculation, we need to know the wavelength of π–π^* transition (λ).

$$E_g^{opt} = \frac{1240}{\lambda}; \quad (22)$$

The value was subsequently compared with the results from CV:

$$E_g^{calc} = E_{LUMO} - E_{HOMO}. \quad (23)$$

Spectroelectrochemistry

The measurement cell was based on cuvette for spectroscopy, type 100-Qs, optical part length 5 mm, Hellma Analytics. The electrochemical cell comprised of the ITO electrode as a working electrode (or Pt net in case of CBZ-containing compounds), $Ag|Ag^+$ electrode as a pseudoreference electrode, a platinum coil as an auxiliary electrode, and a Teflon strap as a gasket between the wall of cuvette and ITO electrode (**Figure 30**). The polarization potential of ITO is between -0.45 V and 1.92 V vs reversible hydrogen electrode (RHE) [103], or -1.39 V and 0.98 V vs Fc/Fc+ couple. Spectroelectrochemical analysis including simultaneous registration of UV-Vis-NIR spectra and voltammogram was performed using Ocean Optics QE6500 and Autolab PGSTAT100 (Metrohm Autolab) potentiostat.

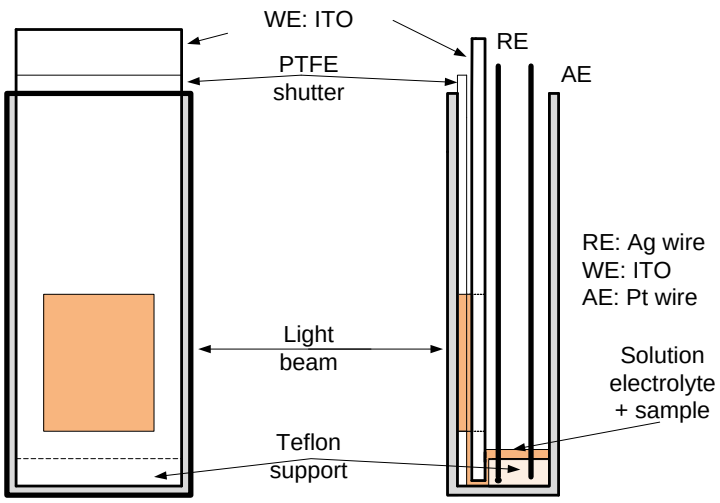

Figure 30. Cell for spectroelectrochemistry.

The absorption coefficient at wavelength longer than 400 nm was sufficiently small, so the concentration was increased by 3 mM for clearer visualization of changes. Cyclic voltammetry measurements were conducted using 3.0 mM concentrations of all compounds. Electrochemical studies were carried out in 0.1 M solutions of Bu_4NBF_4, 99% (Sigma Aldrich) in dichloromethane (DCM). Samples have high solubility in DCM CHROMASOLV, 99.9% (Sigma Aldrich).

The formation of polymer layers on the electrode surface was realized using the ITO electrode (platinum net was used in case of CBZ substituent due to the high oxidation potential of CBZ) during 10 scans, and after thus electrode was immersed into the solution of an electrolyte. The initial potential for all spectroelectrochemical measurements was 0V to enable observation of neutral particle redox transformation. The increase of absorption was associated with the generation of cations, radical cations, and various products of the oxidation reaction.

The sample at 0 V was taken as a reference (background) spectrum. The positive changes, in this case, correspond to the increase of absorption related to the formation of the oxidized particle, and the negative changes - to the decrease related to the decomposition of the initial compound.

Electron Spin Resonance (ESR)

Cell for measurement was made using a glass Pasteur pipette with a melted ending. The electrochemical cell is comprised of the platinum electrode as a working electrode and

$Ag|Ag^+$ electrode as a pseudoreference electrode and a platinum net as an auxiliary electrode. (**Figure 31**) Electrochemical measurements were conducted in 3.0 mM concentrations of all compounds. Electrochemical studies were undertaken in 0.1 M solutions of Bu4NBF4, 99% (Sigma Aldrich) in DCM CHROMASOLV, 99.9% (Sigma Aldrich). In situ EPR spectroelectrochemical experiments were performed using a JES-FA 200 (JEOL) spectrometer using Autolab PGSTAT100 (Metrohm Autolab) potentiostat. The *g*-factor value was determined using JEOL internal manganese oxide standard, taking into account that the third line of the Mn-standard spectrum has a *g*-factor of 2.03324. The width of the EPR signal has been calculated as a distance in mT between the minimum and the maximum of the spectrum.

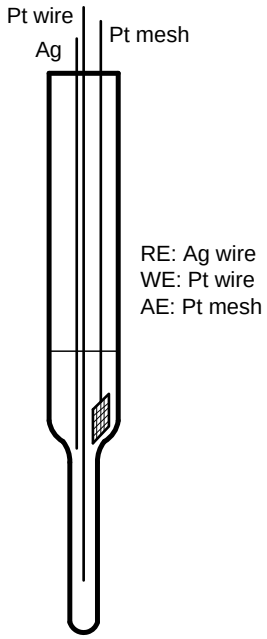

Figure 31. Cell for ESR measurement.

The experiment starts from neutral potential, further, the potential is increased up to a rate of 50 mV/s to the oxidation potential and was kept at a constant value during the record of the spectra.

The attention was driven to the magnetic field range between the 3rd and 4th peaks of Mn standard. The peaks, which appeared in the presence of the organic compound, referred to the generation of radical cations and radical anions (i.e. presence of unpaired electrons), which are paramagnetic in the magnetic field. For measurements are used next parameters:

- Amplitude 500
- Modulation 0.06 mT

- Time constant 0.03 s
- Centerfield value to *ca.* 338 mT

g factor was calculated using the position of the magnetic field of the 3rd Mn line and position of the central peak from the sample (B_s)

$$g\ factor = \frac{B(Mn\ 3^{rd})\cdot 2.03324}{B_s} \tag{24}$$

The Winsim program was used for the simulation of the hyperfine structure by adjusting electronic parameters. In the case of non-symmetrical signals, the structure was not simulated using Winsim, to avoid a high mathematical error. A mathematical separation of peaks was proposed for this type of signal.

For example, the signal from ESR is unsymmetrical (as it showed in **Figure 32a**) and it was known from the previous investigation, that compounds during oxidation form not only radical cation but also product. Both of them have signals in the ESR spectrum. Radical cation and product have similar nature, so that constant of signal coupling is quite similar, thus the simulation becomes difficult and the coefficient of correlation appears to be less than 0.90. (**Figure 32b**). In this case, there is no interpretation of the shoulder on the left side. If the beginning signal is divided into two different signals: one from radical cation (I) and another from the product (II), these signals can be simulated separately. (**Figure 32c**). In this case, the correlation is much higher (R^2 = 0.9956) and the summarized curve is quite similar for an experimental signal. (**Figure 32d**) This method can be used not only in the case of two singlet signals, but it can also be used for the interpretation of more difficult signals.

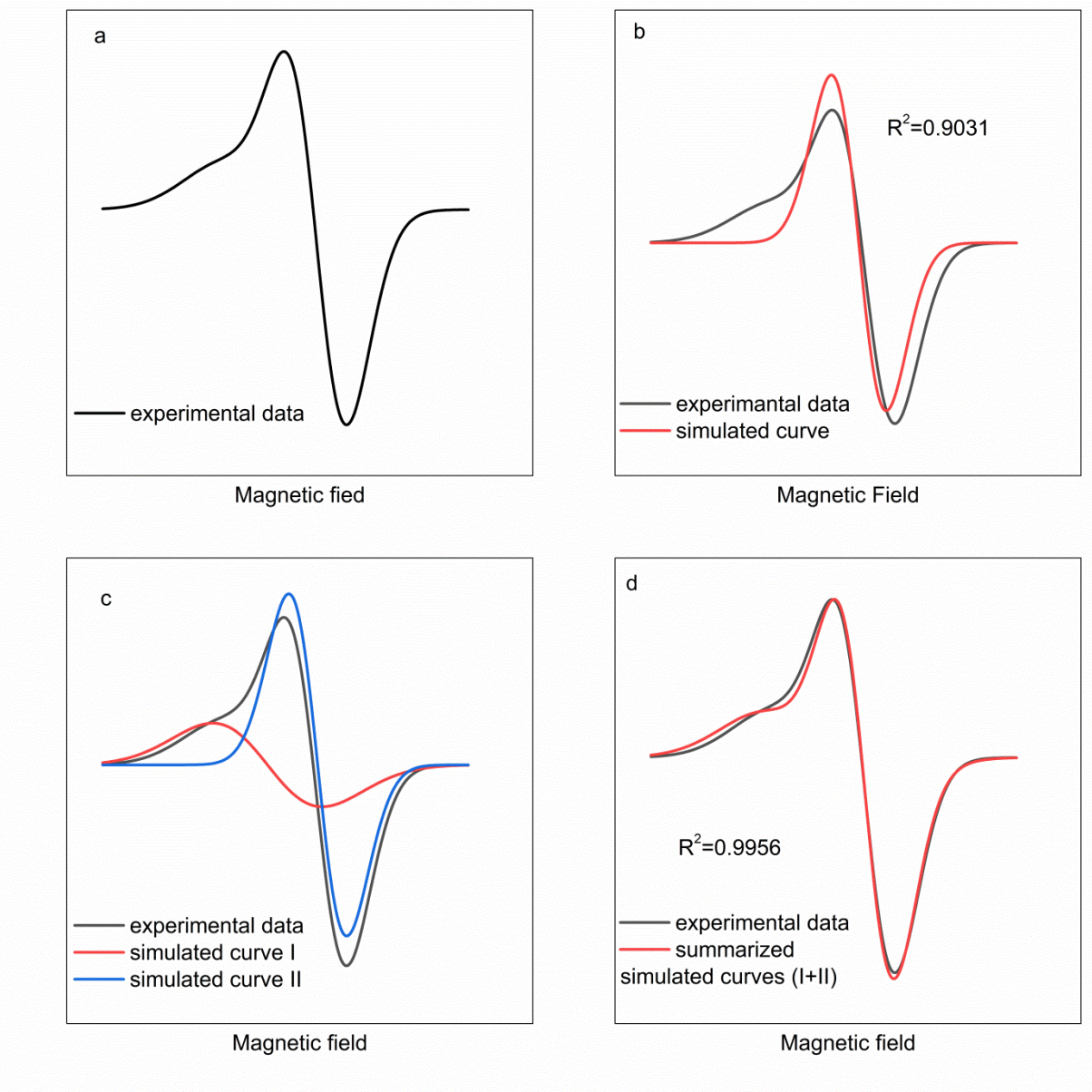

Figure 32. Example of simulation of unsymmetrical structure a) experimental unsymmetrical ESR signal, b) comparison of the experimental signal (black) and simulation signal (red - based on symmetrical signal), c) comparison of the experimental signal (black) with fitted two curves based on radical cation (I-red) and product (II-blue) signals, d) comparison experimental signal and the sum of fitted curves presented in "c".

Another problem of interpretation ESR spectra is a signal disturbance by noise. The solution to this problem included an approximation of a noisy signal (about 500 points) by a polynomial function of 5th order using the Savitzky-Golay method without boundary conditions.

DFT calculations

Quantum theoretical calculations were performed using DFT with the long-range correction exchange-correlation hybrid functional B3LYP (for neutral particle) [104] and CAM-B3LYP (for ions) [105] and the 6-31G++ basis set. The calculations were performed using the ORCA software [106]. The geometrical configuration of a particle in the singlet ground state was optimized in DCM as well as other ions and absorbance spectra.

When comparing data from the calculation and the experiment it is worth mentioning, that sometimes differences between HOMO and $HOMO^{-1}$ (the HOMO orbital of an oxidized particle) are quite small so that two steps of oxidation are undistinguishable on a CV curve. Ratio 2: 1 between the height of oxidation and reduction peaks was evidence of fast electron transfer at a one-step oxidation process (**Figure 33**).

The DFT can be applied not only to calculate energy levels but also to determine the angle between the planes of the donor and acceptor groups. For example, the structure in **Figure 33** has a donor part (marked in green) and an acceptor part (marked in red).

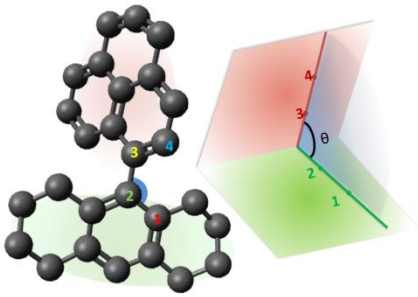

Figure 33. The dihedral angle between donor and acceptor part

The dihedral angle marked in blue in Figure 20 (between points 1-4) equals 49.9°.

4.2 List of compounds

A description of the synthesis is given in Supplement 1 and Supplement 2.

Structure	Abbreviation	Name
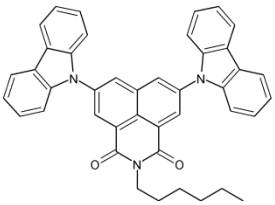	2CBZ-NPTI	3,6-bis (*N*-carbazole)-*N*-hexyl-1,8-naphthalimide
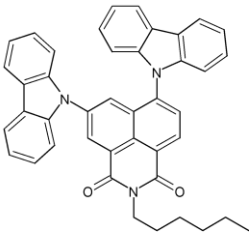	I-2CBZ-NPTI	3,5-bis (*N*-carbazole)-*N*-hexyl-1,8-naphthalimide
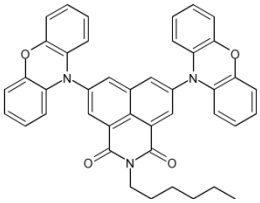	2PXZ-NPTI	3,6-bis (*N*-phenoxazine)-*N*-hexyl-1,8-naphthalimide
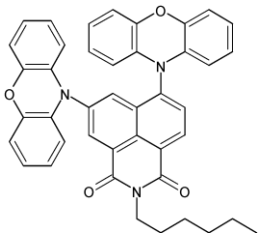	I-2PXZ-NPTI	3,5-bis (*N*-phenoxazine)-*N*-hexyl-1,8-naphthalimide
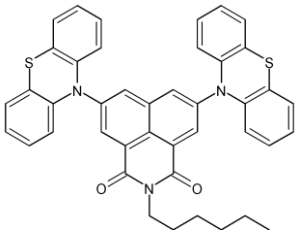	2PTZ-NPTI	3,6-bis (*N*-phenothiazine)-*N*-hexyl-1,8-naphthalimide
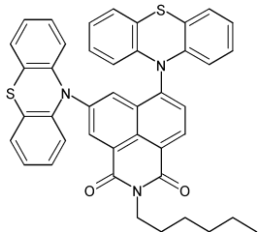	I-2PTZ-NPTI	3,5-bis (*N*-phenothiazine)-*N*-hexyl-1,8-naphthalimide

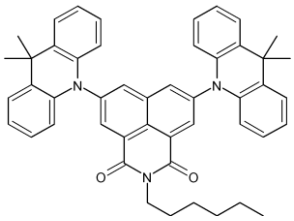	2DMAC-NPTI	3,6-bis (*N*-dimethylacridine)-*N*-hexyl-1,8-naphthalimide
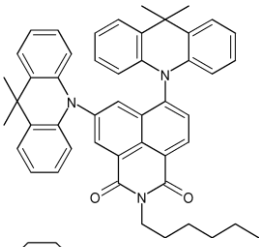	I-2DMAC-NPTI	3,5-bis (*N*-dimethylacridine)-*N*-hexyl-1,8-naphthalimide
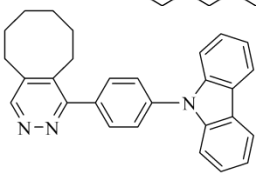	CBZ-DA	1-(4-(*N*-carbazole)phenyl)-5,6,7,8,9,10-hexahydrocycloocta[*d*]pyridazine
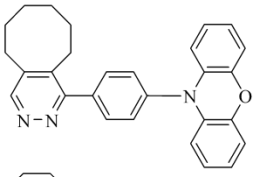	PXZ-DA	1-(4-(*N*-phenoxazine)phenyl)-5,6,7,8,9,10-hexahydrocycloocta[*d*]pyridazine
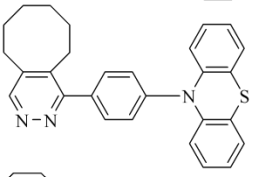	PTZ-DA	1-(4-(*N*-phenothiazine)phenyl)-5,6,7,8,9,10-hexahydrocycloocta[*d*]pyridazine
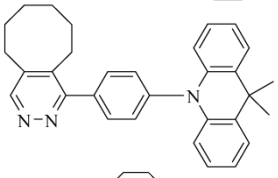	DMAC-DA	1-(4-(*N*-dimethylacridine)phenyl)-5,6,7,8,9,10-hexahydrocycloocta[*d*]pyridazine
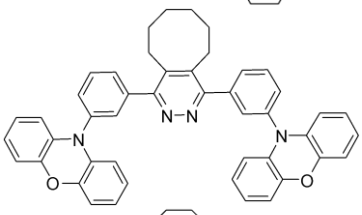	2PXZ-DA	1,4-(3-(*N*-diphenoxazine)pehnyl)-5,6,7,8,9,10-hexahydrocycloocta[*d*]pyridazine
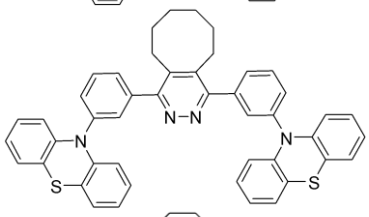	2PTZ-DA	1,4-(3-(*N*-diphenothiazine)phenyl)-5,6,7,8,9,10-hexahydrocycloocta[*d*]pyridazine
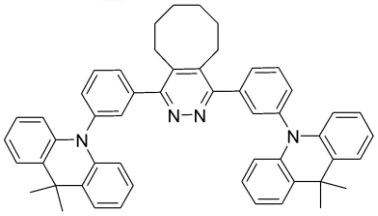	2DMAC-DA	1,4-(3-(*N*-di-dimethylarcidine_pehnyl)-5,6,7,8,9,10-hexahydrocycloocta[*d*]pyridazine

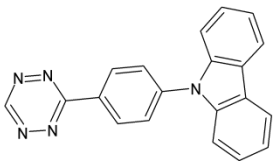	CBZ-TA	3-[4-(*N*-carbazole)phenyl]-1,2,4,5-tetrazine
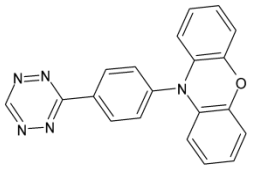	PXZ-TA	3-[4-(*N*-Phenoxazine)phenyl]-1,2,4,5-tetrazine
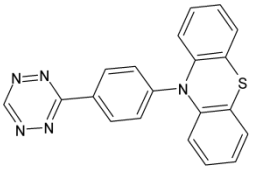	PTZ-TA	3-[4-(*N*-phenothiazine)phenyl]-1,2,4,5-tetrazine
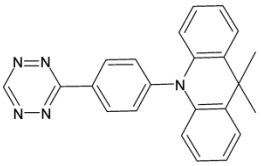	DMAC-TA	3-[4-(*N*-dimethylacridine)phenyl]-1,2,4,5-tetrazine
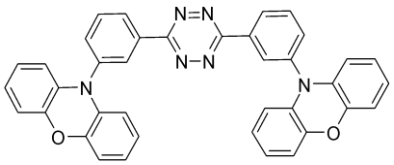	2PXZ-TA	3,6-di(*N*-phenoxazine)phenyl-1,2,4,5-tetrazine
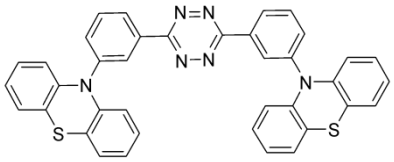	2PTZ-TA	3,6-di(*N*-phenothiazine)phenyl-1,2,4,5-tetrazine
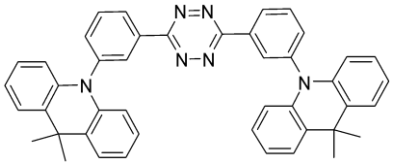	2DMAC-TA	3,6-di(*N*-dimethylacridine)phenyl-1,2,4,5-tetrazine

5 Results and discussion

5.1 Analysis of compounds based on the NPTI acceptor unit

Two types of NPTI-based (acceptor part) were studied: symmetrical (with two donor groups in positions 3,6) and asymmetrical (with two donor groups in positions 3,5) (**Figure 34**).

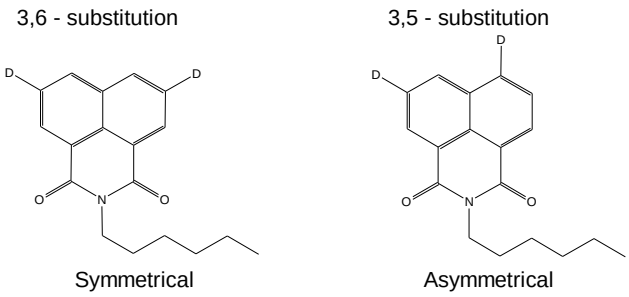

Figure 34. Scheme of studied molecules based on NPTI acceptor unit.

For the reduction process, almost all compounds demonstrate the same behavior; one reversible peak in the range between -0.5 V and -2.0V was observed (**Figure 35**). The reduction potential of non-substituted 1,8-naphthalimide is around -1.71 V. [107] As we showed, reduction potential depends on substituent and ranges between -1.65 V and -1.53 V (symmetrical substitution) and from -1.54 V to -1.49 V (asymmetrical substitution). (**Table 1**) In both cases, the highest reduction potential was observed with CBZ substituents for both types of substitution, the lowest reduction potential was observed with PTZ in case of symmetrical substitution and PXZ in case of unsymmetrical substitution. Substitution in unsymmetrical positions causes a shift to lower potential by 0.02-0.03 V compared with symmetrical ones. The difference in heights of signals of different compounds can be caused by the differences in diffusion coefficients.

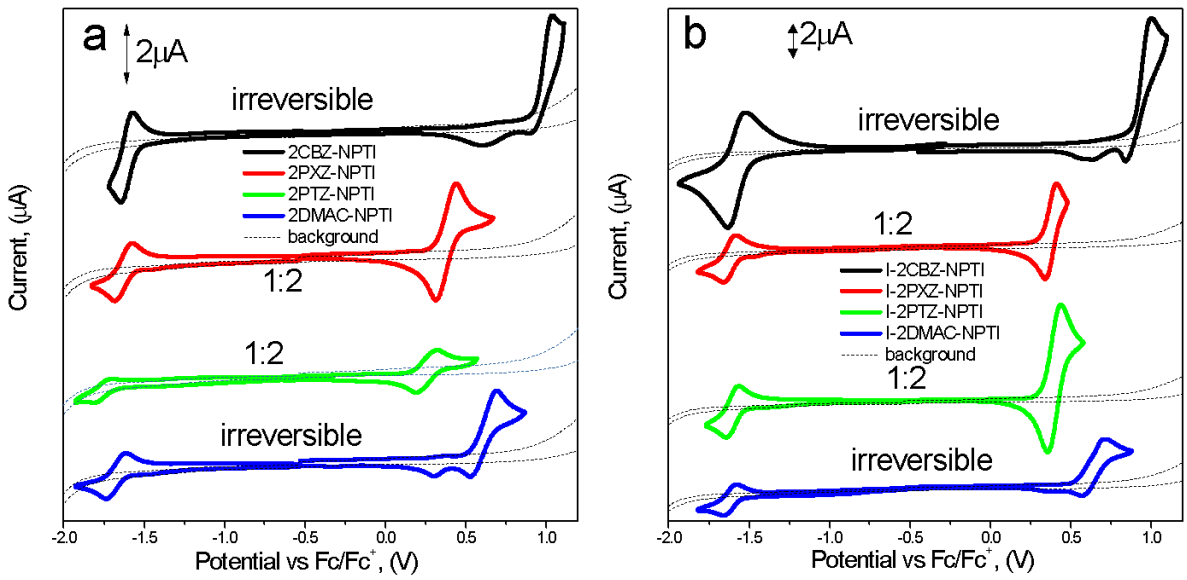

Figure 35. CV curves of compounds based on NPTI: a) symmetrical substitution, b) asymmetrical substitution. Digit caption indicates the ratio between the height of reduction and the oxidation peak.

Table 1 contains the data on redox potentials, HOMO, and LUMO energy levels, and bandgap value estimated from optical measurement and DFT calculation (Table S1).

Table 1. HOMO/LUMO levels, E_g^{opt}, E_g^{calc} for compounds based on NPTI unit.

	E_{ox}^{onset} vs E_{Fc/Fc^+}, V	E_{red}^{onset} vs E_{Fc/Fc^+}, V	HOMO, eV	LUMO, eV	E_g^{opt}, eV	E_g^{calc}., eV	E_g^{el}., eV
2CBZ- NPTI	0.85	-1.53	-5.95	-3.57	2.38	2.57	2.38
I-2CBZ- NPTI	0.87	-1.49	-5.97	-3.61	2.00	2.36	2.36
2PTZ- NPTI	0.13	-1.65	-5.23	-3.45	1.78	1.92	1.78
I-2PTZ- NPTI	0.32	-1.51	-5.42	-3.59	1.83	2.09	1.83
2DMAC- NPTI	0.49	-1.60	-5.59	-3.50	2.09	2.24	2.09
I-2DMAC- NPTI	0.53	-1.52	-5.63	-3.58	2.05	2.20	2.05
2PXZ- NPTI	0.28	-1.57	-5.38	-3.53	1.85	2.12	1.85
I-2PXZ- NPTI	0.31	-1.54	-5.41	-3.56	1.85	1.95	1.85

HOMO = - (E_{ox}^{onset} + 5.1); **LUMO** = - (E_{red}^{onset} + 5.1);
$E_g^{opt} = \frac{1240}{\lambda}$; $E_g^{calc} = LUMO^{DFT} - HOMO^{DFT}$, $E_g^{el} = E_{ox}^{onset} - E_{red}^{onset}$.

Comparing the LUMO level calculated using CV and LUMO level calculated using DFT, one could observe that differences are about 1 eV, the lowest difference (0.84 eV) was at case 2PXZ-NPTI, and the highest (1.20 eV) was in the case of I-2CBZ-NPTI (**Figure 36**).

The probable cause of the difference of LUMO energies between theoretical values and estimated by the electrochemical method is the nature of the acceptor core, this as well-know has the possibility of strong self-interaction and π-π stacking process which affect the overall energy. Such behavior is difficult to measure using the DFT method (Table S1)and the theoretically estimated values present acceptor with lower conjugation properties.[71]

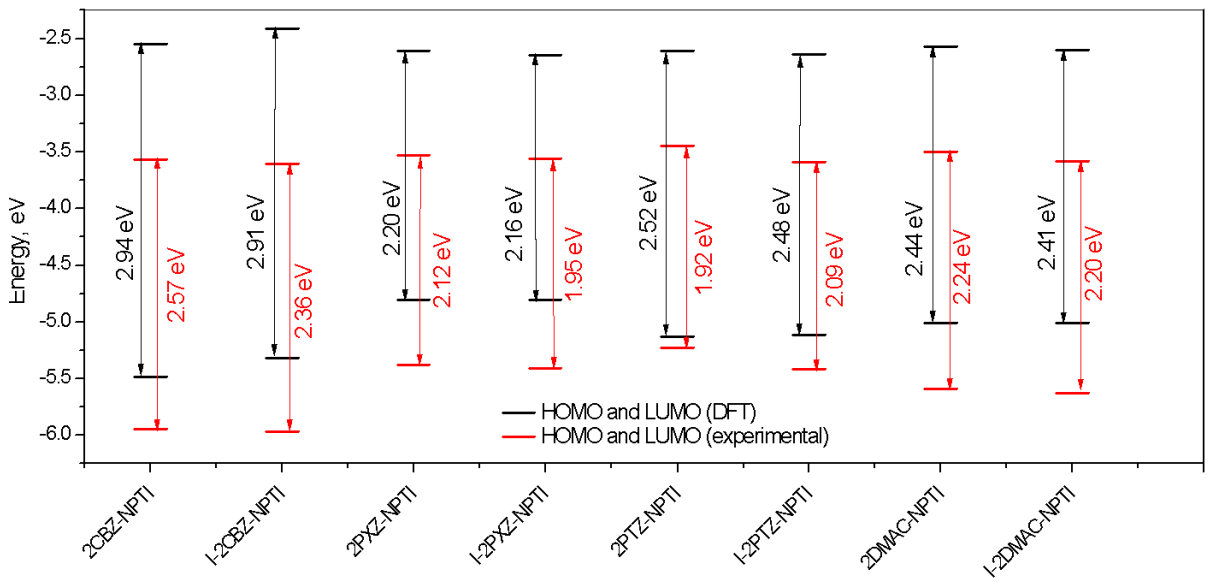

Figure 36. Comparison of the experimental and calculated levels of energy for compounds based on the NPTI acceptor unit.

PXZ and PTZ containing compounds demonstrated reversible oxidation behavior. Regardless of the form of substitution, CBZ and DMAC have an irreversible course of oxidation with the formation of a product that was deposited on the electrode surface or dissolved in solution. For the oxidation process, symmetrical 2PTZ-NPTI has the lowest oxidation potential of 0.13 V, and symmetrical 2CNZ-NPTI has the highest oxidation potential 0.85 V. For unsymmetrically substituted compounds the lowest oxidation potential equals 0.32 V in the case of I-2PTZ-NPTI (I-2PXZ-NPTI has almost the same value 0.31 V), and the highest oxidation potential (0.87 V) is for I-2CBZ-NPTI. Generally, oxidation potentials for unsymmetrically substituted compounds are higher than symmetrically substituted. However, the opposite effect was observed in the case of CBZ substituted compound. Probably, due to the self-aligning of carbazole units.

The smaller difference in oxidation potential between symmetrical and unsymmetrical substitution (0.03 V) was in the case of NPTI substituted by the PXZ group and the same

effect was observed in the case of DMAC substitution (0.04 V). The PTZ substituted compounds have the highest difference (0.19 V). The increase in oxidation potential in the case of asymmetric substitution may be due to the steric hindrance of the donor groups.

Results of DFT calculation overestimated the energy levels concerning experimentally obtained data, especially in the case of the HOMO levels. The lowest difference (0.1 eV) between calculated and experimental HOMO levels is in case 2PTZ-NPTI and the highest (0.62 eV) is in case I-2DMAC-NPTI. Differences between HOMO and $HOMO^{-1}$ are small, the most significant is in case I-2CBZ-NPTI (0.21 eV) and 2PTZ-NPTI (0.11 eV). In other cases, it is quite hard to divide 1st and 2nd oxidation step. comparing shapes of orbitals, in all cases except CBZ and I-CBZ substitution, HOMO levels were located on donor groups without any interaction with the acceptor unit. In the case of compound 2CBZ-NPTI HOMO orbital is located on both donor groups with interaction with the acceptor unit (**Figure 37**).

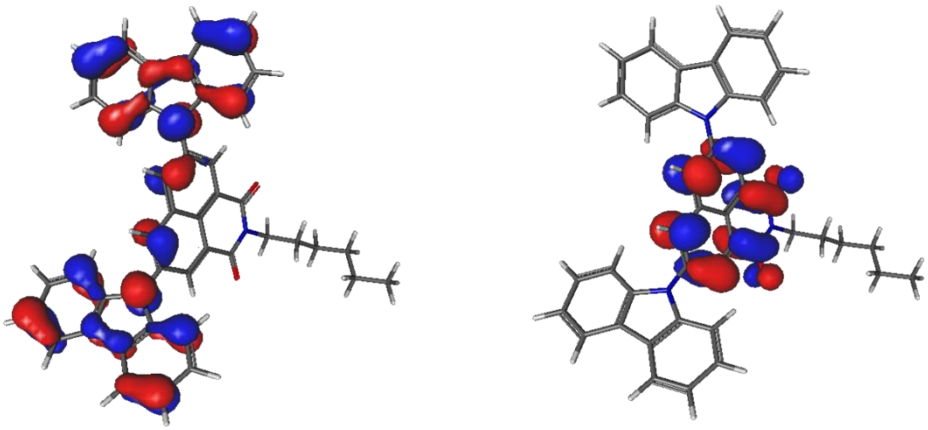

Figure 37. Molecular orbital isosurfaces of 2CBZ-NPTI calculated at B3LYP 6-31g(d) level of theory with iso value of 0.03.

However, in the case of I-2CBZ-NPT, the compound HOMO orbital is localized on the donor group with stronger interaction with the acceptor group (**Figure 38**). This fact can correspond to the irreversible oxidation process.

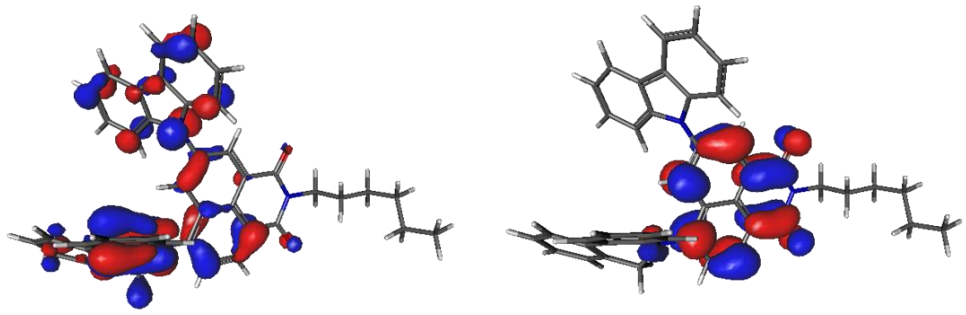

Figure 38. Molecular orbital isosurfaces of I-2CBZ-NPTI calculated at B3LYP 6-31g(d) level of theory with iso value of 0.03.

In this case, we can compare the height of the reduction peak to the oxidation peak (for reversible oxidation process), all of them are characterized by good solubility in DCM. In case PXZ was shown then the ratio of reduction to oxidation peak is 1:2 (ratio for compound I-2PTZ-NPTI is 1:3), the same ratio is in case symmetrically substituted NPTI by PTZ. It means that in the oxidation process take part 2 electrons. So, this potential is the potential of oxidation of two donor groups. In this case, it oxidized to the first and second oxidation stage at the same time.

For calculation, E_g^{opt} has used the absorbance spectrum of the compound. For 1,8-naphthalimide π–π^* transition is around 330 – 340 nm. [60,107] From the literature is known that π–π^* transition for a different donor is around 360 – 380 nm for CBZ [108], 440 nm for PXZ[109], 380 – 550 nm for PTZ[110], and 350 nm for DMAC. [111]

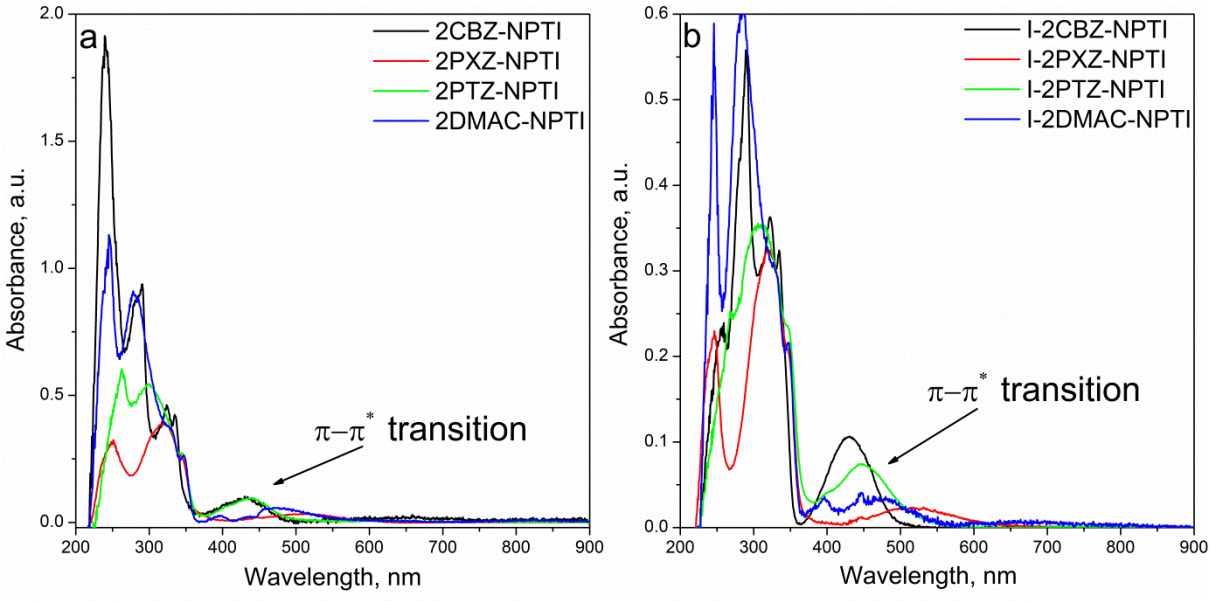

Figure 39. Absorbance spectra in solution of 3mM of compounds based on NPTI acceptor unit with normalized intensity at 330 nm (a) symmetrical substitution, (b)asymmetrical substitution.

From the absorption spectrum, the difference in energy levels for each compound was calculated (**Figure 39**). All compounds are characterized by high absorbance intensity below 330 nm and low above, approximately 6 times. The highest bathochromic shift was observed in the case of PXZ donor groups in the case of symmetrical and unsymmetrical substitution. Bathochromic shift can be ordered by PXZ > DMAC > PTZ=CBZ. Comparing E_g optical and experimental, it is the same order in case unsymmetrical substitution but in the case of symmetrical substitution, the lowest gap was in the case of PTZ instead of PXZ. Comparing the spectral data and CV data, the asymmetrically substituted acceptor may have a slightly smaller difference in energy levels, although this difference is too small to suggest striking differences in the properties of the compounds. Concerning the effect of the donor group, the most influential is PTZ for symmetric substitution, as it has the lowest reduction potential and is also the most electron-donor group for symmetric and asymmetric substitution.

During the spectroelectrochemical experiment, all compounds are characterized by the formation of cation radicals ($+^{\cdot}$), diradical cation (++), and product (M^+, $Pr^{+}\cdot$) of oxidation of compounds. At the same time were registered spectrums from oxidized compounds and products of oxidation (**Figure 40**).

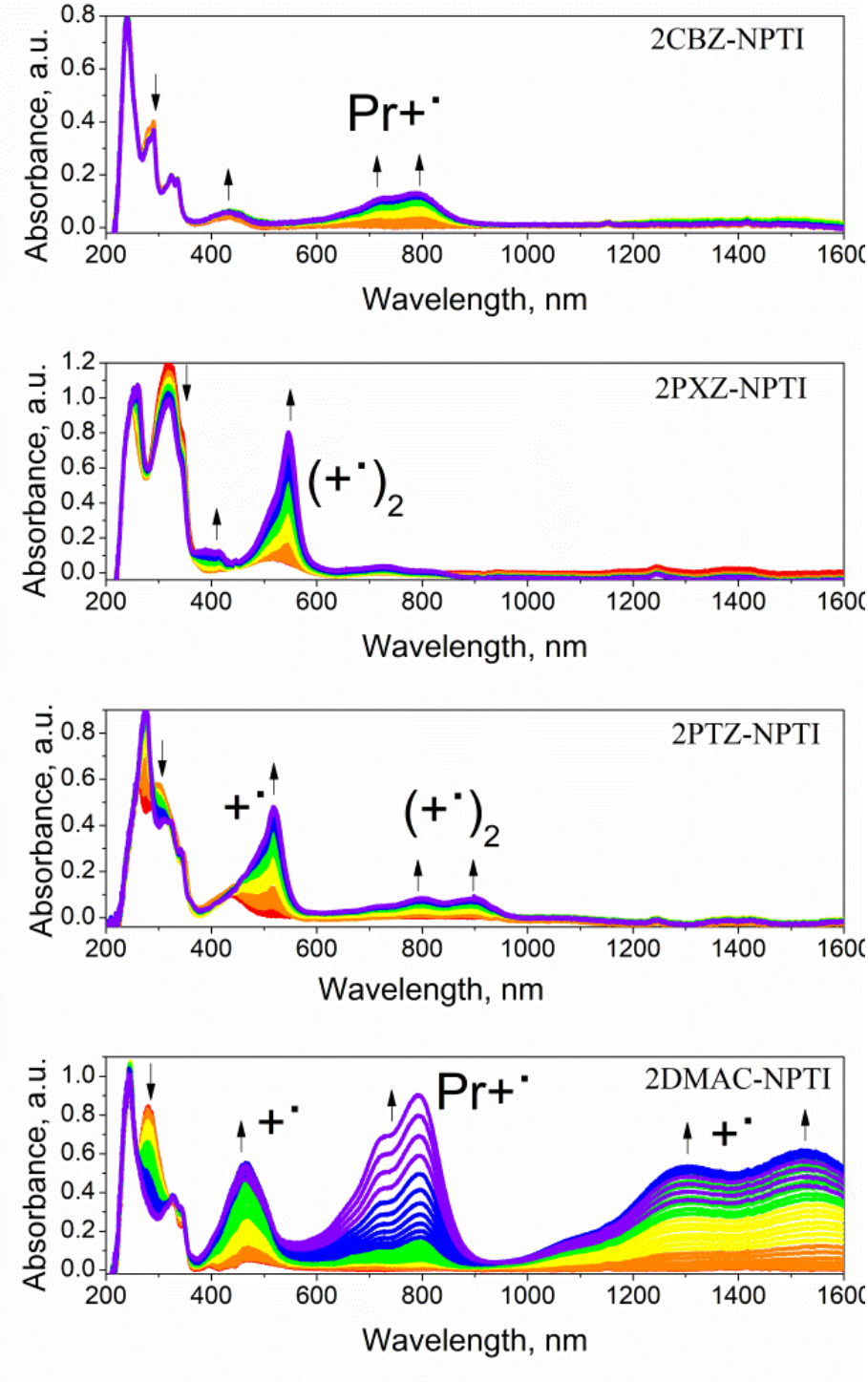

Figure 40. “In-situ” oxidation process spectra of compounds based on 1,8-naphthalimide.

Increasing their concentration is a major factor in increasing the absorption of light at specific wavelengths (**Figure 41**).

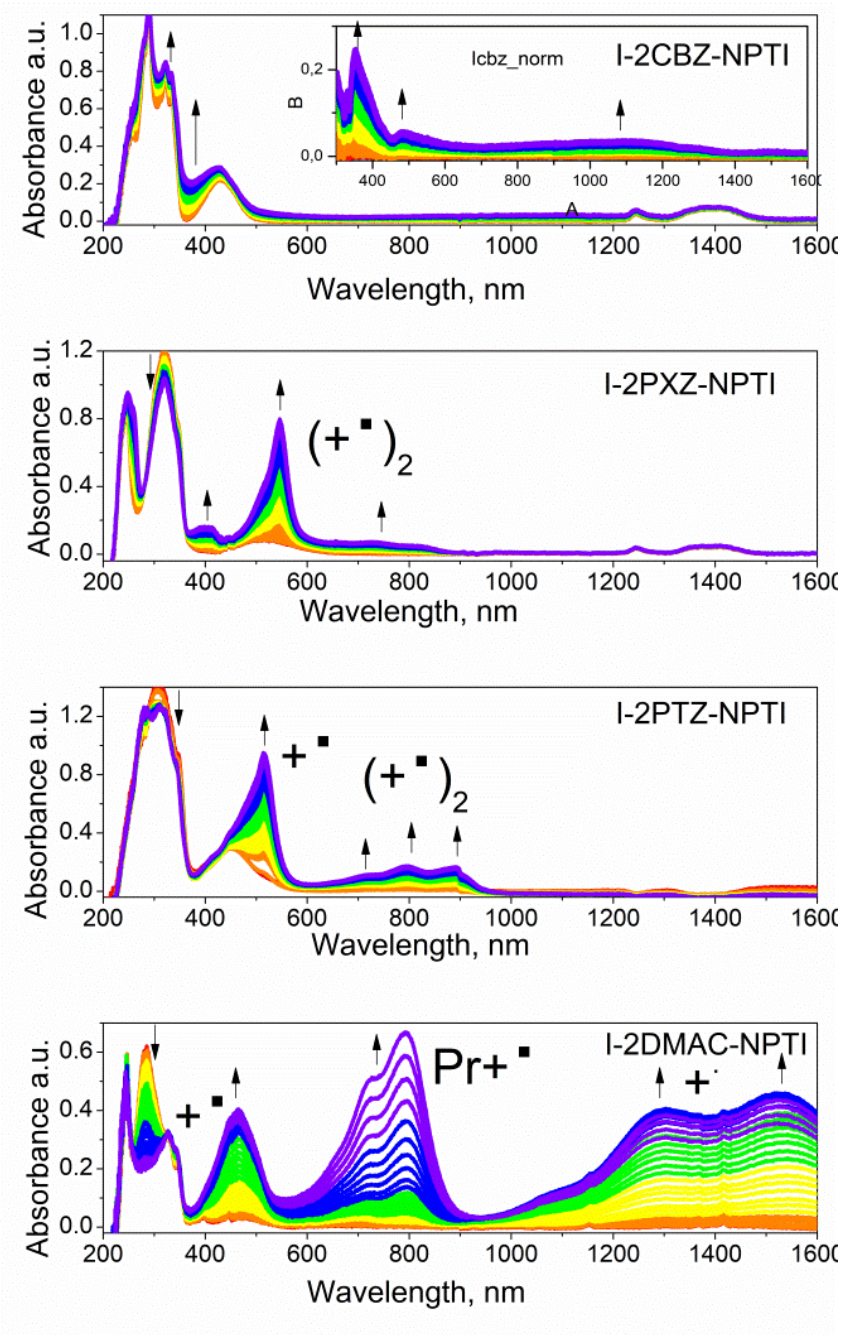

Figure 41. “In-situ” oxidation process spectra of compounds based on 1,8-naphthalimide.

During the oxidation process absorbance intensity at 326 nm didn’t change, it seems to the absorbance of the NPTI unit.

In all cases, there is a decrease in absorbance intensity at the range 270 – 320 nm. Comparing symmetric and asymmetric substitution of the acceptor, the compounds with PXZ and DMAC show similar results. But in the case of PXZ donor groups during oxidation were formed dication radicals [88] instead of DMAC donor group, where oxidized products were

formed. This behavior was revealed from electrochemical measurements. Concerning the acceptor substituted with PTZ, a common signals at wavelengths of 517 nm, 794 nm (800 nm for unsymmetrical), and 896 nm (for unsymmetrical 893 nm), the difference is only in the absorption intensity of absorption at 272 nm (in the case of symmetric substitution) and the appearance of a more pronounced peak at 700 nm (in the case of asymmetric substitution). In both cases, changes correspond to the formation of diradical cation (**Table 2**).[78]

Table 2. Changes in intensity and wavelength of bands registered in the oxidation process.

	Absorbance maximum of			
	The neutral molecule λ↓, nm	**Cation radical λ↑, nm**	**Dication diradical λ↑, nm**	**Product λ↑, nm**
2CBZ-NPTI	292	432	713	798
I-2CBZ-NPTI		330; 464		1106
2PTZ-NPTI	300	272; 514	800; 896	
I-2PTZ-NPTI	308	514	716; 794; 893	
2DMAC-NPTI	278	462; 1287; 1527		720;793
I-2DMAC-NPTI	281	467; 1292; 1532		721; 794
2PXZ-NPTI	314	406	543;724	
I-2PXZ-NPTI	318	396	541;736	

In the case of 2CBZ-NPTI during oxidation we observed peaks at 713 nm and 795 nm and a small increase at 430 nm, however of in case I-2CBZ-NPTI: we observed a small increasing peak at 330 nm and a peak at 464 nm and quite large, but not so intensive at 1100 nm. Increasing at 430 nm is close to characteristic absorbance (455 nm) of formation radical cation.[78] The wide strand at 1100 nm corresponds to the formation of the oxidized polymer which is formed on the ITO electrode surface. For asymmetric CBZ substitution, a differential method (for background spectrum was taken spectrum at 0V) was used to detect changes during the experiment, and it is easy to see what changes occur during the oxidation process.

Molecules that are substituted by DMAC have a peak of increasing intensity during oxidation. For these molecules, characteristic peaks in the IR range are observed and attributed to radical cation. There are peaks in the range 720 – 794 nm (in both cases), which correspond to the formation of products during the oxidation process (which accords with CV measurements) (**Figure 35**).

During the reduction process, both signal with and without hyperfine structure could be observed (**Figure 42b**). Typically, an asymmetrically substituted acceptor produces a much more intense signal than an asymmetrically substituted one. The exception is only PTZ substituted acceptor NPTI, which has the highest *g*-factor (2.003), indicating that the charge is mostly localized on the nitrogen atom (**Table 3**). [93] In other cases, the value of the *g*-factor remains almost unchanged from 2.0034 (in the case of DMAC) to 2.0038 (in the case of substitution with PXZ).

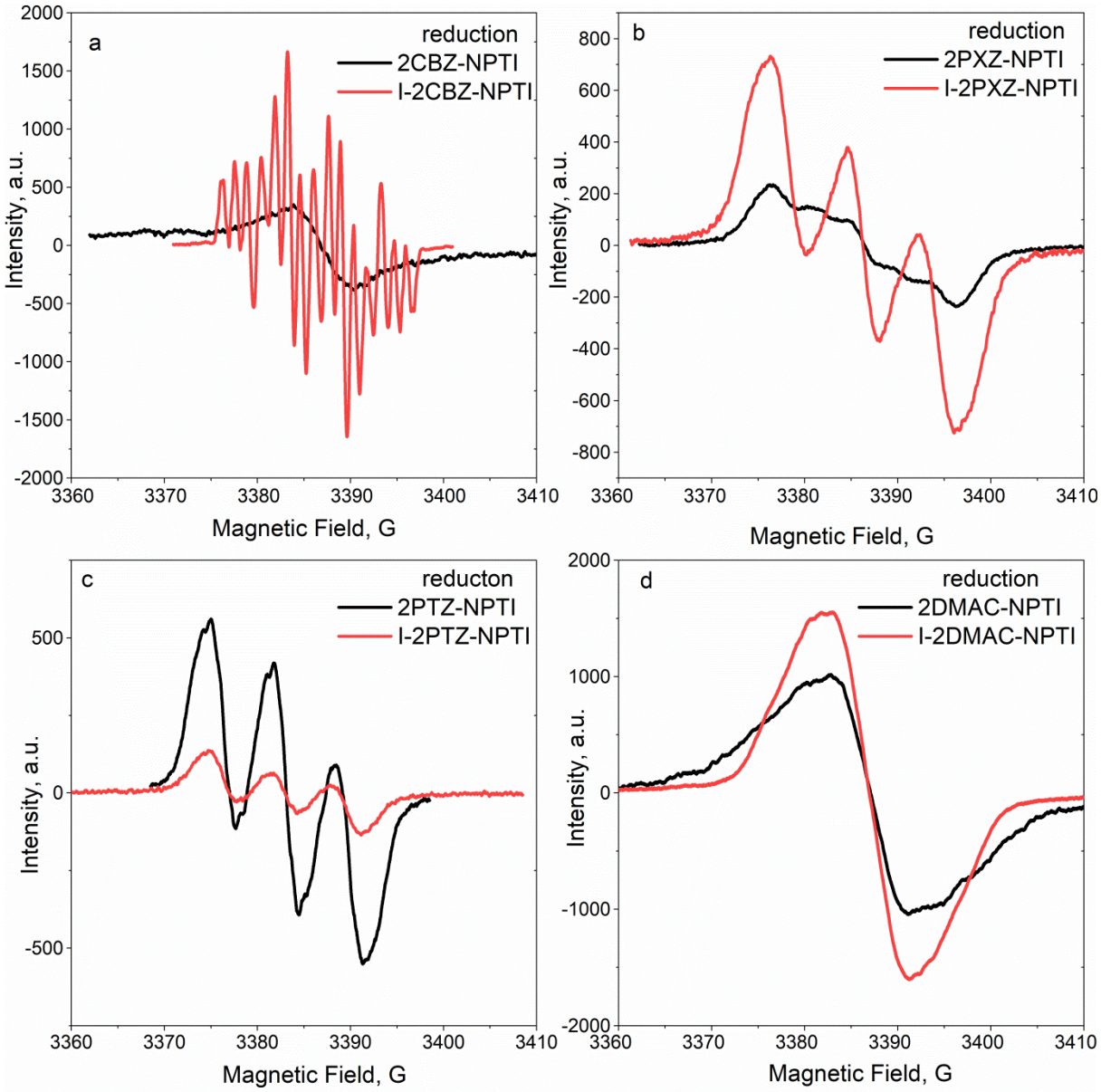

Figure 42. EPR signals for the reduction process measuring at E_{red} modulation 0.06 mT and amplitude 500 (a) ESR signals for 2CBZ-NPTIi and I-2CBZ-NPTI, (b) ESR signals for

2PXZ-NPTIi and I-2PXZ-NPTI, (c) ESR signals for 2PTZ-NPTIi and I-2PTZ-NPTI, (d) ESR signals for 2DMAC-NPTI and I-2DMAC-NPTI.

The simplest case is an acceptor substituted with DMAC. Its ESR spectrum has a singlet signal with the value of the *g*-factor 2.0033 and 2.0034. The singlet signal also gives the acceptor substituted CBZ with a slightly higher value of the g factor. Signals of acceptor signals substituted symmetrically with CBZ and DMAC have a significant peak broadening compared to the asymmetrically substituted dimethylacridine with the NPTI acceptor unit.

Table 3. Calculated *g*-factor from ESR-spectrum.

	Oxidation *g*-factor	**Reduction *g*-factor**	**Oxidation signal width, G**	**Reduction signal width, G**
2CBZ-NPTI	2.0038	2.0037	9	6
i2CBZ-NPTI	2.0036	2.0035	5	6
2PTZ-NPTI	2.0050	2.0050	20	20
i2PTZ-NPTI	2.0060	2.0050	20	20
2DMAC-NPTI	2.0034	2.0034	17	16
i2DMAC-NPTI	2.0033	2.0034	17	16
2PXZ-NPTI	2.0036	2.0038	7	9
i2PXZ-NPTI	2.0039	2.0034	7	9

The effect of the donor group can be seen by comparing the signals from the acceptor symmetrically substituted by DMAC and PXZ. The signals in both cases are quite wide, but in the latter case, a weak hyperfine structure is noticed. The acceptor of asymmetrically substituted by PXZ has a much more pronounced hyperfine structure, the value of the *g*-factor is almost the same, the difference is 0.0004.

For phenothiazine substituted acceptors, for which the *g*-factor is the highest, in the case of asymmetric substitution, the signal has a much lower intensity than symmetrically substituted. It can be explained by different diffusion coefficients. Comparing the shape of the signals, it can be said, that the symmetrical substitution signals have hardly noticeable bifurcated structure, which may indicate the presence of newly formed structures that are similar to the anion radical.

For such a signal with a well-defined hyperfine structure and a high *g*-factor, we could not find a structure that better describes the experimental data than the one shown in **Figure 42**. That is, the signal from this compound is only eliminated by splitting into 1 nitrogen atom with a splitting value of 6.52 G (**Table 4**).

Table 4. Calculated splitting constant of radical signals (using Winsim program).

	Constant, G
2PTZ-NPTI	1N (7.43); 1H (2.35).
I-2PTZ-NPTI	1N (6.52).
I-2PXZ-NPTI	1N (6.12); 2H (1.21); 1H (2.26).
I-2CBZ-NPTI	1NI (1.38): 1NII (1.1); 2H (0.34); 1H (4.37); 1H (4.55); 1H(5.85).

Considering the relatively low intensity, this structure can be described considering that the charge is localized between 1 nitrogen atom (as evidenced by the value of the *g*-factor) with a splitting value of 6.12 G, two equivalents of hydrogen from an alkyl group (with a splitting value of 1.21 G), and one from the naphtalene group (with a splitting value of 2.26 G). It means the charge is well localized, and as a consequence, a stable anion is formed during the reduction process.

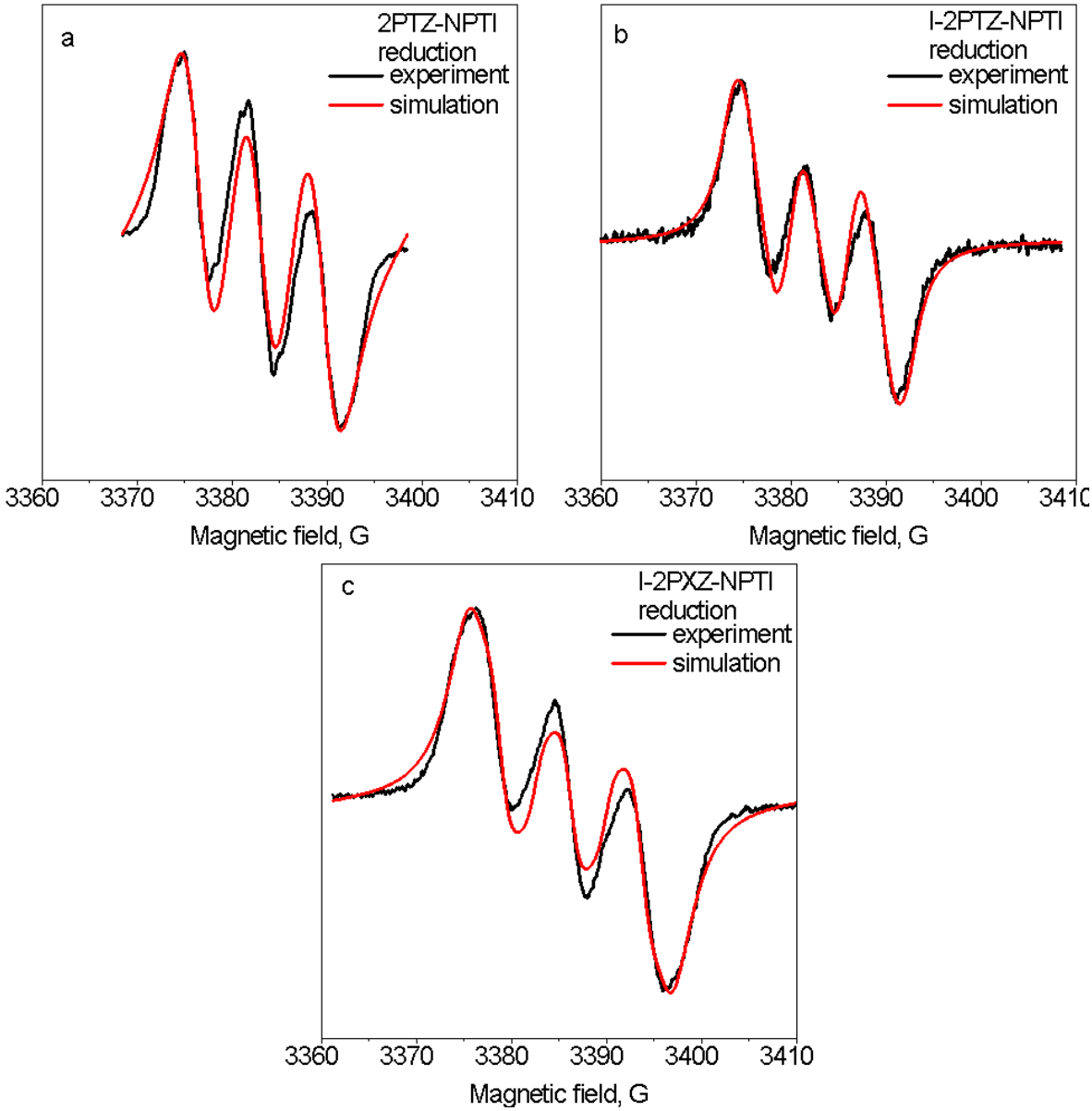

Figure 43. EPR signals and their simulation (using Winsim program) of compounds (reduction part) (a) experimental and simulation signals for 2PTZ-NPTI, (b) experimental and simulation signals for I-2PTZ-NPTI, (c) experimental and simulation signals for I-2PXZ-NPTI.

Comparing the results of simulations of symmetric and asymmetric substitution (**Figure 43a,b**), it was noticed that not always high signal intensity allows describing the structure. Such results can be explained by the fact, that signal from cation of symmetrical substitution is significantly broader compared to the asymmetric substitution, and as a consequence, we have groups of atoms with a high splitting coefficient (nitrogen atom) and a group of atoms with a different small splitting coefficient (atom of splitting) changes its shape.

For an asymmetrically PXZ substituted acceptor (**Figure 43c**), it was possible to calculate the structure, which would correspond to the formation of a hyperfine structure. To calculate the splitting, it was taken, that the formation of the splitting involves 1 nitrogen atom (with a splitting constant of 7.23 G) and two equivalents of hydrogen atoms (with a splitting constant of 2.35 G).

Evaluating the signal from the radical anion of compound I-2CBZ-NPTI (**Figure 44b**) was noticed that the signal was formed as 4 groups with a ratio of 1:2:2:1.

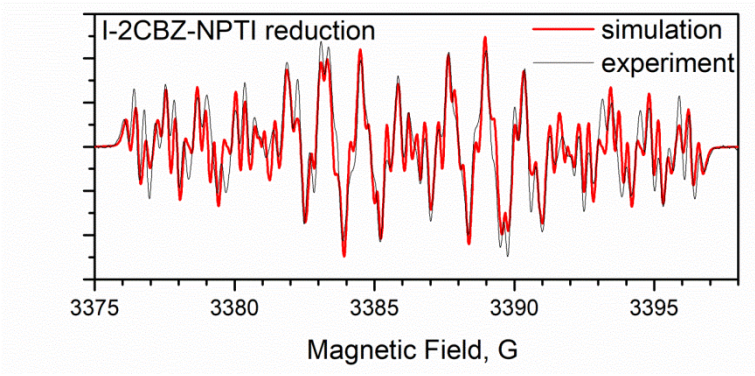

Figure 44. ESR-spectrum of I-2CBZ-NPTI reduction part.

In other cases, the hyperfine structure looks like only the triplet signal, which corresponds to the *N*-atom of naphthalimide. Using the theory of splitting EPR signals, this type of splitting was formed from two types of an atom with spin number 1, like it is shown in **Figure 45.**

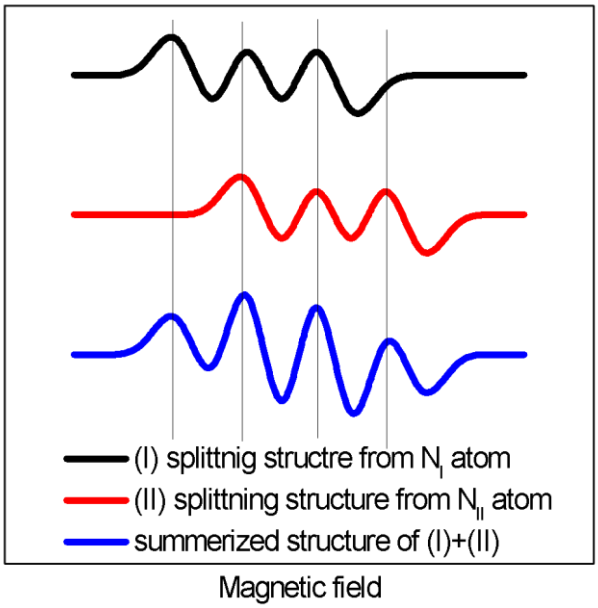

Figure 45. The splitting structure is formed from two *N* atoms. N_I – *N*-atom from NPTI group, N_{II} – *N*-atom from donor group.

Looking at DFT results (**Figure S2**), it was mentioned that the LUMO level was localized on the acceptor group with interaction with the donor group in 5-position (**Figure 46**).

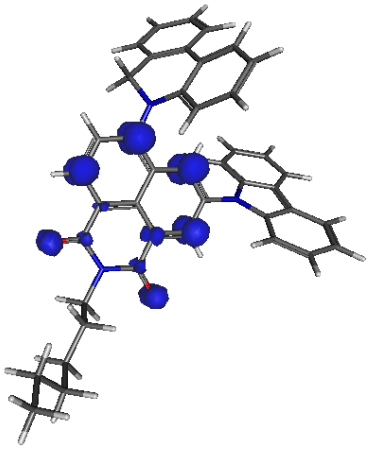

Figure 46. Spin density isosurfaces of I-2CBZ-NPTIfor Radical anion calculated at B3LYP 6-31g(d) level of theory with iso value of 0.005.

It is quite interesting to compare these results (EPR signals from CBZ symmetrical and unsymmetrical substituted NPTI unit), comparing with CV data. Compound I-2CBZ-NPTI has in 2 times higher reduction peak than 2CBZ-NPTI. It can be caused by the influence on

the donor group. Considering the steric hindrance in the case I-2CBZ, it can be a reason for the formation of the stable cation with a well-expressed hyperfine structure.

These calculations and the proposed charge distribution scheme are in full agreement with the value of the *g*-factor. That is, the charge that is tripled during the reduction process is not completely localized on the naphthalene group nitrogen atom, but is somewhat delocalized in the acceptor plane.

Let's assume that acceptor reduction occurs as a one-electron process as shown in **Figure 47.**

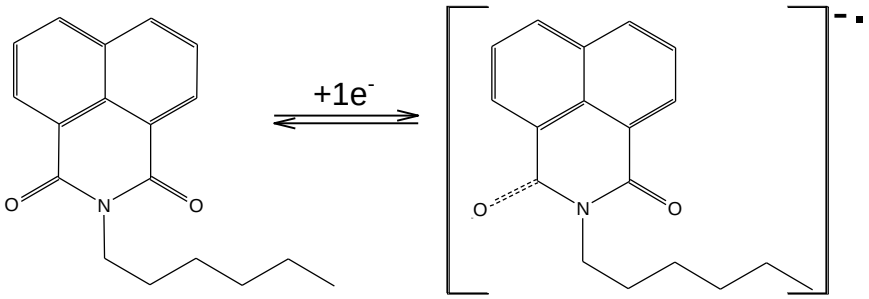

Figure 47. Scheme of reduction of NPTI unit.

During the reduction process, a radical anion was formed and the charge cannot be localized. That is why it's hard to explain directly where is charges exactly. One can compare results from ESR investigation (especially *g*-factor value) to say if the *g*-factor (of each signal) is closer to 2.005 – is higher then in case of electron localized on *N* atom *g*-factor is 2.003. The donor group is involved in the oxidation process, so the nature of the signal depends on the nature of the group. Because of the general situation, we have similar behavior to reduction. Comparing the *g*-factor s, the lowest value in symmetric substitution has of 2DMAC-NPTI (2.0034). Such a compound will be characterized by the formation of paramagnetic particles, which are formed due to the close location of the donor groups or the formation of polymers.

The carbazole unit of the molecule (in case 2CBZ-NPTI and I-2CBZ-NPTI) are similar to each other and could form complex, which is not shown on the EPR spectrum, because of the non-paramagnetic structure of the complex. In the case of compound 2CBZ-NPTI, the signal from radical is not symmetrical (like in theory), but low-intensity makes it impossible to extract data for analysis. In both cases signals, which are shown are from radical cation

(+˙). during oxidation, the main process is the formation of a product and there is a small amount of radical cation, like in the case of spectroelectrochemistry (**Figure 48a**).

The highest value of the *g*-factor of radical cation was calculated for I-2PTZ-NPTI (2.0060) as well as *g*-factor of radical anion. The *g*-factor for other donor groups is in the range of 2.0033 to 2.0038. It means that an electron is mostly localized on the *N*-atom of the donor group. [96]

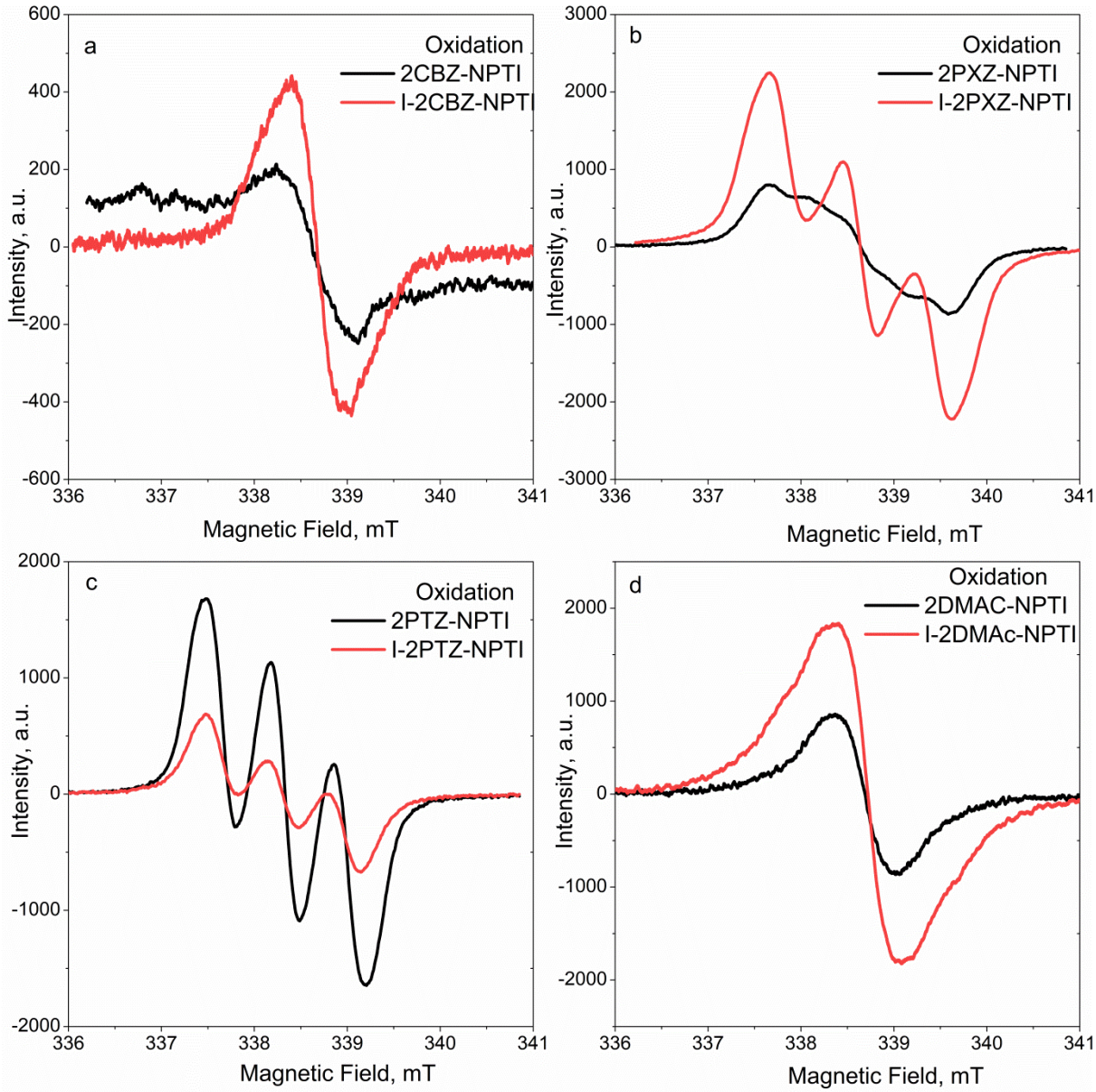

Figure 48. EPR spectra of radicals, formed during the oxidation process, of compounds, based on the NPTI acceptor unit (a) EPR signals for 2CBZ-NPTIi and I-2CBZ-NPTI, (b) EPR signals for 2PXZ-NPTIi and I-2PXZ-NPTI, (c) EPR signals for 2PTZ-NPTIi and I-2PTZ-NPTI, (d) EPR signals for 2DMAC-NPTI and I-2DMAC-NPTI.

Looking at ESR-spectrum for I-2DMAC-NPTI (**Figure 48d**), easy to notice that the signal is a little bit wider (17 G) and looks like two signals are connected, like in case 2CBZ-NPTI. It means, that during the oxidation process were form two different forms of the compound, which is confirmed with CV and spectroelectrochemistry investigation. (**Figure 49**) . During oxidation were formed radical cation and product.

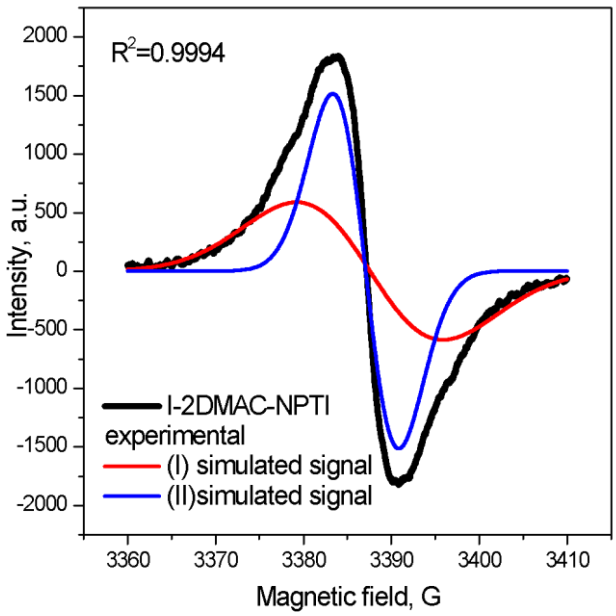

Figure 49. ESR-spectrum of oxidation processof I-2DMAC-NPTI and simulated curves.

Using these simulated curves *g*-factor was calculated and for (I) simulated curve is 2.0035 (from the product) and for (II) simulated curves is 2.0032 (from radical cation). Using data for CV can be supposed that the higher value of the *g*-factor corresponds to oxidation of DMAC substituent and the lower value corresponds to radicals from products of oxidation.

Regarding the signal intensity, as well as in the case of the reduction process, the intensity for the asymmetrically substituted NPTI is higher than for the symmetric one, except PTZ. Compounds with the donor groups PXZ and PTZ (**Figure 50b,c**) have signals with a pronounced hyperfine structure, except for symmetrically substituted PTZ, whose signal intensity is sufficiently low, and quite hard to simulate this structure, and as a consequence to determine optimal parameters.

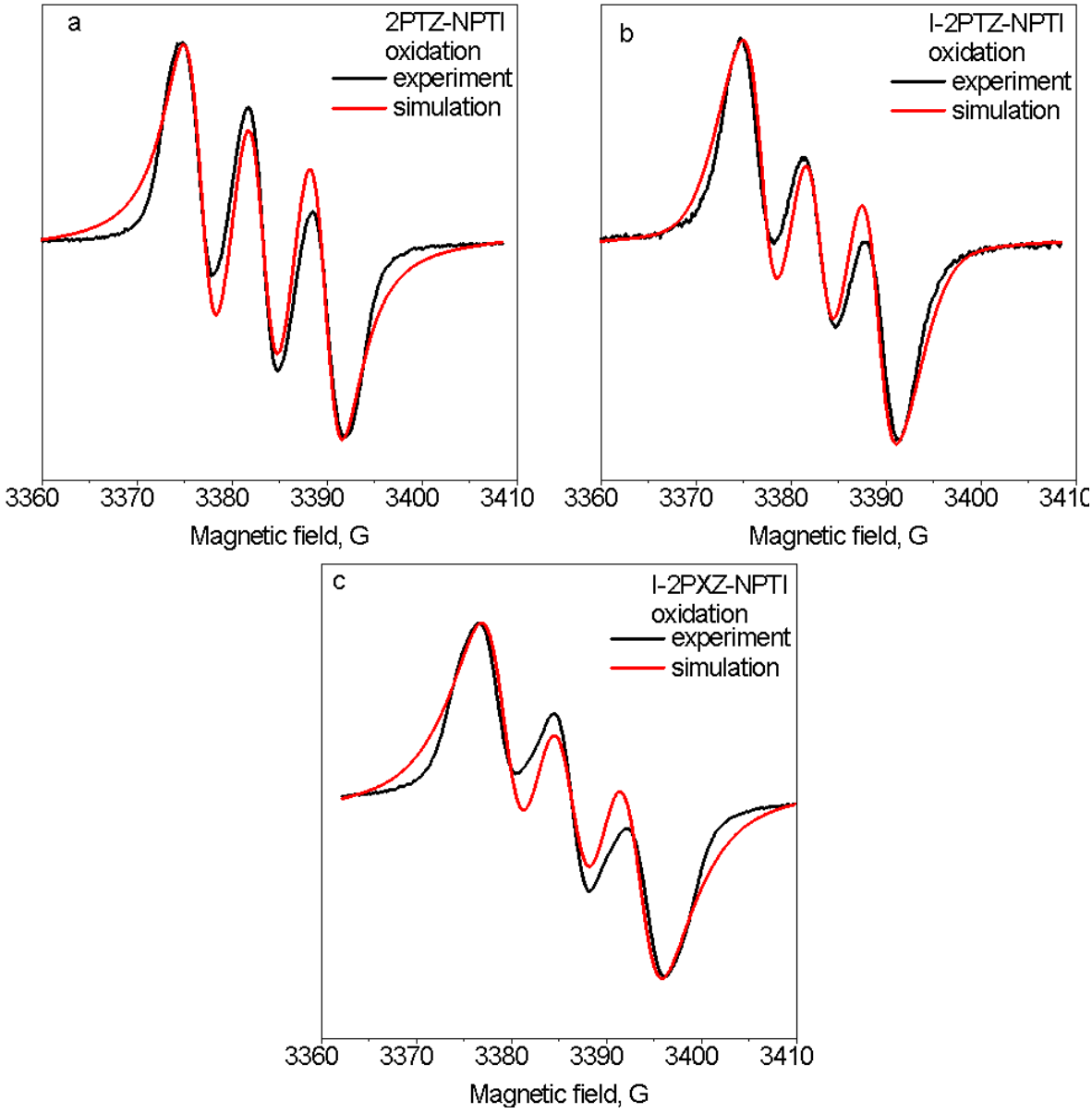

Figure 50. ESR-spectrum and their simulation of compounds (oxidation part) (a) experimental and simulation signals for 2PTZ-NPTI, (b) experimental and simulation signals for I-2PTZ-NPTI, (c) experimental and simulation signals for I-2PXZ-NPTI.

For symmetrically substituted PTZ (**Figure 50a**), the splitting signal intensity is almost the same, which means that it has virtually no interaction with another donor group. This is due to the high *g*-factor and the high splitting value (6.51) (**Table 5**). For non-symmetrically substituted by PTZ, the signal intensity is the same, although the signal is not as wide as the symmetrically substituted (the difference is 2G) and the signal simulation is much better than in the previous case. This type of signal may indicate additional charge redistribution

processes that may occur during the oxidation process, but these processes do not affect the charge localization.

Table 5. Calculated splitting constant of radical signals (using Winsim program).

	Constant
2PTZ-NPTI	1N (7.08)
I-2PTZ-NPTI	1N (6.51).
I-2PXZ-NPTI	1N (6.08)

For phenothiazine substituted compounds, the signal has a practically ideal hyperfine structure. For asymmetrically substituted NPTI acceptor unit, the EPR signal has a clear hyperfine structure, which can be described considering that only one group of atoms - the nitrogen of the donor group - takes part in splitting, with a splitting value of 7.08 G. On this basis, the following scheme of oxidation of the donor group is proposed. It is worth noting that the height of the intensity is different, which may indicate additional interaction between the two donor groups.

5.2 Analysis of compounds based on the DA acceptor unit

The broad analysis of the new group of compounds, based on pyridazine acceptor, revealed the absence of a reduction signal. In all cases, there are no reduction peaks (reduction of compounds is out of the potential range of measurement conditions), nevertheless, the expected E_{red}^{onset} was estimated using DFT data (**Figure 51, Table 6**).

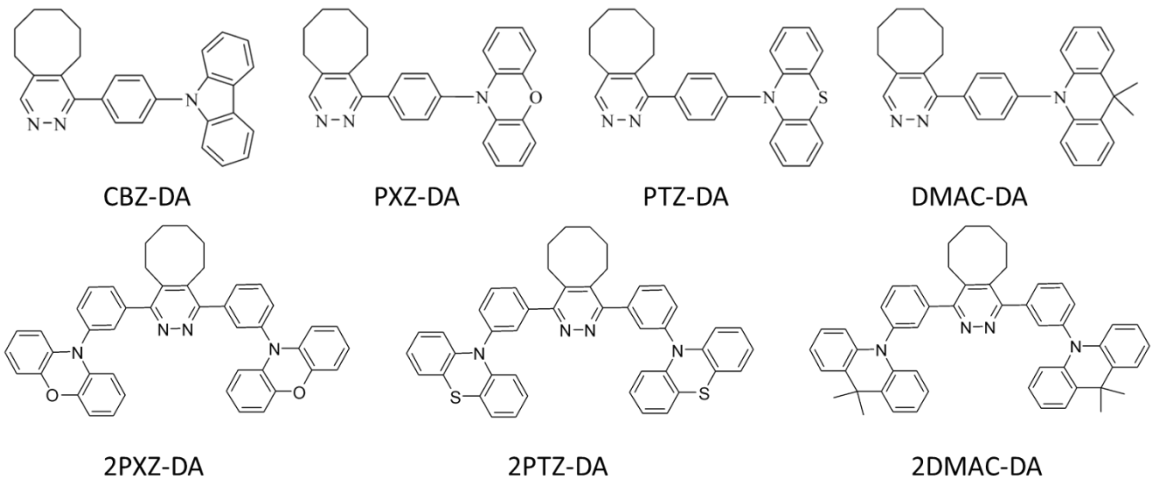

Figure 51. Structures of investigated compounds based on DA acceptor unit.

For PTZ and PXZ substituents oxidation is characterized by a reversible oxidation process. For substitution by CBZ and DMAC – non-reversible. Oxidation potentials of donor groups are less than in case compounds based on NPTI unit with a difference of 0.05 V – 0.10 V. E_g was determined from the absorbance spectrum, and E_g is higher (practically in two times) than in the case NPTI units.

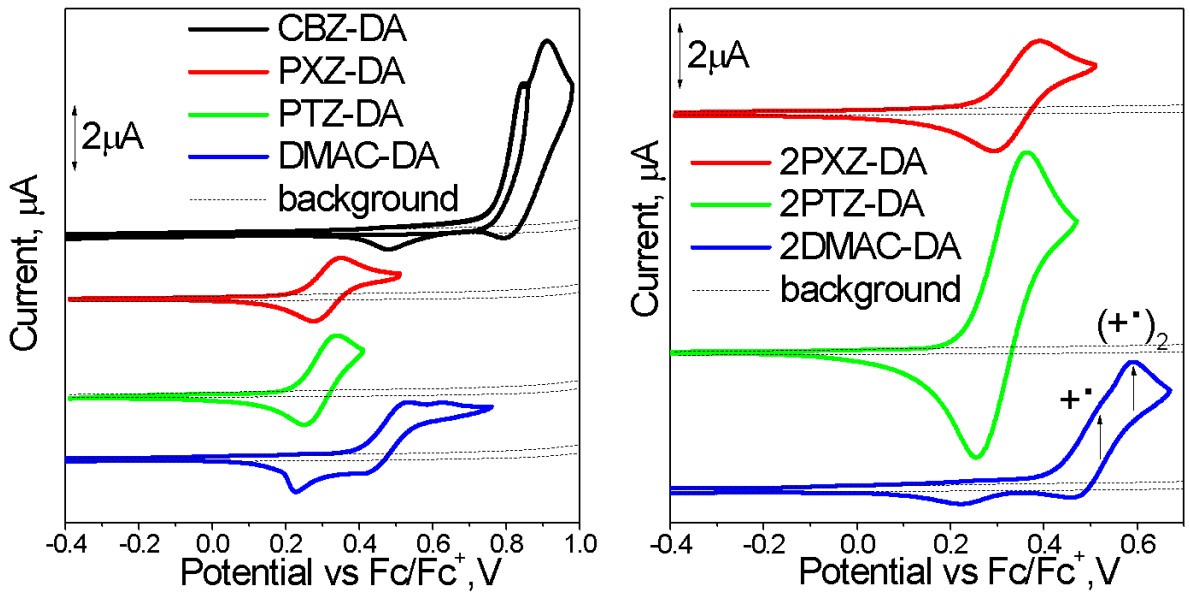

Figure 52. CV curves of oxidation for pyradizine core with different donors.

The lowest HOMO level of compounds with one donor group have compounds with PXZ-DA and PTZ-DA (-5.31 eV) and the highest – compound CBZ-DA (-5.83 eV). Comparing with compounds, which have two donor groups: the lowest value of the HOMO level of energy has compound PXZ-DA (-1.85 eV) and the highest – 2DMAC-DA (-2.19 eV). The compound, which has two phenothiazine donor groups (2PTZ-DA) has a HOMO level of energy at -5.39 eV.

Table 6. HOMO/LUMO levels, E_g^{opt} of compounds based on DA acceptor group.

	E_{ox}^{onset} vs Fc/Fc^+	λ, nm	E_g^{opt}, eV	HOMO, eV	E_{red}^{onset} vs Fc/Fc^+ (calculated), eV
CBZ-DA	0.73	352	3.52	-5.83	-3.65
PXZ-DA	0.21	358	3.46	-5.31	-3.67
PTZ-DA	0.21	367	3.38	-5.31	-3.67
DMAC-DA	0.38	373	3.32	-5.48	-3.59
2PXZ-DA	0.25	375	3.31	-5.35	-3.25
2PTZ-DA	0.29	376	3.30	-5.39	-3.32
2DMAC-DA	0.43	371	3.34	-5.53	-3.30

HOMO = - (E_{ox}^{onset} + 5.1); $\mathbf{E_g^{opt}} = \frac{1240}{\lambda}$; $\mathbf{E_{red}^{onset}} = E_{ox}^{onset} - E_g^{opt}$.

In the case of compound CBZ-DA, there are two oxidation peaks. When the experiment stopped potential at the “first” peak (at 0.85 V), this peak is non-reversible. The “Second” part looks typical for the oxidation process for the CBZ substitution unit, and in the general view of the peak is a rather small contribution of the first part. Comparing this fact with DFT calculation was mentioned that HOMO orbital was located on donor unit of compounds with the exception only the CBZ unit (**Figure 53**).

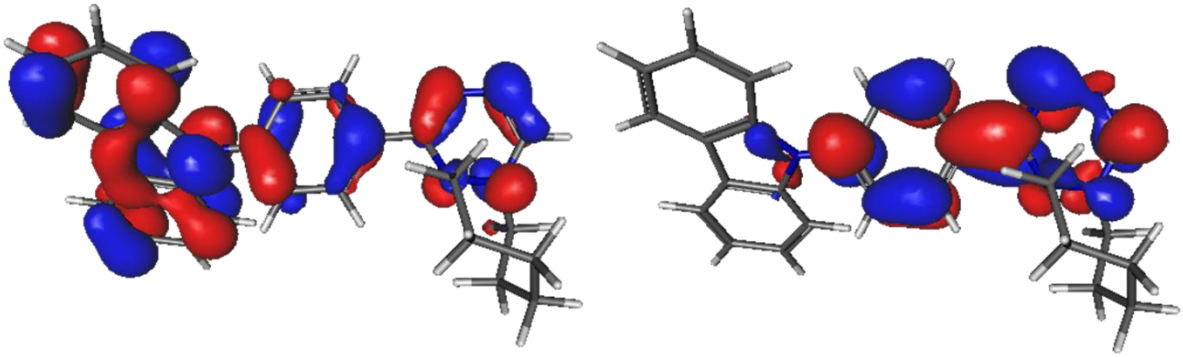

Figure 53. Molecular orbital isosurfaces (HOMO and LUMO) of CBZ-DA calculated at B3LYP 6-31g(d) level of theory with iso value of 0.03.

In the case of compounds with two donor groups registration current of the oxidation process is higher two times comparing with compounds with one donor group. DFT calculations showed that in case 2PXZ-DA HOMO and $HOMO^{-1}$ levels have the same position -4.71 eV. In case 2PTZ-DA difference between these levels is 0.63 eV, but on a CV these peaks are merged. The shape of the oxidation peak DMAC-DA and 2DMAC-DA are similar to each other and similar to compounds with NPTI acceptor unit. The shape of the oxidation peak consists of two peaks, with the difference between peaks potential 0.08 V. Using DFT results, HOMO and $HOMO^{-1}$ have the same position -4.93 eV.

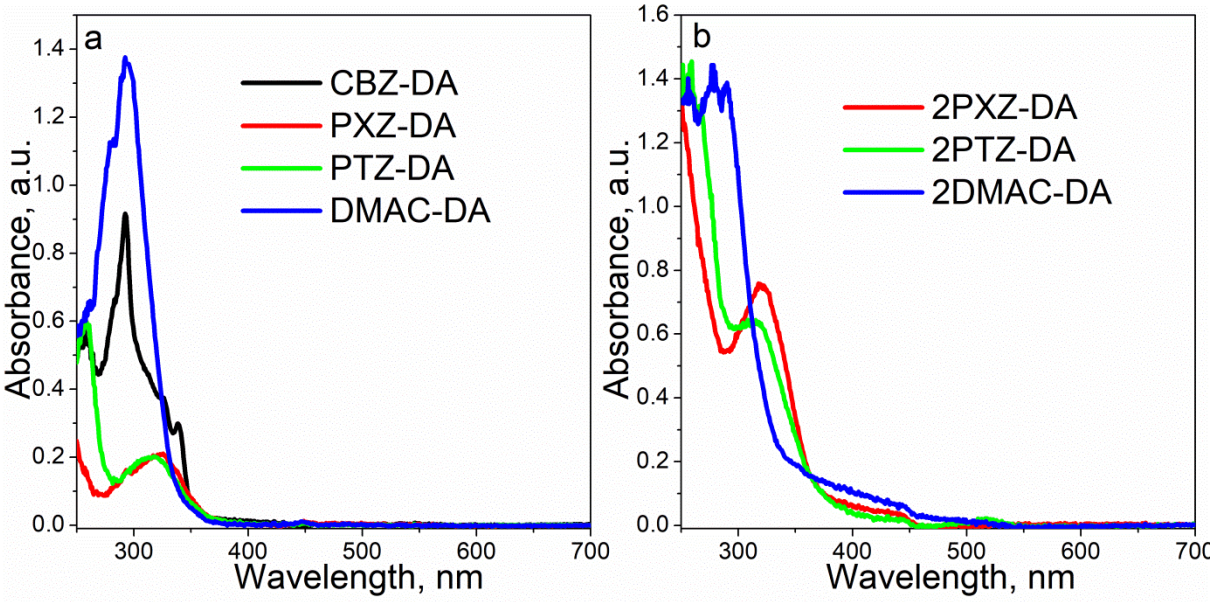

Figure 54. Absorbance spectra of compounds based on the DA acceptor unit (a) spectra for compounds with one donor group, (b) spectra for compounds with two donor groups.

As mentioned the smallest energy gap was calculated for 2PTZ-DA -3.30 eV in the case of two donor groups and PTZ-DA -3.38 eV for one donor group. The highest energy gap was determined for CBZ-DA. Using these values were calculated LUMO levels of energy. The lowest LUMO level is in case PXZ-DA (-1.85 eV) and the highest is in case CBZ-DA (-2.31 eV).

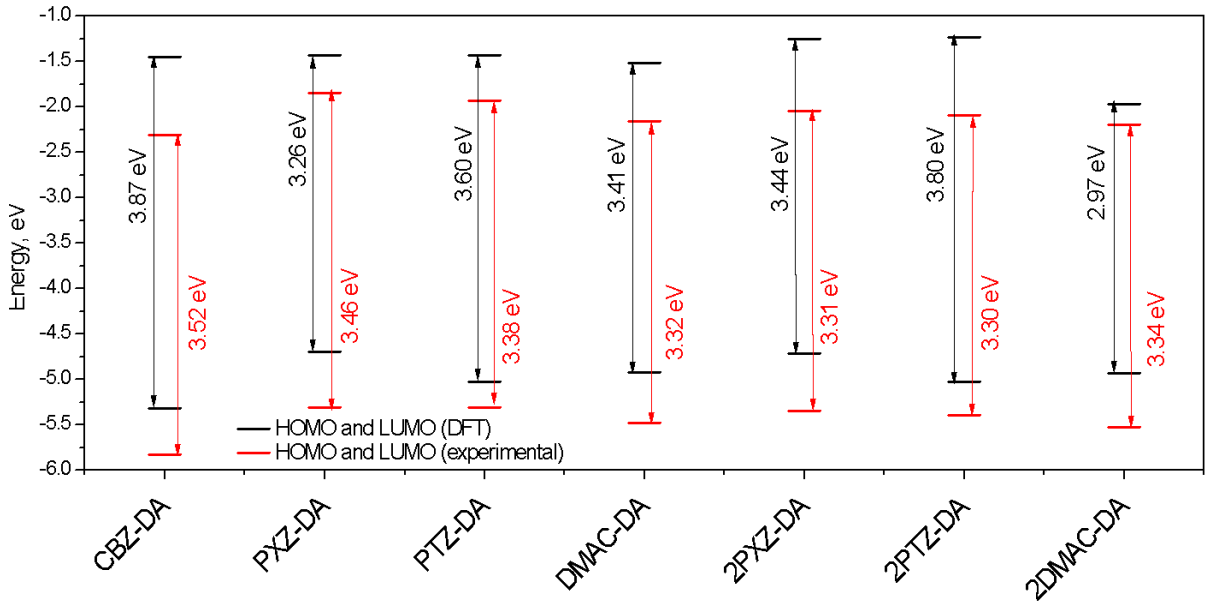

Figure 55. Comparing experimental and calculation levels of energy for compounds based on DA acceptor unit.

The lowest difference (0.28 eV) between calculated and experimental HOMO levels was observed 2PTZ-DA and the highest (0.64 eV) – 2PTZ-DA. (**Figure 44, 45**) Differences in LUMO levels are higher in the case of the monosubstituted DA acceptor unit than the *di*-substituted unit, the lowest difference (0.19 eV) was in case 2PXZ-DA and the highest (0.86 eV) was for CBZ-DA. Comparing HOMO and HOMO-1 levels for DA unit with two donor group, in the case of compounds 2PXZ-DA and 2DMAC-DA levels are typically the same, but in the case of 2PTZ-DA difference is 0.63 eV.

The first and second oxidation peaks of CBZ-DA are so close to each other and it's quick hard to control the value of potential. It is a reason, that the oxidation process took place mainly in the second peak and as a result of the oxidation process was formed dication. Increasing absorbance spectra is correspond to dication. (**Figure 56**)

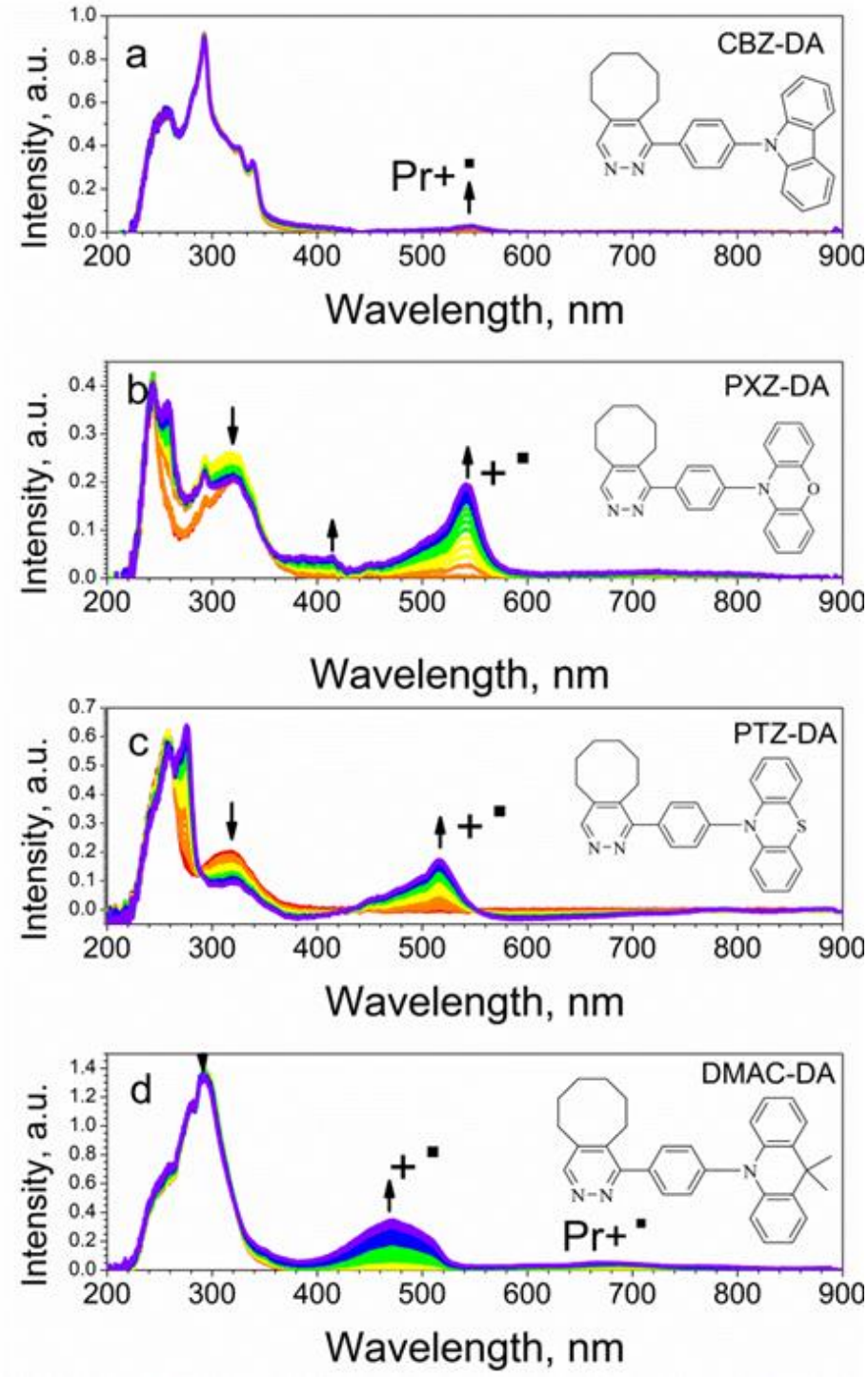

Figure 56. "In-situ" oxidation process spectra of compounds based on DA acceptor unit.

Increasing intensity is associated with the oxidation donor group. It means that compounds, which have two donor groups changes are more significant than compounds that have one donor group (**Figure 57**).

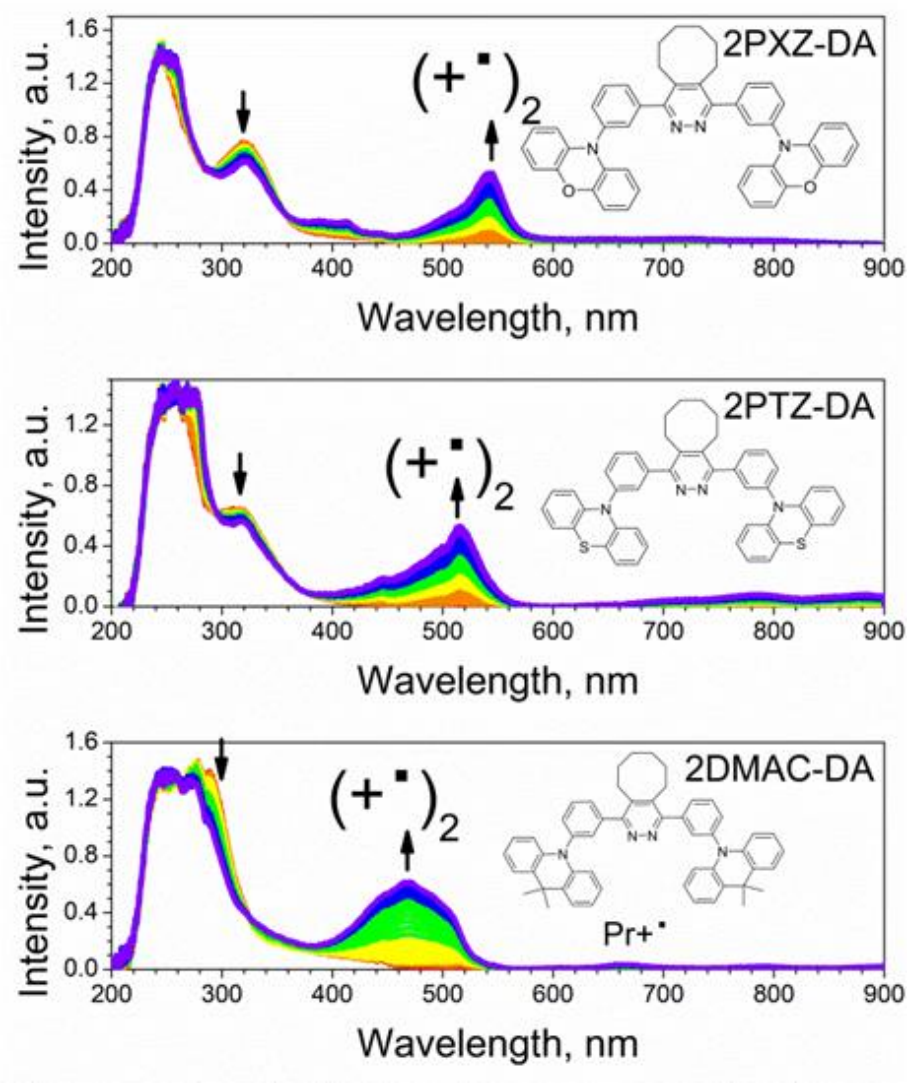

Figure 57. "In-situ" oxidation process spectra of compounds based on DA acceptor unit

Cation radicals of PXZ and PTZ are characterized by an increasing absorbance of 514 nm and 541 nm, respectively, which agrees well with the theoretical calculations. (**Figure 58**).

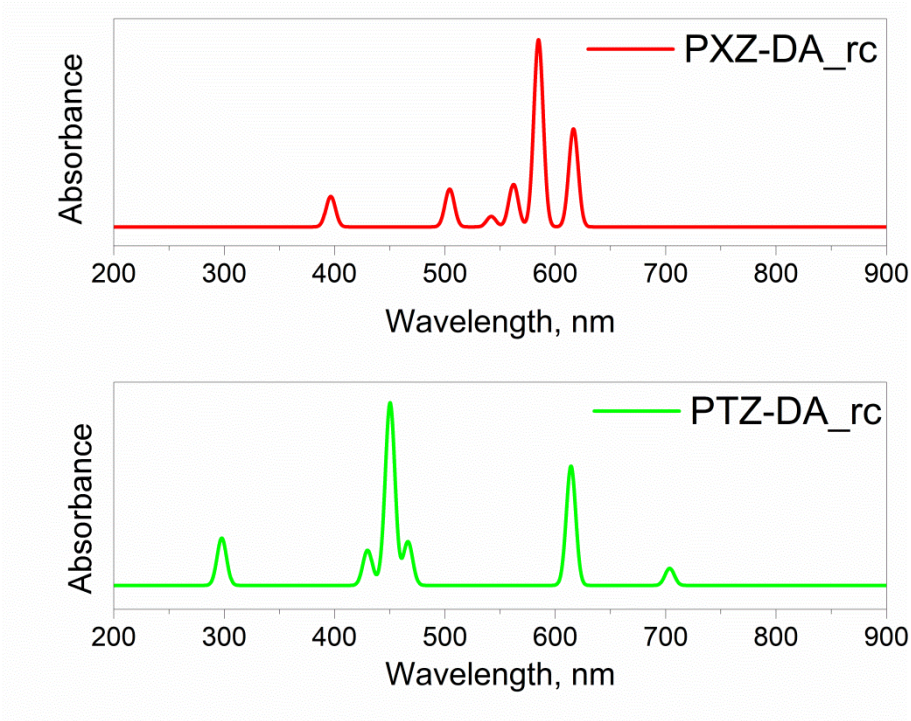

Figure 58. DFT calculation of predictable wavelength (red) for PXZ-DA radical cation (green) for PTZ-DA radical cation.

This corresponds to an increase in the concentration of the cation radical in the investigated volume at oxidation potential. There is increasing in the intensity in the range of long wavelengths (more than 600 nm) for CBZ and DMAC substituted compounds indicates products, and given the irreversibility of the oxidation processes may indicate the formation of the product on the surface of the electrode, that is, the increase in the oxidation process (**Table 7**).

Table 7. Changes in intensity and wavelength of bands registered in the oxidation process.

	Absorbance maximum of			
	neutral molecule,λ nm	**Cation radical λ, nm**	**Dication diradical λ, nm**	**Product λ, nm**
CBZ-DA				570
PXZ-DA	316	414; 542		
PTZ-DA	316	514		
DMAC-DA	290	468		720
2PXZ-DA	318		541	541
2PTZ-DA	317		514	514
2DMAC-DA	288		480	680

The lowest *g*-factor value has a DMAC-DA compound (2.0032), compound substituent dimethyl-acridine (**Table 8b**). The signal with the highest g-value (2.0058) has recorded during the oxidation of PTZ-DA. As well as the case of one donor group, in the case of two substituents, the highest value of *g*-factor (2.0059) has PTZ-DA and practically the same (2.0058) for DMAC-DA and the lowest value (2.0038) for 2PXZ-DA.

For compounds, which are substituent by CBZ substituent, the signal is so low and quite noisy. (**Figure 60a**) It means, that molecules can form non-paramagnetic structures. The scheme of this structure is shown in **Figure 59.**

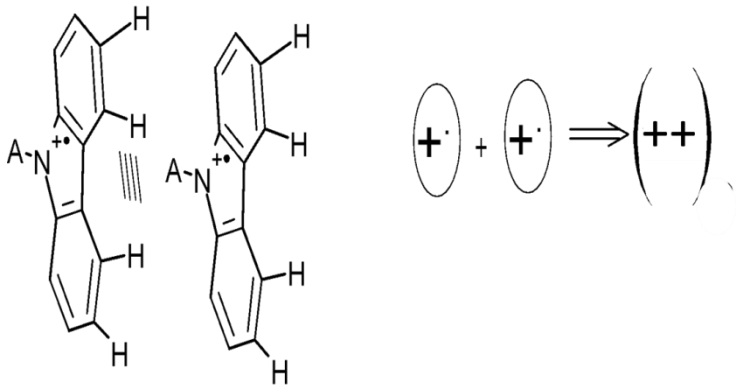

Figure 59. Scheme of formation of non-paramagnetic structure.

As described above, there are difficulties in registration EPR-spectra for CBZ-containing compounds. In the case of compound CBZ-DA, no signal from the cation of CBZ-DA was recorded (**Figure 60a**). this fact can be caused by the formation of a non-paramagnetic structure, especially the product of oxidation of CBZ-DA.

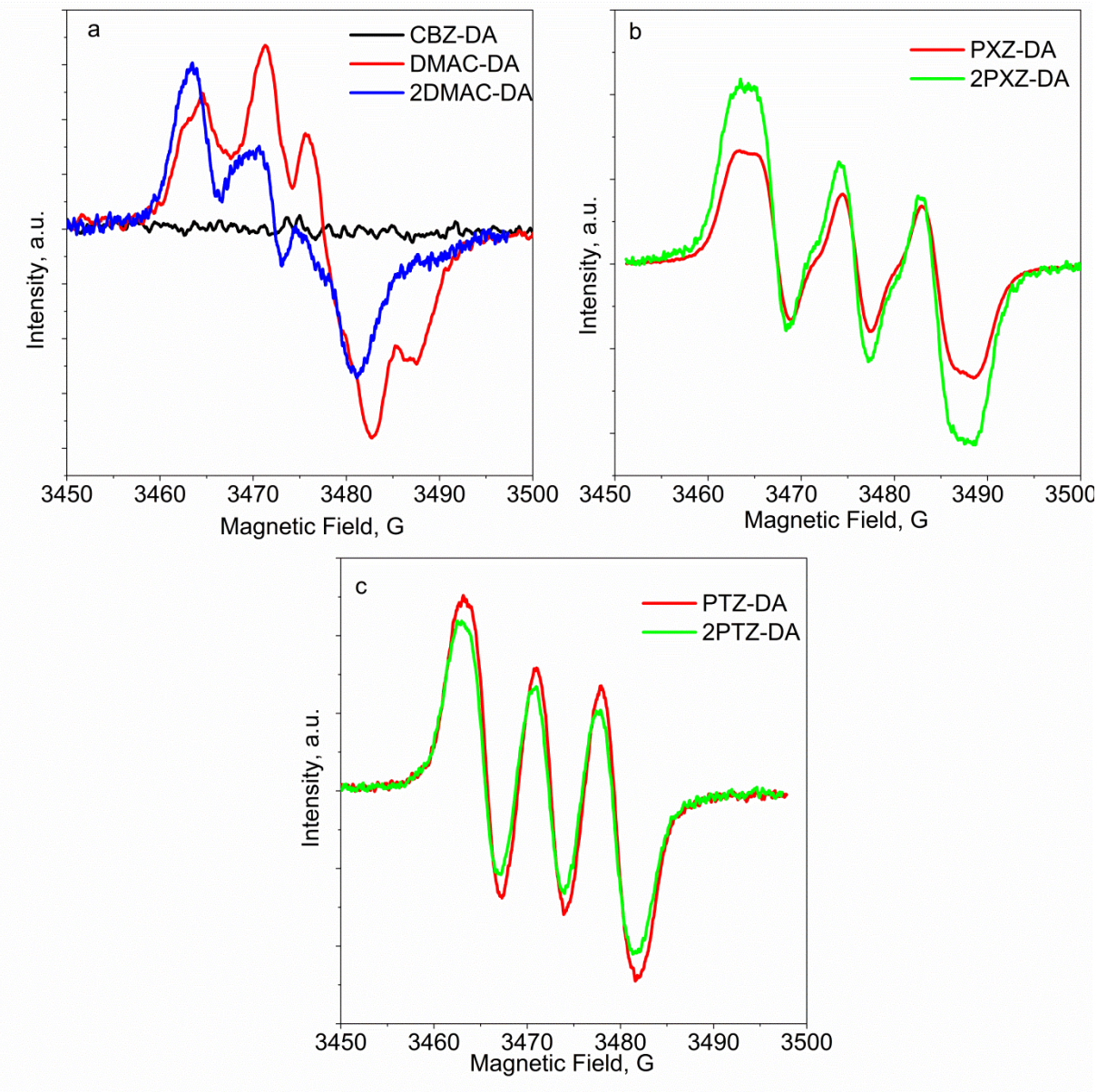

Figure 60. ESR-spectra of compounds based on DA acceptor unit at E_{ox}^{first}, modulation 0.06 mT and amplitude 500 normalized at 3rd Mn line a) EPR spectra of CBZ-DA, DMAC-DA, 2DMAC-DA b) EPR spectra of PXZ-DA, 2PXZ-DA c) EPR spectra of PTZ-DA and 2PTZ-DA.

Table 8. *g*-factor value for oxidation cations from compounds based on DA acceptor unit.

	***g*-factor**	**Signal width, G**
CBZ-DA	NA	NA
PXZ-DA	2.0037	26
PTZ-DA	2.0058	18
DMAC-DA	2.0032	17
2PXZ-DA	2.0038	25
2PTZ-DA	2.0059	19
2DMAC-DA	2.0058	19

NA – signal was not obserwed due to bipolaron formation.

Compound DMAC-DA (**Figure 60a,b**) has a hyperfine structure, but this structure is hard to simulate because this structure is not symmetrical. The simulation of this structure has so high mathematical error. For that reason, the spectrum was not simulated.

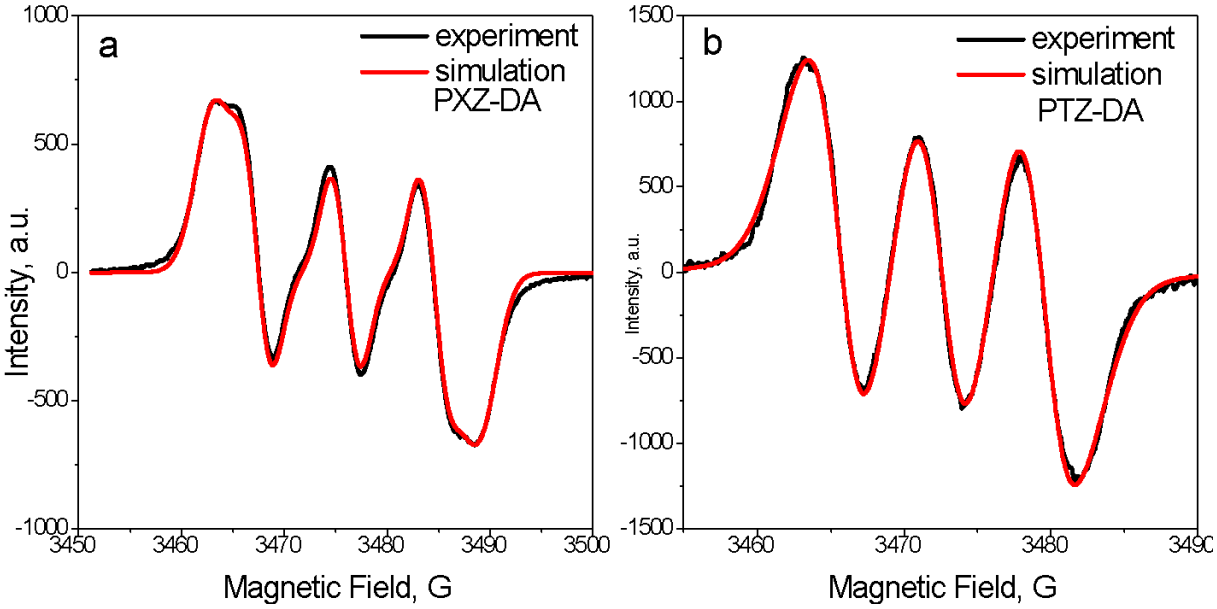

Figure 61. Experimental and simulated ESR spectra (oxidation part) a) PXZ-DA b) PTZ-DA

For PXZ DA (**Figure 61a**), the signal has slightly wide (the difference is above 7G), comparing PTZ-DA (**Figure 61b**). The first peak is broadly spread (into 2), and it seems as if it consists of two peaks. The following are peaks with the shoulder at the mid-height. In a simulation, it was taken that splitting occurs on a nitrogen atom (with a splitting value of 8.57 G) and two groups of equivalents of hydrogen (with a splitting value of 3.14 G and 0.22 ¸G).

Table 9. Calculated splitting constant of cation radicals signals (using Winsim program).

	Constant, G
PXZ-DA	1N (8.51); 2H (3.14); 2H(0.22).
PTZ-DA	1N (6.95); 2H(0.87); 2H(0.66).

For PTZ substitution, the same scheme as in the previous case was taken. But this compound is characterized only by signal expansion. The simulation was performed based on splitting on a nitrogen atom (with a splitting value of 6.95 G) and two groups of equivalent hydrogens with a fairly close splitting value (0.87 G and 0.66 G, respectively) (**Table 9**).

Signals of compounds with two donor groups are similar to signals to compound with one donor group (**Figure 62**). For 2 PXZ substituted DA, the signal is similar to a monosubstituted acceptor, but the signal is significantly broadened. It could be said that the superfine structure was a result of the interaction of the two donor groups, but they are located on opposite sides of the acceptor to the same connection through the linker, so it is possible to exclude this type of interaction.

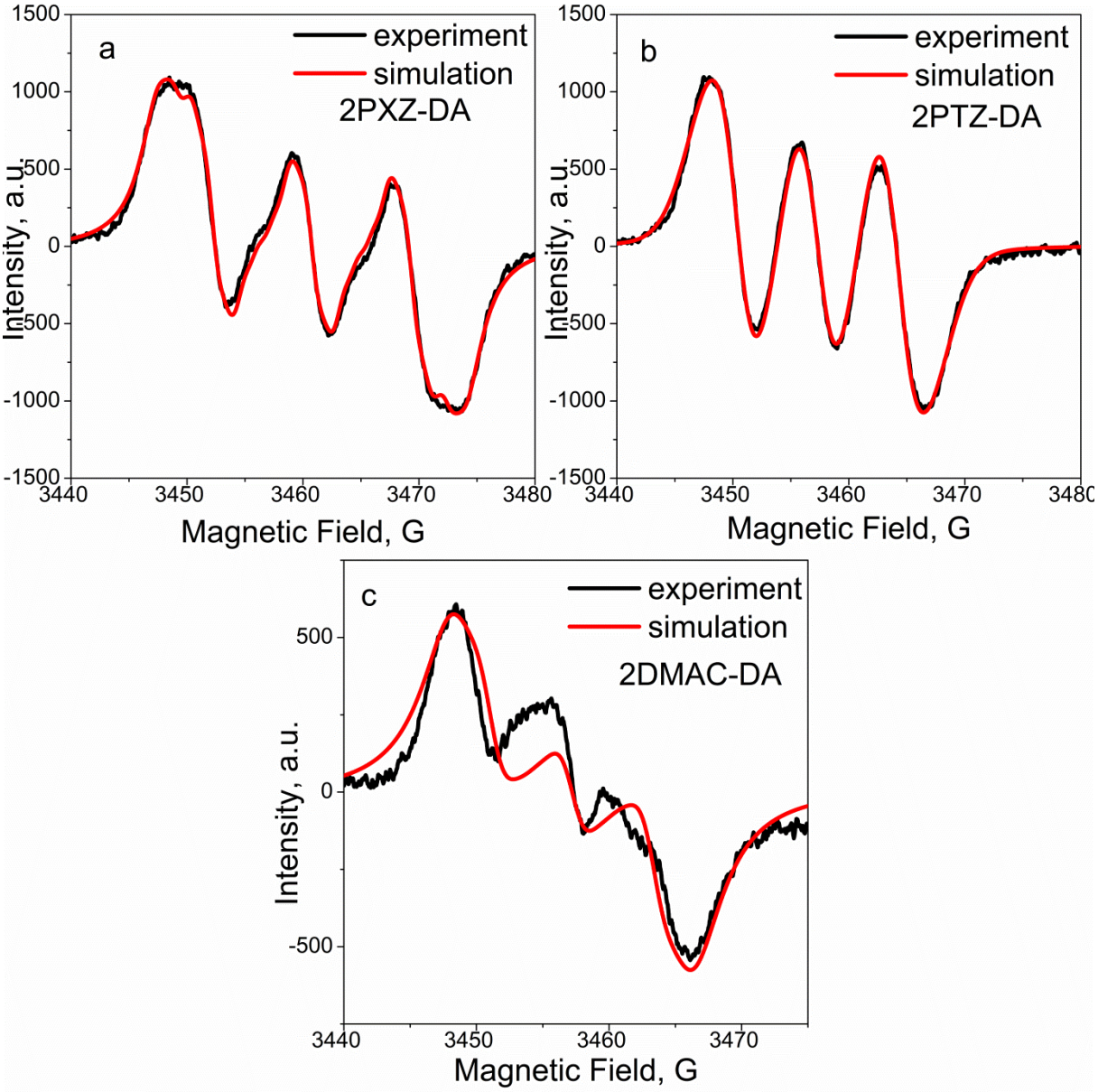

Figure 62. Experimental and simulated ESR spectra of compounds based on DA acceptor unit with two donor groups (oxidation part) a) experimental and simulation spectra of 2PXZ-DA b) experimental and simulation spectra of 2PTZ-DA c) experimental and simulation spectra of 2DMAC-DA.

The simulation of such a structure was carried out based on splitting on a nitrogen atom (with a splitting value of 8.58 G) and two groups of equivalent hydrogens (with a splitting value of 2.99 G and 1.29 G, respectively) (**Table 10**). In this case, the splitting values on the hydrogen atom differ by less than twice, which means that it is unlikely that the latter can be neglected, as in the case of PXZ substitution.

Table 10. Calculated splitting constant (using Winsim program) of radical signals.

	Constant, G
2PXZ-DA	1N (8.58); 2H (2.99); 2H(1.29).
2PTZ-DA	1N (6.94); 2H(0.63).
2DMAC-DA	1N (6.16); 2H(2.06).

For PTZ substitution we have a superfine structure, that can be simulated using only two atomic groups, unlike mono-PTZ-substituted. For the simulation, splitting on a nitrogen atom (with a splitting value of 6.94 G) and two equivalent hydrogens with a splitting of 0.63 G were used. Comparing the splitting values with the monosubstituted PTZ, the splitting constants for nitrogen are almost the same, but slightly different splitting values for hydrogen, and also for this simulation only one group of hydrogens, not two.

The signal DMAC substituted DA has a relatively low intensity compared to other signals. For such a signal, the simulation will have a fairly high mathematical error (**Figure 62c**).

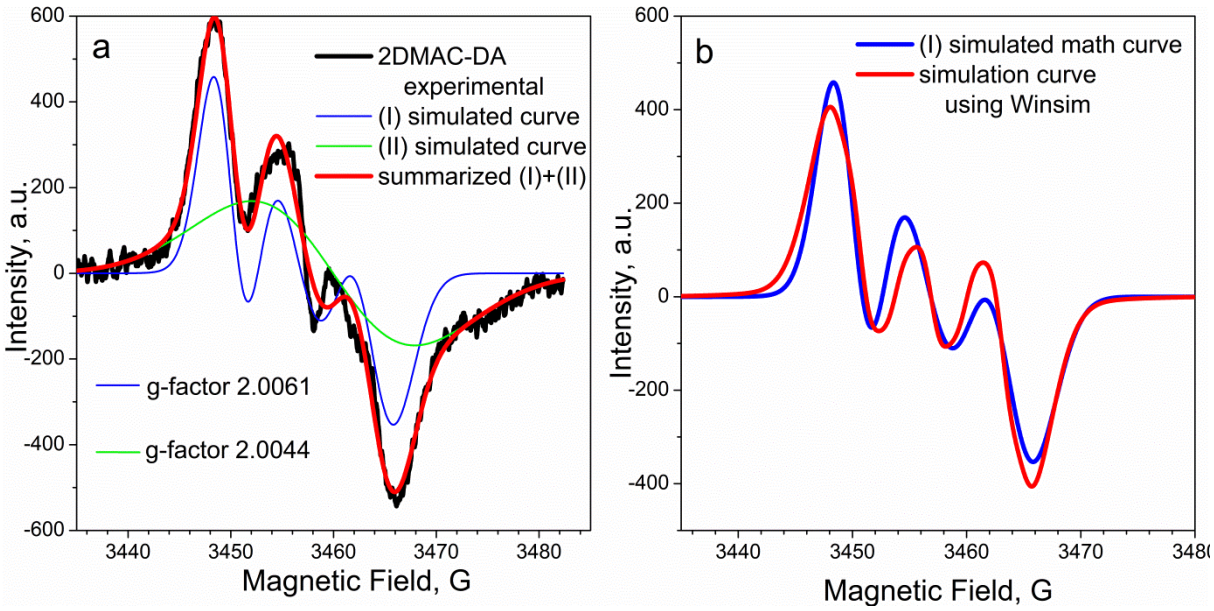

Figure 63. Experimental and simulated EPR curves for 2DMAC-DA (oxidation part) a) experimental curve of 2DMAC-DA, simulated curves using mathematical dividing into two different signals (I) and (II), summarized curve of (I) and (II) b) comparison curve using mathematical dividing and simulation curve using Winsim.

Probably recorded signal was derivate into two different signals: from cation (I) and the product of the oxidation process (II) (**Figure 63a**). Simulation has R^2 = 0.9997. For this mixture of cations was calculated *g*-factor. *G* –factor with value 2.0044 corresponds to the cation of the product of oxidation. Another *g*–factor is much higher (2.0061) corresponds to the cation of oxidation of 2DMAC-DA, the charge is localized on the *N* atom.

The signal DMAC substituted DA has a relatively low intensity compared to other signals. The simulation was created considering the splitting of a nitrogen atom and two equivalents of hydrogen with splitting values of 6.16 G and 2.06 G, respectively. For this simulation R^2 is 0.963, which is lower than in the case of the signal derivate from two signals, But considering that it is a simulation not from the real spectrum, this value can be enough. The figure shows that the simulation is good enough to describe only the extreme peaks and the central part is rather bad.

5.3 Analysis of compounds based on the TA acceptor unit

The last investigated group presented very interesting behavior and present reversible reduction redox couple. In all cases, there is a peak from the oxidation and reduction process (**Figure 65**).

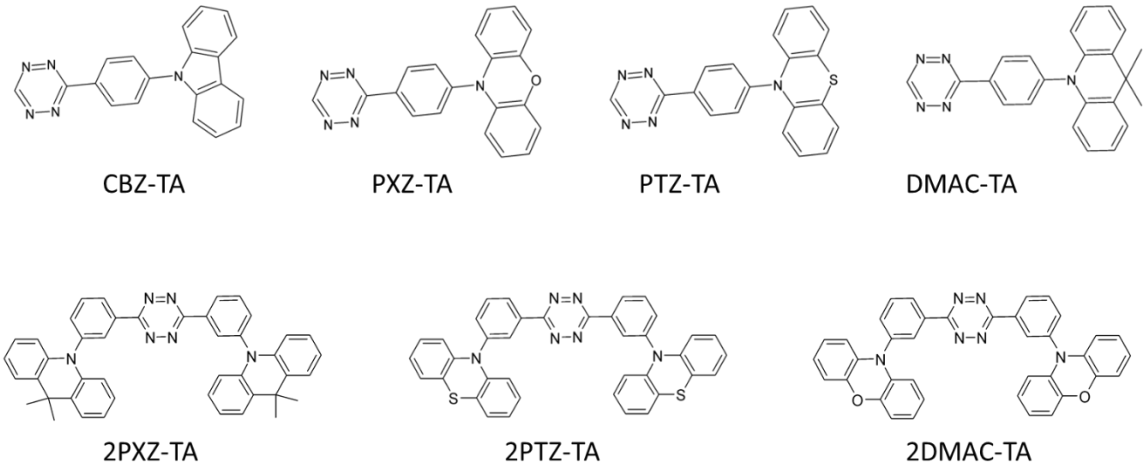

Figure 64. Structures of investigated compounds based on TA acceptor unit.

Reduction peaks are reversible and similar to each other (from -1.24 V to -1.14 V), especially the shape and position in the potential range and the values of LUMO levels are close to each other. The difference between the lowest value of -3.88 eV was in case PXZ-TA (**Figure 65a**) and -3.96 eV was in case 2DMAC-TA (**Figure 65b**). The difference is 0.08 eV and it is too small to compare (**Table 11**).

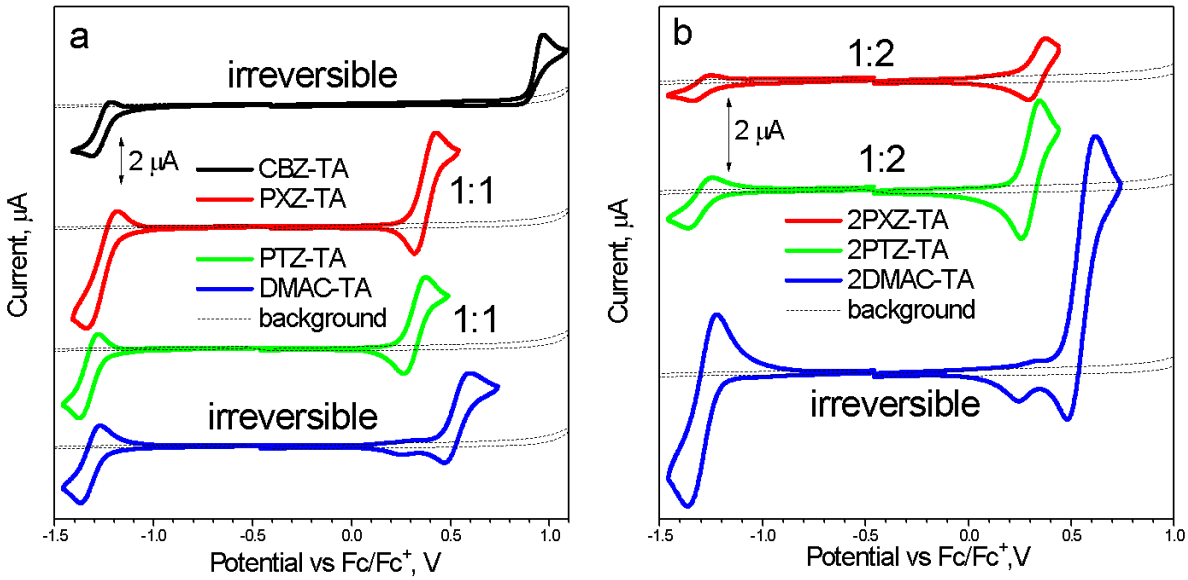

Figure 65. CV curves of compounds based on tetrazine with a) one donor group, b) two donor groups.

TA acceptor unit substituted by PXZ and PTZ has a reversible oxidation process. For CBZ and DMAC substituents were a non-reversible oxidation process. PTZ-TA and 2PTZ-TA have the lowest HOMO levels -5.34 eV and 5.31 eV respectively. The highest HOMO level was in the case of CBZ-TA (-5.96 eV) (**Table 11**). Let's suppose that the reduction process is characterized as a one-electron process. Comparing the height of the reduction and oxidation peak, oxidation of PXZ-TA and PTZ-TA is characterized by a one-electron reversible process (**Figure 65a**). However, the oxidation process of 2PXZ-TA and 2PTZ-TA is characterized by a two-electron reversible process (**Figure 65b**). It means, that E_{ox} oxidizes two donor groups at a similar potential. DFT calculation showed small differences between HOMO and HOMO $^{-1}$, that is why on CV it can be merged in one peak.

Table 11. HOMO/LUMO levels E_g^{calc}, E_g^{opt} of compounds based on TA acceptor unit

	E_{ox}^{onset} vs Fc/Fc$^+$, V	E_{red}^{onset} vs Fc/Fc$^+$, V	HOMO, eV	LUMO, eV	E_g^{el}, eV	E_g^{opt} eV
CBZ-TA	0.86	-1.17	-5.96	-3.93	2.03	1.91
PXZ-TA	0.29	-1.17	-5.39	-3.93	1.46	1.90
PTZ-TA	0.24	-1.24	-5.34	-3.86	1.48	1.90
DMAC-TA	0.40	-1.21	-5.50	-3.89	1.61	1.92
2PXZ-TA	0.27	-1.22	-5.37	-3.88	1.49	2.13
2PTZ-TA	0.21	-1.20	-5.31	-3.90	1.41	2.13
2DMAC-TA	0.45	-1.14	-5.55	-3.96	1.59	2.13

HOMO = - (E_{ox}^{onset} + 5.1); **LUMO** = - (E_{red}^{onset} + 5.1); $E_g^{el} = E_{ox}^{onset} - E_{red}^{onset}$; $E_g^{opt} = \frac{1240}{\lambda}$;

Else, E_g^{opt} was calculated from the absorbance spectra. In the case of compounds acceptor with two donor groups, there is so small peak in the range of 560 nm. The LUMO level was calculated using this value (**Figure 66**).

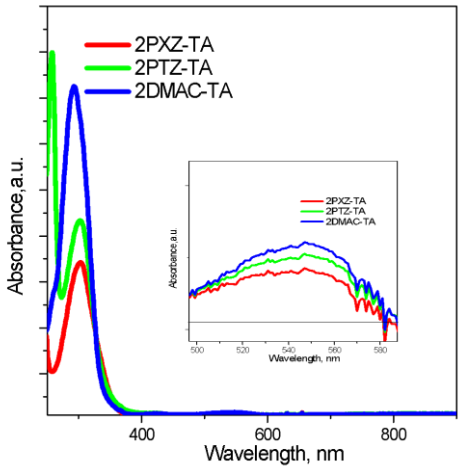

Figure 66. UV-VIS spectra of 2PXZ-TA, 2PTZ-TA, 2DMAC-TA.

The smallest difference between experimental and calculated LUMO level was in case CBZ-TA (0.13 eV) and the higher was in case 2PXZ-TA (0.64 eV).

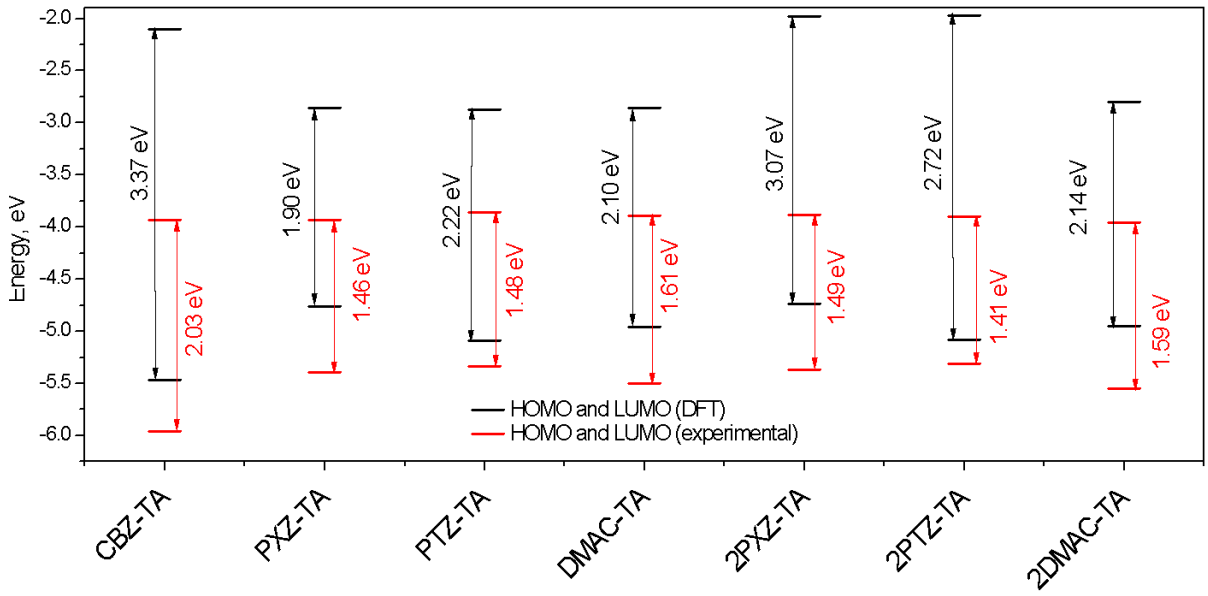

Figure 67. Comparison experimental and calculation levels of energy for compounds based on TA acceptor unit.

2PTZ-TA has the lowest difference (0.23 eV) between calculated and experimental HOMO levels and PXZ-TA and 2PXZ-TA have the highest (0.63 eV) (**Figure 67**). There are practically the same differences in LUMO levels in the case monosubstituted and di-substituted acceptor unit, except compound CBZ-TA (LUMO level is -2.10 eV), the lowest difference (0.99 eV) was in PXZ-TA and the highest (1.83 eV) has CBZ-TA. Comparing HOMO and $HOMO^{-1}$ levels for TA unit with two donor groups are practically the same.

Almost all, except for CBZ, during oxidation is a decrease in absorption in the range of 300 nm – 325 nm (**Figure 68**).

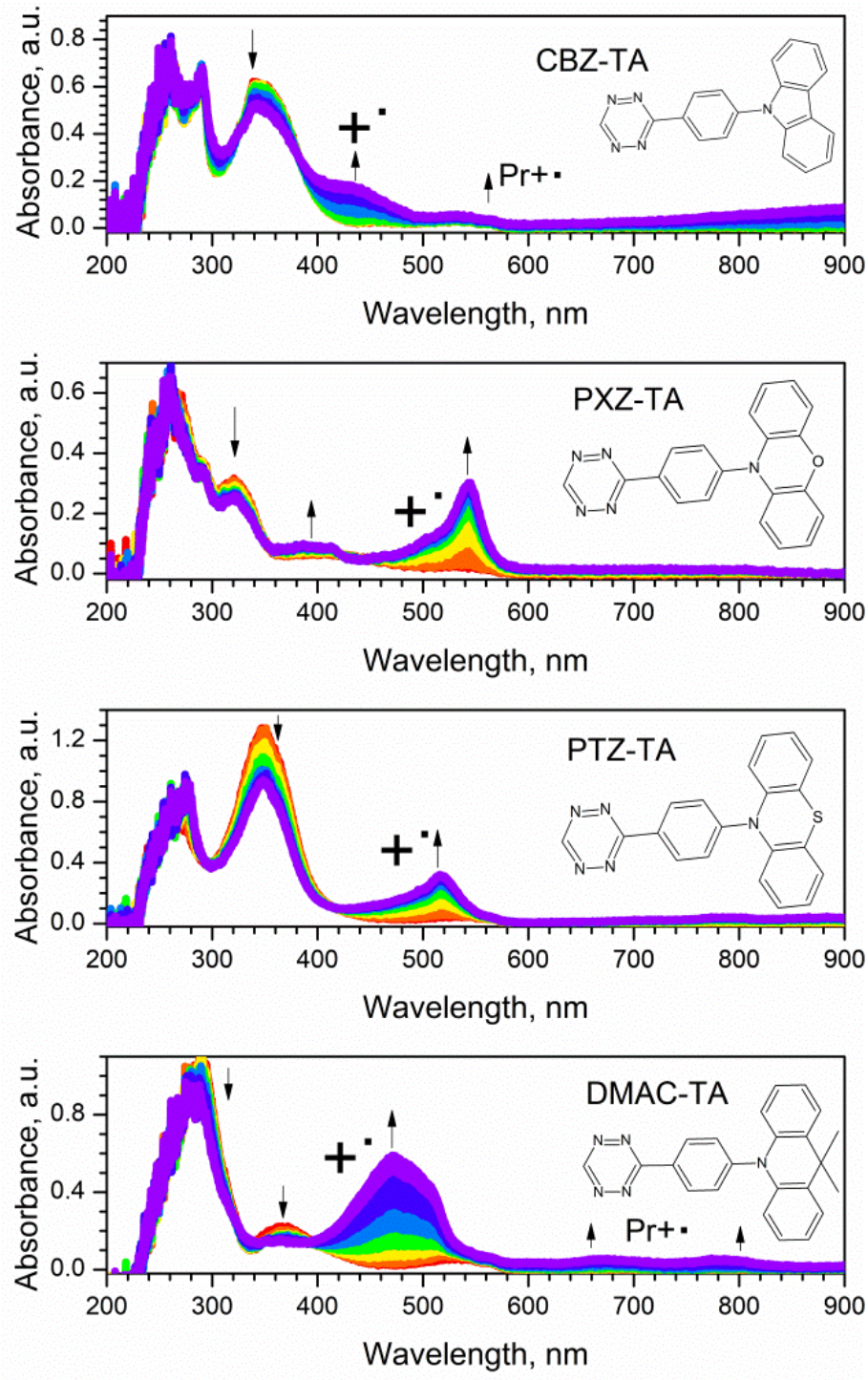

Figure 68. “In-situ” oxidation process spectra of compounds based on tetrazine.

During the oxidation process of CBZ-TA, it was observed small visible changes in absorbance spectra range from 342 nm to 800 nm (**Table 12**).

Table 12. Wavelengths, which changed during the experiment.

	Absorbance maximum of		
	the neutral particle, nm	**the radical cation , nm**	**product, nm**
CBZ-TA	342	436	554
PXZ-TA	321; 391; 409	541	
PTZ-TA	348	516	
DMAC-TA	287; 366	473	665; 780
2PXZ-TA	299	543	
2PTZ-TA	274; 296	514	
2DMAC-TA	243; 295	469	661; 780

For compounds having two donor groups, the decrease in intensity is significantly less pronounced than for compounds having one donor group (**Figure 69**).

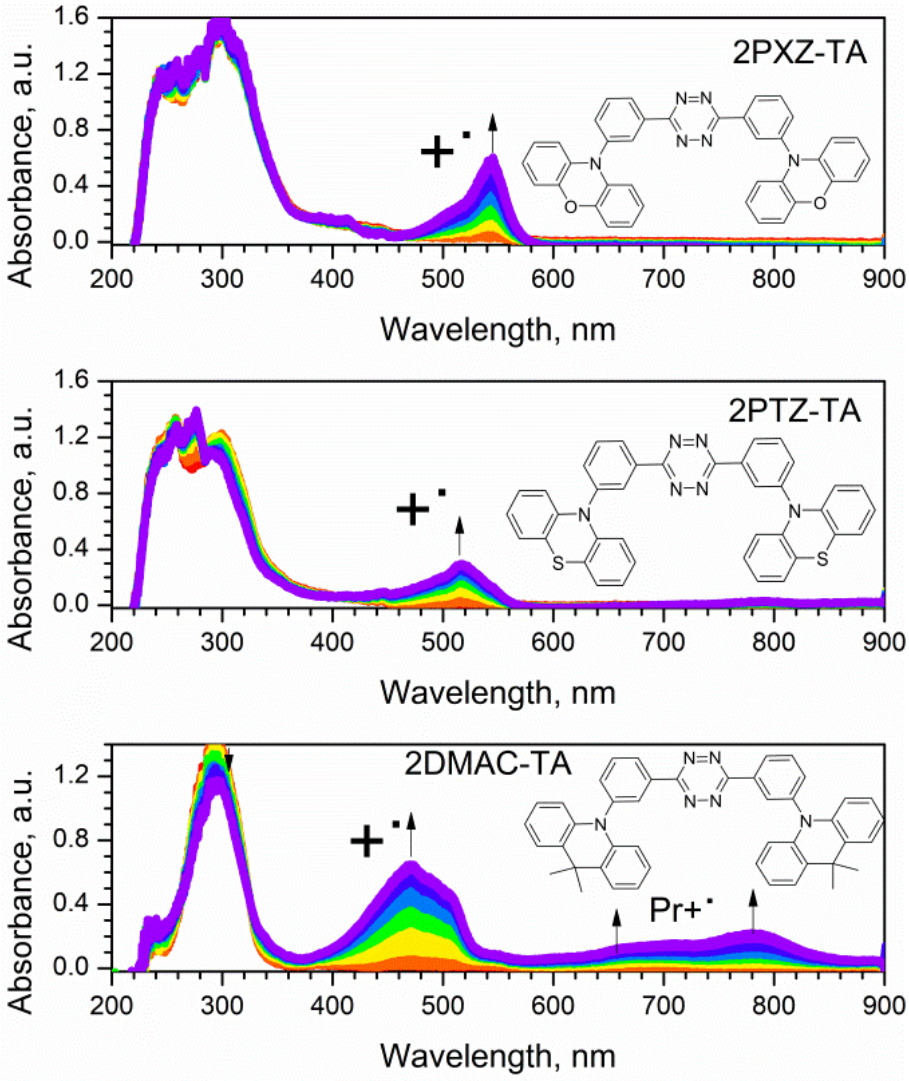

Figure 69. “in-situ” oxidation process spectra of compounds based on tetrazine.

Comparing other compounds, changes of absorbance spectra were significant, nevertheless, the position of wavelengths was similar to the previously analyzed groups with similar donors. It means, that compounds substituted by phenoxazine (PXZ-TA, 2PXZ-TA) have changed at 541 nm, a phenothiazine (PTZ-TA and 2PTZ-TA) have changed at 516 nm and compounds, which is substituted by dimethyl-acridine (DMAC-TA and 2DMAC-TA) have changed at 470 nm. For compounds DMAC-TA and 2DMAC-TA were observed increasing absorbance spectra above 660 nm, it can be caused by the formation of a product). Also, these compounds have changed at the IR range (above 900 nm).

No changes were observed during the oxidation process at wavelengths over 900 nm, so this part of the spectrum is not shown.

Compound CBZ-TA during oxidation didn't show any signal in the magnetic field, which means that the product of oxidation is a non-paramagnetic moiety. It can be caused by formation structure, which is invisible in a magnetic field, which means – paramagnetic structure, etc. other atoms. Molecule DMAC-TA has a "singlet" signal with delicate splitting by 3 on the top. But this splitting is too small to simulate hyperfine structure (**Figure 69**). Compound 2DMAC-TA, has only a "singlet" signal, without splitting on a top, like as in the case compound DMAC-TA.

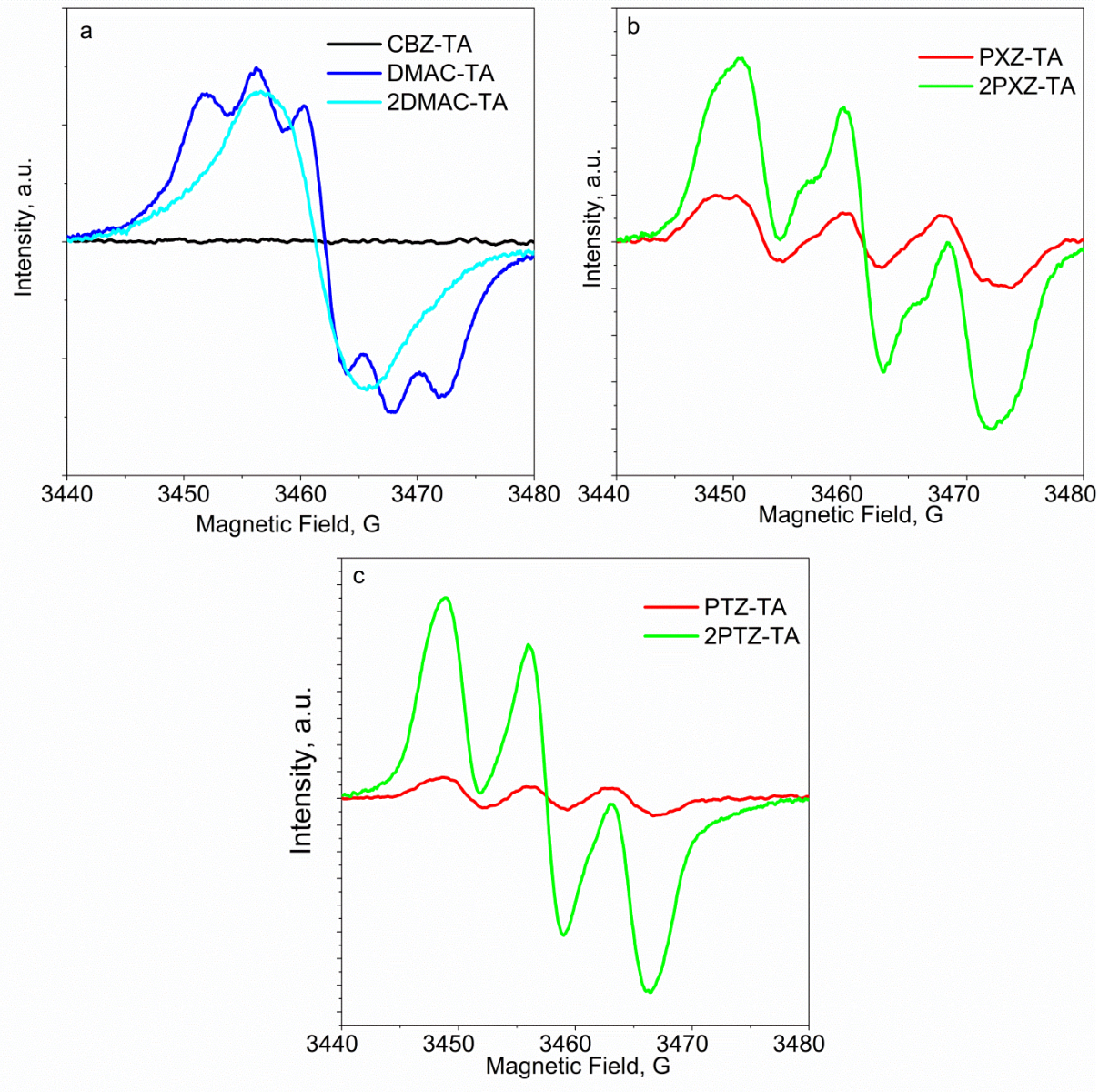

Figure 69. EPR spectra of radicals, formed during the oxidation process, of compounds based on the TA acceptor unit a) EPR spectra of CBZ-TA, DMAC-TA, and 2DMAC-TA b) EPR spectra of PXZ-TA and 2PXZ-TA c) EPR spectra of PTZ-TA and 2PTZ-TA.

For compounds, which have signals in a magnetic field, the *g*-factor was found. In all cases, values of *g*-factors suggest that the charge is localized at the *N* atom. Regardless of the amount of donor group, the highest values (2.0059) were in case compounds substituted by phenothiazine (comp. PTZ-TA and 2PTZ-TA), and the lowest (2.0039) value was in case of *g*-factor have compounds substituted by phenoxazine (comp. PXZ-TA and 2PXZ-TA) (**Table 13**).

Table 13. *g*-factor value of compounds based on the TA acceptor unit.

	***g*-factor value**	**Signal width**
CBZ-TA	NA	NA
PXZ-TA	2.0039	22
PTZ-TA	2.0059	18
DMAC-TA	2.0033	12
2PXZ-TA	2.0039	21
2PTZ-TA	2.0059	18
2DMAC-TA	2.0056	9

NA – signal was not obserwed due to bipolaron formation.

Radical cations of compounds PXZ-TA and PTZ-TA give hyperfine structure, and the character of the signal is typical when splitting was for on atom with spin 1.

For the mathematical simulation in the case of PXZ, splitting is poisoned by three groups of atoms: on nitrogen (with a splitting value of 8.59 G) and two groups of equivalent Hydrogen (with splitting values 2.97 G and 1.26 G, respectively) (**Table 14**). For PTZ substituted acceptor, three groups of atoms were also taken for simulation, with splitting values of 6.91 G, 0.91 G, and 0.60 G, respectively. in the case of substitution with PTZ, but splitting values are much smaller than in the case of substitution with PXZ (**Figure 70**).

Table 14. Calculated splitting constant of radical signals (using Winsim program).

	Constant, G
PXZ-TA	1N (8.59); 2H (2.97); 2H(1.26).
PTZ-DA	1N (6.91); 2H (0.91); 2H(0.60).
2PXZ-DA	1N (8.10); 2H(2.72).
2PTZ-DA	1N (6.53); 2H(1.12).

In the case of substitution with two donor groups, the mathematical simulations have a much higher mathematical error, which is seen in the figure. Signal optimization for the two donor groups did not produce good results when using the same scheme as replacing one donor group

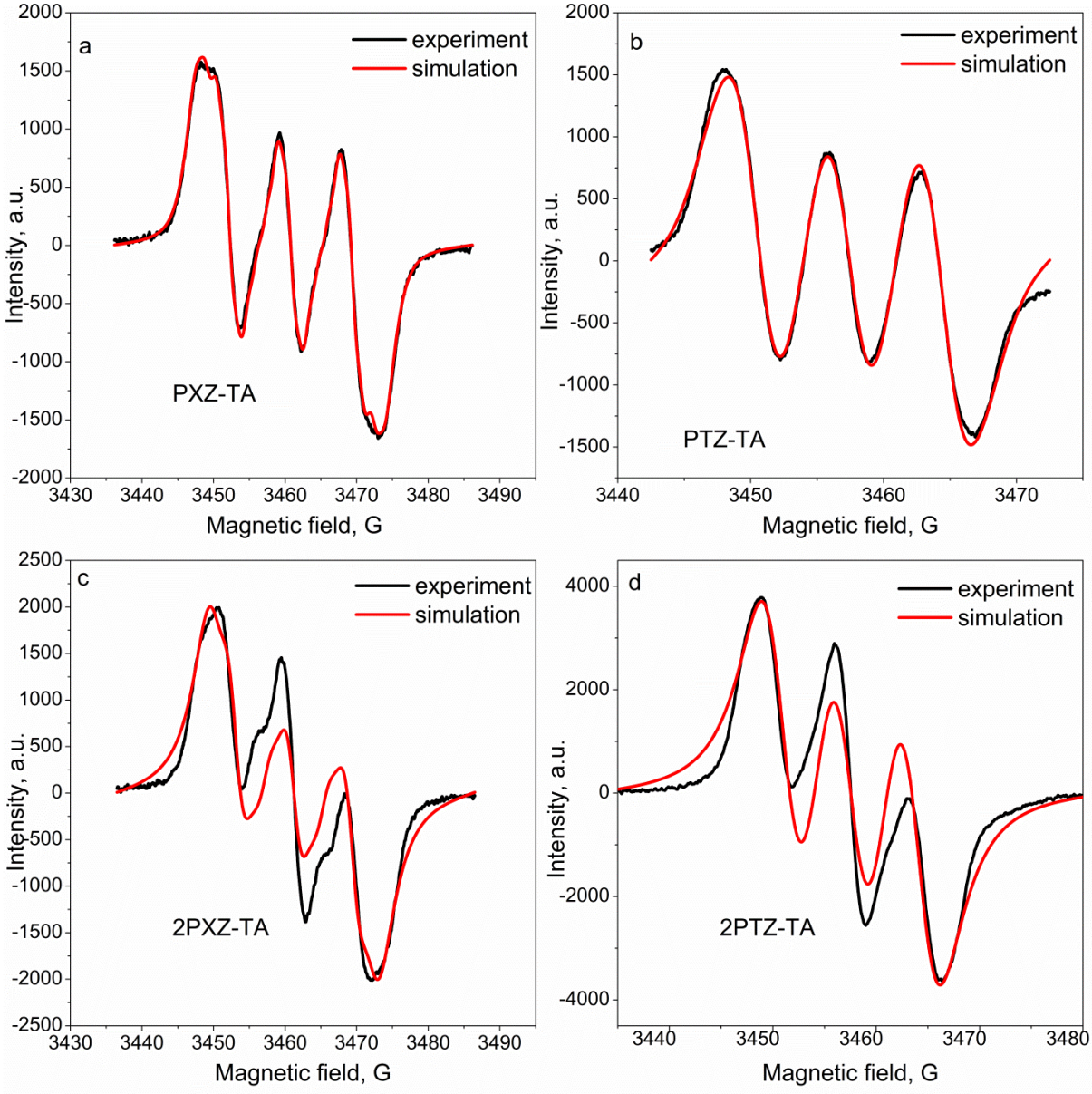

Figure 70. Experimental and simulated EPR curves of compounds based on TA acceptor unit (oxidation process) a) experimental and simulation curve of PXZ-TA b) experimental and simulation curve of PTZ-TA c) experimental and simulation curve of 2PXZ-TA d) experimental and simulation curve of 2PTZ-TA.

For PXZ substitution is characterized by the appearance of the shoulder, which could be described by splitting on adjacent hydrogen atoms, but in this case, the simulation using two groups (splitting on nitrogen with a splitting value of 8.10 G and with splitting on hydrogen atoms 2.72 G) does not improve good results. The same situation applies in the case of PTZ substitution, the simulation which is most true to reality, given the splitting of two types of atoms: a nitrogen atom (with a splitting value of 6.53 G) and two hydrogen atoms (with a

splitting value of 1.12). In the case of such unsuccessful optimization, it can be assumed that a large error is related to the interaction between the two donor groups, since there is no steric hindrance in the case of acceptor TA, as in the case of DA acceptors.

5.4 Polymerization

Compounds based on naphtylimide with carbazole substituted group, where the polymer was synthesized in 10 CV cycles, have good conductive properties (current reaches 5 mA) but is quite unstable (**Figure 71a, b, c, d**).

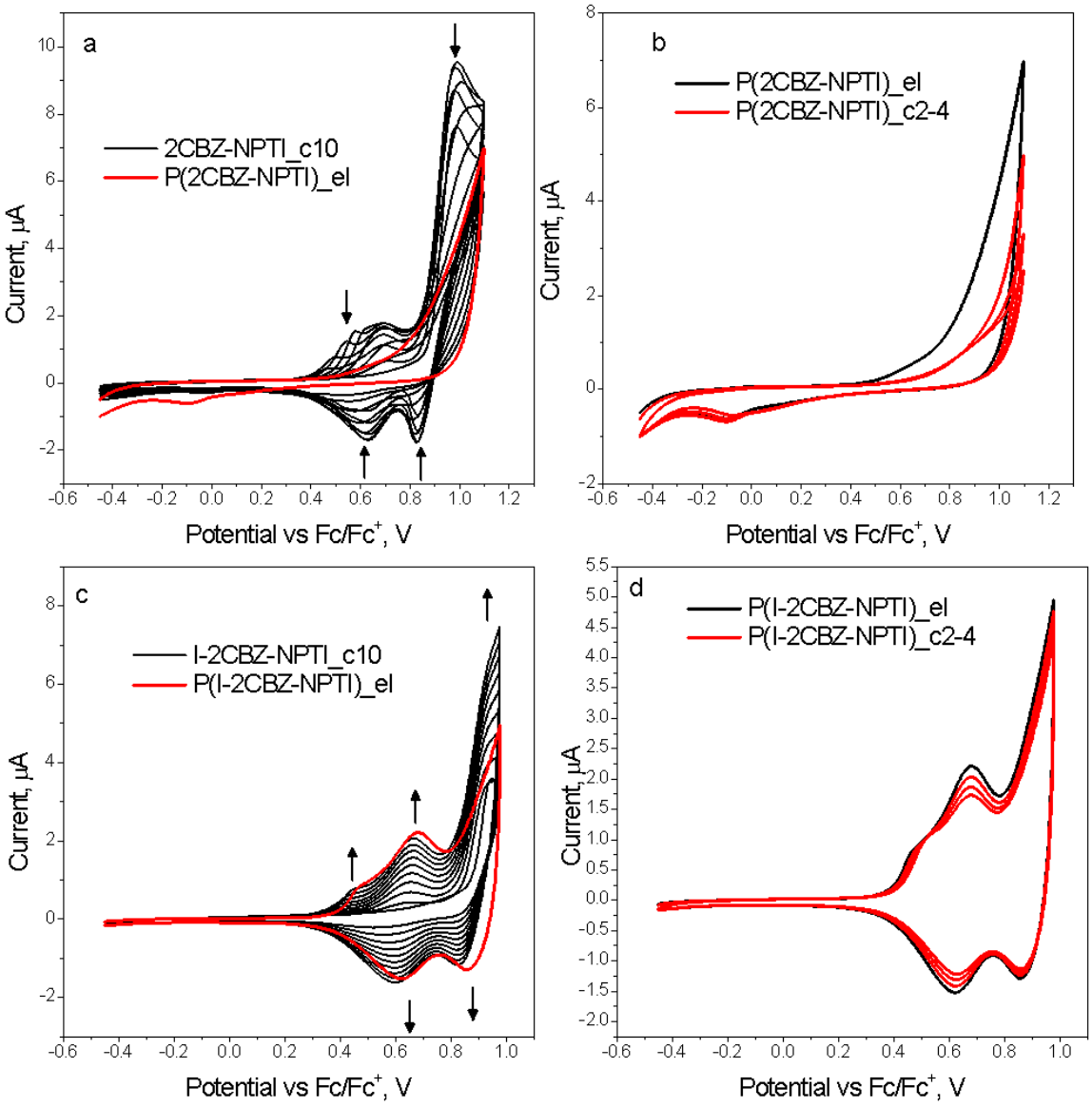

Figure71. CV curves of polymers based on CBZ and NPTI a) polymerization CV curve of 2CBZ-NPTI and polymer on the surface of electrode b) CV curve of polymer based on 2CBZ-NPTI first scan and subsequent 3 scans. c) polymerization CV curve of I-2CBZ-NPTI and polymer on the surface of electrode d) CV curve of polymer based on I-2CBZ-NPTI first scan and subsequent 3 scans.

When carrying out more cycles, the current strength decreases, and thus the number of charge carriers of the surface of the electrode decreases, which may indicate rather small stability of such polymers.

CV curves od polymers based on CBZ-DA and CBZ-TA were shown in **Figure 72**.

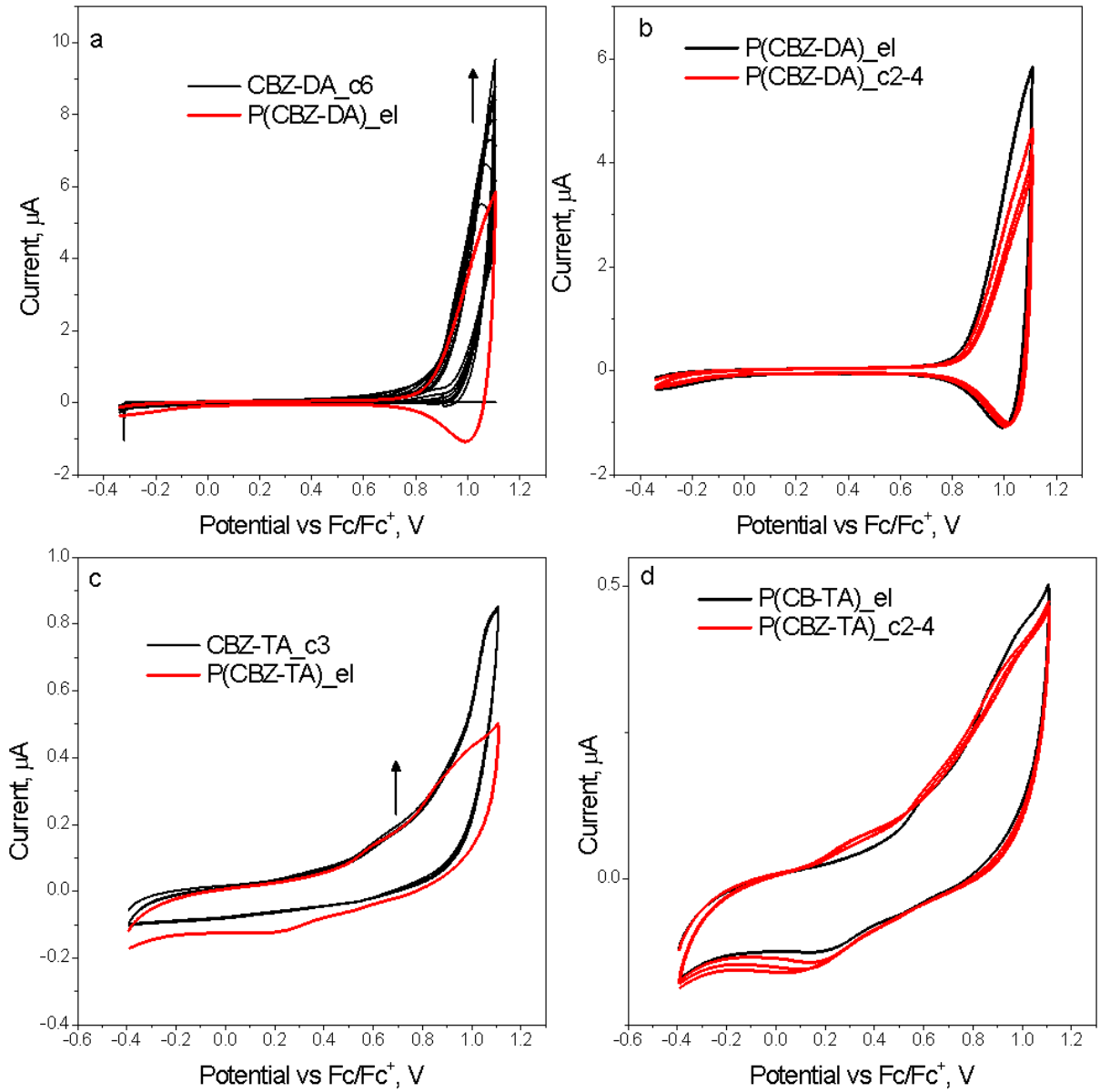

Figure 72. CV curves of polymers based on CBZ and DA or TA acceptor unit a) polymerization CV curve of CBZ-DA and polymer on the surface of electrode b) CV curve of polymer-based on CBZ-DA first scan and subsequent 3 scans. c) polymerization CV curve of CBZ-TA and polymer on the surface of electrode b) CV curve of polymer based on CBZ-TA first scan and subsequent 3 scans.

For polymers based on CBZ-DA and CBZ-TA, the polymerization products have rather low conductivity (quite small changes in current, less than 1 μA) and also do not have sufficiently high stability with the increasing number of cycles **(Figure 72).** In the form of curves in the case of the carbazole donor group, visually all of them have a similar shape, except for asymmetrically substituted naphthalene carbazole. In the case of acceptors DA and TA, the polymer curve of the oxidation part is similar to the monomer curve.

The lowest HOMO energy level was for CBZ-DA substituted with carbazole (-5.94 eV), and the highest level was observed for asymmetrically substituted naphthalene I2CBZ-NPTI(-5.52 eV) (**Table 15**).

Table 15. HOMO level of formatted polymers.

	E_{ox}, V	**HOMO, eV**
Poly-2CBZ-NPTI	0.71	-5.81
Poly-2ICBZ-NPTI	0.42	-5.52
Poly-CBZ-DA	0.84	-5.94
Poly-CBZ-TA	0.54*	-5.64

* small difference in current, thas why E_{ox} can be determined with the mistake.

Comparing to NPTI-based polymers, as in the case of DMAC, symmetrically substituted naphthalene has less stability than unsymmetrically substituted. In both cases, the polymer has two peaks one of which (at a higher potential) can correspond to the oxidation potential of the monomer. In the case of a product of symmetric substitution, when carrying out more cycles, it is easy to notice that the first peak on CV (0.28 V) is more stable than the second (at 0.50 V). not symmetrically substituted naphthalene has slightly higher potential values for the polymer, but the peak difference remains the same around 0.22 V (**Figure 73**).

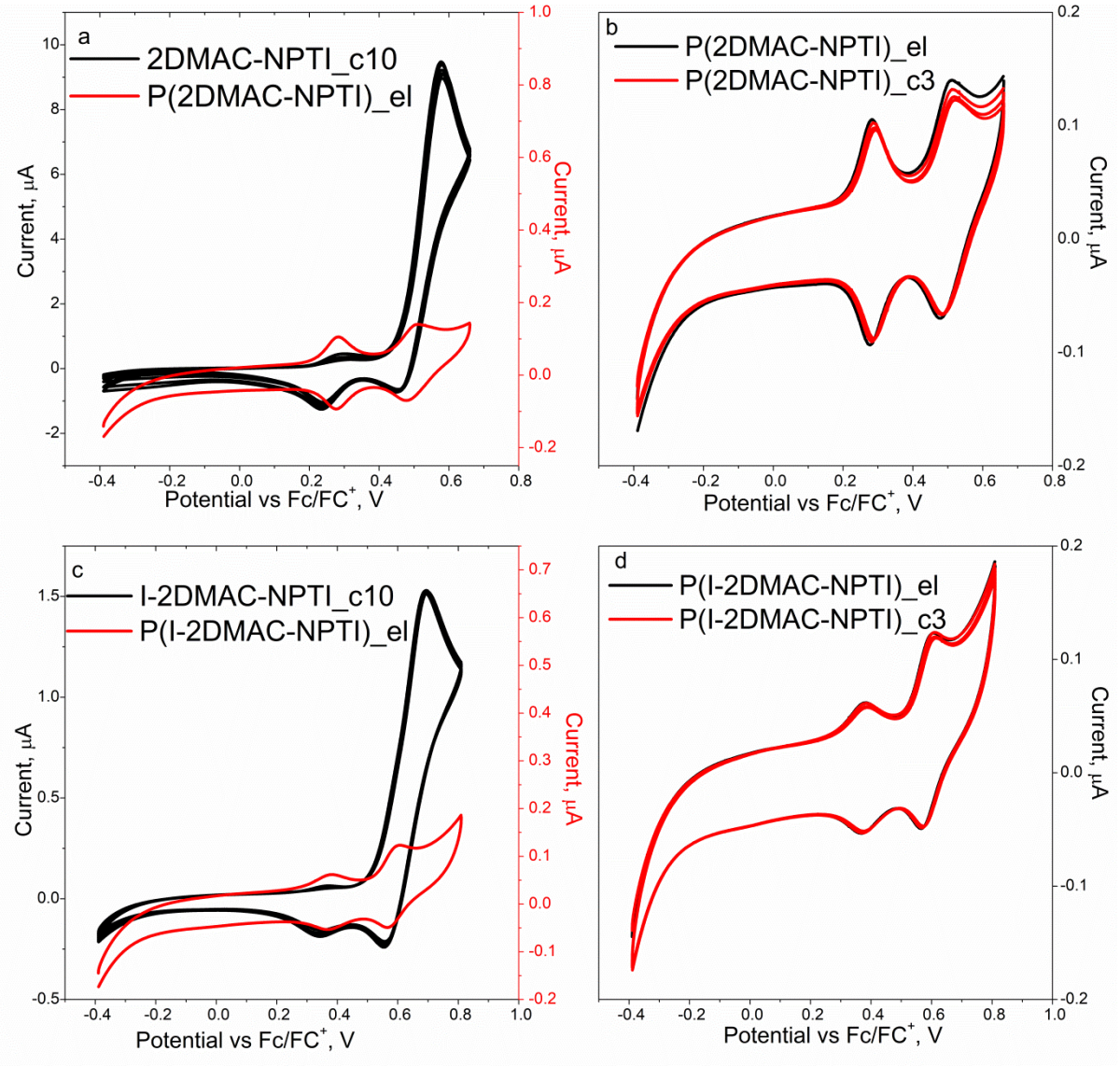

Figure 73. CV curves of polymers based on DMAC and NPTI a) polymerization CV curve of 2DMAC-NPTI and polymer on the surface of electrode b) CV curve of polymer based on 2DMAC-NPTI first scan and subsequent 3 scans. c) polymerization CV curve of I-2DAMC-NPTI and polymer on the surface of electrode b) CV curve of polymer based on I-2DMAC-NPTI first scan and subsequent 3 scans.

Comparing the height of the peaks, we can say that in the case of symmetric substitution, the ratio is 1:1, and in the case of non-symmetric substitution 1:2 (**Figure 74**).

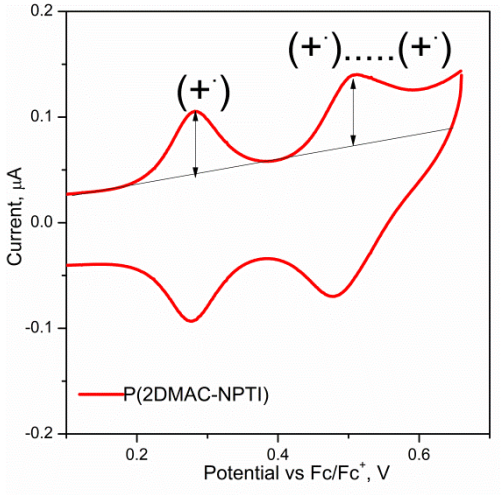

Figure 74. CV curve of polymer 2DMAC-NPTI on the electrode surface.

In this case, we can assume that the second oxidation peak corresponds to a complex of two cation radicals. this shape of the oxidation peak corresponds to the product with isolative red-ox centers. In case unsymmetrical substitution onset of oxidation (0.29 V) was shifted to higher potentials, but differences between 1st and 2nd oxidations peaks are the same 0.23 V.

For DMAC-DA and 2DMAC-DA compounds as in the previous case, we have two or three oxidation peaks, the last of which has the same potential as the monomer oxidation potential (**Figure 75**). The product remaining on the electrode of the DMAC-DA polymerization, as in the case of carbazole substituted NPTI, is not very stable, especially comparing the first cycle and the following. The conductivity is sharply reduced. For acceptor DA substituted by two DMAC groups, the polymerization shows two peaks at 0.22V and 0.33 V with a ratio of 1:1. The peak at 0.65 V most likely corresponds to the oxidized monomer. Onsets of the oxidation potential of polymers are lower than in the case of polymers containing NPTI acceptor groups.

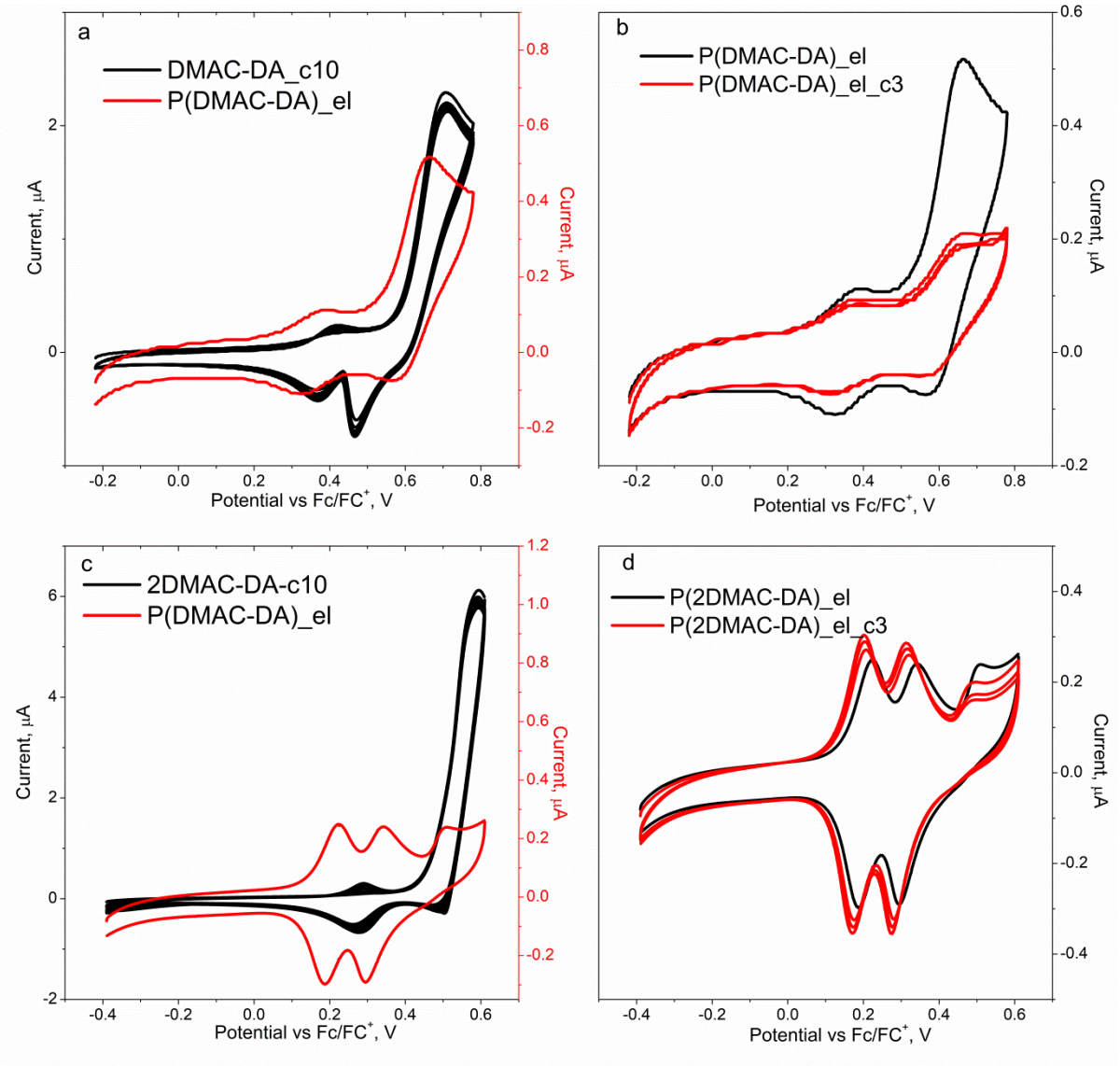

Figure 75. CV curves of polymers based on DMAC and DA acceptor unit a) polymerization CV curve of DMAC-DA and polymer on the surface of electrode b) CV curve of polymer based on DMAC-DA first scan and subsequent 3 scans. c) polymerization CV curve of 2DMAC-DA and polymer on the surface of electrode b) CV curve of polymer based on 2DMAC-DA first scan and subsequent 3 scans.

It can be assumed that during the polymerization monomer is being occluded in the polymer structure. This explains the presence of two peaks during the oxidation process: one from the polymer and the other from the monomer. For naphtylimide based derivatives, we have two types of substitution, which in turn will form a cross-linked structure. Comparing polymers containing the DMAC donor group and their behavior in the electric field was mentioned that NPTI is the strongest acceptor between other acceptors.

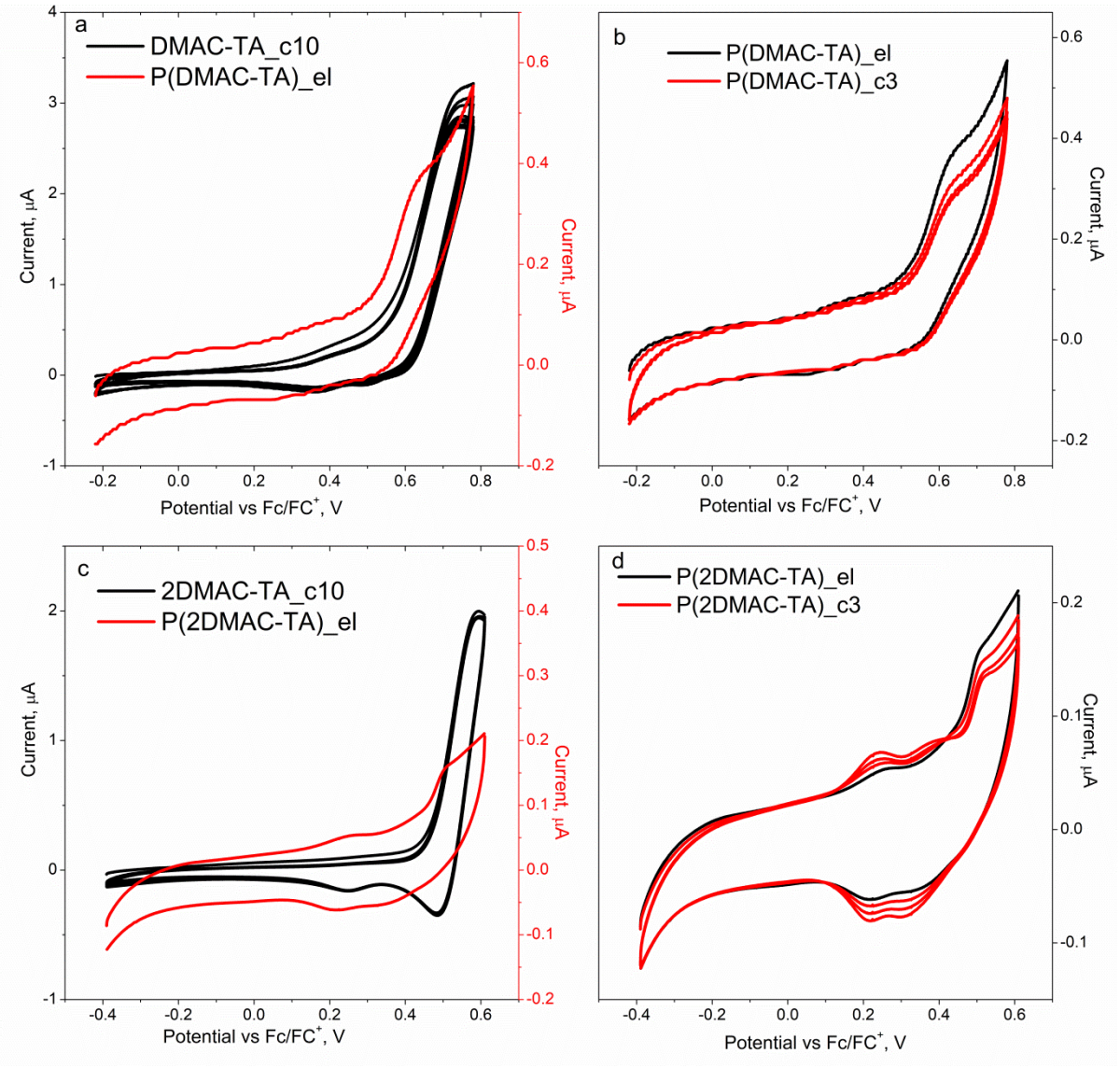

Figure 76. CV curves of polymers based on DMAC and TA acceptor unit a) polymerization CV curve of DMAC-TA and polymer on the surface of electrode b) CV curve of polymer based on DMAC-TA first scan and subsequent 3 scans. c) polymerization CV curve of 2DMAC-TA and polymer on the surface of electrode b) CV curve of polymer based on 2DMAC-TA first scan and subsequent 3 scans.

For compounds, it is based on a TA acceptor and substituted by one or two donor groups. As in the previous case, the polymers formed on the surface of the electrode are also not stable but have a lower conductivity (**Figure 76**). Concerning the polymer 2DMAC-TA, as the number of polymerization cycles increases, the value of the current increases with decreasing potentials (up to 0.4V), and at higher conversions, increases. This may be due to the decrease in the number of the monomer (peak at 0.5V) corresponds to the oxidation of the monomer.

Table 16. HOMO level of formatted polymers.

	E_{onset}, V	HOMO, eV
Poly-2DMAC-NPTI	0.21	-5.31
Poly-2IDMAC-NPTI	0.29	-5.39
Poly-DMAC-DA	0.28	-5.38
Poly-2DMAC-DA	0.13	-5.23
Poly-DMAC-TA	0.50	-5.60
Poly-2DMAC-TA	0.15	-5.25

Comparing the energy levels, the lowest energy level (-5.6 eV) was observed for polymer-based on TA with one donor group of DMAC and the highest (-5.23 eV) – for polymer-based on DA with two donor groups of DMAC (**Table 16**). In general, the energy value for the polymer with the donor group is significantly lower than for polymers with CBZ.

For polymers, which formed by polymerization of CBZ, was used Pt mesh electrode as the working electrode due to the fact of the high potential of the doping process.

The CBZ based polymers deposited on the platinum net upon oxidation show very small changes in absorption, which are only noticeable when using the differential analysis method. Like it was observable in the monomer analysis, the lack of UV-Vis-NIR change suggests that this type of compound has a very low absorption coefficient. The other electrochemical analysis proof that both monomers and polymers are stable (excluding the electropolymerization process) and the lack of electrochromic response is due to the electronic band properties. All other polymers have an increase in absorption at 410 nm (**Figure 76**). The polymer with the NPTI acceptor group and DA group has a joint absorption increase at 900 nm, which may correspond exactly to the oxidized form of the polymer. The decrease in absorption is difficult to see at lower wavelengths (as was the case for the monomer) due to the considerable noise from the platinum grid.

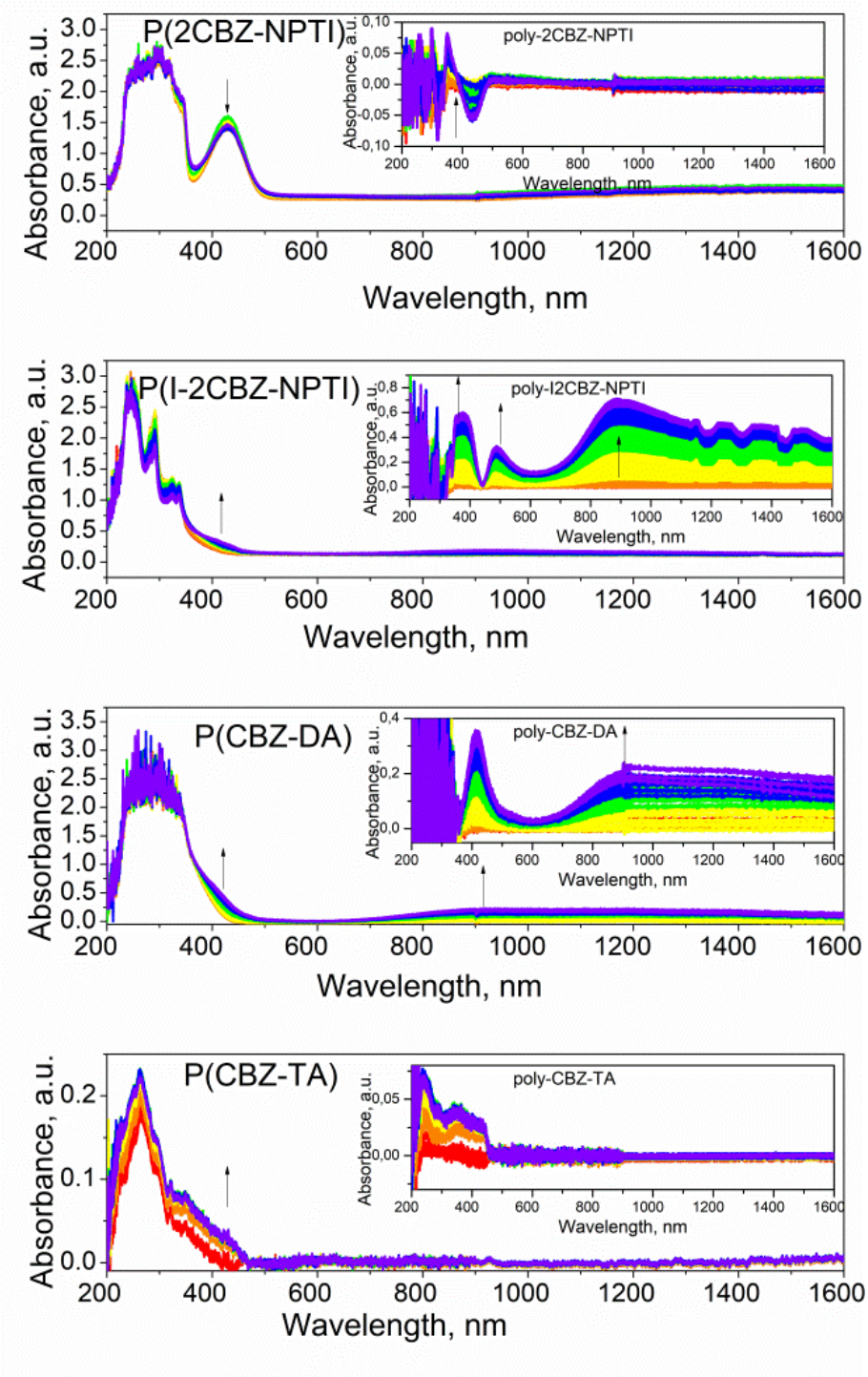

Figure 77. “in-situ” oxidation process spectra of polymers based on CBZ donor group.

For polymers with the composition of 2DMAC, we observe a much more significant response in comparison to CBZ derivatives. For polymers with two donor groups, a decrease in absorption at 300 nm is observed, as well as a characteristic increase at 450 nm, 770 nm,

and 1240 nm, which, as in the previous case, may be characterized by an oxidized polymer (**Table 17**).

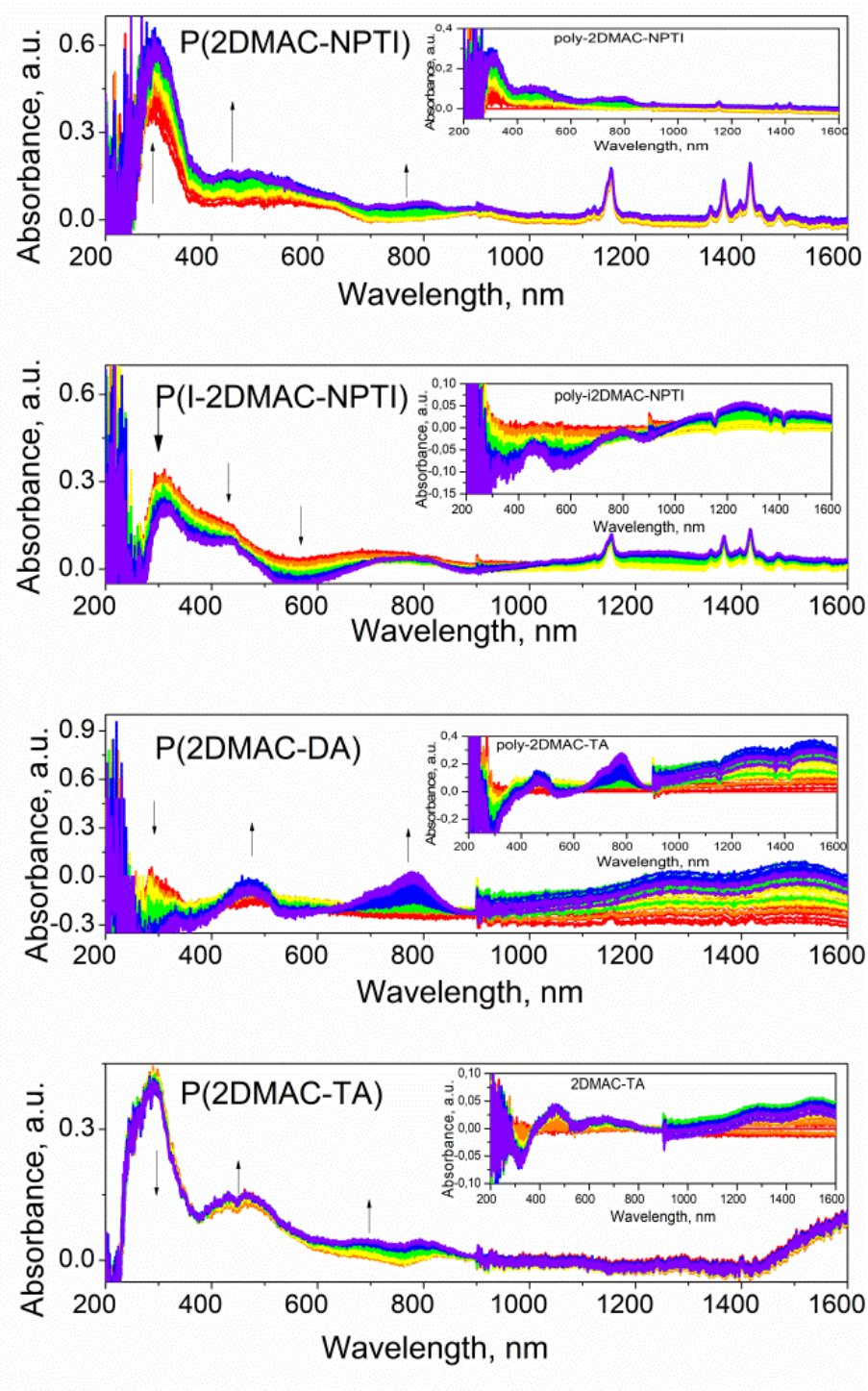

Figure 78. "In-situ" oxidation process spectra of polymers based on DMAC donor group.

The only example that has the opposite course of the reaction is I-2DMAC-NPTI, where it has a total decrease in absorption in the visible range, and also an increase in absorption in

the infrared range. This indicates that under the oxidation itself, most of the polymerization product departs from the electrode and goes into the bulk part, which means that it does not oxidize, and the part remaining on the electrode surface, with oxidation, has a much smaller absorption intensity.

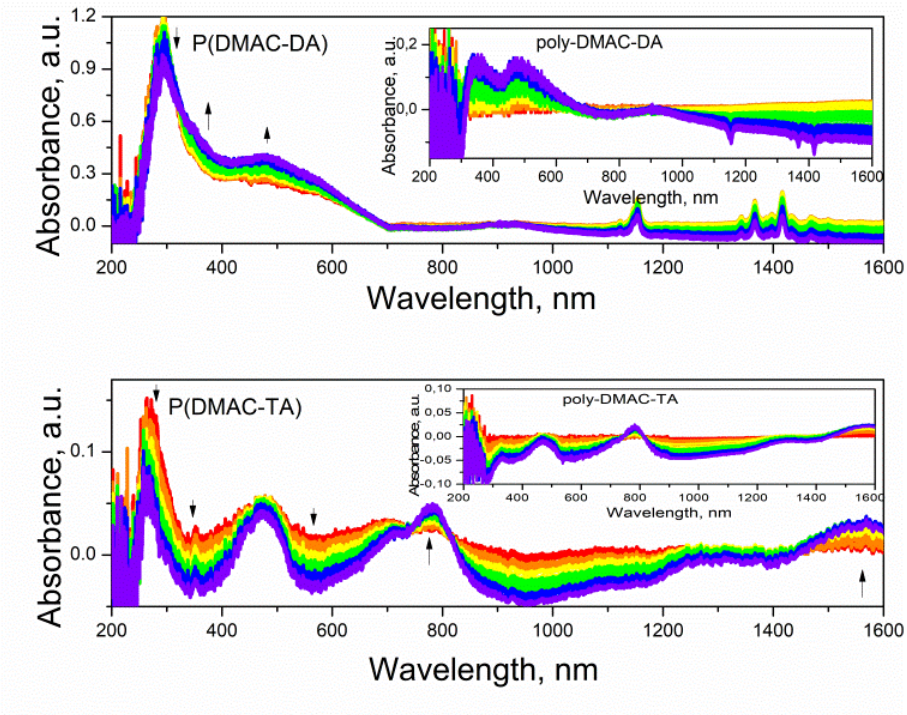

Figure 79. "In-situ" oxidation process spectra of polymers based one DMAC group

For polymerization products with one group of DMAC, the same decrease in absorption intensity at 300 nm is observed (**Figure 79**). There is virtually no change in absorption at 1240 nm, as in the previous case, which may indicate a different product structure depending on the number of donor groups. Such behavior proof that both of the derivatives with one and two donor groups present similar response and results.

Table 17. Wavelengths, which changed during the experiment.

	From 0V to E_{ox}	
	λ↓, nm	**λ↑, nm**
P(2CBZ-NPTI)		410; 430
P(I-2CBZ-NPTI)		410; 510; 900
P(2DMAC-NPTI)		300; 450; 770
P(I-2DMAC-NPTI)	300; 530; 880	1240
P(CBZ-DA)		410; 900
P(DMAC-DA)	300	350; 450
P(2DMAC-DA)	300	450; 770; 1240
P(CBZ-TA)		410; 430
P(DMAC-TA)	300; 350; 530	770
P(2DMAC-TA)	300	450; 770; 1240

The polymer with TA-based acceptor possesses a very poor electrochemical response and from the CV it was concluded that the layers formed are very thin and unstable which in the end affect the spectroelectrochemical results. So, even that we observe the oxidation process, the EPR or UV-Vis-NIR signals are barely visible.

As for the ESR analysis, It was quite hard to register any signal from P(2CBZ-NPTI), and it couldn't be compared with other derivatives. The same situation is for compound P(CBZ-DA) and P(DMAC-TA) (**Figure 80**).

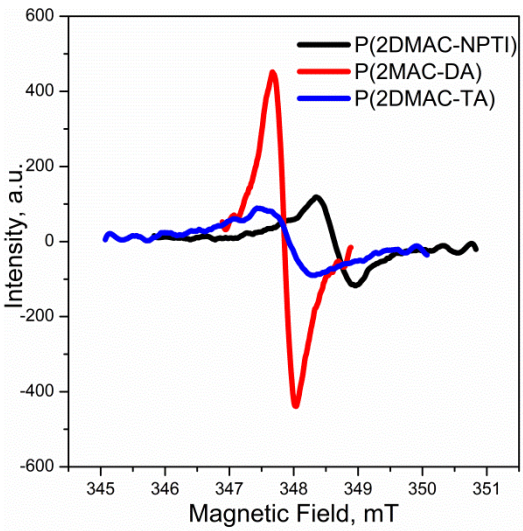

Figure 80. ESR spectra of formed polymers based and DMAC group.

Signals from the rest of the polymers characterized intensity between 50 to 400 (in case P(2DMAC-DA). The average value of the *g*-factor is 2.0033 with small differences in case

P(2DMAC-DA) and (2DMAC-TA) it is 2.0031 and the highest value was calculated for P(CBZ-TA) 2.0036 (**Table 18**).

Table 18. *g*-factor values of polymers based on CBZ and DMAC group.

	***g*-factor**
P(2CBZ-NPTI)	-
P(I-2CBZ-NPTI)	2.0032
P(2DMAC-NPTI)	2.0034
P(I-2DMAC-NPTI)	2.0035
P(CBZ-DA)	-
P(DMAC-DA)	2.0034
P(2DMAC-DA)	2.0031
P(CBZ-TA)	2.0036
P(DMAC-TA)	-
P(2DMAC-TA)	2.0031

Polymers, which have a CBZ as a donor group have wider signals, without any hyperfine structure which suggests a more conjugated structure. Polymer-based on 2 DMAC are characterized singlet signal with high intensity without hyperfine structure, except poly-2IDMAC-NPTI where the radical is localized. This signal is wide, with small splitting. Comparing P(I-2DMAC-NPTI) and P(DMAC-DA), it is to explain the more visible splitting of the signal, but this splitting is too small to make any simulation.

6 Conclusions

The thesis covers a wide range of analyses which gave very interesting results on the redox behavior of a set of organic electroactive materials. A combination of spectroscopic and electrochemical techniques revealed transformations of organic conjugated structures and how the change is affected by the donor or acceptor groups.

DFT simulation results showed moderate consistency with experimental data. The simulation data appeared to be the most compatible in the case of compounds with PTZ donor groups. However, the biggest difference took place in the case of the CBZ donor group. In the case of acceptor groups NPTI and TA there are differences in calculated and experimental LUMO level about 1 eV, but in the case, DA group these differences are smaller, which can be caused that $LUMO^{EXP}$ level was determined using absorbance spectra, instead of CV. Such effect is probably connected with strong charge transfer properties, even that the common approach for conjugated derivatives was conducted, the donor-acceptor interaction affects the HOMO-LUMO properties.

The IP (Ionization potential) and EA (Electron affinity) energy levels for compounds based on NPTI and TA acceptor unit were determined using CV and then compare with theoretical values. The compounds based on DA (pyradizine) acceptor didn't allow EA estimation by CV due to the high LUMO energies. Comparing compound with the same donor group, Compounds with CBZ substituents have a HOMO (similar to IP) level from -5.96 eV to -5.61 eV; for PXZ substituents from -5.41 eV to -5.31 eV; for PTZ substituents from -5.42 eV to -5.23 eV, and for DMAC substituents from -5.63 eV to -5.48eV. For acceptor units, NPTI based compounds have LUMO (similar to EA) level from -3.61 eV to -3.45eV, for TA series from -3.96 eV to -3.86 eV. In the case of two donor groups, the oxidation potential of each of them is the same (or has a difference is under the registration threshold).

All registered reduction processes and oxidation of PTZ and PXZ substituents are reversible presenting redox couple, but compounds with CBZ and DMAC substituents have a non-reversible oxidation process where the conjugated polymers are formed as the product. Further investigation of polymerization compounds based on CBZ and DMAC donor groups shown, that products of polymerization were formed on the surface of the working electrode. The NPTI based monomers present the best electropolymerization properties and both CBZ and DMAC donor-based polymers were stable.

As for the UV-Vis-NIR spectroelectrochemical behavior and electrochromic properties, absorbance spectra were registered from neutral molecules, radical cation, and diradical dication, and product of the interaction between molecules. Despite the acceptor, the changes in absorption bands are similar for the same donor groups. CBZ based derivatives present change in absorption bands with a peak at 430 nm for radical cation and above 570 nm for diradical dication. The PTZ and PXZ group based compounds exhibit only changes of absorption bands with maxima at 520 nm (PTZ) and 550 nm (PXZ) for the radical cation formation. Similar to CBZ derivative, in DMAC derivatives we observe the rise of 460 nm peak for the radical cation formation and above 680 nm band for diradical formation. Based on spectroelectrochemical analysis comparison of monomers and polymers can be concluded that the additional higher wavelength bands for DMAC and CBZ derivatives are not directly connected with polymers obtained on the electrode but only of diradical dication formation on monomer. On the other hand, is proof that to form a polymer on the electrode, both donors must be oxidation (diradical dication formation, one radical cation per donor) to allow for electrochemical polymerization.

The EPR analysis reveals the formation of radical cation, radical anions, and diradical dication in the investigated compounds. The most difficult to register the paramagnetic signal was for CBZ containing compounds this was probably affected by direct polymer formation and dissipation of radical over the conjugated chain. For the reduction process, the *g*-factor value for the NPTI based compounds presents the radical anion at 2.0034 to 2.0038 in a form of semiquinone radicals on the acceptor core. Most of the compounds have the hyperfine structure of reduction process and simulation revealed that charge is mainly localized at *N* atom of acceptor and in some cases is splitting with one or two pairs of equivalent H influence by increased of conjugation.

The EPR signals of the oxidation process of the derivatives with symmetrical substitution of NPTI have stronger structured signals than asymmetrical ones. When the acceptor influence was compared with the same donors present that the *g*-factor values are quite close, and hyperfine structures were simulated using similar schemes which suggest very small influence. A significant difference was observed for only DMAC donor-based derivatives where the *g*-factor increases from 2.003 (in case NPTI acceptor unit) to 2.0058 (in case DA acceptor unit) which suggests the change from delocalized free electron to a more localized one. In one case, where the DMAC was connected to the DA acceptor, the asymmetrical EPR signal of mono and bi-substituted derivatives was observed. The follow-up deconvolution of the signals was needed and two g-factor were estimated. One of these

structures is was a radical cation from the monomer and the second, radical cation of the polymer.

The simulation of the rest of the derivatives revealed that the charge is localized at the *N* atom of the donor group with splitting with one pair of equivalent *H* (in case of PTZ substituents) or with two pairs of equivalent H (in case of PXZ substituents).

7 Bibliography

1. Tsujimura, T. *OLED Disp. Fundam. Appl.*, **2017** 7–59.
2. Morokuma, K., and Iwata, S. *Chem. Phys. Lett.*, **1972**, 16 (1), 192–197.
3. Brink, D.M., and Boeker, E. *Nucl. Physics, Sect. A*, **1967**, 91 (1), 1–26.
4. Medvedev, M.G., Bushmarinov, I.S., Sun, J., Perdew, J.P., and Lyssenko, K.A. (2017) *Science* ., **2017**, 356 (6337), 496c.
5. Oliveira, L.N., Gross, E.K.U., and Kohn, W. *Int. J. Quantum Chem.*, **1990**, 38 (24 S), 707–716.
6. Jödicke, C.J., and Lüthi, H.P. *J. Am. Chem. Soc.*, **2003**, 125 (1), 252–264.
7. Fabian, J. *Dye. Pigment.*, **2010**, 84 (1), 36–53.
8. Stephens, P.J., Devlin, F.J., Chabalowski, C.F., and Frisch, M.J. (1994) *J. Phys. Chem.*, **1994**, 98 (45), 11623–11627.
9. Pereira, F., Xiao, K., Latino, D.A.R.S., Wu, C., Zhang, Q., and Aires-De-Sousa, J. *J. Chem. Inf. Model.*, **2017**, 57 (1), 11–21.
10. El-Azhary, A.A., and Suter, H.U. *J. Phys. Chem.*, **1996**, 100 (37), 15056–15063.
11. Bredas, J.L. *Mater. Horizons*, **2014**, 1 (1), 17–19.
12. Bouvet, M. *Adv. Org. and In. Opt. Mater.* **2003**, 5122, 144–155.
13. Zhou, J., Xie, S., Amond, E.F., and Becker, M.L. *Macromolecules*, **2013**, 46 (9), 3391–3394.
14. Cardona, C.M., Li, W., Kaifer, A.E., Stockdale, D., and Bazan, G.C. *Adv. Mater.*, **2011**, 23 (20), 2367–2371.
15. Bard, A.J. *Pure Appl. Chem.*, **1971**, 25 (2), 379–394.
16. Hendel, S.J., and Young, E.R. *J. Chem. Educ.*, **2016**, 93 (11), 1951–1956.
17. De Paoli, M.A., Gazotti, W.A. *J. Braz. Chem. Soc.*, **2002**, 13 (4), 410–424.
18. Barón-Jaimez, J., Joya, M.R., Barba-Ortega, J. *J. Phys. Conf. Ser.*, **2013**, 466 (1).
19. Scholz, F. Electroanalytical Methods Guide to Experiments and Applications 2nd, revised and extended edition. *Springer*. **2009**.
20. Aristov, N., Habekost, A. *World J. Chem. Educ.* **2015**, 3 (5), 115–119.
21. Gritzner, G., and Kůta, J. *Electrochim. Acta*, **1984**, 29 (6), 869–873.
22. SATO, N. *Tetsu-to-Hagane*, **1990**, 76 (9), 1423–1436.
23. Vannikov, A. V., Saidov, A.C. *Mol. Cryst. Liq. Cryst.*, **1993**, 228 (1), 87–92.

24. Jangid, N.K., Chauhan, N.P.S., Ameta, R., Meghwal, K. *Res. J. of Pharm. , Bio. and Chem. Sc*., **2014**, 5(3), 383-412

25. Kornyushin, Y., arXiv:cond-mat/0702259, **2007**, 2–5.

26. Pron, A., Gawrys, P., Zagorska, M., Djurado, D., and Demadrille, R. *Chem. Soc. Rev.*, **2010**, 39 (7), 2577–2632.

27. Brédas, J.L., Scott, J.C., Yakushi, K., Street, G.B. *Phys. Rev. B*, **1984**, 30 (2), 1023–1025.

28. Seeber, R., Terzi, F., Zanardi, C. Functional Materials in Amperometric Sensing. *Springer* .**2014**.

29. Neugebauer, H. *J. Electroanal. Chem.*, **2004**, 563 (1), 153–159.

30. Furukawa, Y. *J. Phys. Chem.*, **1996**, 100 (39), 15644–15653.

31. Ohshita, J., Kai, H., Takata, A., Iida, T., Kunai, A., Ohta, N., Komaguchi, K., Shiotani, M., Adachi, A., Sakamaki, K., and Okita, K. *Organometallics*, **2001**, 20 (23), 4800–4805.

32. Rathnayake, H.P., Cirpan, A., Delen, Z., Lahti, P.M., and Karasz, F.E. *Adv. Funct. Mater.*, **2007**, 17 (1), 115–122.

33. Patil, A.O., Heeger, A.J., and Wudl, F. *Chem. Rev.*, **1988**, 88 (1), 183–200.

34. Saleh, M., Baumgarten, P.M., and Müllen, P.K. *Macromol. Rapid Commun.* **2004**, 35(2), 264.

35. Zade, S.S., Bendikov, M. *Org. Lett.*, **2006**, 8 (23), 5243–5246.

36. Leclerc, M. *Adv. Mater.*, **1999**, 11 (18), 1491–1498.

37. Data, P., Lapkowski, M., Motyka, R., Suwinski, J. *Electrochim. Acta*, **2012**, 83, 271–282.

38. Jarosz, T., Lapkowski, M., and Ledwon, P. *Macromol. Rapid Commun.*, **2014**, 35 (11), 1006–1032.

39. Wu, J.H., Guan, Z., Xu, T.Z., Xu, Q.H., Xu, G.Q. *Langmuir*, **2011**, 27 (10), 6374–6380.

40. Schouwink, P., Schäfer, A.H., Seidel, C., Fuchs, H. *Thin Solid Films*, **2000**, 372 (1), 163–168.

41. Tang, C.W., and Vanslyke, S.A. *Appl. Phys. Lett.*, **1987**, 51 (12), 913–915.

42. Park, Y., Kim, B., Lee, C., Hyun, A., et al. *J. Phys. Chem. C*, **2011**, 115 (11), 4843–4850.

43. Tsuji, H., Yokoi, Y., Mitsui, C., Ilies, L., Sato, Y., Nakamura, E. *Chem. - An Asian J.*, **2009**, 4 (5), 655–657.

44. Jiang, Z., Ye, T., Yang, C., Yang, D., Zhu, M., Zhong, C., Qin, J., and Ma, D. *Chem. Mater.*, **2011**, 23 (3), 771–777.

45. Pan, J.H., Chiu, H.L., Chen, L., and Wang, B.C. *Comput. Mater. Sci.*, **2006**, 38 (1), 105–112.

46. Shin, H., Lee, J.H., Moon, C.K., Huh, J.S., Sim, B., and Kim, J.J. *Adv. Mater.*, **2016**, 28 (24), 4920–4925.

47. Zhou, X., Blochwitz, J., Pfeiffer, M., Nollau, A., Fritz, T., Leo, K. *Adv. Funtional Mater.*, **2001**, 11 (4), 310–314.

48. Jinnai, S., Ie, Y., Karakawa, M., Aernouts, T., Nakajima, Y., Mori, S., Aso, Y. *Chem. Mater.*, **2016**, 28 (6), 1705–1713.

49. Sasabe, H., Kido, J. *Chem. Mater.*, **2011**, 23 (3), 621–630.

50. Im, Y., Kim, M., Cho, Y.J., Seo, J.A., Yook, K.S., and Lee, J.Y. *Chem. Mater.*, **2017**, 29 (5), 1946–1963.

51. Chai, W., Jin, R. *J. Mol. Struct.*, **2016**, 1103, 177–182.

52. Kulhánek, J., Bureš, F., Pytela, O., Mikysek, T., Ludvík, J. *Chem. - An Asian J.*, **2011**, 6 (6), 1604–1612.

53. Lee, J.Y., Kim, K.S., and Mhin, B.J. *J. Chem. Phys.*, **2001**, 115 (20), 9484–9489.

54. Bureš, F., Bernd Schweizer, W., May, J.C., Boudon, C., Gisselbrecht, J.P., et al. *Chem. - A Eur. J.*, **2007**, 13 (19), 5378–5387.

55. Spitler, E.L., Shirtcliff, L.D., Haley, M.M. *J. Org. Chem.*, **2007**, 72 (1), 86–96.

56. Li, Y., Li, X.L., Chen, D., Cai, X., et al. *Adv. Funct. Mater.*, **2016**, 26 (38), 6904–6912.

57. Gudeika, D., Grazulevicius, J.V., Volyniuk, D., Butkute, R., et al. *Dye. Pigment.*, **2015,** 114 (C), 239–252.

58. Triboni, E.R., Fernandes, M.R., Garcia, J.R., Carreira, M.C., et al. *J. Taibah Univ. Sci.*, **2015**, 9 (4), 579–585.

59. Gudeika, D., Grazulevicius, J. V., Volyniuk, D., Juska, G., et al. *J. Phys. Chem. C*, **2015**, 119 (51), 28335–28346.

60. Ledwon, P., Brzeczek, A., Pluczyk, S., Jarosz, T., et al. *Electrochim. Acta*, **2014**, 128, 420–429.

61. Ozdemir, S., Varlikli, C., Oner, I., Ocakoglu, K., Icli, S. *Dye. Pigment.*, **2010**, 86 (3), 206–216.

62. Schab-Balcerzak, E., Siwy, M., Filapek, M., Kula, S., et al. *J. Lumin.*, **2015**, 166, 22–39.

63. Pluczyk, S., Laba, K., Schab-Balcerzak, E., Bijak, K., Kotowicz, S., Lapkowski, M. *J. Electroanal. Chem.*, **2017**, 795, 90–96.

64. Bai, H., Chen, Q., Li, C., Lu, C., Shi, G. *Polymer (Guildf).*, **2007**, 48 (14), 4015–4020.

65. Beaujuge, P.M., Reynolds, J.R. *Chem. Rev.*, **2010**, 110 (1), 268–320.

66. Moral, M., García, G., Peñas, A., Garzón, A., et al. *Chem. Phys.*, **2012**, 408, 17–27.

67. Quinton, C., Alain-Rizzo, V., Dumas-Verdes, C., Miomandre, F., Audebert, P. *Electrochim. Acta*, **2013**, 110, 693-701.

68. Dumas-Verdes, C., Miomandre, F., Lépicier, E., Galangau, O., et al. *European J. Org. Chem.*, **2010**, (13), 2525–2535.

69. Pluczyk, S., Zassowski, P., Quinton, C., Audebert, P.,et al. *J. Phys. Chem. C*, **2016**, 120 (8), 4382–4391.

70. Li, S.W., Yu, C.H., Ko, C.L., Chatterjee, T., et al. *ACS Appl. Mater. Interfaces*, **2018**, 10 (15), 12930–12936.

71. Bezvikonnyi, O., Gudeika, D., Volyniuk, D., Mimaite, V., et al. *J. Lumin.*, **2019**, 206, 250–259.

72. Hudson, Z.M., Wang, Z., Helander, M.G., Lu, Z.H., Wang, S. *Adv. Mater.*, **2012**, 24, (21), 2922–2928.

73. Kurowska, A., Brzeczek-Szafran, A., Zassowski, P., Lapkowski, M., et al. *Electrochim. Acta*, **2018**, 271, 685–698.

74. Zassowski, P., Ledwon, P., Kurowska, A., Herman, A.P., et al. *Synth. Met.*, **2017**, 223, 1–11.

75. Data, P., Pander, P., Lapkowski, M., Swist, A., et al. *Electrochim. Acta*, **2014**, 128, 430–438.

76. Ramírez, C.L., Mangione, M.I., Bertolotti, S.G., Arbeloa, E.M., Parise, A.R. *J. Photochem. Photobiol. A Chem.*, **2018**, 365, 199–207.

77. Pander, P., Swist, A., Zassowski, P., Soloducho, J., et al. *Electrochim. Acta*, **2017**, 257, 192–202.

78. Data, P., Zassowski, P., Lapkowski, M., Grazulevicius, J. V., Kukhta, N.A., Reghu, R.R. *Electrochim. Acta*, **2016**, 192, 283–295.

79. Aydin, A., Kaya, I. *J. Electroanal. Chem.*, **2013**, 691, 1–12.

80. Kaleeswaran, D., Vishnoi, P., Kumar, S., Chithiravel, S., et al. *ChemistrySelect*, **2016**, 1 (21), 6649–6657.

81. Karon, K., Lapkowski, M., Dabuliene, A., Tomkeviciene, A., et al. *Electrochim. Acta*, **2015**, 154, 119–127.

82. Qu, Y., Pander, P., Bucinskas, A., Vasylieva, M., et al. *Chem. - A Eur. J.*, **2019**, 25 (10), 2457–2462.

83. Zhao, Y., Wang, Y., Li, X., Li, Y., Wang, Y., Yu, T. *Chem. Pap.*, **2019**, 74 (1), 305–310.

84. Yu, L., Wu, Z., Xie, G., Zeng, W., Ma, D., Yang, C. *Chem. Sci.*, **2018**, 9 (5), 1385–1391.

85. Yu, T., Li, X., Zhao, Y., Yang, Q., Li, Y., Zhang, H., Li, Z. *J. Photochem. Photobiol. A Chem.*, **2018**, 360, 58–63.

86. Park, G.S., Back, J., Choi, E.M., Lee, E., Son, K. *Eur. Polym. J.*, **2019**, 117, 347–352.

87. Kulys, J., Vidziunaite, R., Janciene, R., Palaima, A. *Electroanalysis*, **2006**, 18 (18), 1771–1777.

88. Olech, K., Sołoducho, J., Laba, K., Data, P., Lapkowski, M., Roszak, S. *Electrochim. Acta*, **2014**, 141, 349–356.

89. Lin, T.S., Retsky, J. *J. Phys. Chem.*, **1986**, 90 (12), 2687–2689.

90. Haumesser, J., Pereira, A.M.V.M., Gisselbrecht, J.P., Merahi, K., et al. *Org. Lett.*, **2013**, 15 (24), 6282–6285.

91. Poddar, M., Gautam, P., Rout, Y., and Misra, R. *Dye. Pigment.*, **2017**, 146, 368–373.

92. Chen, D.G., Lin, T.C., Chen, Y.A., Chen, Y.H., et al. *J. Phys. Chem. C*, **2018**, 122 (23), 12215–12221.

93. Karimata, A., Suzuki, S., Kozaki, M., Kimoto, K., et al. *J. Phys. Chem. A*, **2014**, 118 (47), 11262–11271.

94. Wan, Z., Jia, C., Duan, Y., Zhang, J., Lin, Y., and Shi, Y. *Dye. Pigment.*, **2012**, 94 (1), 150–155.

95. Sakamaki, D., Kumano, D., Yashima, E., Seki, S. *Chem. Commun.*, **2015**, 51 (97), 17237–17240.

96. Zhou, Z., Franz, A.W., Bay, S., Sarkar, B., et al. *Chem. - An Asian J.*, **2010**, 5 (9), 2001–2015.

97. Ganesan, P., Ranganathan, R., Chi, Y., Liu, X.K., et al. *Chem. - A Eur. J.*, **2017**, 23 (12), 2858–2866.

98. Seo, J.A., Jeon, S.K., Lee, J.Y. *Org. Electron.*, **2016**, 34, 33–37.

99. Yang, X., Walpita, J., Zhou, D., Luk, H.L., et al. *J. Phys. Chem. B*, **2013**, 117 (49), 15290–15296.

100. Zhou, D., Khatmullin, R., Walpita, J., Miller, N.A., et al. *J. Am. Chem. Soc.*, **2012**, 134 (28), 11301–11303.

101. Grivet, J.P. *Chem. Phys. Lett.*, **1971**, 11 (3), 267–270.

102. Rybakiewicz, R., Gawrys, P., Tsikritzis, D., Emmanouil, K., et al. *Electrochim. Acta*, **2013**, 96, 13–17.

103. Benck, J.D., Pinaud, B.A., Gorlin, Y., Jaramillo, T.F. *PLoS One*, **2014**, 9 (10), 1-10.

104. Raghavachari, K. *Theor. Chem. Acc.*, **2000**, 103 (3–4), 361–363.

105. Mennucci, B., Cancès, E., Tomasi, J. *J. Phys. Chem. B*, **1997**, 101 (49), 10506–10517.

106. Neese, F. *Wiley Interdiscip. Rev. Comput. Mol. Sci.*, **2012**, 2 (1), 73–78.

107. Martín, E., Weigand, R. *Chem. Phys. Lett.*, **1998**, 288, 52–58.

108. Naga, N., Tano, N., Tomoda, H. *J. Polym. Sci. Part A Polym. Chem.*, **2012**, 50 (20), 4223–4229.

109. Nowakowska-Oleksy, A., Sołoducho, J., Cabaj, J. *J. Fluoresc.*, **2011**, 21 (1), 169–178.

110. Birel, Ö. *EJOVOC Electron. J. Vocat. Coll.*, **2015**, 5 (1), 89-98.

111. Cheng, D., Xu, D., Wang, Y., Zhou, H., et al. *Dye. Pigment.*, **2020**, 173, 1-10.

8 Supplements

8.1 Supplement 1

This work was a part of the Oleh Vybornyi Ph.D. thesis. The whole thesis is available http://theses.gla.ac.uk/40944/

Experimental part

Caution: Please review all relevant material safety data sheets (MSDS) before use. Several of the chemicals used in the synthesis are highly toxic and carcinogenic. When working with silica gel a protective respiratory mask must be worn to prevent particle inhalation. Please observe all appropriate safety rules when performing a chemical reaction including the use of engineering controls (fume cupboard) and personal protective equipment (safety glasses, gloves, lab coat, full-length pants, closed-toe shoes).

All reagents and solvents were purchased commercially and were used without any further purification. ^{1}H and ^{13}C NMR spectra were recorded on a Bruker AVR 400 NMR spectrometer using $CDCl_3$ as the solvent. Proton NMR chemical shifts are reported as δ values in ppm relative to deuterated solvents: $CDCl_3$ (7.26). Data are presented as follows: chemical shift, multiplicity, and coupling constant(s) (*J*) are in Hz. Multiplets are reported over the range (in ppm) they appeared. Carbon NMR data were collected relative to the corresponding solvent signals $CDCl_3$ (77.16). Melting points were measured using a Stuart Scientific melting point apparatus. Matrix-assisted laser desorption ionization-time-of-flight (MALDI-TOF) mass spectrometry was run on a Shimadzu Axima-CFR spectrometer (mass range 1–150 000 Da).

General procedure for the preparation of naphthalimide D-A-D compounds

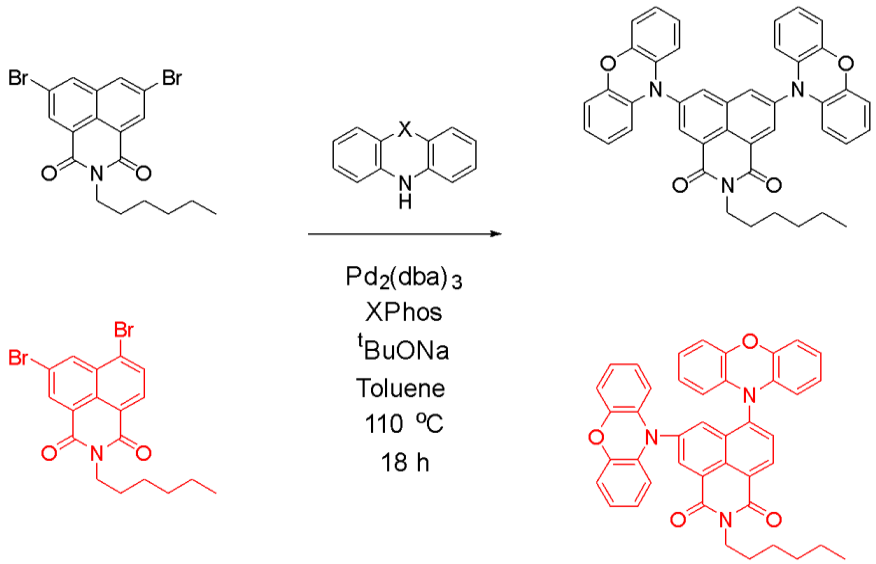

To a 100 ml two-neck round bottom flask equipped with a stir bar, a 1:1 mixture of brominated naphthalimide isomers (1 g, 2.7 mmol), a donor molecule (5.4 mmol), and 40 ml of anhydrous toluene were added. The reaction mixture was degassed by bubbling through nitrogen for 15 min under vigorous stirring. Then $Pd_2(dba)_3$ (160 mg, 0.17 mmol) and XPhos (166 mg, 0.35 mmol) were added and degassed for another 15 min. After this, sodium *tert*-butoxide (564 mg, 5.92 mmol) was added and the mixture degassed for an additional 10 min. The reaction mixture was heated to 110 °C under a nitrogen atmosphere and left overnight. The reaction mixture was then cooled down to room temperature and extracted with

dichloromethane. The organic phase was dried over anhydrous magnesium sulfate ($MgSO_4$), filtered, and concentrated under reduced pressure. The products were purified using column chromatography (Dichloromethane: Hexane = 1:2 volume ratio) to give two products. It's worth mentioning that the Rf of the compounds is different enough which allows us to separate them. Symmetrical 4,7-disubstituted products (shown in black) comes first from the column, whereas asymmetrical 4,6-isomer (shown in red) has lower polarity and therefore comes second.

Synthesis of 2DPA-NPTI (4,7-bis(diphenylamino)-2-hexyl-*1H*-benzo[*de*]isoquinoline-1,3(*2H*)-dione)

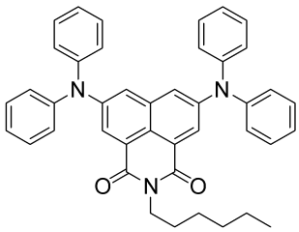

Compound 2DPA-NPTI was prepared following the general procedure using diphenylamine as a donor molecule. An orange solid was obtained after column chromatography (Dichloromethane: Hexane = 1:2 volume ratio) (44.4 mg, yield: 61%).

^{1}H nmR (400 MHz, $CDCl_3$, δ ppm): 8.21 (d, J = 2.1 Hz, 2H), 7.38 (d, J = 2.2 Hz, 2H), 7.34 – 7.27 (m, 8H), 7.16 – 7.09 (m, 12H), 4.13 – 4.06 (t, 2H), 1.74 – 1.63 (m, 2H), 1.45 – 1.26 (m, 6H), 0.90 (t, J = 6.8 Hz, 3H).

^{13}C nmR (100 MHz, $CDCl_3$, δ ppm): 163.51, 146.85, 146.45, 134.13, 129.20, 125.22, 124.54, 123.64, 123.06, 121.82, 119.84, 76.88 (s), 76.56 (s), 40.00, 31.01, 27.51, 26.28, 22.05, 13.57.

MS $[M+H]^+$ m/z: calcd. for $[C_{42}H_{37}N_3O_2]^+$ 615.29, found 615.21.

Melting point: 285 °C.

Synthesis of i-2DPA-NPTI (4,6-bis(diphenylamino)-2-hexyl-*1H*-benzo[*de*]isoquinoline-1,3(*2H*)-dione)

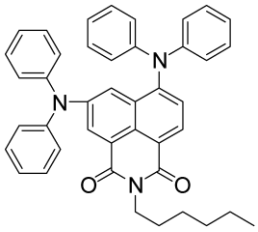

Compound i-2DPA-NPTI was prepared following the general procedure using diphenylamine as a donor molecule. An orange solid was obtained after column chromatography (Dichloromethane: Hexane = 1:2 volume ratio) (44.4 mg, yield: 61%).

^{1}H nmR (400 MHz, $CDCl_3$, δ ppm): 8.35 (s, 1H), 8.33 (d, J = 5.7 Hz, 1H), 7.77 (d, J = 2.4 Hz, 1H), 7.32 (d, J = 8.0 Hz, 1H), 7.23 – 7.15 (m, 8H), 7.05 (m, 4H), 6.98 – 6.94 (d, J = 8.0 Hz, 4H), 6.92 – 6.88 (d, J = 8.0 Hz, 4H), 4.19 – 4.14 (t, 2H), 1.76 – 1.72 (m, 2H), 1.50 – 1.28 (m, 6H), 0.92 (t, 3H).

^{13}C nmR (100 MHz, $CDCl_3$, δ ppm): 163.51, 163.36, 148.77, 147.75, 146.07, 145.98, 129.28, 128.92, 126.84, 125.84, 125.45, 124.45, 123.81, 123.61, 122.88, 122.82, 119.63, 118.41, 39.91, 31.08, 27.60, 26.32, 22.13, 13.62.

MS $[M+H]^+$ m/z: calcd. for $[C_{42}H_{37}N_3O_2]^+$ 615.29, found 615.26.

Melting point: 285 °C.

Synthesis of 2CBZ-NPTI (4,7-di(*9H*-carbazol-9-yl)-2-hexyl-*1H*-benzo[*de*]isoquinoline-1,3(*2H*)-dione)

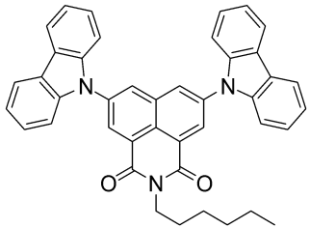

Compound 2CBZ-NPTI was prepared following the general procedure using *9H*-carbazole as a donor molecule. A yellow solid was obtained after column chromatography (Dichloromethane: Hexane = 1:2 volume ratio) (44.4 mg, yield: 61%).

^{1}H nmR (400 MHz, $CDCl_3$, δ ppm): 8.90 (d, J = 1.9 Hz, 2H), 8.45 (d, J = 1.9 Hz, 2H), 8.20 (d, J = 0.8 Hz, 2H), 8.19 (d, J = 0.8 Hz, 2H), 7.54 (s, 2H), 7.52 (s, 2H), 7.47 (ddd, J = 8.2, 7.1, 1.2 Hz, 4H), 7.37 (ddd, J = 8.2, 7.1, 1.2 Hz, 4H), 4.27 – 4.22 (t, 2H), 1.83 – 1.78 (m, 2H), 1.52 – 1.25 (m, 6H), 0.90 (t, 3H).

^{13}C nmR (100 MHz, $CDCl_3$, δ ppm): 163.37, 140.64, 138.08, 130.26, 130.01, 126.62, 125.74, 125.32, 124.13, 121.09, 120.82, 110.70, 109.50, 41.08, 31.69, 28.25, 26.96, 22.73, 14.21.

MS $[M+H]^+$ m/z: calcd. for $[C_{42}H_{33}N_3O_2]^+$ 611.26, found 611.31.

Melting point: 325 °C.

Synthesis of i-2CBZ-NPTI (4,6-di(*9H*-carbazol-9-yl)-2-hexyl-*1H*-benzo[*de*]isoquinoline-1,3(*2H*)-dione)

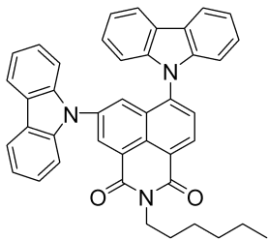

Compound i-2CBZ-NPTI was prepared following the general procedure using *9H*-carbazole as a donor molecule. An orange solid was obtained after column chromatography (Dichloromethane: Hexane = 1:2 volume ratio) (44.4 mg, yield: 61%).

^{1}H nmR (400 MHz, $CDCl_3$, δ ppm): 8.93 (d, J = 2.1 Hz, 1H), 8.86 (d, J = 7.7 Hz, 1H), 8.14 (d, J = 7.5 Hz, 2H), 8.06 – 8.00 (m, 3H), 7.79 (d, J = 2.1 Hz, 1H), 7.45 (ddd, J = 8.3, 7.3, 1.2 Hz, 2H), 7.37 – 7.32 (ddd, J = 8.3, 7.3, 1.2 Hz, 2H), 7.28 – 7.19 (m, 6H), 7.15 (d, J = 8.1 Hz, 2H), 4.28 (t, 2H), 1.85 – 1.80 (m, 2H), 1.57 – 1.23 (m, 6H), 0.91 (t, 3H).

^{13}C nmR (100 MHz, $CDCl_3$, δ ppm): 163.37, 163.24, 141.41, 140.03, 139.51, 139.42, 137.33, 131.32, 130.11, 128.45, 125.93, 125.72, 125.58, 123.68, 120.42, 119.86, 109.27, 108.76, 40.46, 31.23, 27.85, 26.44, 22.38, 13.73.

MS $[M+H]^+$ m/z: calcd. for $[C_{42}H_{33}N_3O_2]^+$ 611.26, found 611.29.

Melting point: 325 °C.

Synthesis of 2PTZ-NPTI (2-hexyl-4,7-di(*10H*-phenothiazin-10-yl)-*1H*-benzo[*de*]isoquinoline-1,3(*2H*)-dione)

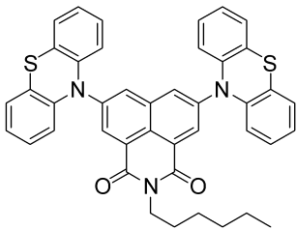

Compound 2PTZ-NPTI was prepared following the general procedure using *10H*-phenothiazine as a donor molecule. A red solid was obtained after column chromatography (Dichloromethane: Hexane = 1:2 volume ratio) (44.4 mg, yield: 61%).

^{1}H nmR (400 MHz, $CDCl_3$, δ ppm): 8.47 (d, J = 2.1 Hz, 2H), 7.86 (d, J = 2.1 Hz, 2H), 7.26 (d, J = 1.1 Hz, 2H), 7.24 (d, J = 1.6 Hz, 2H), 7.11 – 6.99 (m, 8H), 6.77 (d, J = 1.4 Hz, 2H), 6.75 (d, J = 1.3 Hz, 2H), 4.15 (t, 2H), 1.77 – 1.65 (m, 2H), 1.47 – 1.23 (m, 6H), 0.90 (t, 3H).

^{13}C nmR (100 MHz, $CDCl_3$, δ ppm): 163.04, 142.25, 142.14, 127.45, 127.36, 126.80, 126.33, 125.87, 124.15, 124.11, 120.54, 40.29, 31.04, 30.41, 26.30, 22.05, 13.54.

MS $[M+H]^+$ m/z: calcd. for $[C_{42}H_{33}N_3O_2S_2]^+$ 675.20, found 675.09.

Melting point: 320 °C.

Synthesis of i-2PTZ-NPTI (2-hexyl-4,6-di(*10H*-phenothiazin-10-yl)-*1H*-benzo[*de*]isoquinoline-1,3(*2H)*-dione)

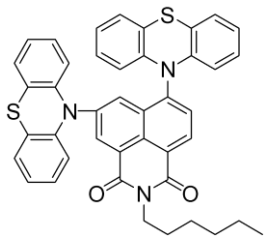

Compound i-2PTZ-NPTI was prepared following the general procedure using *10H*-phenothiazine as a donor molecule. A red solid was obtained after column chromatography (Dichloromethane: Hexane = 1:2 volume ratio) (44.4 mg, yield: 61%).

^{1}H nmR (400 MHz, $CDCl_3$, δ ppm): 8.68 (d, *J* = 7.7 Hz, 1H), 8.50 (d, *J* = 2.4 Hz, 1H), 8.11 (d, *J* = 2.4 Hz, 1H), 7.92 (d, *J* = 7.7 Hz, 1H), 7.30 – 7.27 (m, 2H), 7.09 – 7.05 (m, 6H), 6.89 – 6.77 (m, 6H), 6.14 (dd, *J* = 8.1, 1.3 Hz, 2H), 4.20 (t, 2H), 1.79 – 1.70 (m, 2H), 1.39 (m, 10H), 0.91 (t, 3H).

^{13}C nmR (100 MHz, $CDCl_3$, δ ppm): 163.55, 163.33, 142.71, 142.13, 141.45, 141.18, 130.97, 129.14, 129.05, 127.75, 126.93, 126.49, 126.42, 126.18, 124.82, 122.67, 120.18, 115.26, 40.20, 30.94, 27.57, 26.29, 22.01, 13.54.

MS $[M+H]^+$ m/z: calcd. for $[C_{42}H_{33}N_3O_2S_2]^+$ 675.20, found 675.04.

Melting point: 320 °C.

Synthesis of 2PXZ-NPTI (2-hexyl-4,7-di(*10H*-phenoxazin-10-yl)-*1H*-benzo[*de*]isoquinoline-1,3(*2H*)-dione)

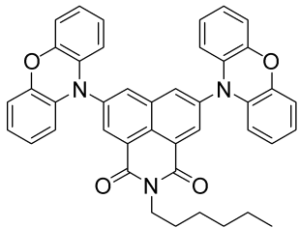

Compound 2PXZ-NPTI was prepared following the general procedure using *10H*-phenoxazine as a donor molecule. A dark-violet solid was obtained after column chromatography (Dichloromethane: Hexane = 1:2 volume ratio) (44.4 mg, yield: 61%).

^{1}H nmR (400 MHz, $CDCl_3$, δ ppm): 8.66 (d, *J* = 1.9 Hz, 2H), 8.26 (d, *J* = 1.9 Hz, 2H), 6.79 (d, *J* = 1.6 Hz, 1H), 6.77 (d, *J* = 1.6 Hz, 3H), 6.75 (d, *J* = 1.4 Hz, 1H), 6.73 (d, *J* = 1.4 Hz, 2H), 6.71 (d, *J* = 1.4 Hz, 1H), 6.63 (d, *J* = 1.7 Hz, 1H), 6.61 (d, *J* = 1.6 Hz, 2H), 6.60 (d, *J* = 1.6 Hz, 1H), 5.98 (d, *J* = 1.3 Hz, 2H), 5.97 (d, *J* = 1.3 Hz, 2H), 4.22 – 4.16 (t, 2H), 1.77 – 1.74 (m, 2H), 1.50 – 1.23 (m, 6H), 0.89 (t, 3H).

^{13}C nmR (100 MHz, $CDCl_3$, δ ppm): 162.31, 143.61, 138.54, 135.41, 135.15, 134.77, 134.20, 133.04, 126.05, 122.85, 121.90, 115.54, 113.02, 40.30, 31.02, 27.55, 26.26, 22.04, 13.55.

MS $[M+H]^+$ m/z: calcd. for $[C_{42}H_{33}N_3O_4]^+$ 643.25, found 643.28.

Melting point: 330 °C.

Synthesis of i-2PXZ-NPTI (2-hexyl-4,6-di(*10H*-phenoxazin-10-yl)-*1H*-benzo[*de*]isoquinoline-1,3(*2H*)-dione)

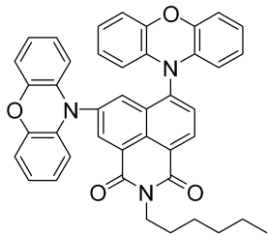

Compound i-2PXZ-NPTI was prepared following the general procedure using *10H*-phenoxazine as a donor molecule. A dark-violet solid was obtained after column chromatography (Dichloromethane: Hexane = 1:2 volume ratio) (44.4 mg, yield: 61%).

^{1}H nmR (400 MHz, $CDCl_3$, δ ppm): 8.83 (d, *J* = 7.7 Hz, 1H), 8.65 (d, *J* = 2.0 Hz, 1H), 8.43 (d, *J* = 2.0 Hz, 1H), 7.92 (d, *J* = 7.7 Hz, 1H), 6.77 – 6.63 (m, 8H), 6.55 (ddd, *J* = 7.5, 6.4, 1.6

Hz, 2H), 6.47 (ddd, *J* = 8.0, 7.3, 1.7 Hz, 2H), 5.90 – 5.86 (dd, *J* = 8.0, 1.3 Hz, 2H), 5.78 (dd, *J* = 8.0, 1.3 Hz, 2H), 4.21 (t, 2H), 1.84 – 1.68 (m, 2H), 1.52 – 1.20 (m, 6H), 0.90 (t, 3H).

^{13}C nmR (100 MHz, $CDCl_3$, δ ppm): 162.60, 162.32, 143.68, 143.32, 140.78, 138.55, 134.05, 132.96, 132.54, 132.36, 131.52, 131.47, 130.68, 130.66, 129.01, 126.95, 122.88, 122.72, 122.02, 121.88, 115.71, 115.48, 112.91, 112.71, 40.30, 31.08, 27.58, 26.29, 22.15, 13.60.

MS $[M+H]^+$ m/z: calcd. for $[C_{42}H_{33}N_3O_4]^+$ 643.25, found 643.28.

Melting point: 330 °C.

Synthesis of 2DMAC-NPTI (4,7-bis(9,9-dimethylacridin-10(*9H*)-yl)-2-hexyl-*1H*-benzo[*de*]isoquinoline-1,3(*2H*)-dione)

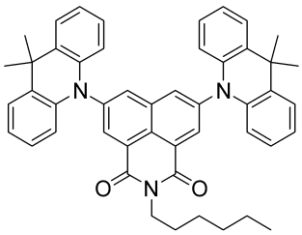

Compound 2DMAC-NPTI was prepared following the general procedure using 9,10-Dihydro-9,9-dimethylacridine as a donor molecule. An orange solid was obtained after column chromatography (Dichloromethane: Hexane = 1:2 volume ratio) (44.4 mg, yield: 61%).

^{1}H nmR (400 MHz, $CDCl_3$, δ ppm): 8.66 (d, *J* = 1.9 Hz, 2H), 8.27 (d, *J* = 1.9 Hz, 2H), 7.55 – 7.49 (m, 4H), 7.02 – 6.95 (m, 8H), 6.34 – 6.28 (m, 4H), 4.21 (t, 2H), 1.81 – 1.76 (m, 2H), 1.74 (s, 12H), 1.51 – 1.23 (m, 6H), 0.90 (t, 3H).

^{13}C nmR (100 MHz, $CDCl_3$, δ ppm): 162.61, 140.46, 139.97, 135.44, 134.91, 134.70, 133.07, 130.34, 126.02, 125.79, 125.05, 120.98, 113.82, 40.31, 35.63, 31.08, 30.58, 27.61, 26.27, 22.15, 13.61.

MS $[M+H]^+$ m/z: calcd. for $[C_{48}H_{45}N_3O_2]^+$ 695.35, found 695.31.

Melting point: 295 °C.

Synthesis of i-2DMAC-NPTI (4,6-bis(9,9-dimethylacridin-10(*9H*)-yl)-2-hexyl-*1H*-benzo[*de*]isoquinoline-1,3(*2H*)-dione)

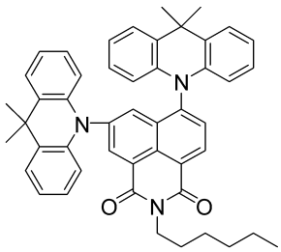

Compound i-2DMAC-NPTI was prepared following the general procedure using 9,10-Dihydro-9,9-dimethylacridine as a donor molecule. An orange solid was obtained after flash column chromatography (Dichloromethane: Hexane = 1:2 volume ratio) (44.4 mg, yield: 61%).

^{1}H nmR (400 MHz, $CDCl_3$, δ ppm): 8.89 (d, *J* = 7.7 Hz, 1H), 8.58 (d, *J* = 2.0 Hz, 1H), 8.06 (d, *J* = 2.0 Hz, 1H), 7.89 (d, *J* = 7.7 Hz, 1H), 7.47 (dd, *J* = 7.4, 1.8 Hz, 2H), 7.40 (dd, *J* = 7.7, 1.4 Hz, 2H), 6.97 – 6.87 (m, 6H), 6.84 – 6.79 (m, 2H), 6.14 (dd, *J* = 8.2, 1.0 Hz, 2H), 6.08 (dd, *J* = 7.8, 1.6 Hz, 2H), 4.24 (t, 2H), 1.85 – 1.65 (m, 2H), 1.71 (s, 3H), 1.68 (s, 3H), 1.62 (s, 6H), 1.53 – 1.24 (m, 6H), 0.91 (t, 3H).

^{13}C nmR (100 MHz, $CDCl_3$, δ ppm): 162.88, 162.61, 143.71, 140.51, 139.67, 135.45, 134.68, 132.51, 132.16, 130.82, 130.57, 129.65, 126.76, 126.09, 125.88, 125.32, 125.06, 124.68, 122.63, 121.03, 120.93, 113.96, 113.83, 113.45, 40.28, 35.51, 31.08, 30.53, 30.13, 27.62, 26.32, 22.09, 13.59.

MS $[M+H]^+$ m/z: calcd. for $[C_{48}H_{45}N_3O_2]^+$ 695.35, found 695.33.

Melting point: 295 °C.

8.2 Supplement 2

This part was done by Yangyang Qu from Ecole Normale Supérieure de Cachan, Department of Chemistry.

Synthesis of CBZ-TA (TA1)

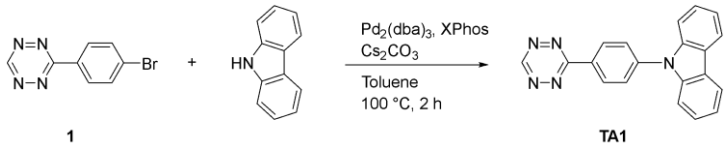

Procedure A: To a 100 ml two-neck round bottom flask equipped with a stir bar, tetrazine **1** (0.2 mmol, 47.6 mg), carbazole donor (0.24 mmol, 40.1 mg), cesium carbonate (0.4 mmol, 130 mg), and 10 ml of anhydrous toluene were added. The reaction mixture was degassed by bubbling through nitrogen for 15 min under vigorous stirring. Then $Pd_2(dba)_3$ (0.006 mmol, 5.5 mg) and XPhos (0.024 mmol, 11.5 mg) were added and degassed for another 15 min. The reaction mixture was heated to 100 °C under a nitrogen atmosphere for 2 h. The reaction mixture was then cooled down to room temperature, extracted with dichloromethane. The organic phase was dried over anhydrous magnesium sulfate ($MgSO_4$), filtered, and concentrated under reduced pressure. The product was purified using flash column chromatography (Petroleum ether: CH_2Cl_2= 3:1) to give 46.5 mg of **TA1** as a red solid (yield: 72%).

^{1}H nmR (400 MHz, $CDCl_3$, δ): 10.27 (s, 1H), 8.89 (d, *J* = 8.24 Hz, 2H), 8.17 (d, *J* = 7.80 Hz, 2H), 7.88 (d, *J* = 8.24 Hz, 2H), 7.56 (d, *J* = 7.80 Hz, 2H), 7.46 (t, *J* = 7.80 Hz, 2H), 7.34 (t, *J* = 7.80 Hz, 2H) ppm; ^{13}C nmR (100 MHz, $CDCl_3$, δ): 166.11, 157.96, 142.56, 140.29, 130.10, 130.06, 127.40, 126.41, 124.05, 120.84, 120.65, 109.99 ppm; HRMS $[M+H]^+$ m/z calc. for $[C_{20}H_{14}N_5]^+$ 324.1249, found 324.1253; m.p. 180 °C.

Synthesis of PXZ-TA (TA2)

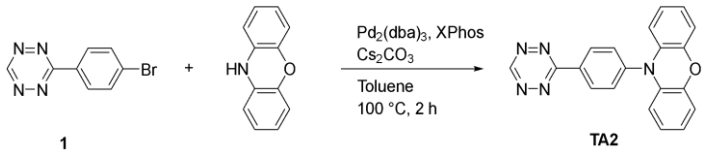

TA2 was prepared following **Procedure A** using phenoxazine as a donor. A deep red solid was obtained after flash column chromatography (Petroleum ether:CH_2Cl_2 = 3:1) (48.1 mg, yield: 71%). A single crystal of **TA2** has grown from slow eVaporation of petroleum ether/CH_2Cl_2 (3:1) mixture.

^{1}H nmR (400 MHz, $CDCl_3$, δ): 10.28 (s, 1H), 8.87 (d, *J* = 8.24 Hz, 2H), 7.63 (d, *J* = 8.24 Hz, 2H), 6.79–6.59 (m, 6H), 6.05 (dd, *J* = 7.80 Hz, *J* = 1.50 Hz, 2H) ppm; ^{13}C nmR (100 MHz, $CDCl_3$, δ): 166.08, 158.04, 144.18, 144.06, 133.78, 132.01, 131.62, 131.16, 123.47, 122.08, 115.92, 113.53 ppm; HRMS $[M+H]^+$ m/z calcd. for $[C_{20}H_{14}N_5O]^+$ 340.1198, found 340.1192; m.p. 243 °C.

Synthesis of PTZ-TA (TA3)

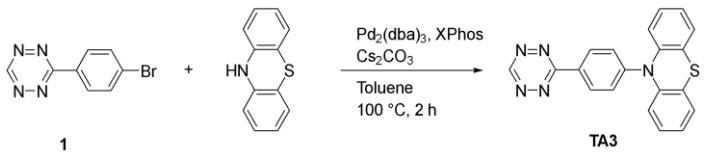

TA3 was prepared following **Procedure A** using phenothiazine as a donor. A deep red solid was obtained after flash column chromatography (Petroleum ether:CH_2Cl_2 = 3:1) (45.4 mg, yield: 64%). A single crystal of **TA3** has grown from slow eVaporation of petroleum ether/CH_2Cl_2 (3:1) mixture.

^{1}H nmR (400 MHz, $CDCl_3$, δ): 10.13 (s, 1H), 8.56 (d, *J* = 8.24 Hz, 2H), 7.37 (d, *J* = 7.80 Hz, 2H), 7.32 (d, *J* = 8.24 Hz, 2H), 7.24 (d, *J* = 7.80 Hz, 2H), 7.17–7.10 (m, 4H) ppm; ^{13}C nmR (100 MHz, $CDCl_3$, δ): 166.16, 157.47, 148.93, 141.92, 130.72, 130.17, 128.58, 127.40, 125.79, 125.55, 124.14, 120.14 ppm; HRMS $[M+H]^+$ m/z calcd. for $[C_{20}H_{14}N_5S]^+$ 356.0970, found 356.0977.

Synthesis of DMAC-TA (TA4)

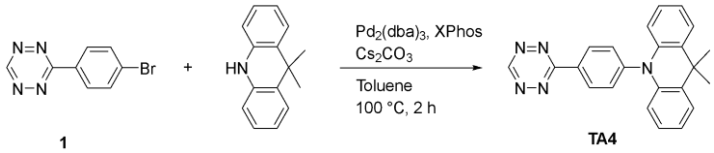

TA4 was prepared following **Procedure A** using 9,10-dihydro-9,9-dimethylacridine as a donor. A red solid was obtained after flash column chromatography (Petroleum ether:CH_2Cl_2 = 3:1) (44.4 mg, yield: 61%).

^{1}H nmR (400 MHz, $CDCl_3$, δ): 10.28 (s, 1H), 8.89 (d, *J* = 8.24 Hz, 2H), 7.62 (d, *J* = 8.24 Hz, 2H), 7.49 (dd, *J* = 7.80 Hz, *J* = 1.80 Hz, 2H), 7.05–6.95 (m, 4H), 6.40 (dd, *J* = 7.80 Hz, *J* = 1.80 Hz, 2H) ppm; ^{13}C nmR (100 MHz, $CDCl_3$, δ): 166.22, 158.00, 146.42, 140.55, 131.94, 131.14, 131.00, 126.59, 125.52, 121.37, 114.61, 36.26, 31.18 ppm; HRMS $[M+H]^+$ m/z calcd. for $[C_{23}H_{20}N_5]^+$ 366.1719, found 366.1725.

Synthesis of 2PXZ-TA (TA5)

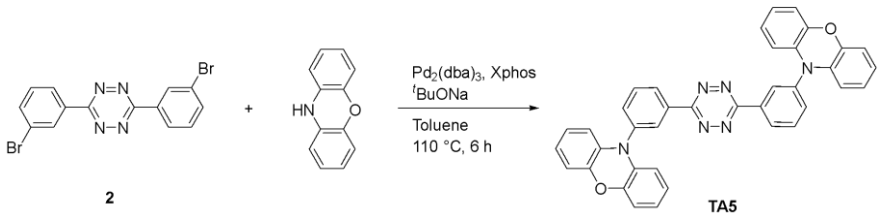

Procedure B: To a 100 ml two-neck round bottom flask equipped with a stir bar, tetrazine **2** (0.2 mmol, 78.4 mg), phenoxazine donor (0.48 mmol, 87.9 mg), sodium *tert*-butoxide (0.48 mmol, 46.1 mg), and 15 ml of anhydrous toluene were added. The reaction mixture was degassed by bubbling through nitrogen for 15 min under vigorous stirring. Then $Pd_2(dba)_3$ (0.012 mmol, 11 mg) and XPhos (0.048 mmol, 23 mg) were added and degassed for another 15 min. The reaction mixture was heated to 110 °C under a nitrogen atmosphere for 6 h. The reaction mixture was then cooled down to room temperature, extracted with dichloromethane. The organic phase was dried over anhydrous magnesium sulfate ($MgSO_4$), filtered, and concentrated under reduced pressure. The product was purified using flash column chromatography (Petroleum ether: CH_2Cl_2= 4:1) to give 78.3 mg of **TA5** as a purple solid (yield: 66%).

^{1}H nmR (400 MHz, $CDCl_3$, δ): 8.77 (d, *J* = 8.24 Hz, 2H), 8.69 (t, *J* = 1.80 Hz, 2H), 7.87 (t, *J* = 8.24 Hz, 2H), 7.67 (d, *J* = 8.24 Hz, 2H), 6.77–6.56 (m, 12H), 6.00 (dd, *J* = 7.80 Hz, *J* = 1.80 Hz, 4H) ppm; ^{13}C nmR (100 MHz, $CDCl_3$, δ): 163.61, 144.12, 140.55, 135.84, 135.04, 134.13, 132.37, 131.05, 128.16, 123.45, 121.87, 115.82, 113.44 ppm; HRMS $[M]^+$ m/z calc. for $[C_{38}H_{24}N_6O_2]^+$ 596.1961, found 596.1947; m.p. >260 °C.

Synthesis of 2PTZ-TA (TA6)

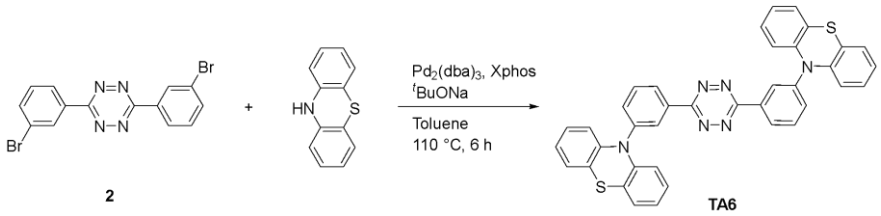

TA6 was prepared following **Procedure B** using phenothiazine as a donor. A red solid was obtained after flash column chromatography (Petroleum ether:CH_2Cl_2 = 4:1) (76.3 mg, yield: 61%).

^{1}H nmR (400 MHz, $CDCl_3$, δ): 8.74–8.67 (m, 4H), 7.81 (t, *J* = 8.24 Hz, 2H), 7.66 (d, *J* = 8.24 Hz, 2H), 7.11 (dd, *J* = 7.80 Hz, *J* = 1.80 Hz, 4H), 6.97–6.85 (m, 8H), 6.44 (dd, *J* = 7.80 Hz, *J* = 1.80 Hz, 4H) ppm; ^{13}C nmR (100 MHz, $CDCl_3$, δ): 163.74, 143.83, 143.02, 134.48, 133.95, 131.80, 129.07, 127.32, 127.15, 127.06, 123.35, 122.44, 117.59 ppm; HRMS $[M]^+$ m/z calcd. for $[C_{38}H_{24}N_6S_2]^+$ 628.1504, found 628.1500; m.p. >260 °C.

Synthesis of 2DMAC-TA (TA7)

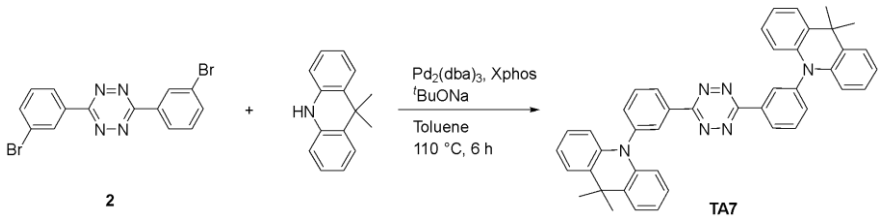

TA7 was prepared following **Procedure B** using 9,10-dihydro-9,9-dimethylacridine as a donor. A red solid was obtained after flash column chromatography (Petroleum ether:CH_2Cl_2 = 4:1) (89.9 mg, yield: 69%).

^{1}H nmR (400 MHz, $CDCl_3$, δ): 8.81 (d, *J* = 8.24 Hz, 2H), 8.67 (t, *J* = 1.80 Hz, 2H), 7.90 (t, *J* = 8.24 Hz, 2H), 7.66 (d, *J* = 8.24 Hz, 2H), 7.49 (dd, *J* = 7.80 Hz, *J* = 1.80 Hz, 4H), 7.03–6.91 (m, 8H), 6.34 (dd, *J* = 7.80 Hz, *J* = 1.80 Hz, 4H), 1.72 (s, 12H) ppm; ^{13}C nmR (100 MHz, $CDCl_3$, δ): 163.68, 142.60, 140.79, 136.41, 134.89, 132.07, 131.43, 130.37, 127.92, 126.57, 125.46, 121.02, 114.14 ppm; HRMS $[M+H]^+$ m/z calcd. for $[C_{44}H_{37}N_6]^+$ 649.3080, found 649.3093; m.p. >260 °C.

General procedure for the synthesis of CBZ-TA, PXZ-TA, PTZ-TA, DMAC-TA (DA1-DA4)

To a 50 mL round bottom flask equipped with a stir bar, 0.1 mmol of **TA1-TA4**, and 10 mL of DCM were added. Then 0.4 mmol of cyclooctyne (50 μL) was added with stirring at room temperature. The color of the solution turned from red to colorless after several minutes and N_2 gas evolved. The reaction mixture was allowed to stir for another 20 min. All the volatiles

were evaporated under vacuum and the residue was purified using flash column chromatography.

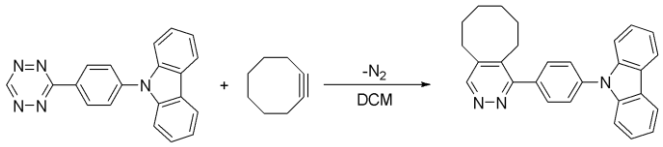

TA1 DA1

DA1: A white solid was obtained after flash column chromatography (Petroleum ether:EtOAc = 2:3) (39.6 mg, yield: 98%).

^{1}H nmR (400 MHz, $CDCl_3$, δ): 8.96 (s, 1H), 8.17 (d, *J* = 8.24 Hz, 2H), 7.78–7.68 (m, 4H), 7.51 (d, *J* = 7.80 Hz, 2H), 7.44 (t, *J* = 7.80 Hz, 2H), 7.32 (t, *J* = 7.80 Hz, 2H), 2.94–2.85 (m, 4H), 1.90–1.80 (m, 2H), 1.76–1.66 (m, 2H), 1.54–1.40 (m, 4H) ppm; ^{13}C nmR (100 MHz, $CDCl_3$, δ): 161.33, 151.75, 141.58, 140.82, 138.87, 138.25, 136.96, 130.84, 126.93, 126.19, 123.66, 120.51, 120.30, 109.94, 31.28, 30.56, 29.70, 26.77, 26.10, 25.57 ppm; HRMS $[M+H]^+$ m/z calcd. for $[C_{28}H_{26}N_3]^+$ 404.2127, found 404.2127; m.p. 251 °C (dec.).

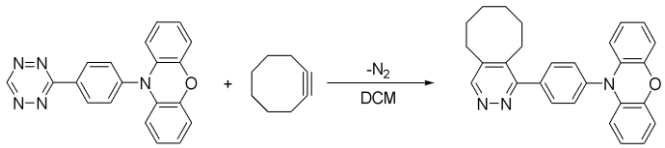

TA2 DA2

DA2: A white solid was obtained after flash column chromatography (Petroleum ether:EtOAc = 2:3) (41.5 mg, yield: 99%). Single crystal of **DA2** was grown from slow evaporation of petroleum ether/EtOAc (2:3) mixture.

^{1}H nmR (400 MHz, $CDCl_3$, δ): 8.97 (s, 1H), 7.73 (d, *J* = 8.24 Hz, 2H), 7.48 (d, *J* = 8.24 Hz, 2H), 6.76–6.57 (m, 6H), 6.01 (d, *J* = 7.80 Hz, 2H), 2.95–2.81 (m, 4H), 1.89–1.79 (m, 2H), 1.71–1.61 (m, 2H), 1.55–1.38 (m, 4H) ppm; ^{13}C nmR (100 MHz, $CDCl_3$, δ): 161.27, 151.32, 144.11, 142.19, 139.69, 139.62, 137.79, 134.29, 132.03, 131.01, 123.42, 121.67, 115.67, 113.50, 31.25, 30.47, 29.76, 26.87, 26.09, 25.53 ppm; HRMS $[M+H]^+$ m/z calcd. for $[C_{28}H_{26}N_3O]^+$ 420.2076, found 420.2090; m.p. 182 °C.

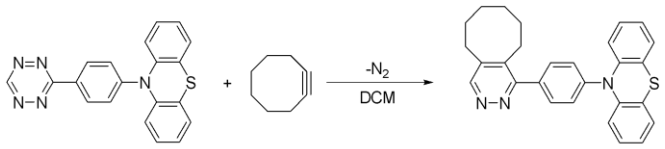

TA3 DA3

DA3: A light yellow solid was obtained after flash column chromatography (Petroleum ether:EtOAc = 2:3) (42.6 mg, yield: 98%). Single crystal of **DA3** was grown from slow evaporation of petroleum ether/EtOAc (2:3) mixture.

^{1}H nmR (400 MHz, $CDCl_3$, δ): 8.94 (s, 1H), 7.71 (d, *J* = 8.24 Hz, 2H), 7.49 (d, *J* = 8.24 Hz, 2H), 7.07 (d, *J* = 7.80 Hz, 2H), 6.96–6.82 (m, 4H), 6.38 (d, *J* = 7.80 Hz, 2H), 2.93–2.81 (m, 4H), 1.89–1.78 (m, 2H), 1.71–1.61 (m, 2H), 1.54–1.38 (m, 4H) ppm; ^{13}C nmR (100 MHz, $CDCl_3$, δ): 161.27, 151.72, 144.09, 141.87, 141.54, 138.79, 137.39, 131.61, 129.89, 127.08, 127.05, 123.01, 121.51, 117.10, 31.25, 30.48, 29.68, 26.79, 26.09, 25.56 ppm; HRMS $[M+H]^+$ m/z calcd. for $[C_{28}H_{26}N_3S]^+$ 436.1847, found 436.1855; m.p. 204 °C.

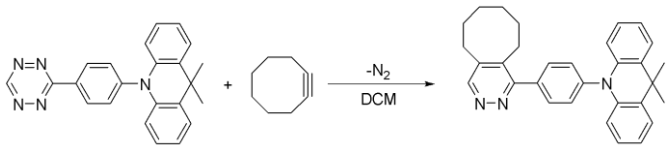

TA4 DA4

DA4: A white solid was obtained after flash column chromatography (Petroleum ether:EtOAc = 2:3) (44.1 mg, yield: 99%).

^{1}H nmR (400 MHz, $CDCl_3$, δ): 8.97 (s, 1H), 7.77 (d, *J* = 8.24 Hz, 2H), 7.54–7.44 (m, 4H), 7.05–6.91 (m, 4H), 6.37 (d, *J* = 7.80 Hz, 2H), 2.94–2.84 (m, 4H), 1.89–1.80 (m, 2H), 1.71 (s, 6H), 1.71–1.65 (m, 2H), 1.55–1.40 (m, 4H) ppm; ^{13}C nmR (100 MHz, $CDCl_3$, δ): 161.34, 151.76, 141.68, 141.54, 140.88, 138.82, 137.87, 131.80, 131.42, 130.20, 126.50, 125.35, 120.82, 114.23, 36.11, 31.29, 31.24, 30.43, 29.66, 26.80, 26.07, 25.54 ppm; HRMS $[M+H]^+$ m/z calcd. for $[C_{31}H_{32}N_3]^+$ 446.2596, found 446.2606; m.p. 194 °C.

General procedure for the synthesis of 2PXZ-TA, 2PTZ-TA, 2DMAC-TA (DA5-DA7)

To a 50 mL round bottom flask equipped with a stir bar, 0.1 mmol of **TA5-TA7**, and 15 mL of DCM were added. Then 0.4 mmol of cyclooctyne (50 μL) was added with stirring at room temperature. The reaction mixture was heated to 50 °C and allowed to stir for 1 hour. The color of the solution turned from red to colorless indicating the completion of the reaction. The reaction mixture was then cooled down to room temperature. All the volatiles were evaporated under vacuum and the residue was purified using flash column chromatography.

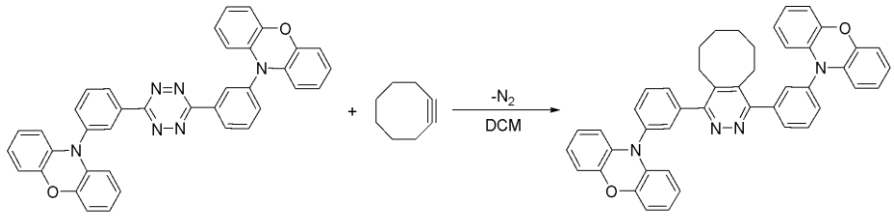

TA5 DA5

DA5: A light yellow solid was obtained after flash column chromatography (Petroleum ether:EtOAc = 2:1) (65.8 mg, yield: 97%).

^{1}H nmR (400 MHz, $CDCl_3$, δ): 7.75 (t, *J* = 8.24 Hz, 2H), 7.66 (d, *J* = 8.24 Hz, 2H), 7.52 (s, 2H), 7.48 (d, *J* = 8.24 Hz, 2H), 6.74–6.56 (m, 12H), 6.03 (d, *J* = 7.80 Hz, 4H), 2.84 (s, br, 4H), 1.60 (s, br, 4H), 1.41 (s, br, 4H) ppm; ^{13}C nmR (100 MHz, $CDCl_3$, δ): 160.39, 144.01, 141.04, 139.70, 139.01, 134.34, 131.66, 131.49, 131.24, 129.57, 123.44, 121.61, 115.62, 113.43, 30.37, 27.49, 25.91 ppm; HRMS $[M+H]^+$ m/z calcd. for $[C_{46}H_{37}N_4O_2]^+$ 677.2917, found 677.2923; m.p. >260 °C.

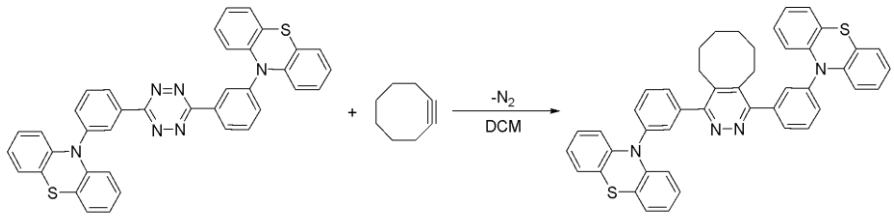

TA6 DA6

DA6: A light yellow solid was obtained after flash column chromatography (Petroleum ether:EtOAc = 2:1) (69.3 mg, yield: 98%).

^{1}H nmR (400 MHz, $CDCl_3$, δ): 7.73 (t, *J* = 8.24 Hz, 2H), 7.63 (d, *J* = 8.24 Hz, 2H), 7.54 (s, 2H), 7.51 (d, *J* = 8.24 Hz, 2H), 7.04 (dd, *J* = 7.80 Hz, *J* = 1.80 Hz, 4H), 6.93–6.79 (m, 8H), 6.36 (d, *J* = 7.80 Hz, 4H), 2.85 (s, br, 4H), 1.60 (s, br, 4H), 1.40 (s, br, 4H) ppm; ^{13}C nmR (100 MHz, $CDCl_3$, δ): 160.54, 144.11, 141.26, 140.61, 139.66, 131.21, 131.04, 130.39, 128.94, 127.08, 127.02, 122.92, 120.99, 116.76, 30.42, 27.51, 25.94 ppm; HRMS $[M+H]^+$ m/z calcd. for $[C_{46}H_{37}N_4S_2]^+$ 709.2460, found 709.2485; m.p. 250 °C.

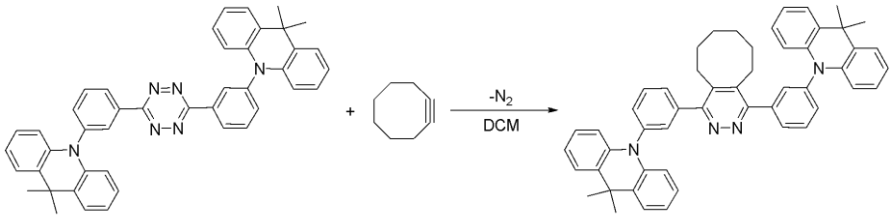

DA7: A white solid was obtained after flash column chromatography (Petroleum ether:EtOAc = 2:1) (72.1 mg, yield: 99%).

^{1}H nmR (400 MHz, $CDCl_3$, δ): 7.78 (t, *J* = 8.24 Hz, 2H), 7.70 (d, *J* = 8.24 Hz, 2H), 7.52 (t, *J* = 1.80 Hz, 2H), 7.50–7.43 (m, 6H), 7.03–6.90 (m, 8H), 6.39 (d, *J* = 7.80 Hz, *J* = 1.80 Hz, 4H), 2.94–2.82 (m, 4H), 1.70 (s, 12H), 1.60 (s, br, 4H), 1.38 (s, br, 4H) ppm; ^{13}C nmR (100 MHz, $CDCl_3$, δ): 160.54, 141.21, 141.02, 140.99, 139.43, 132.22, 131.57, 131.27, 130.19, 129.32, 126.55, 125.32, 120.82, 114.21, 36.14, 31.25, 30.33, 27.45, 25.93 ppm; HRMS $[M+H]^+$ m/z calcd. for $[C_{52}H_{49}N_4]^+$ 729.3957, found 729.3975; m.p. 221 °C.

8.3 Supplement 3

DFT results of compounds based on NPTI acceptor unit

Table S1. Calculated HOMO, LUMO levels of energy.

	HOMO, eV	**HOMO $^{-1}$, eV**	**LUMO, eV**	**Dihedral angle**	
2CBZ-NPTI	-5.49	-5.50	-2.55	54.3°	53.6°
I-2CBZ-NPTI	-5.32	-5.53	-2.41	54.3°	33.7°
2PXZ-NPTI	-4.81	-4.83	-2.61	95.5°	81.6°
I-2PXZ-NPTI	-4.81	-4.88	-2.65	94.3°	85.5°
2PTZ-NPTI	-5.13	-5.15	-2.61	98.2°	98.4°
I-2PTZ-NPTI	-5.12	-5.22	-2.64	77.9°	80.7°
2DMAC-NPTI	-5.01	-5.03	-2.57	91.8°	86.3°
I-2DMAC-NPTI	-5.01	-5.07	-2.60	85.4°	86.3°

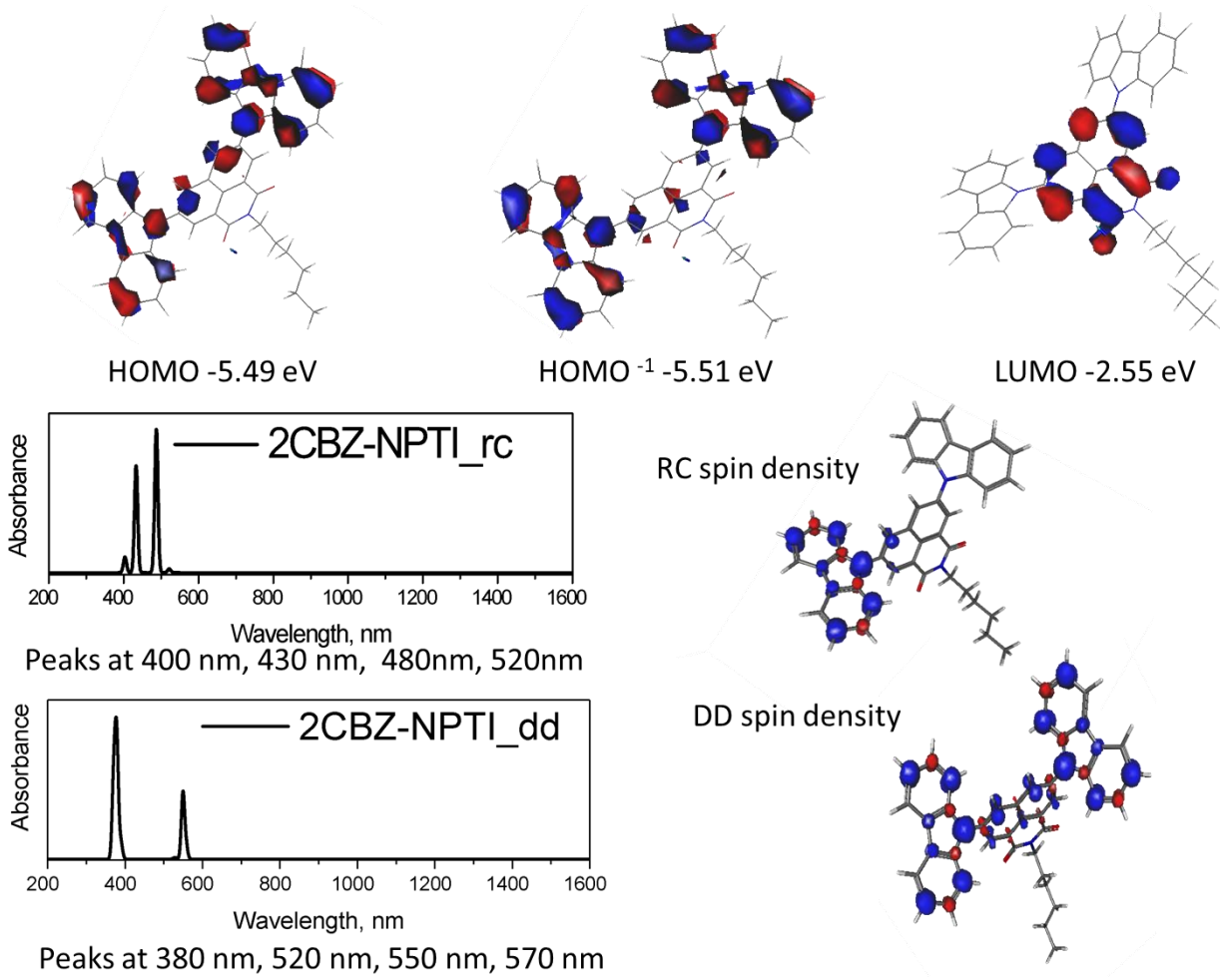

Figure S1. Calculation results for 2CBZ-NPTI

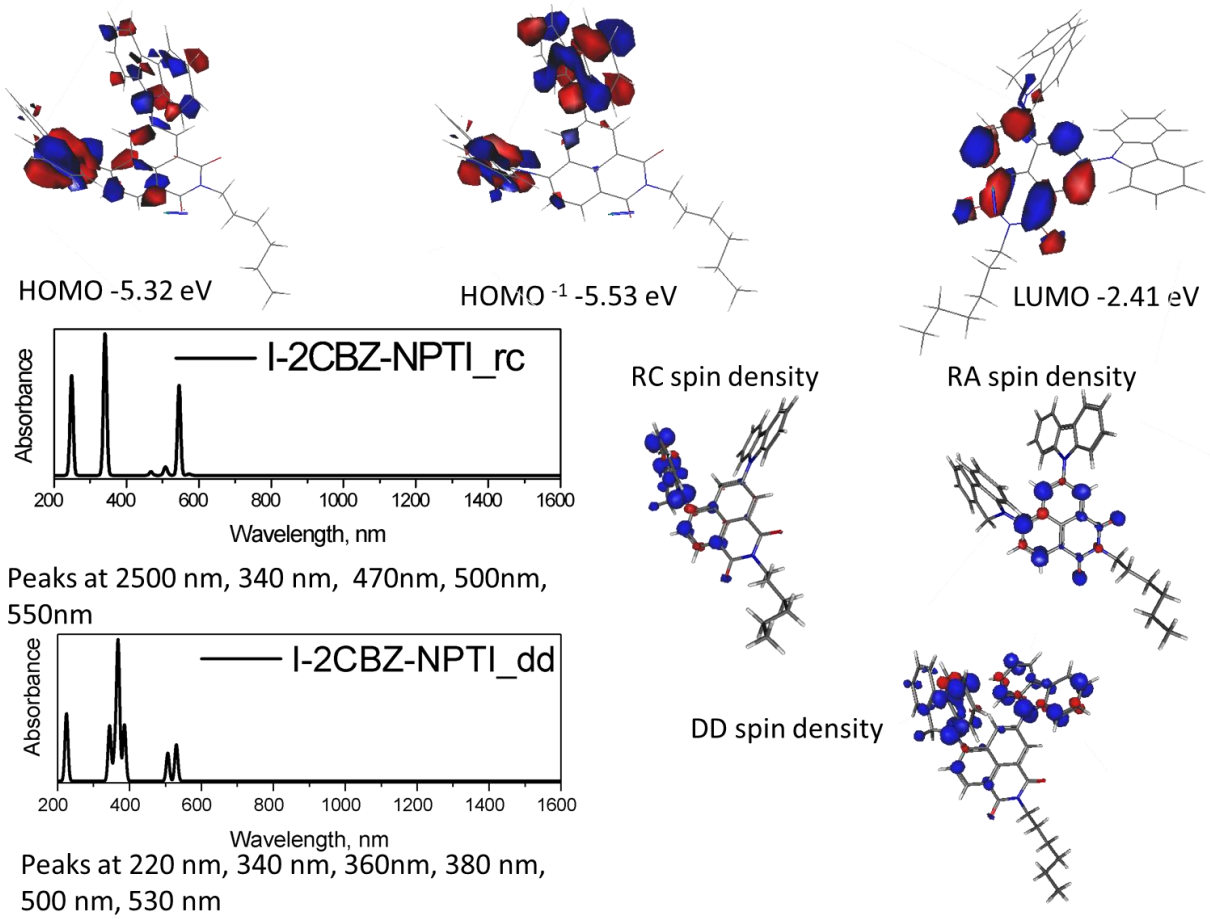

Figure S2. Calculation results for I-2CBZ-NPTI

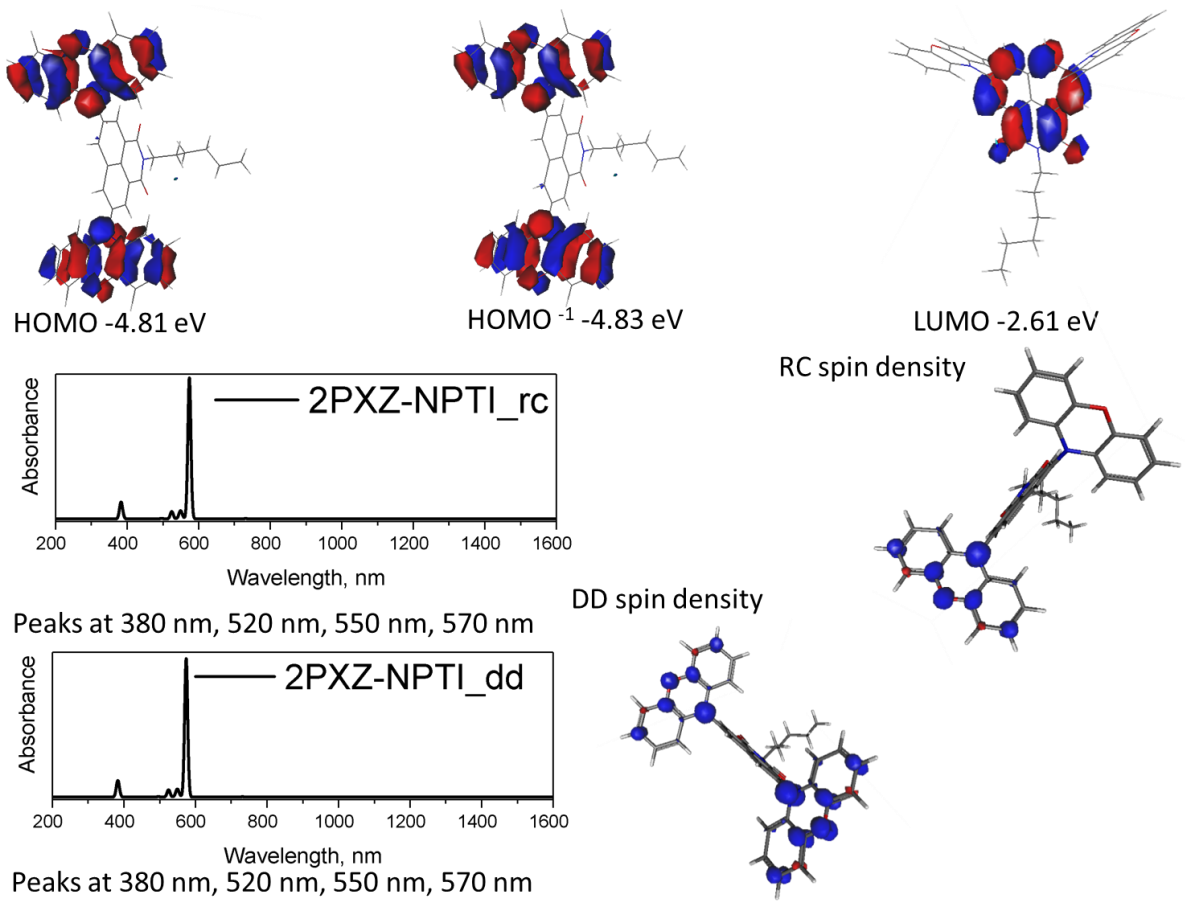

Figure S3. Calculation results for 2PXZ-NPTI

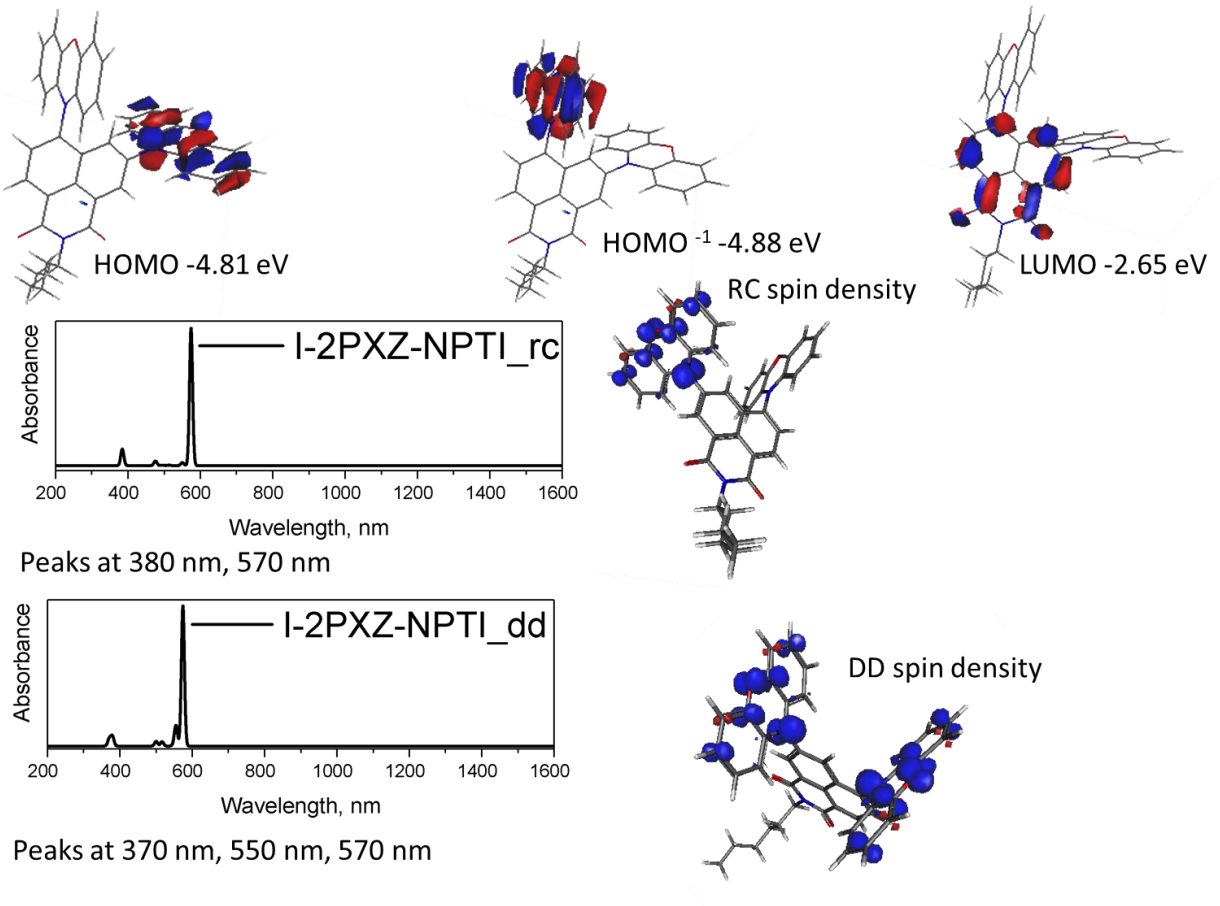

Figure S4. Calculation results for I-2PXZ-NPTI

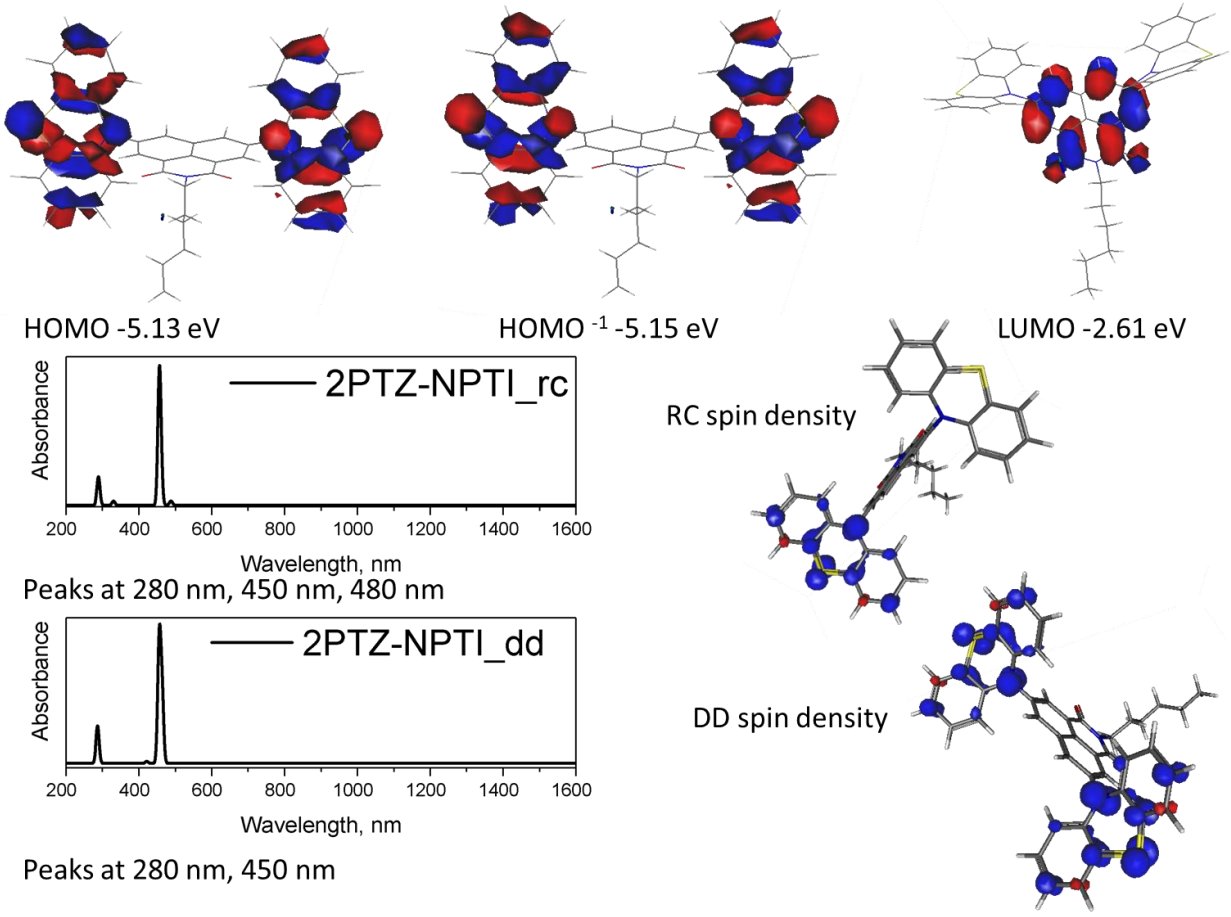

Figure S5. Calculation results for 2PTZ-NPTI

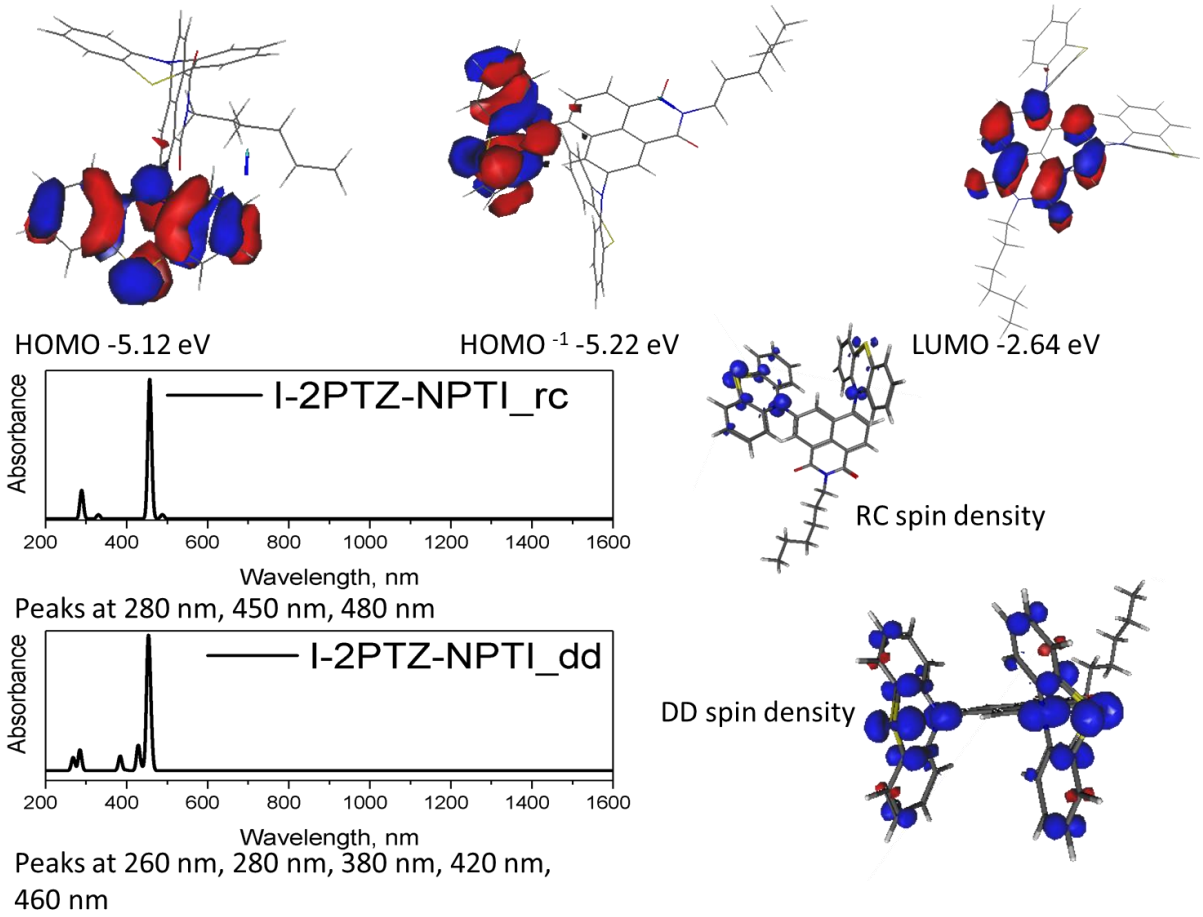

Figure S6. Calculation results for I-2PTZ-NPTI

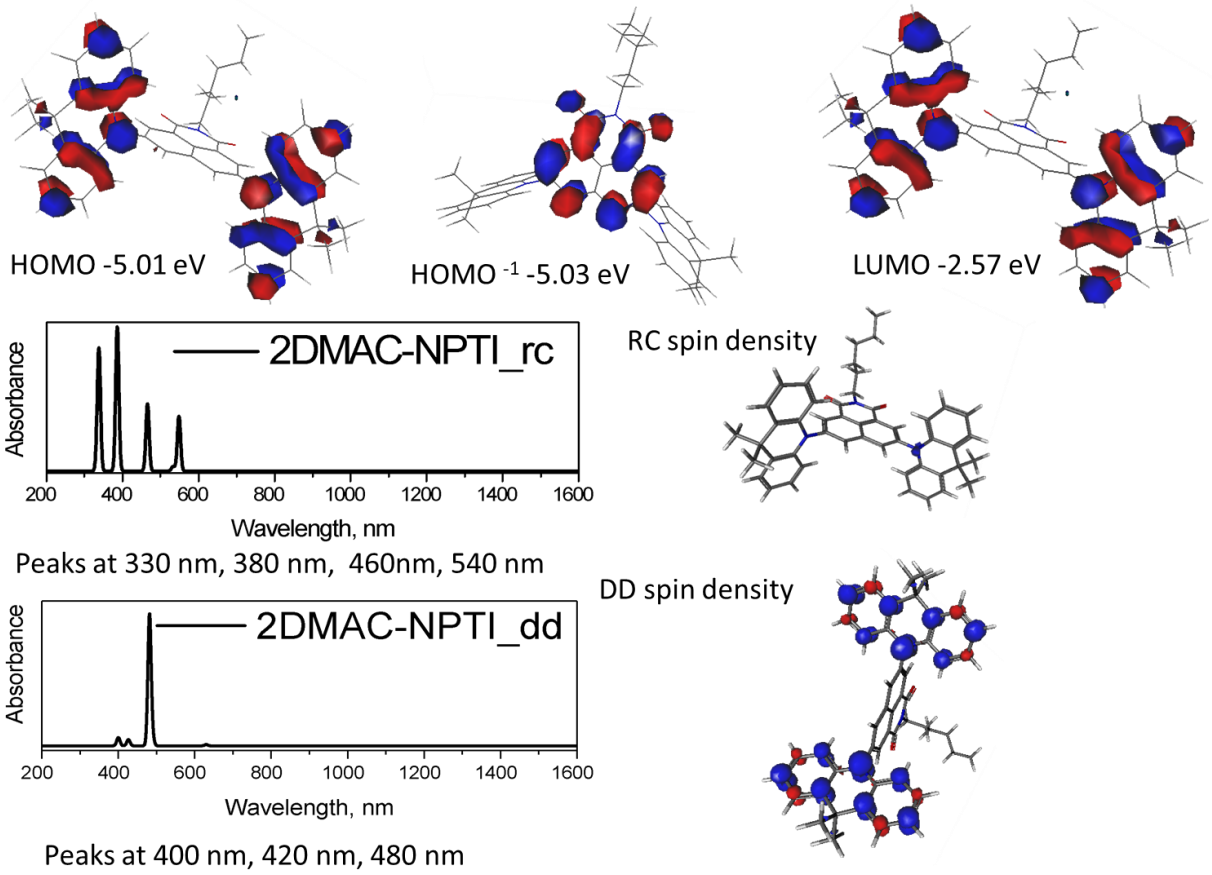

Figure S7. Calculation results for 2DMAC-NPTI

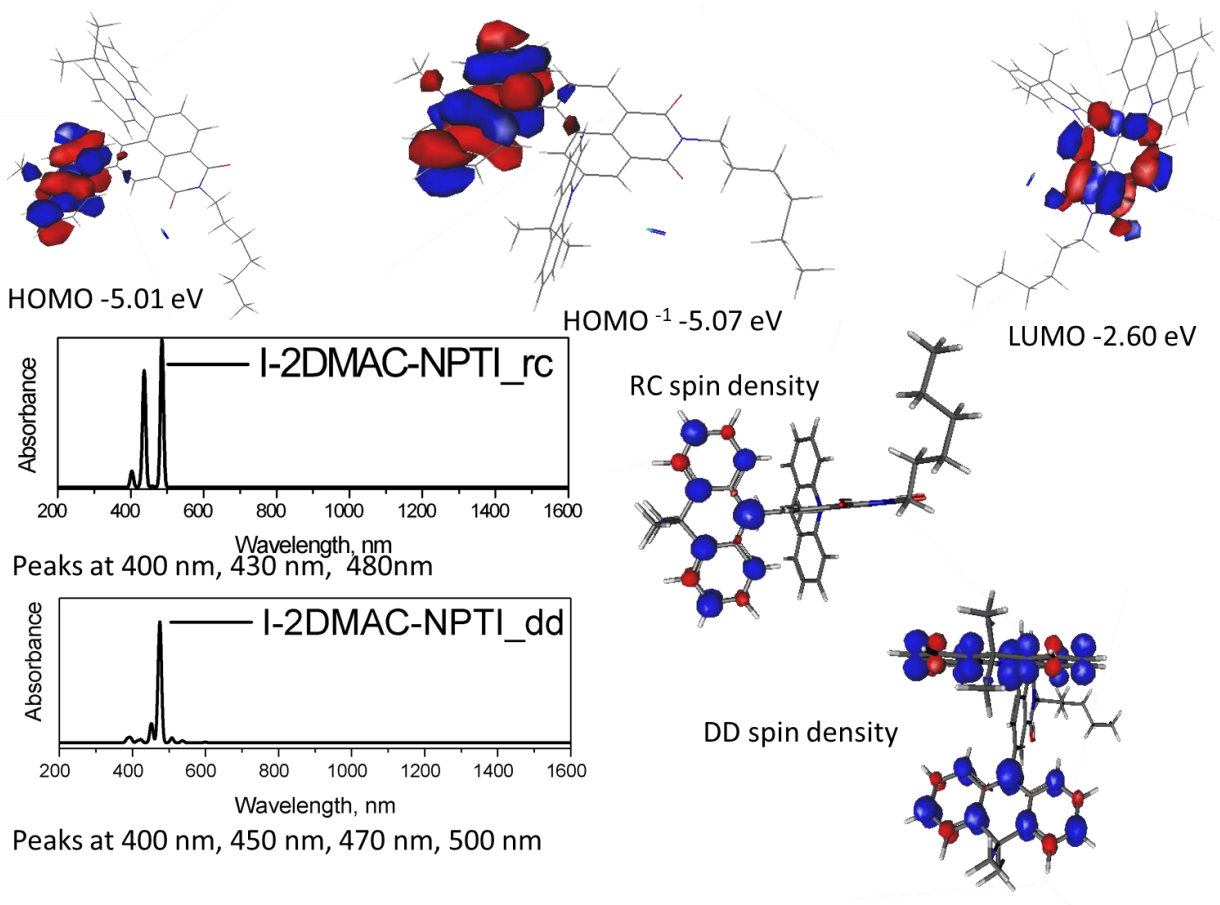

Figure S8. Calculation results for I-2DMAC-NPTI

8.4 Supplement 4

DFT results of compounds based on the DA acceptor unit.

Table S2. Calculated HOMO, LUMO levels of energy.

	HOMO, eV	HOMO $^{-1}$, eV	LUMO, eV	Dihedral angle	
CBZ-DA	-5.32		-1.45	53.5°	
PXZ-DA	-4.69		-1.43	89.5°	
PTZ-DA	-5.03		-1.43	96.6°	
DMAC-DA	-4.92		-1.51	88.8°	
2PXZ -DA	-4.69	-4.71	-1.25	87.2°	87.9°
2PTZ-DA	-5.04	-5.67	-1.24	82.0°	81.6°
2DMAC-DA	-4.90	-4.93	-1.98	87.9°	90.8°

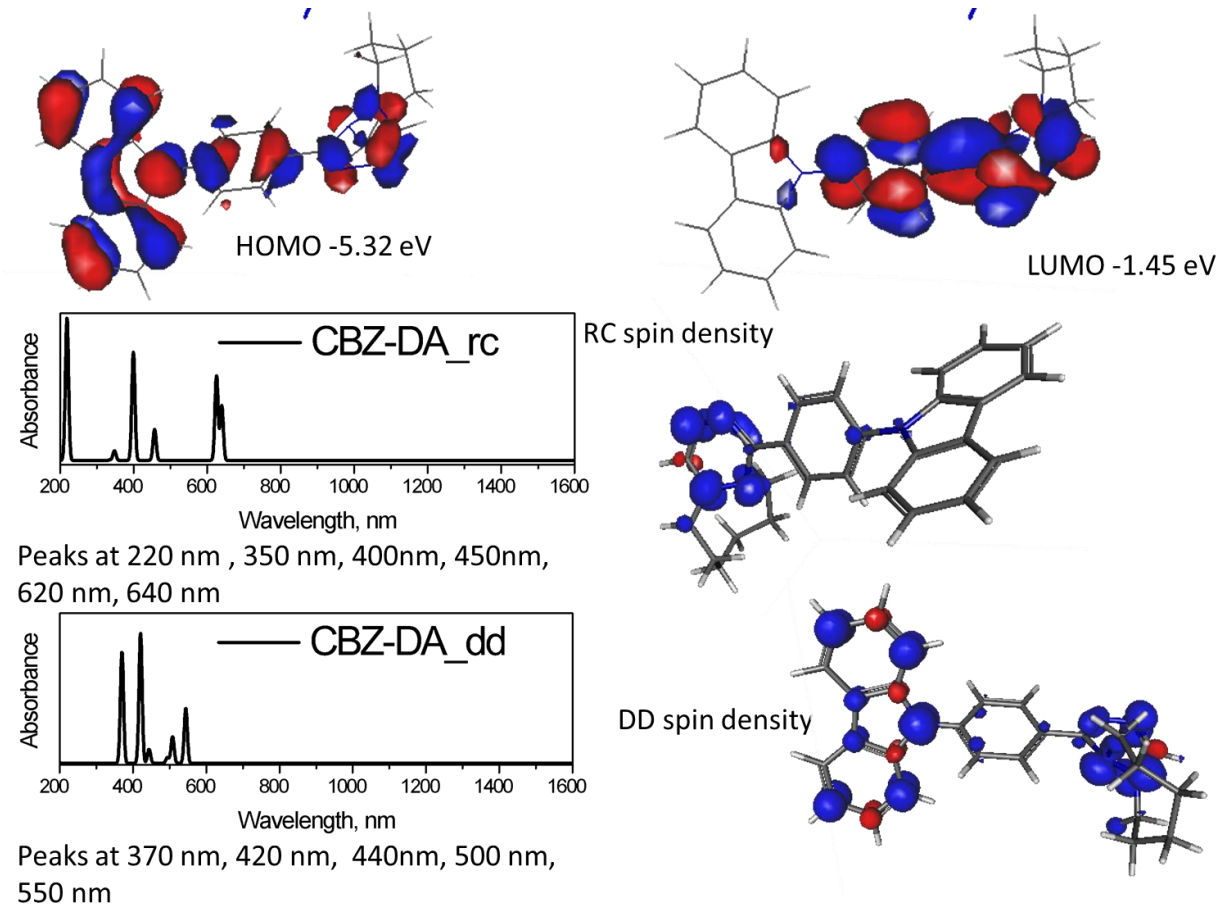

Figure S9. Calculation results for CBZ-DA

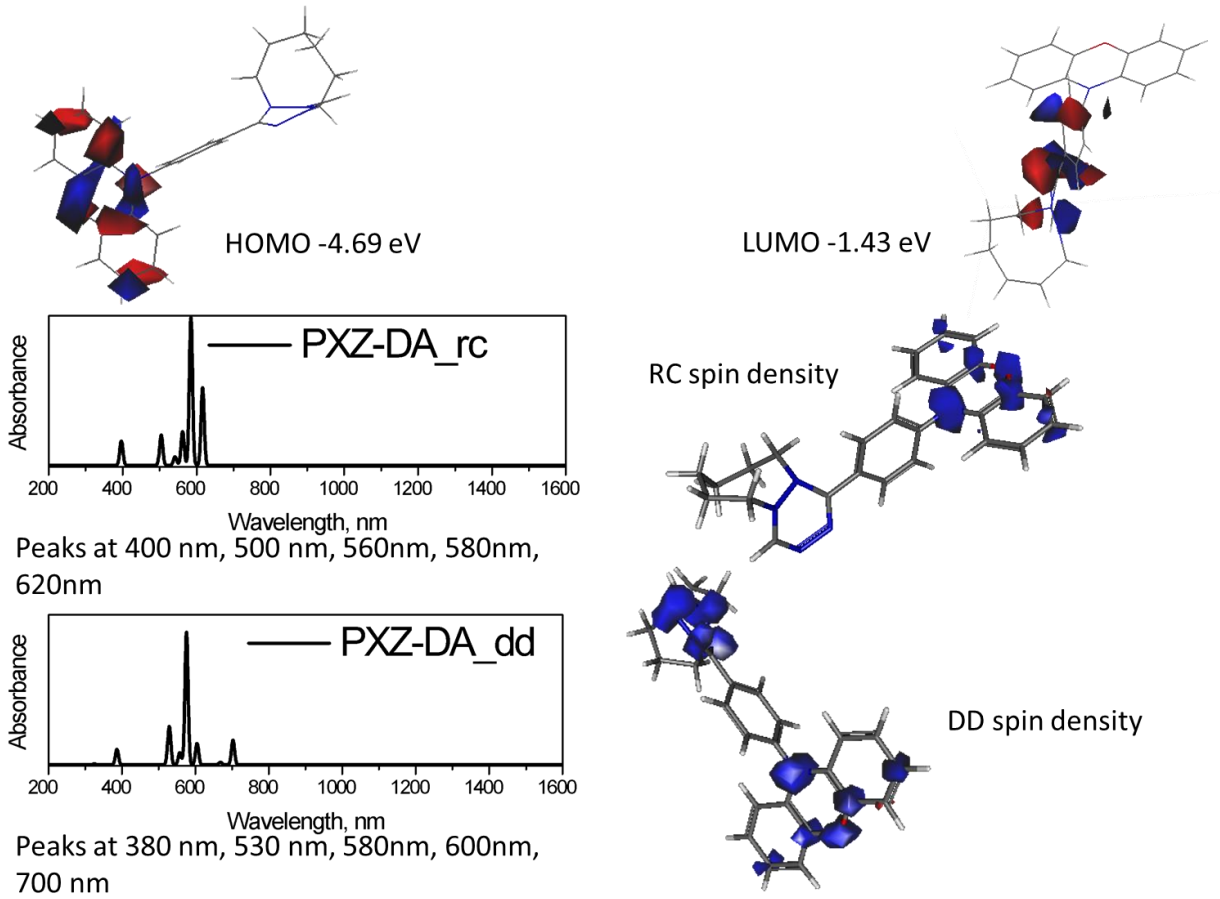

Figure S10. Calculation results for PXZ-DA

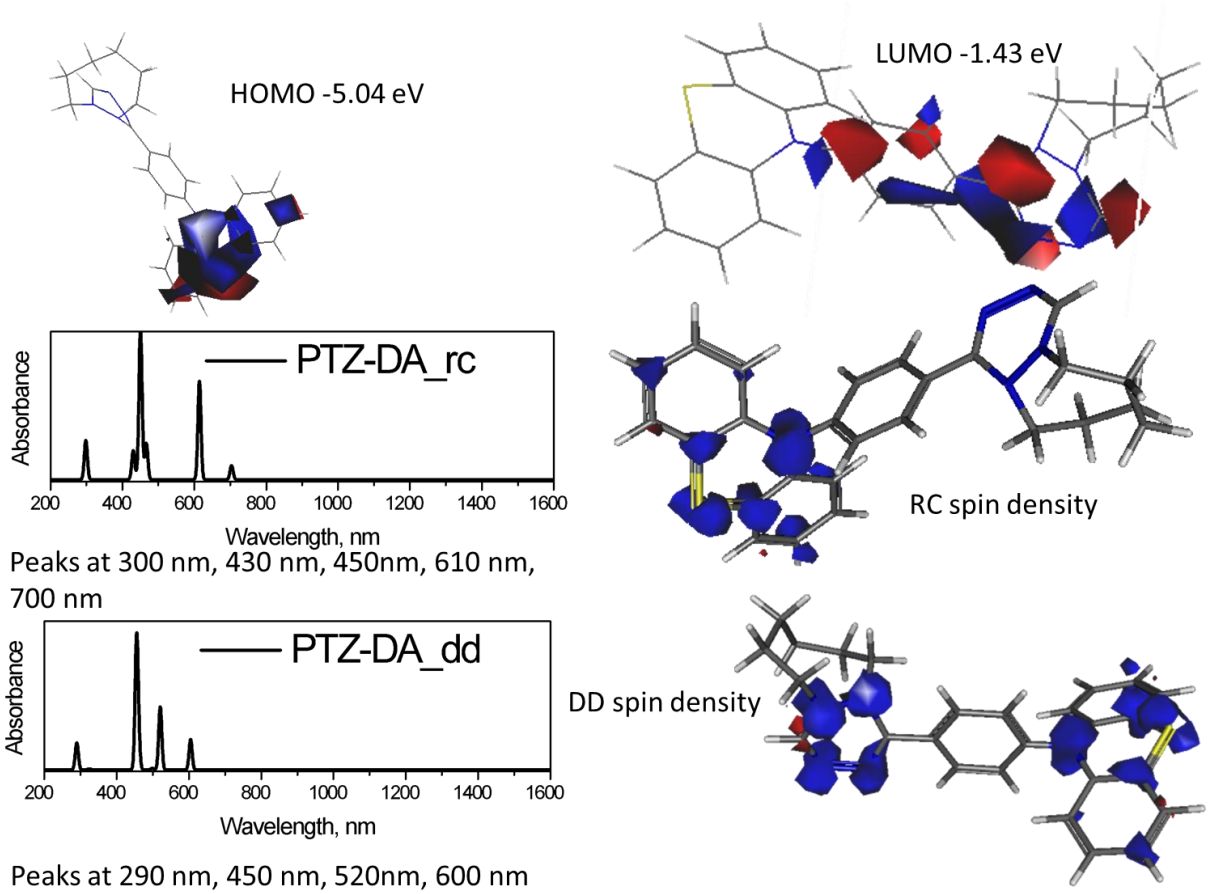

Figure S11. Calculation results for PTZ-DA

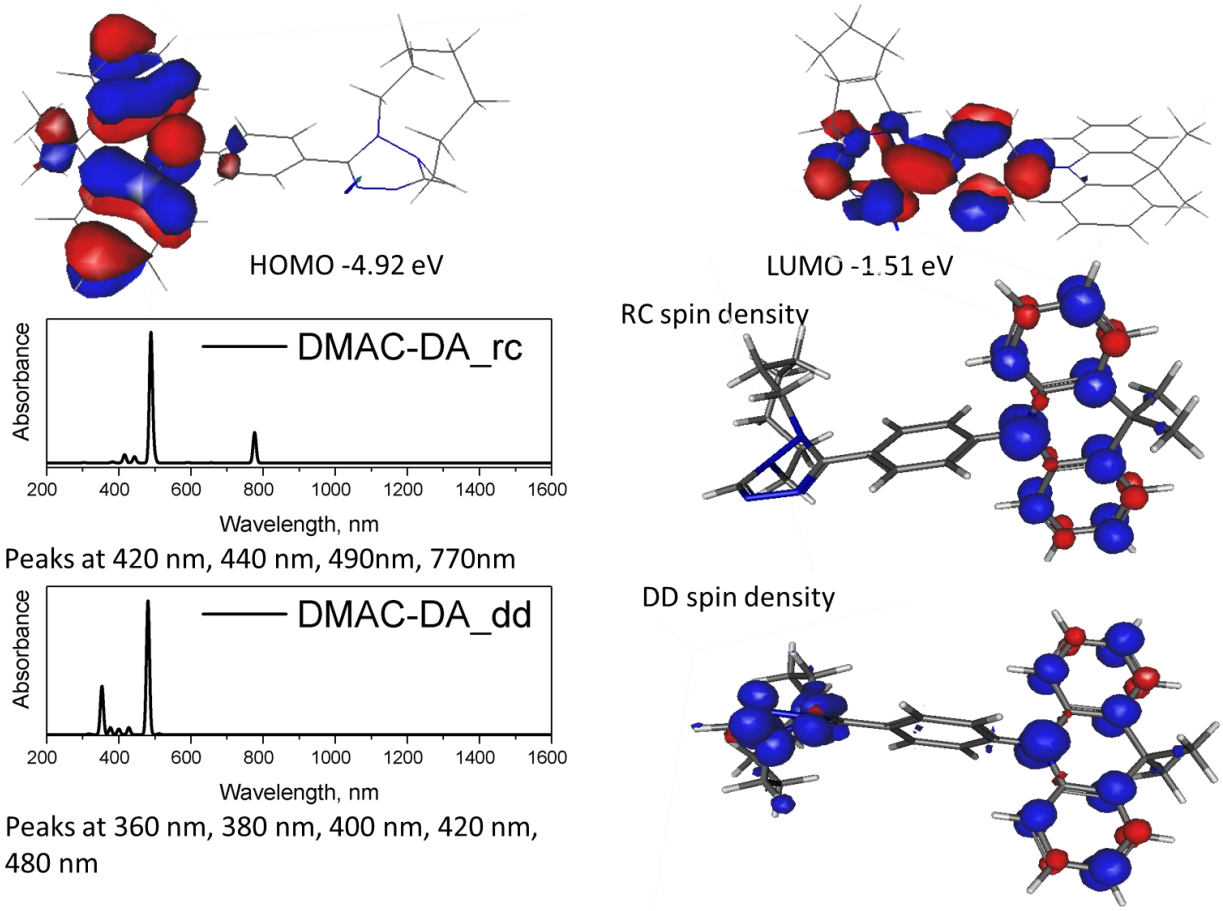

Figure S12. Calculation results for DMAC-DA

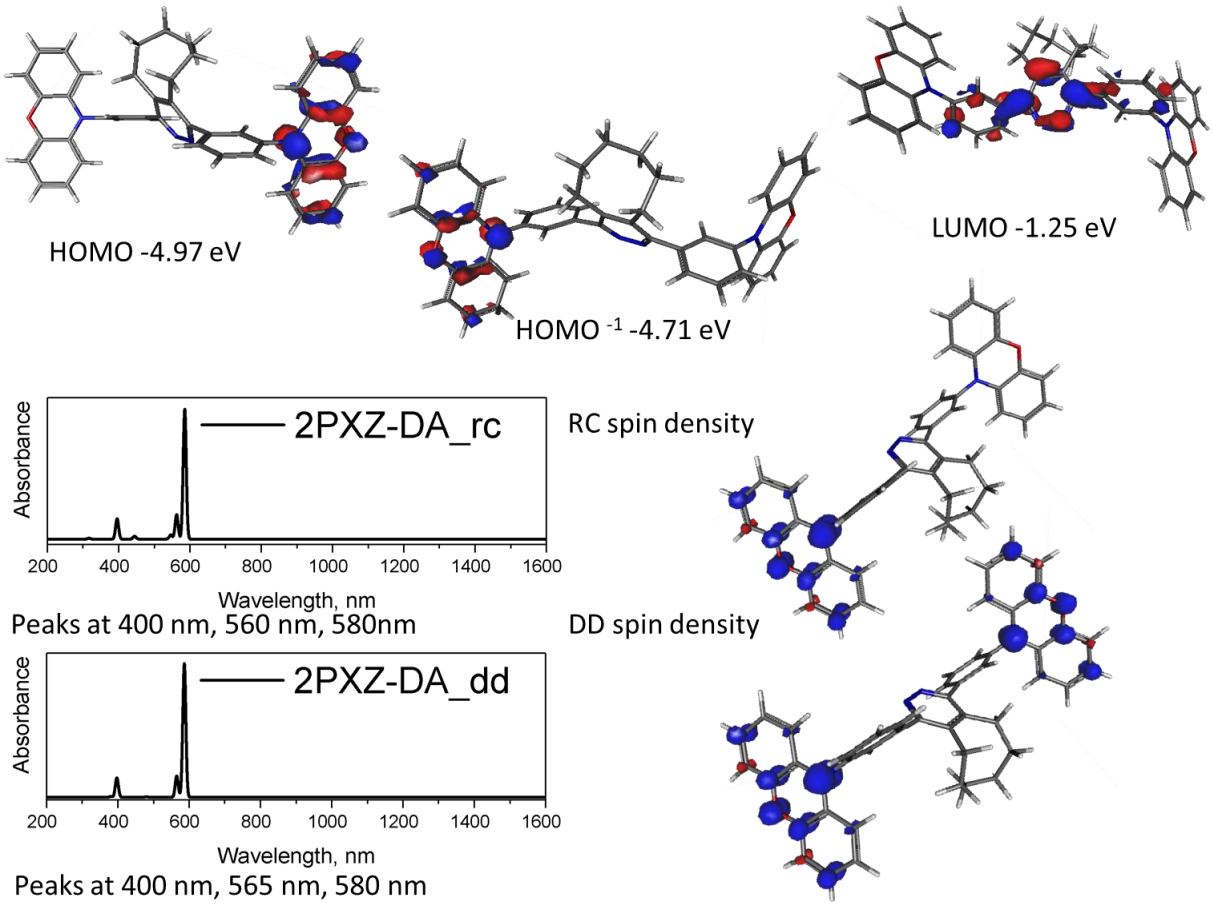

Figure S13. Calculation results for 2PXZ-DA

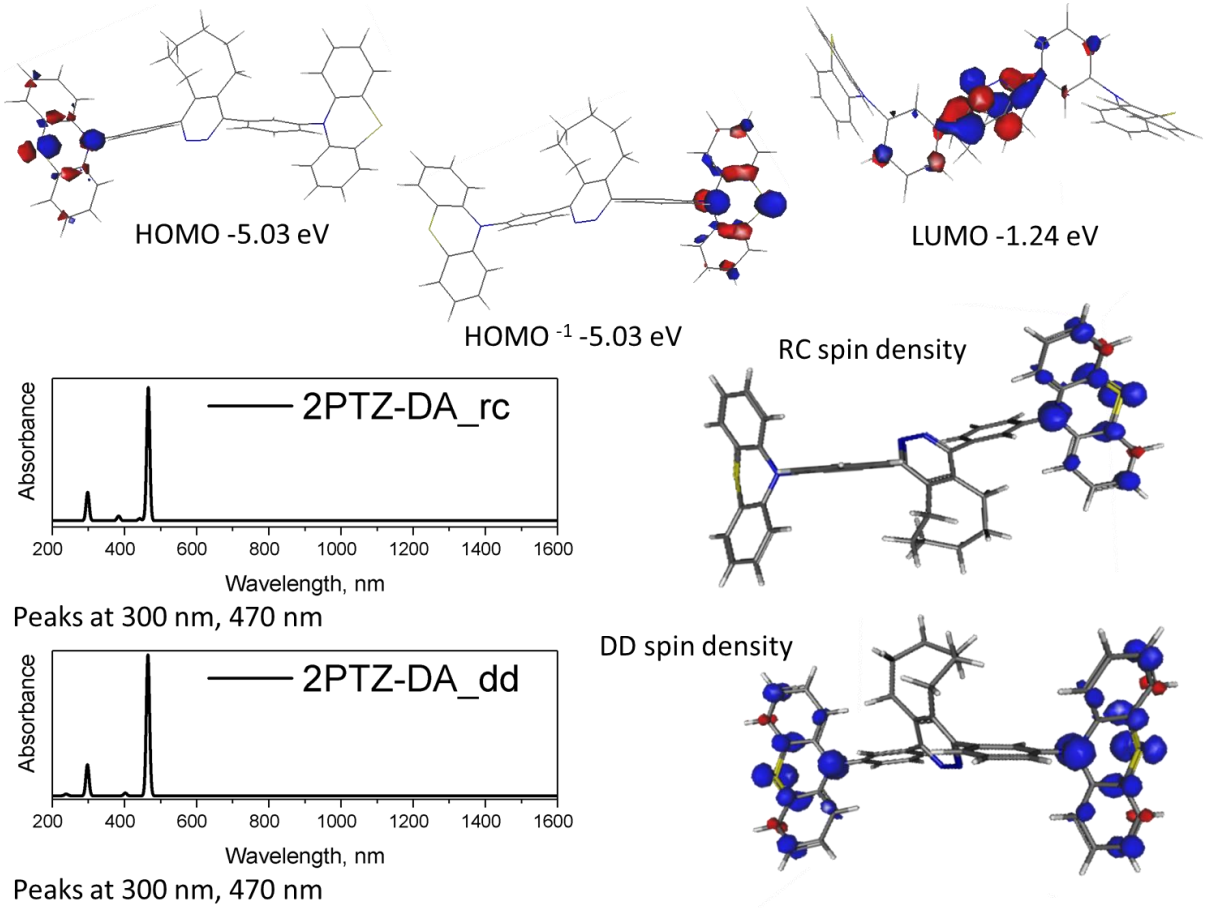

Table S14. Calculation results for 2PTZ-DA

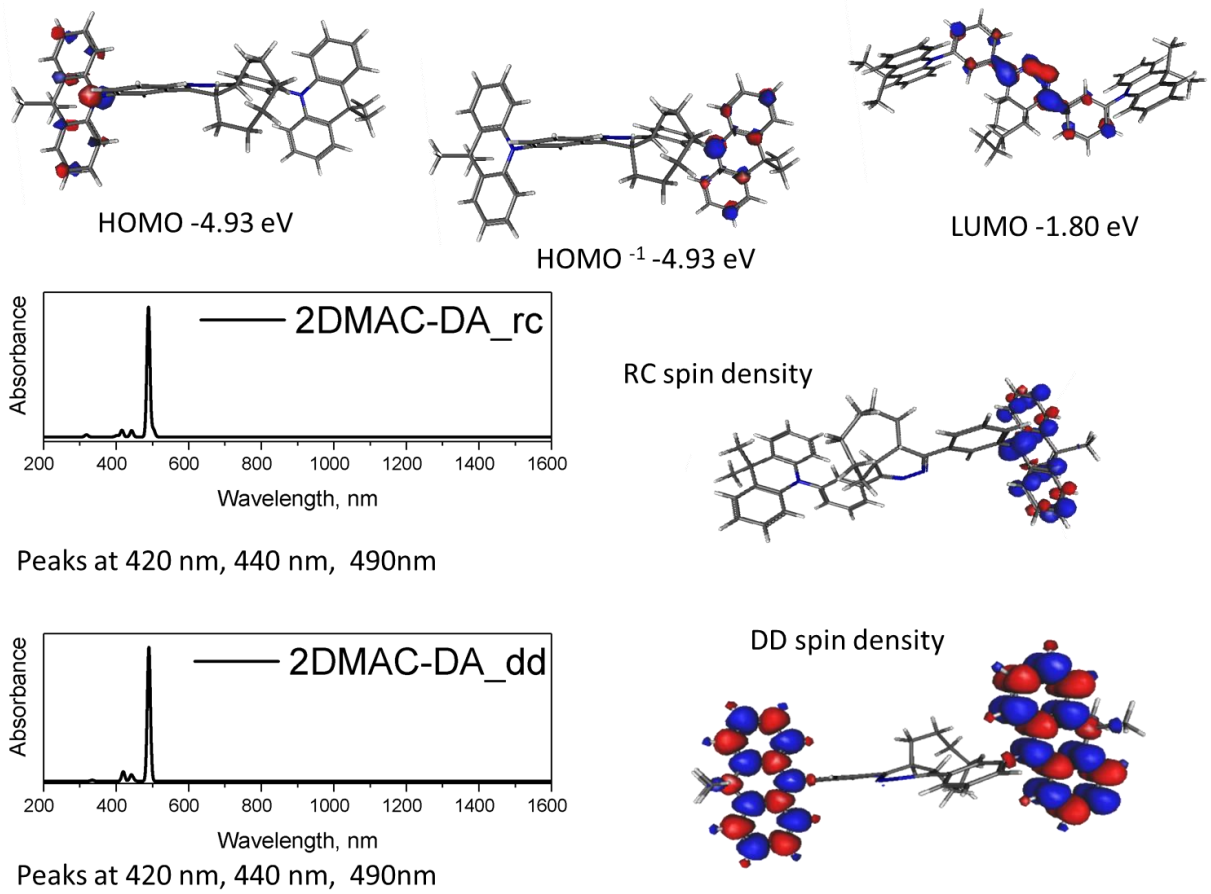

Figure S15. Calculation results for 2DMAC-DA

8.5 Supplement 5

DFT results of compounds based on TA acceptor unit.

Table S3. Calculated HOMO, LUMO levels of energy.

	HOMO, eV	HOMO $^{-1}$, eV	LUMO, eV	Dihedral angle	
CBZ-TA	-5.47		-2.10	50.1°	
PXZ-TA	-4.76		-2.86	75.6°	
PTZ-TA	-5.09		-2.87	95.8°	
DMAC-TA	-4.96		-2.86	88.7°	
2PXZ –TA	-4.70	-4.79	-1.98	79.1°	89.9°
2PTZ-TA	-5.03	-5.08	-1.96	83.1°	81.0°
2DMAC-TA	-4.95	-4.95	-2.80	87.5°	91.6°

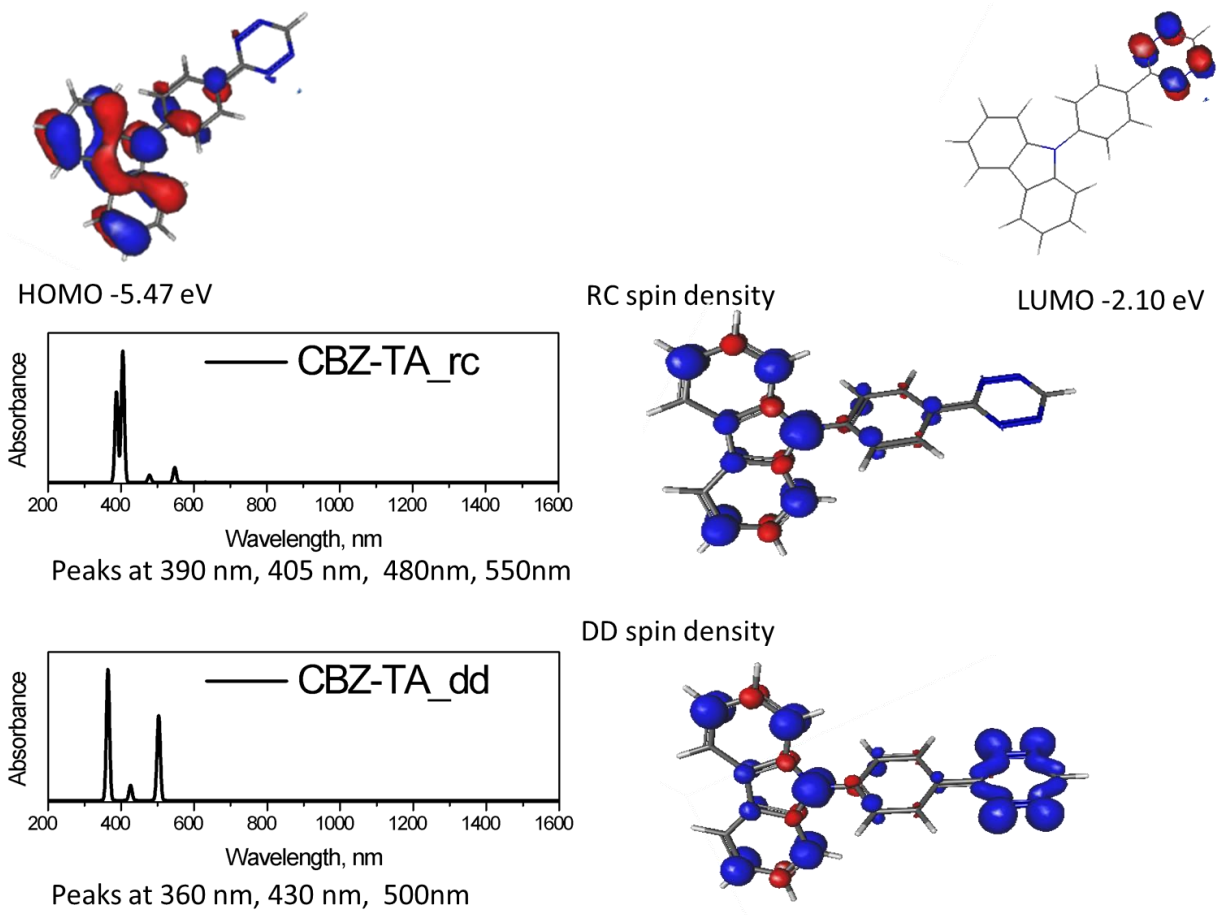

Figure S16. Calculation results for CBZ-TA

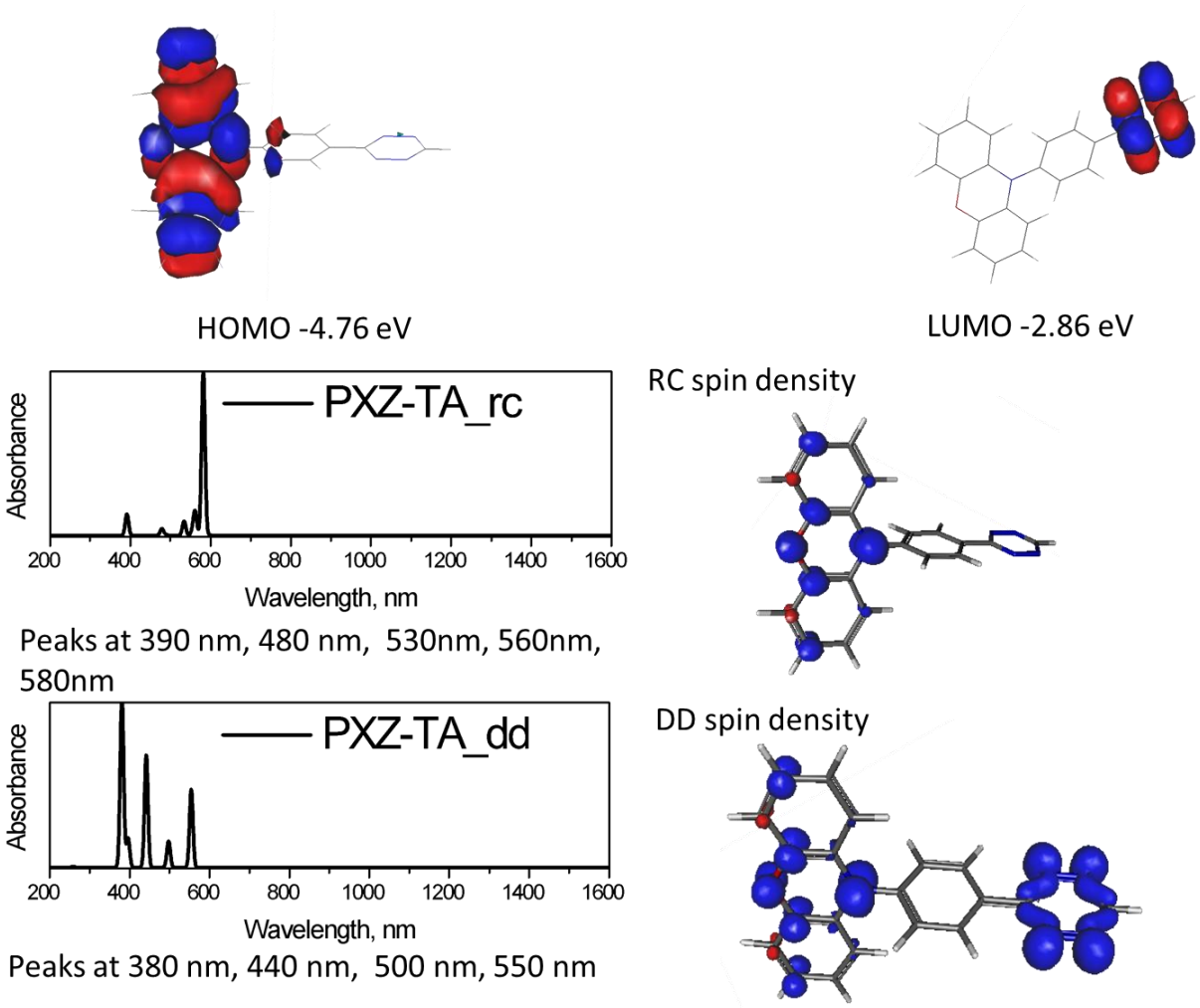

Figure S17. Calculation results for PXZ-TA

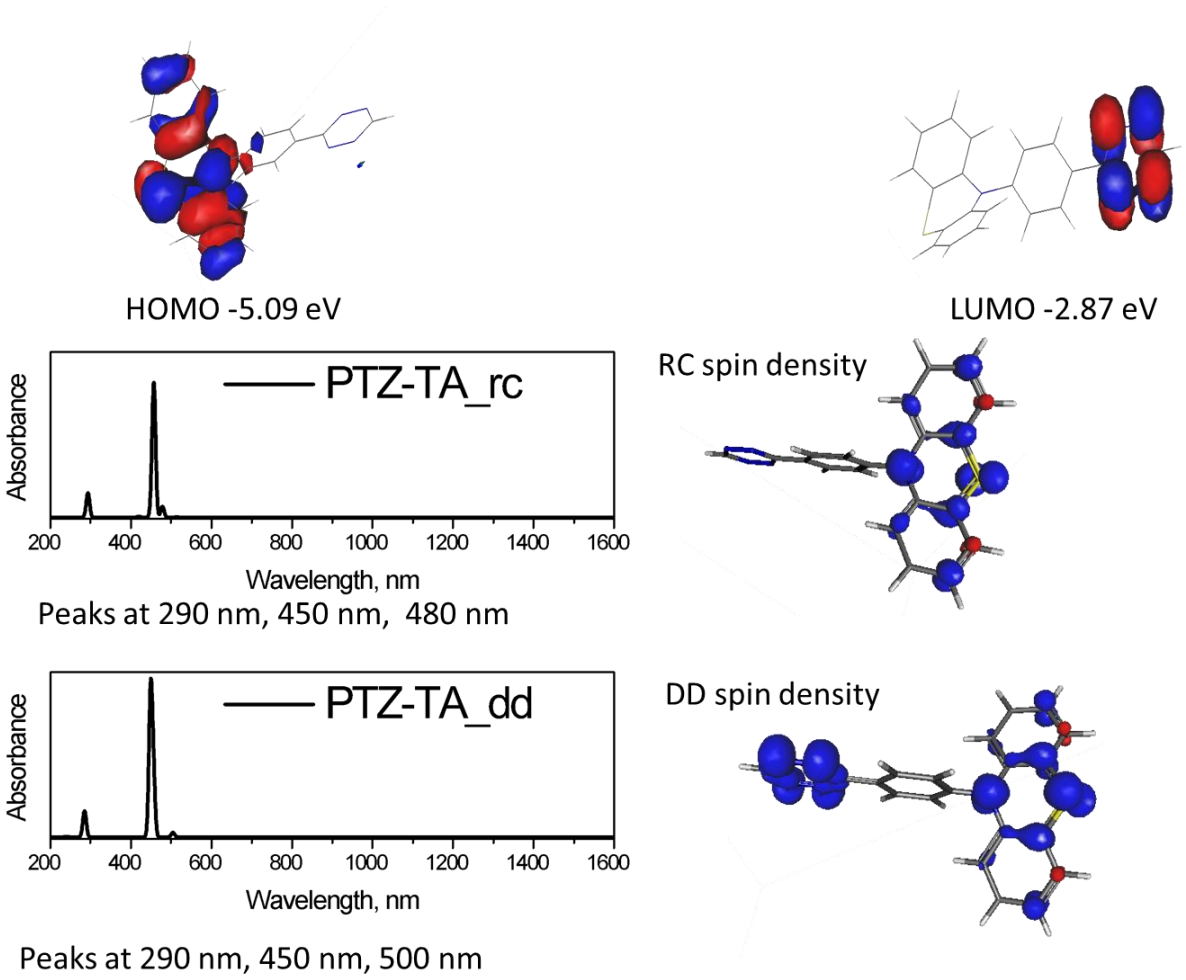

Figure S18. Calculation results for PTZ-TA

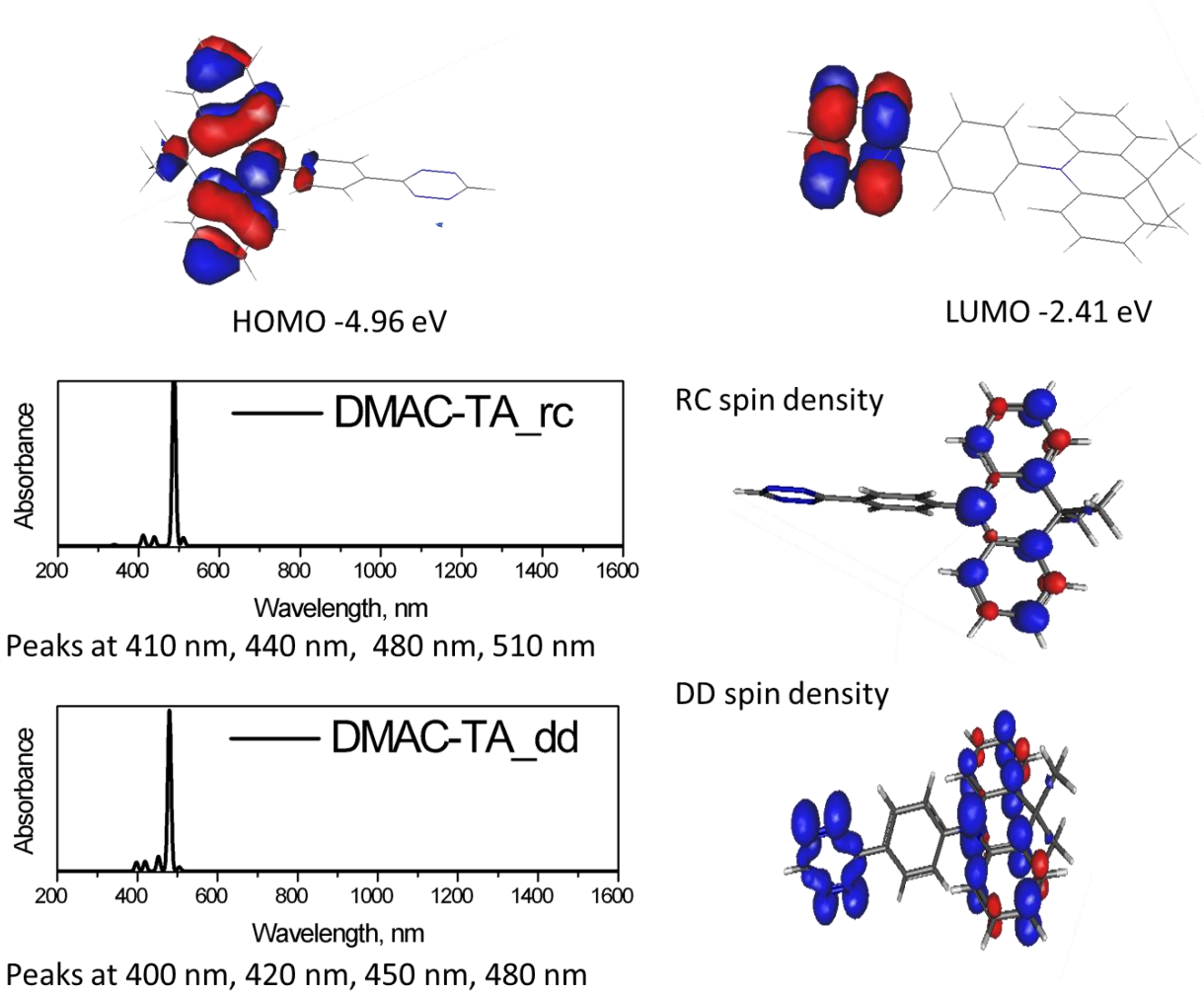

Figure S19. Calculation results for DMAC-TA

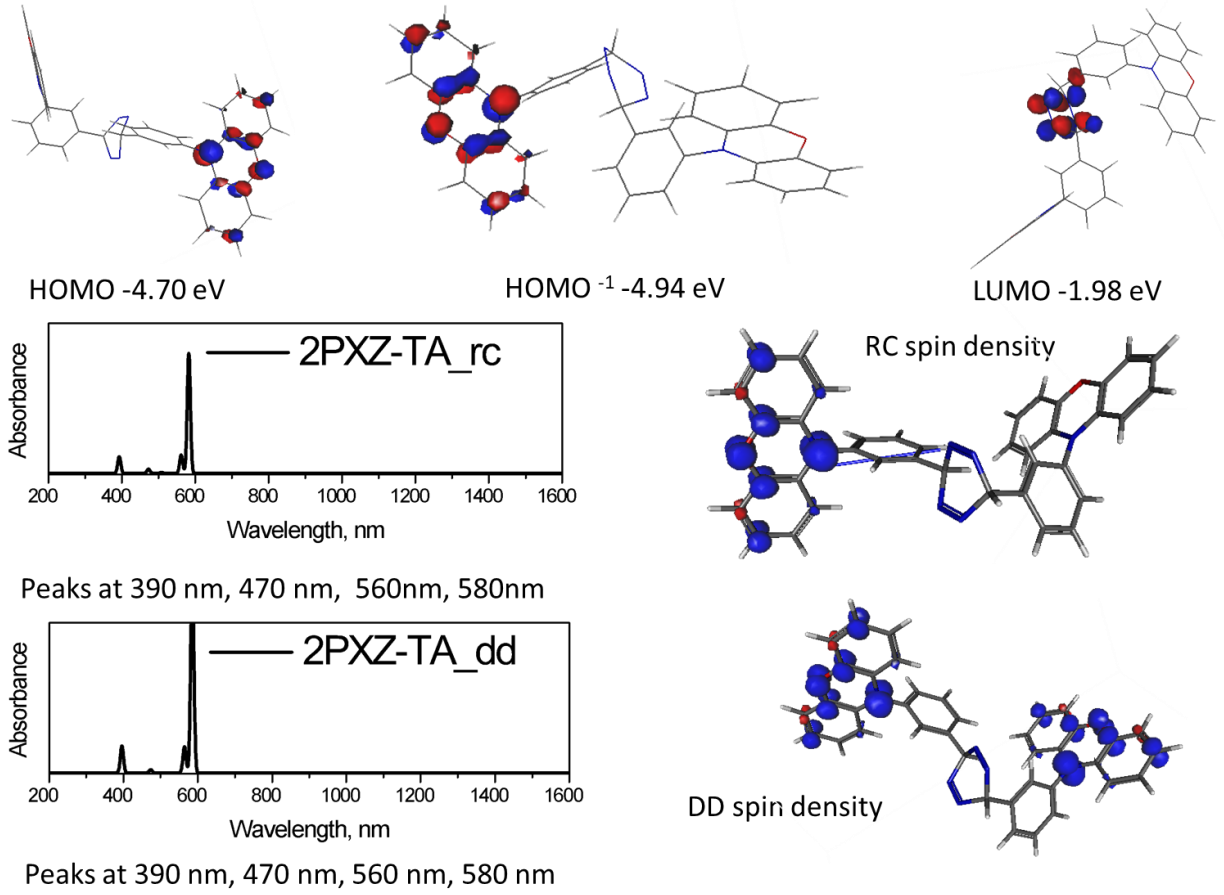

Figure S20. Calculation results for 2PXZ-TA

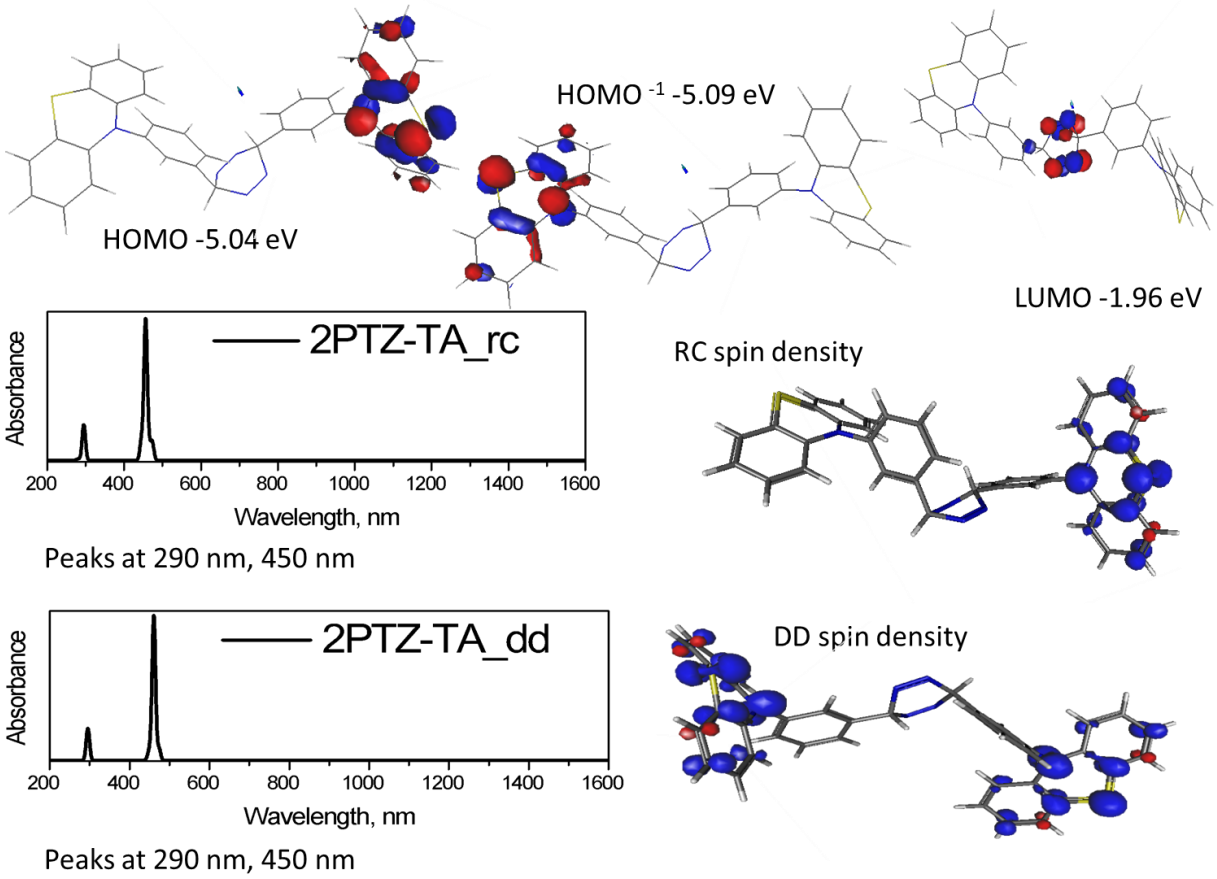

Figure S21. Calculation results for 2PTZ-TA

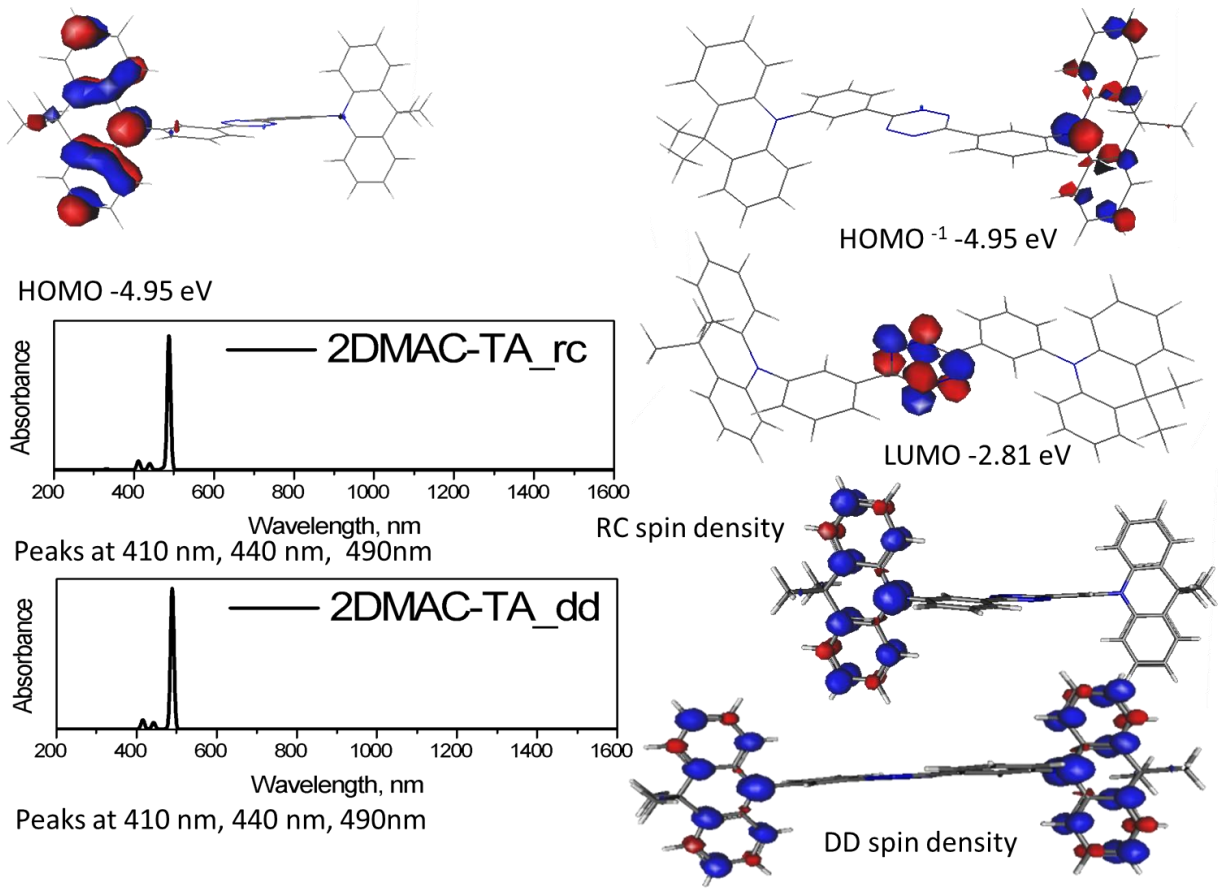

Figure S22. Calculation results for 2DMAC-TA